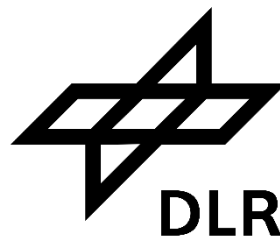


---

# **Flood mapping in rural and urban areas with multi-temporal SAR intensity and InSAR coherence**

---

Dissertation zur Erlangung des Doktorgrades  
an der Fakultät für Geowissenschaften  
der Ludwig-Maximilians-Universität München



Vorgelegt von

Yu Li

Aus Hubei, VR China

München, den 26.11.2019

Erstgutachter: Prof. Dr. Ralf Ludwig, LMU Munich

Zweitgutachter: Prof. Dr. Günter Strunz, German Aerospace Center (DLR)

Tag der mündlichen Prüfung: 11.08.2020



## Acknowledgements

The work presented in this thesis would not have been possible without the support and guidance of many people. I would like to express my sincere gratitude to all of them for their accompanying during the long and unforgettable PhD journey.

First of all, I would like to sincerely thank my supervisors, Prof. Dr. Ralf Ludwig and Prof. Dr. Günter Strunz for granting me the opportunity to pursue my PhD at LMU Munich and the German Aerospace Center (DLR). Their continuous support and help make the completion of this thesis possible.

I would like to extend my gratitude to my mentor Dr. Sandro Martinis for introducing me to this interesting and exciting research field of SAR remote sensing and natural disaster mapping. I appreciate his endless patience, support, and encouragement throughout my PhD. Without his guidance and constant feedback the research outcomes in this thesis would not have been achievable.

I am also grateful to my colleague Dr. Marc Wieland for sharing his knowledge and experience in computer vision and machine learning and offering me consistent valuable input. He inspired me a lot in method employment and development.

I gratefully acknowledge the China Scholarship Council (CSC) for funding my PhD. Many thanks also go to all my colleagues and friends at DLR, especially Dr. Simon Plank, Dr. Stefan Schlaffer, and Dr. Ryo Natsuaki from The University of Tokyo for their support and the enjoyable collaboration.

Finally, I would like to express my heartfelt to my family for their unlimited trust and love, especially to Chen, who has been by my side throughout the PhD with her full understanding and support.

## Summary

Remote sensing systems have been widely recognized as suitable resources to offer a synoptic view over large areas and provide valuable information on flood extent and dynamics. Synthetic aperture radar (SAR) sensors are most commonly used in flood mapping due to their day-night and all-weather imaging capability. Nowadays, the growing number of SAR satellite missions in orbit with high revisit rates facilitate rapid flood mapping in the context of emergency response. At the same time, more reliable and efficient methods are required to produce precise flood extent maps in operational activities. Urban areas with a high percentage of impervious surfaces are particularly vulnerable to flooding and at high risk of loss of human lives and property. However, the complicated backscattering mechanisms in urban areas make urban flood mapping challenging and call for more sophisticated methods.

This thesis presents an automatic and reliable change detection approach for flood mapping in rural areas based on SAR intensity and introduces two methods to map floodwater in urban areas by fusing multi-temporal SAR intensity and InSAR coherence. For rural flood mapping, a Jensen-Shannon (JS) divergence-based index is introduced to select an adequate pre-event reference image for change detection. A saliency-guided generalized Gaussian mixture model (SGGMM) is proposed to address the data imbalanced problem (e.g., the flooded area only covers a small fraction of the SAR scene). Finally, the fully-connected conditional random field (FCRF) is employed to incorporate global spatial information to smooth out false alarms and preserve the fine flooded structures simultaneously. Experiments of flood events at Evros River (Greece) and York (England) with Sentinel-1 Ground Range Detected (GRD) data demonstrate the effectiveness, efficiency, and robustness of the proposed method.

The fusion of multi-temporal SAR intensity and InSAR coherence in urban flood

## Summary

---

mapping is investigated through deep Convolutional Neural Network (CNN) and Bayesian Network. Multi-temporal intensity and coherence are fused at the image level with a Convolutional Neural Network (CNN), whereas these two information sources are combined at the decision level via a Bayesian Network. Experiments conducted on a flood event in Houston (US) based on TerraSAR-X and Sentinel-1 data as well as in Joso (Japan) based on ALOS-2/PALSAR-2 data demonstrate that coherence can profitably complement intensity for urban flood mapping.

In the scenario that limited labeled training samples are available in urban flood mapping, a novel active self-learning (A-SL) temporal-ensembling CNN framework is proposed to improve the classification accuracy. Within this framework, informative samples are queried from unlabeled data and subsequently filtered and pseudo-labeled. This procedure is iterated several times until a stop criterion is met. Experiments on Houston (US) flood event with TerraSAR-X data illustrate that the proposed framework outperforms its pure supervised counterpart significantly without any extra human efforts. An unsupervised Bayesian Network fusion method is proposed for the operational activities that no training samples are available. Image segmentation is first performed on the stacked intensity and coherence series based on the finite Gaussian mixture model (GMM). Subsequently, the flood probability of each Gaussian component is estimated with the change information between pre- and co-event intensity and coherence. The final flood posterior probability of each pixel is calculated through the Bayes rule. Moreover, the contributions of intensity and coherence in flood mapping at each pixel can be visualized through the posterior probability based on each information. Experiments on Houston (US) flood event based on Sentinel-1 data and Joso (Japan) flood event based on ALOS-2/PALSAR-2 data show satisfactory mapping results with the proposed method, however, some special flood situations such as flooded parking lots and very dense building blocks are still hard to detect.

## Contents

<b>Acknowledgements .....</b>	<b>I</b>
<b>Summary.....</b>	<b>II</b>
<b>Contents .....</b>	<b>IV</b>
<b>List of Figures.....</b>	<b>VI</b>
<b>List of Tables.....</b>	<b>VII</b>
<b>List of Abbreviations.....</b>	<b>VIII</b>
<b>1. Introduction.....</b>	<b>1</b>
1.1 Background and Motivation.....	1
1.2 Research objectives.....	11
1.3 Thesis structure .....	12
<b>2. Synthetic Aperture Radar imaging system.....</b>	<b>14</b>
2.1 Basic principles of SAR.....	14
2.2 Image geometry.....	16
2.3 Backscattering signal .....	17
2.3.1 Surface scattering.....	18
2.3.2 Volume scattering.....	19
2.3.3 Hard target scattering.....	20
2.3.4 Speckle effect.....	21
2.4 Interferometric coherence .....	21
<b>3. Physical principles of flood mapping with SAR intensity and InSAR coherence .....</b>	<b>24</b>
3.1 Flood mapping with SAR intensity.....	24
3.2 Flood mapping with InSAR coherence.....	33
<b>4. An automatic change detection approach for rapid flood mapping in Sentinel-1 SAR data.....</b>	<b>36</b>
<b>5. Urban flood mapping with an active self-learning convolutional neural network based on TerraSAR-X intensity and interferometric coherence .....</b>	<b>50</b>
<b>6. Urban flood mapping using SAR intensity and interferometric coherence via Bayesian network fusion .....</b>	<b>65</b>
<b>7. Conclusion and Outlook.....</b>	<b>88</b>
7.1 Conclusion .....	88
7.2 Outlook .....	91

## **Contents**

---

<b>References .....</b>	<b>93</b>
<b>Curriculum Vitae .....</b>	<b>110</b>

## List of Figures

Fig. 1.1 Global distribution of recorded flood events during 1985 - 2018, darker blue means more frequent occurrence. (data source: Dartmouth Flood Observatory). .....	2
Fig. 1.2 Percentage of different types of disasters in each continent during 2008 - 2017 (data source: EM-DAT The Emergency Events Database). .....	3
Fig. 1.3 Timeline of a river flood event and GFP product types to support disaster risk reduction before and during the event (based on Alfieri et al., 2018). ....	5
Fig. 1.4 Summary of spaceborne SAR missions with different wavelength bands. ....	7
Fig. 2.1 Illustration of the SAR imaging geometry. ....	16
Fig. 2.2 Terrain distortions in SAR image. ....	17
Fig. 2.3 Common scattering mechanisms of land surfaces. ....	18
Fig. 3.1 Schematic illustration of dominant backscattering mechanisms of short (e.g., X/C) and long (e.g., L/P) wavelength electromagnetic signals for various land cover under non-flood and flood conditions (adapted from Schumann and Moller, 2015). ....	25
Fig. 3.2 Shadow (AB) and layover (CD) regions in a flooded road (AD) between adjacent buildings of height $h_1$ and $h_2$ , $\theta$ is the incidence angle (adapted from Mason et al., 2014). ....	31
Fig. 3.3 Composition of different contributions from a building in the SAR slant range (adapted from Guida et al., 2010). BW, backscattering from wall; BR, backscattering from roof; BG, backscattering from ground; D, double-bounce scattering; T, triple scattering; S, shadow; $L_r$ , slant range size of layover; $S_r$ , slant range size of shadow. ....	31
Fig. 3.4 Illustration of aspect angle $\phi$ of a building. The buildings in gray are oriented parallel to the azimuth direction with $\phi = 0^\circ$ , while the buildings with black lines are rotated counterclockwise by $\phi$ with respect to the azimuth direction (adapted from Brunner et al., 2010). ....	32

## List of Tables

Table 1.1 Summary of some key literature in flood mapping with SAR-based change detection .....	9
Table 1.2 Summary of literature in urban flood mapping with SAR data .....	10
Table 2.1 Microwave bands used for radar systems. ....	14

## List of Abbreviations

Acronym	Description
ALOS	Advanced Land Observing Satellite
APRSAF	Asia-Pacific Space Agency Forum
ASAR	Advanced Synthetic Aperture Radar
A-SL	Active Self-Learning
CEOS	Committee on Earth Observation Satellites
CNES	National Center for Space Studies
CNN	Convolutional Neural Network
CRED	Centre for Research on the Epidemiology of Disasters
CRF	Conditional Random Field
DEM	Digital Elevation Model
DLR	Deutsches Zentrum für Luft- und Raumfahrt (German Aerospace Center)
EM	Expectation-Maximization
EMS	Emergency Management Service
ENVISAT	Environmental Satellite
ERS	European Remote Sensing
ESA	European Space Agency
EU	European Union
FCRF	Fully-connected Conditional Random Field
GFP	Global Flood Partnership
GMM	Gaussian Mixture Model
GO	Geometrical Optics
GPU	Graphics Processing Unit
GRD	Ground Range Detected
IDMC	Internal Displacement Monitoring Centre
IPCC	Intergovernmental Panel on Climate Change



## List of Abbreviations

---

JS	Jensen-Shannon
KI	Kittler-Illingworth
MLE	Maximum Likelihood Estimator
MODIS	Moderate Resolution Imaging Spectroradiometer
MRF	Markov Random Field
NASA	National Aeronautics and Space Administration
NDVI	Normalized Difference Vegetation Index
NISAR	NASA-ISRO Synthetic Aperture Radar
PALSAR	Phased Array type L-band Synthetic Aperture Radar
RP	Return Period
SAR	Synthetic Aperture Radar
SGGM	Saliency-guided Generalized Gaussian Mixture Model
SNR	Signal to Noise Ratio
UN-SPIDER	United Nations Platform for Space-based Information for Disaster Management and Emergency Response
VGI	Volunteered Geographic Information
ZKI	Zentrum für satellitengestützte Krisensinformation (Center for Satellite Based Crisis Information)

# 1. Introduction

## 1.1 Background and Motivation

Natural disasters are increasing in frequency and severity in the modern world. The impacts of disaster events on human lives and the economy are increasing globally due to growing urbanization and an increase in extreme weather events (CEOS, 2015). The increased demand for crisis information on natural disasters has been recognized worldwide. The United Nations program “United Nations Platform for Space-based Information for Disaster Management and Emergency Response – UN-SPIDER” (<http://www.un-spider.org/>) was established in December 2006. Along with such UN programs, increased regional and international activities have been developed to provide crisis information and mapping services for natural disaster management using space-based data and technology. The International Charter “Space and Major Disasters” (<http://www.disasterscharter.org>) was initiated by the European Space Agency (ESA) and the National Center for Space Studies (CNES) after the UNISPACE III conference in 1999, which aims to provide a unified system for the rapid acquisition and delivery of satellite data to support disaster response effort. The “Sentinel Asia” (<https://sentinel.tksc.jaxa.jp>) was proposed in 2004 by the Asia-Pacific Space Agency Forum (APRSAF), aiming to support disaster management activity in the Asia-Pacific region by applying the WEB-GIS and space-based technology. The “SERVIR” program (<https://www.servirglobal.net>) developed in 2004 at the National Aeronautics and Space Administration (NASA) provides satellite-based critical information for rapid response and damage assessment from natural disasters. Also, services such as the European Union’s (EU) Copernicus Emergency Management Service (CEMS) and the Center for Satellite-Based Crisis Information (ZKI) of the German Aerospace Center (DLR) provide satellite-based information for emergency response in the context of disaster management, civil protection, and relief organization.

## Introduction

Floods have affected more people than any other type of natural disaster in the 21<sup>st</sup> century. In 2018 alone, there were 315 natural disaster events recorded with over 68 million people affected and US \$131.7 billion in economic losses across the globe (CRED, 2018). Floods were the most frequent (127 events) disasters among these events and affected the highest number of people, accounting for 50% (34.2 million) of the total affected with US \$19.7 billion economic losses. Flood is not only frequent but also widespread and spatially heterogeneous. The data of large flood events during 1985 - 2018 recorded by the Dartmouth Flood Observatory (DFO) shows that the US, China, India, Indonesia, and the Philippines are the five countries most frequently hit by floods (Fig. 1.1). Over the last decade (2008 - 2017), floods were the largest portion of the total disasters in Africa (47%), Asia (41%), Europe (41%) and Americas (36%) according to the Emergency Events Database (EM-DAT, 2019) (Fig. 1.2).

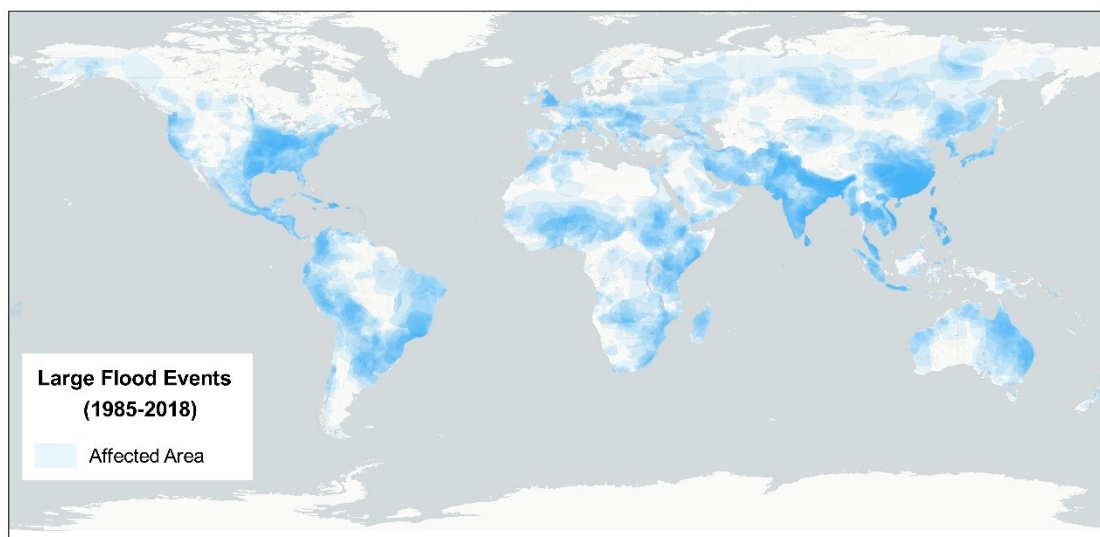


**Fig. 1.1** Global distribution of recorded flood events during 1985 - 2018, darker blue means more frequent occurrence. (data source: Dartmouth Flood Observatory).

Flood is defined as “the overflowing of the normal confines of a stream or other body of water, or the accumulation of water over areas that are not normally submerged. Floods include river (fluvial) floods, flash floods, urban floods, pluvial floods, sewer floods, coastal floods, and glacial lake outburst floods” (IPCC, 2012). Flood is a complex phenomenon and affected by various characteristics of precipitation (e.g., intensity, duration, amount, timing, and phase – rain or snow) and temperature

## Introduction

patterns (responsible for soil freezing, snow/ice melt, and ice jam formation). Floods are also affected by drainage basin conditions such as water levels in the rivers, snow and ice cover, soil characteristics and status (soil moisture and vertical distribution), soil sealing, and the existence of dikes, dams, and reservoirs (Bates et al., 2008; Kundzewicz et al., 2014). Climate change might be a significant driver of changes in flood frequency (Hall et al., 2014; Merz et al., 2014; Viglione et al., 2016). A recent study (Willner et al., 2018) has indicated that climate change will put tens of millions more people across the world at risk of exposure to river floods over the next 25 years. River engineering such as dikes and reservoirs that regulate the flow of rivers and land use may also affect floods (Hossain et al., 2009; Kundzewicz et al., 2014; Rogger et al., 2017).

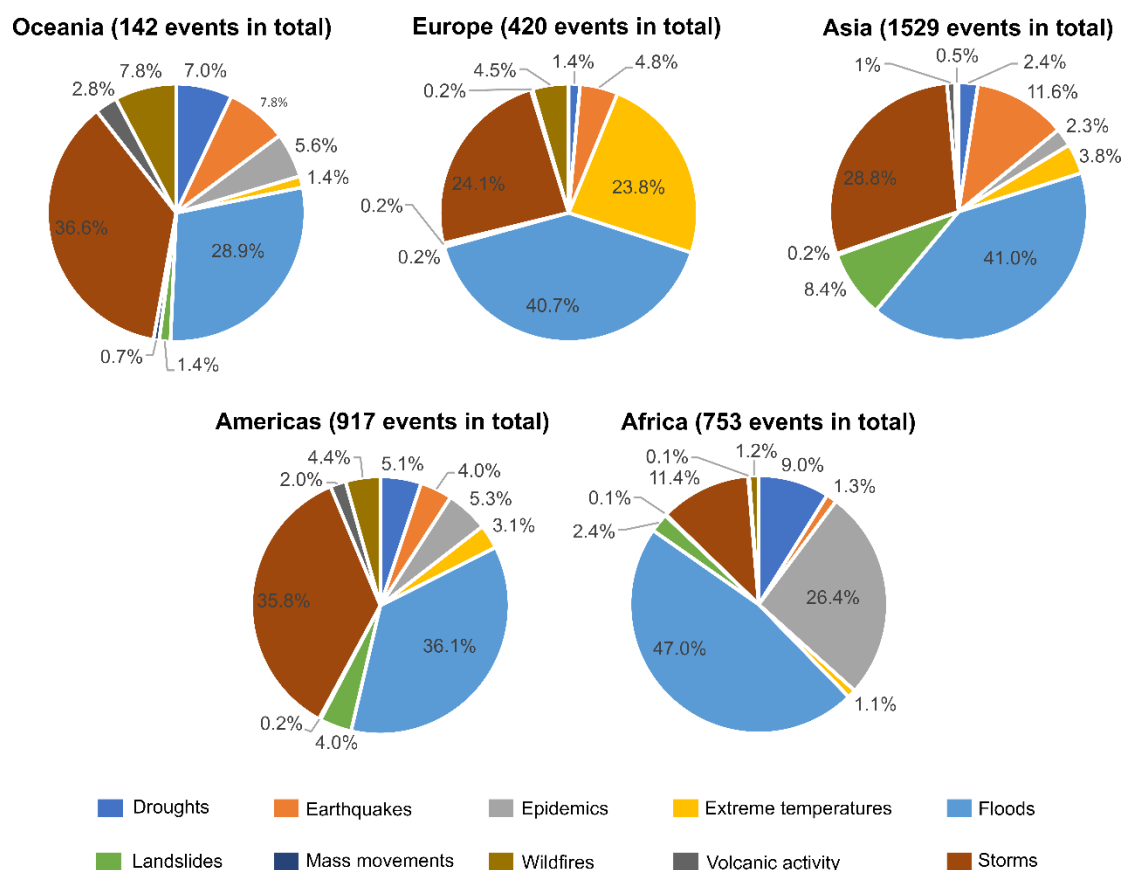


**Fig. 1.2 Percentage of different types of disasters in each continent during 2008 - 2017 (data source: EM-DAT The Emergency Events Database).**

Urban flooding is a special type of flood that differs from flooding in rural areas as

## Introduction

---

urbanization leads to an adverse impact on hydrological processes, increasing flood risk and causing serious losses (Chen et al., 2015; Grove et al., 2001). Urban flooding can occur due to heavy rainfall, river overbank flow, and high tides or storm surges (Tingsanchali, 2012). Large impervious surface areas across cities severely reduce the capacity of local landscapes to absorb, store, infiltrate, and detain rainwater, exacerbating urban runoff and leading to an increase of flood peaks and significant flood damages (Jiang et al., 2018; Pauleit and Duhme, 2000; Tingsanchali, 2012). According to the Global Report on Internal Displacement 2019 (IDMC, 2019), there are on average 17.8 million people worldwide at risk of being displaced by floods every year, 80% (14.2 million) live in urban and peri-urban areas. Flood displacement risk is highest in South Asia, East Asia, and the Pacific. Large cities are found along rivers, in deltas, and along the coast. By 2050, 70% of the world population is projected to live in an urban environment. The global urban area is expected to expand by more than 70%, not only in riparian and coastal areas and in deltas, but also in water-stressed regions such as drylands (Ligtvoet et al., 2018). The average annual losses of the ten cities with the highest flood loss in 2050 are projected to over US \$39 billion (Hallegatte et al., 2013). Therefore, urban flooding has severe economic and human impacts and should be drawn more attention in the context of flood disaster mapping and management.

Spaceborne remote sensing furnishes valuable information and a reliable way for monitoring flood disasters in a time- and cost-efficient manner over large-scale areas, thanks to the increasing spatial/temporal resolution and data variability of the variety of satellite sensors. As mentioned at the beginning of this chapter, several international and regional activities have largely leveraged satellite data in emergency response of natural disasters including floods. The Global Flood Partnership (GFP, <https://gfp.jrc.ec.europa.eu>) is an open international group of academics, research institutes, practitioners, public and private organizations that aims to improve the future flood management worldwide (Alfieri et al., 2018; De Groeve et al., 2015).

## Introduction

The GFP network uses multi-source data and various toolboxes in supporting flood risk management and satellite data plays a significant role in discharge estimation and inundation mapping during the peak of flood inundation period (Fig. 1.3) (Alfieri et al., 2018).

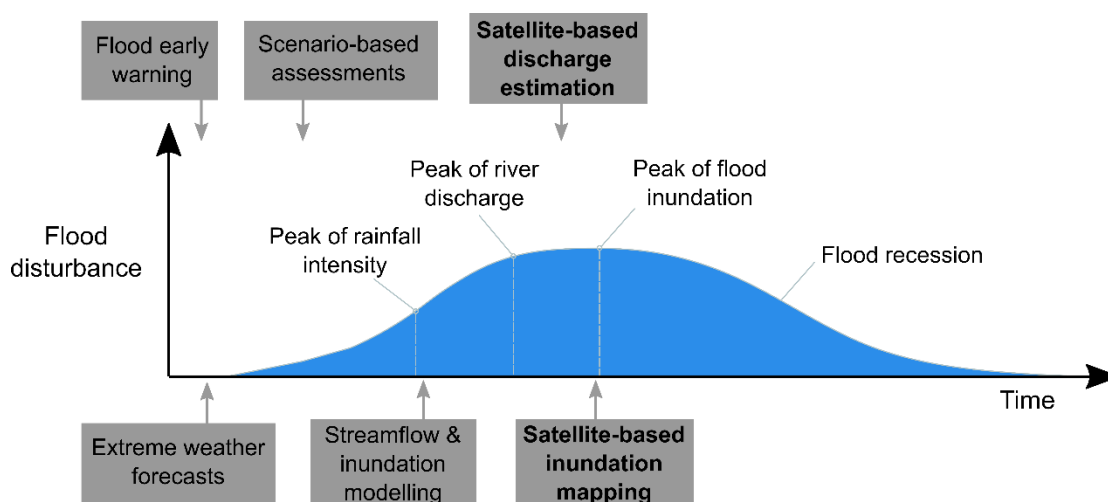


**Fig. 1.3 Timeline of a river flood event and GFP product types to support disaster risk reduction before and during the event (based on Alfieri et al., 2018).**

Both optical and synthetic aperture radar (SAR) data have been successfully applied in flood monitoring (Joyce et al., 2009; Klemas, 2015; Smith, 1997; Tralli et al., 2005). Optical data has the advantage of data availability back to the 1970s as many optical sensors have been launched by governments or commercial companies since that time (Christopherson et al., 2019). Another advantage of optical data compared to SAR data in flood monitoring is that the spectral signature of floodwater is more straightforward and easier to interpret. The NASA Near Real-Time Global Flood Mapping System (<https://floodmap.modaps.eosdis.nasa.gov/>) provides global flood water at approximately 250 m resolution at daily time steps, based on the twice-daily overpass of the Moderate Resolution Imaging Spectroradiometer (MODIS) instrument on-board the Terra and Aqua satellites (Nigro et al., 2014). Mid-resolution (e.g., Landsat Thematic Mapper), high-resolution (e.g., Sentinel-2), and very high-resolution optical sensors (e.g., IKONOS, WorldView-2) have been widely used

## Introduction

---

for flood mapping at a smaller scale (Amini, 2010; Drusch et al., 2012; Malinowski et al., 2015; Ogashawara et al., 2013; Sadek and Li, 2019; Thomas et al., 2011; Volpi et al., 2013; Wang, 2004; Wieland and Martinis, 2019). However, flood events are usually accompanied by bad weather with long-lasting cloud coverage. This factor hampers the systematic usability of optical data in flood mapping and monitoring, especially in the context of emergency response. Moreover, floodwater beneath vegetation canopies is hardly detectable by optical data due to its weak penetration capability. In contrast to optical sensors, SAR systems are configured as active sensing instruments that have day/night all-weather imaging capability. Microwaves of SAR sensors have a higher penetration capability than the visible, infrared and thermal spectrum, which can penetrate vapors and clouds thus providing coherent monitoring of the flood extent. The high penetration capability also enables SAR sensors to capture the flood conditions under vegetation canopies in some cases (Canisius et al., 2019; Martinez and Le Toan, 2007; Plank et al., 2017; Tsyganskaya et al., 2018a; Voormansik et al., 2014; Wang et al., 1995).

SAR satellite sensors operate at designated microwave frequencies in the X-band (8 - 12.5 GHz), C-band (4 - 8 GHz), and L-band (1 - 2 GHz) domain. More than 20 spaceborne SAR missions have been launched or are going to be launched in the near future, as shown in Fig. 1.4. The increasing spatial resolution and revisit frequency enable SAR satellites to monitor more detailed information of flood dynamics. Some SAR missions such as TerraSAR-X/TanDEM-X and Cosmo-SkyMed can provide data with a spatial resolution of lower than 1 m, which can capture very detailed characteristics of land surface and are suitable for mapping flood in complicated environments such as urban areas. The long-wavelength missions such as ALOS-2/PALSAR-2, and the planned missions NISAR and TanDEM-L are useful to map flooded vegetation. The Sentinel-1 mission with a high repetition rate (6-day with the constellation of Sentinel-1A and -1B) and systematic observation scenario is proper for operational purposes, enabling the rapid provision of the inundation extent

## Introduction

during disaster response.

Even if SAR data interpretation and processing is not easy due to the inherent speckle effect and the side-looking geometry there has been a huge success in flood mapping within the last years. Usually, change detection is used for reducing false alarm caused by water look-alike objects and for isolating the floodwater from permanent water bodies. Some key literature of flood mapping with SAR-based change detection is summarized in Table 1.1. According to the studies in the literature, contextual information is beneficial to achieve a precise flood map. How to integrate appropriate contextual information effectively and efficiently needs further exploration.

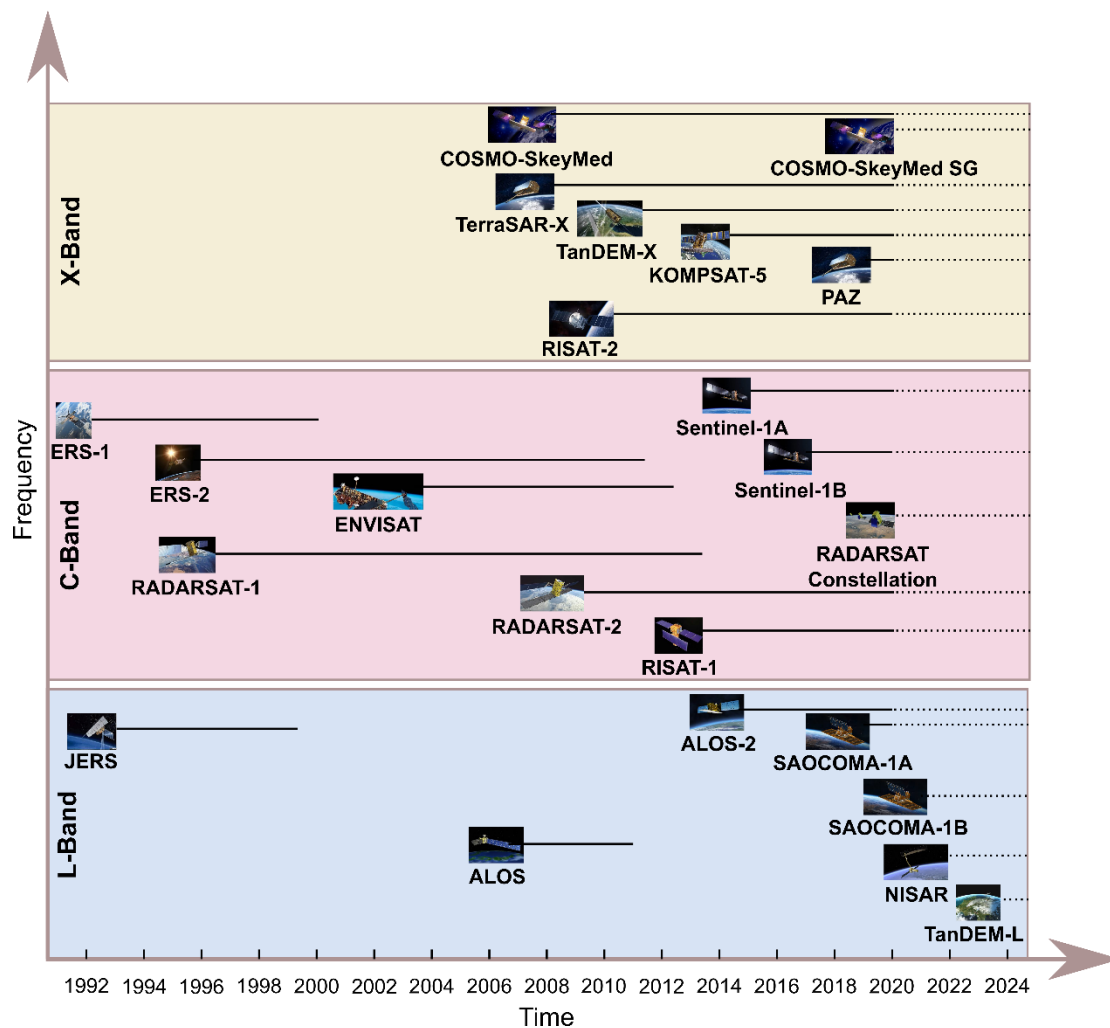


Fig. 1.4 Summary of spaceborne SAR missions with different wavelength bands.



## **Introduction**

---

Furthermore, most works in the literature and the current existent flood mapping service such as the Sentinel-1 Flood Service (Twele et al., 2016) of the German Aerospace Center (DLR) only focus on flood mapping in rural areas. Studies of SAR-based urban flood mapping are rarely found in the literature, Table 1.2 summarizes the relevant studies. It is known that it is challenging to map floodwater in urban areas with SAR intensity due to the complicated backscattering mechanisms associated with the varying land cover types and object structures. Some previous studies in Table 1.2 demonstrate that the employment of InSAR coherence seems to pave the way for improving flood mapping in urban areas. The valuable information from InSAR coherence needs further understanding experimentally and theoretically. It is also indispensable to develop new data fusion and classification methods to effectively leverage SAR intensity and InSAR coherence in urban flood mapping.

## Introduction

**Table 1.1 Summary of some key literature in flood mapping with SAR-based change detection**

Study	Data source	Methods	Key results
Bazi et al., 2005	ERS-2	<ul style="list-style-type: none"> <li>- Log-ratio operator</li> <li>- Generalized Gaussian model</li> <li>- Kittler-Illingworth (KI) threshold</li> </ul>	<ul style="list-style-type: none"> <li>- Generalized Gaussian distribution performs better than Gaussian distribution</li> <li>- Automatic and simple method</li> </ul>
Moser and Serpico, 2009	SIR-C XSAR	<ul style="list-style-type: none"> <li>- Ratio operator</li> <li>- Expectation-maximization (EM)</li> <li>- Markov random field (MRF)</li> </ul>	<ul style="list-style-type: none"> <li>- Unsupervised contextual method</li> <li>- Log-Normal, Nakagami-ratio, and Weibull-ratio models perform similarly</li> <li>- MRF yields higher accuracy</li> </ul>
Matgen et al., 2011	ENVISAT-ASAR RADARSAT-1	<ul style="list-style-type: none"> <li>- Difference operator</li> <li>- Iterative threshold</li> <li>- Region growing</li> </ul>	<ul style="list-style-type: none"> <li>- Outperforms manual approached</li> <li>- Automatic and reliable approach</li> </ul>
Martinis et al., 2011	TerraSAR-X	<ul style="list-style-type: none"> <li>- Normalized change index</li> <li>- Tile-based KI threshold</li> <li>- MRF</li> </ul>	<ul style="list-style-type: none"> <li>- Achieve high classification accuracy</li> <li>- Unsupervised and efficient method</li> <li>- MRF increases classification accuracy</li> </ul>
Long et al., 2014	ENVISAT-ASAR	<ul style="list-style-type: none"> <li>- Difference operator</li> <li>- Mean and standard deviation based threshold</li> <li>- Segmentation</li> </ul>	<ul style="list-style-type: none"> <li>- Very simple and fast method</li> <li>- Map flooded vegetation</li> <li>- Monitor flood dynamics</li> </ul>
Schlaffer et al., 2015	ENVISAT-ASAR	<ul style="list-style-type: none"> <li>- Harmonic analysis</li> <li>- Otsu threshold</li> </ul>	<ul style="list-style-type: none"> <li>- Noise is greatly reduced by using time series data</li> <li>- Do not need manually select a pre-flood reference</li> </ul>
Chini et al., 2017	ENVISAT TerraSAR-X	<ul style="list-style-type: none"> <li>- Log-ratio operator</li> <li>- Hierarchical split</li> <li>- Otsu threshold</li> <li>- Region growing</li> </ul>	<ul style="list-style-type: none"> <li>- Unsupervised method</li> <li>- Suitable for wide swath acquisitions</li> </ul>
Cian et al., 2018	Sentinel-1 COSMO-SkyMed TerraSAR-X RADARSAT-2	<ul style="list-style-type: none"> <li>- Multi-temporal statistics</li> <li>- Normalized Difference Flood Index</li> <li>- Normalized Flood in short Vegetation Index</li> <li>- Mean and standard deviation based threshold</li> <li>- Morphological filters</li> </ul>	<ul style="list-style-type: none"> <li>- Multi-temporal references based indices</li> <li>- Simple and robust method</li> <li>- Detect floodwater in short vegetation</li> </ul>

## Introduction

**Table 1.2 Summary of literature in urban flood mapping with SAR data**

Study	Data used	Methods	Key results
Mason et al., 2010	TerraSAR-X	<ul style="list-style-type: none"> <li>- Active contour model</li> <li>- Region growing</li> </ul>	<ul style="list-style-type: none"> <li>- Radar incidence angle impacts the result</li> <li>- Mask out radar shadow and layover areas achieves higher classification accuracy</li> </ul>
Mason et al., 2012	TerraSAR-X	<ul style="list-style-type: none"> <li>- Multi-resolution segmentation</li> <li>- Bayesian classification</li> <li>- Region growing</li> </ul>	<ul style="list-style-type: none"> <li>- Automatic near real-time method</li> <li>- Classification accuracy in urban areas is inferior to that in rural areas</li> </ul>
Chini et al., 2012	COSMO-SkyMed	<ul style="list-style-type: none"> <li>- RGB composite based on SAR intensity and InSAR coherence</li> <li>- Visual interpretation</li> </ul>	<ul style="list-style-type: none"> <li>- Map the receding of the floodwater and the moving of debris</li> <li>- Detect floodwater in urbanized areas with interferometric coherence</li> </ul>
Giustarini et al., 2013	TerraSAR-X	<ul style="list-style-type: none"> <li>- Intensity change detection</li> <li>- Iterative threshold</li> <li>- Region growing</li> </ul>	<ul style="list-style-type: none"> <li>- Automatic and objective method</li> <li>- Overestimation caused by radar shadow and water look-alike areas is reduced with an additional pre-flood reference</li> </ul>
Mason et al., 2014	TerraSAR-X	<ul style="list-style-type: none"> <li>- Intensity change detection</li> <li>- Geometrical Optics (GO)-GO model</li> <li>- Canny edge detector</li> </ul>	<ul style="list-style-type: none"> <li>- Detect floodwater in layover regions in urban areas using double scattering</li> </ul>
Pulvirenti et al., 2016	COSMO-SkyMed	<ul style="list-style-type: none"> <li>- Intensity change detection</li> <li>- Coherence change detection</li> <li>- Rule-based classification</li> <li>- Region growing</li> </ul>	<ul style="list-style-type: none"> <li>- Multi-temporal trend of InSAR coherence improves flood mapping accuracy in vegetated areas</li> <li>- InSAR coherence profitably complement intensity for flood mapping in urban settlements</li> </ul>
Tanguy et al., 2017	RADARSAT-2	<ul style="list-style-type: none"> <li>- Flood return period (RP) data integration</li> <li>- Multi-resolution segmentation</li> <li>- Fuzzy rule-based classification</li> </ul>	<ul style="list-style-type: none"> <li>- Combine SAR data and RP data for urban flood mapping</li> <li>- Address overestimation due to radar shadow and water look-alike areas</li> </ul>
Chini et al., 2019	Sentinel-1	<ul style="list-style-type: none"> <li>- Built-up area mapping</li> <li>- Intensity change detection</li> <li>- Coherence change detection</li> </ul>	<ul style="list-style-type: none"> <li>- Automatic method</li> <li>- InSAR coherence successfully detect flooded built-up areas</li> </ul>

### 1.2 Research objectives

Based on the state of the art in SAR-based flood mapping (Table 1.1 and Table 1.2) and open research questions mentioned earlier, the research objectives of this thesis are defined as blow.

The first research objective focuses on Sentinel-1 data-based automatic change detection for rapid flood mapping in rural areas:

- (1) Considering the huge archive of Sentinel-1 data, how to choose an optimal reference data for the change detection based flood mapping? The inundation extent can spread spatially broad but can also only occupy a small portion of the study area. How to deal with the (highly) unbalanced dataset? How to integrate appropriate contextual information effectively and efficiently that can mitigate the adverse speckle impact and preserve the fine flood structures simultaneously?

Urban flood mapping with SAR data is a very challenging and less solved problem, the synergistic usage of SAR intensity and InSAR coherence is still less understood and explored. Therefore, the following two research objectives have a focus on urban flood mapping with SAR intensity and InSAR coherence:

- (2) Develop a fusion and classification method to a) assess the different roles of SAR intensity, InSAR coherence, and the combination of intensity and coherence in urban flood mapping, b) improve classification results with limited labeled training samples by leveraging additional unlabeled data.
- (3) Training samples are not always available in operational practices. Therefore, it is required to develop an unsupervised method for mapping urban flood based on the fusion of SAR intensity and InSAR coherence. The method needs to account for the uncertainty

of intensity and coherence, and be easy to interpret and visualize the contributions of intensity and coherence in urban flood mapping.

### 1.3 Thesis structure

This thesis is mainly based on three papers that have been published in peer-reviewed journals. The first one paper introduces an automatic change detection method for rapid flood mapping in rural areas and answers the questions of research objective (1); the last two papers tackle urban flood mapping with SAR intensity and InSAR coherence and accomplish research objective (2) and (3), respectively. The detailed thesis structure is as follows:

Chapter 2 provides an introduction to the basics of the SAR imaging system. Chapter 3 presents the physical principles of flood mapping with SAR intensity and InSAR coherence under different conditions (e.g., open floodwater, flooded vegetation, and flooded urban area). Next, Chapters 4-6 are three scientific publications. Finally, Chapter 7 sums up the results of this thesis and gives an outlook for potential future research.

Chapter 4 focuses on flood mapping in rural areas. It introduces a two-step automatic change detection approach based on Sentinel-1 Ground Range Detected (GRD) data. First, an adequate reference image is automatically selected from the archive via a Jensen-Shannon (JS) divergence-based index. A saliency-guided generalized Gaussian mixture model (SGGMM) is employed on log-ratio data computed based on the selected reference image and the flood target image. Finally, a post-processing refinement with a fully-connected conditional random field (FCRF) incorporating global spatial information is accomplished.

Chapters 5 and 6 work on the problem of flood mapping in urban areas. Chapter 5 first evaluates the roles of SAR intensity, InSAR coherence and their combination in urban flood mapping with a deep Convolutional Neural Network (CNN) model. Then a novel temporal-ensembling active self-learning deep convolutional neural network (A-SL CNN) framework is presented. It fuses multi-temporal intensity and coherence to classify open

## Introduction

---

floodwater and flooded built-up areas in urban areas. This work is conducted under the assumption that in some urban flood cases, it is feasible to collect labeled training data but with limited volume. To improve the classification accuracy in this scenario, the proposed framework employs two parallel CNN models to leverage both labeled training data and unlabeled data. Based on the findings in Chapter 5, Chapter 6 further investigates the benefit of the combination of SAR intensity and InSAR coherence in urban flood mapping with different SAR sensors and case studies. The fusion of intensity and coherence in Chapter 6 is implemented from a viewpoint of probability via a Bayesian Network. Apart from open floodwater and flooded built-up areas, floodwater in vegetated areas is also considered in Chapter 6. Moreover, the method presented in Chapter 6 is unsupervised and can be applied to a varying length of intensity and coherence time series. The contributions of intensity and coherence at each pixel are visible and easily interpretable.

## 2. Synthetic Aperture Radar imaging system

### 2.1 Basic principles of SAR

SAR imaging is an active microwave remote sensing technique. The SAR imaging system generates and transmits microwave radiation from a transmitter and receives the backscattered energy from the Earth's surface by a receiver. The transmitter and receiver can be located separately or co-located on board an aircraft or spacecraft. The former configuration is called *bistatic* and the latter is referred to as *monostatic*. The monostatic mode has been the most common configuration in remote sensing. As the active microwave remote sensing is based on the principles of radar which measures distance through the two-way travel time of the microwave pulse, it is side-looking (Fig. 2.1). The microwave length of interest in SAR imaging systems is commonly in the range of 0.75 cm to about 1 m (Table 2.1). The X-, C-, and L-bands are the most used frequency bands on spaceborne SAR systems. The Earth's atmosphere is virtually transparent in the microwave spectrum that is not smaller than about 1 cm (Richards, 2009). Heavy rainfall can be a problem, but only for very short imaging wavelengths like X-band (Danklmayer et al., 2009). Since imaging wavelengths used in SAR systems are no shorter than 3 cm (X band), SAR imaging is in general a day/night all-weather technology. When a low-frequency band passes through the ionospheric layers, there is an effect on the plane of polarization of the wave and it will suffer Faraday rotation (Richards, 2009). The rotation is quite severe at P- and L- bands but less a problem at C- and X- bands. For instance, the rotation magnitude is 16 times greater at L-band than at C-band (Wright et al., 2003).

**Table 2.1 Microwave bands used for radar systems.**

Band	Ka-band	K-band	Ku-band	X-band	C-band	S-band	L-band	P-band
Wavelength (cm)	0.75 – 1.1	1.1 – 1.7	1.7 – 2.4	2.4 – 3.8	3.8 – 7.5	7.5– 15	15 – 30	30 – 100
Frequency (GHz)	40 – 26.5	26.5 – 18	18 – 12.5	12.5 – 8	8 – 4	4 – 2	2 – 1	1 – 0.3

A two-dimensional resolution is required to be an imaging radar: resolution in slant-range

## Synthetic Aperture Radar imaging system

---

(cross-track) direction ( $\delta_r$ ) and resolution in azimuth (along-track) direction ( $\delta_a$ ). The slant-range resolution  $\delta_r$  is proportional to the transmitted pulse width  $\tau$ , high  $\delta_r$  needs narrow  $\tau$ . However, the energy carried by narrowing pulse is reduced, limiting the sensitivity of the radar and making it harder to detect weaker targets. To overcome the problem, SAR systems utilize frequency-modulated pulsed waveforms for transmission, the so-called *chirp* signals (Moreira et al., 2013). It involves transmitting a long pulse, but within which the frequency is varied in a linear manner over time according to a chirp rate  $k_r$ , yielding the bandwidth  $B_r = k_r \tau$ . On reception, the chirp waveform is compressed into an equivalent narrow pulse. Then the slant-range resolution in a pulse compression radar system is:

$$\delta_r = \frac{c_0}{2B_r} \quad (1)$$

where  $c_0$  is the speed of light. The resolution along the ground direction is more interesting to users, with an incidence angle  $\theta$ , the ground-range resolution ( $\delta_g$ ) is:

$$\delta_g = \frac{c_0}{2B_r \sin \theta} \quad (2)$$

The azimuth resolution is set by the along-track beamwidth of the antenna. For an antenna of length  $l_a$  in the along-track direction, and the pulse wavelength of  $\lambda$ , the corresponding angular beamwidth is given by

$$\Theta_a = \frac{\lambda}{l_a} \quad (3)$$

The azimuth resolution for this system is given by

$$\delta_a = \frac{\lambda}{l_a} R_0 \quad (4)$$

where  $R_0$  is the slant distance between the sensor and the point target at the ground. As  $\delta_a$  depends on  $R_0$ , for the spaceborne systems with a very large  $R_0$ , a very long antenna (e.g., at the scale of a kilometer) is required to achieve high  $\delta_a$ , which is practically infeasible. To solve the problem the *synthetic aperture radar* solution is adopted, which synthesizes a very long antenna. The length of the synthetic aperture is defined by the time that a point target is irradiated by the radar. The long duration of irradiation needs a very broad beam. Thus a very short antenna in the along-track direction is suggested. The azimuth resolution of a SAR



## Synthetic Aperture Radar imaging system

system is then given by

$$\delta_a = \frac{l_a}{2} \quad (5)$$

Therefore, the azimuth resolution only depends on the length of the physical antenna carried on the platform and is independent of the operating wavelength and slant range.

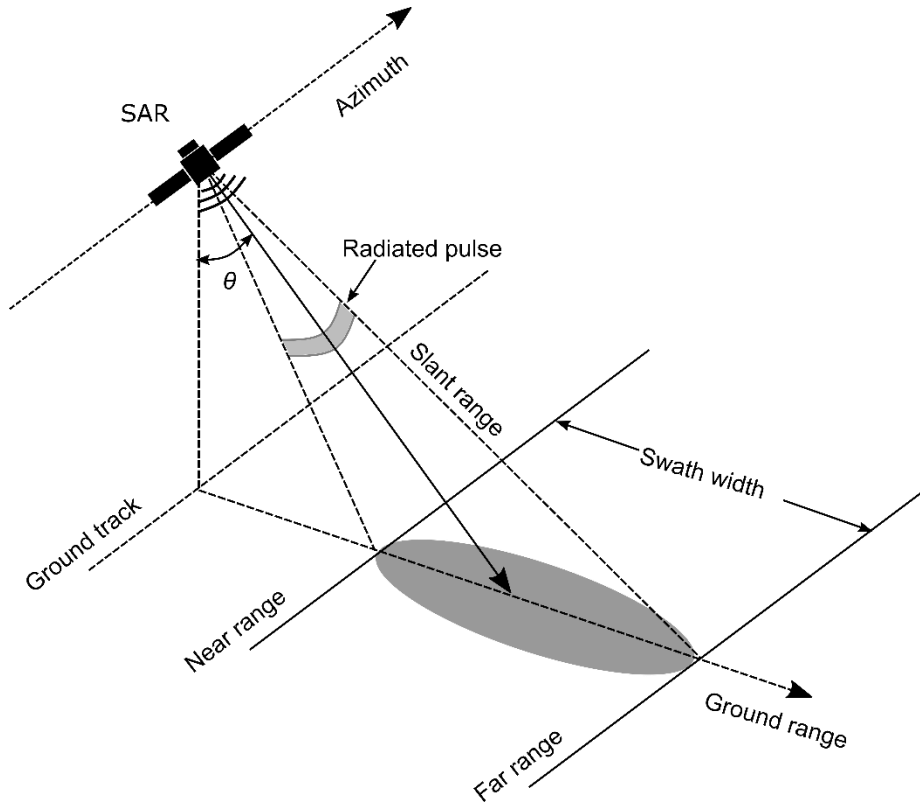


Fig. 2.1 Illustration of the SAR imaging geometry.

## 2.2 Image geometry

A SAR imaging system records the time of the signals that interact with objects at the ground and return to the antenna. These times are then converted to distances in slant-range geometry. In practice, it is more interesting to know the distances on the ground, the so-called ground-range distances. Due to the side-looking imaging geometry of SAR systems, the transformation from sensor-object distances to object-object distances leads to some geometric distortions especially in mountainous and urban areas, known as layover, foreshortening, and shadowing (Fig 2.2). *Layover* is an extreme case of relief displacement. It

## Synthetic Aperture Radar imaging system

happens when the backscattered targets at a specific elevation can be seen closer to the sensor as targets at lower elevations with the same and even shorter ground-range distance. The layover effect is common at steep mountains and buildings, where the radar echo from the top of objects arrives back at the radar before that from the bottom section. The amount of layover is a function of the incidence angle. It is most extreme at small incidence angles (near range) and diminishes as the incidence angle becomes larger in the far range portion of the scene (Lusch, 1999). The effect when terrain front slope (i.e. towards the radar) is compressed and looks shorter than the back slope is called *foreshortening*. SAR imagery shortens terrain slopes in all cases except where the local incidence angle is equal to  $90^\circ$ , and terrain slopes imaged at a  $0^\circ$  incidence angle are foreshortened to a bright line on the image (Lusch, 1999). *Shadowing* occurs when the terrain back slope angle is greater than the depression angle, where it is not illuminated by the signal at all due to terrain obscuration. Radar shadowing is more frequent and severe in the far range and for larger incidence angles.

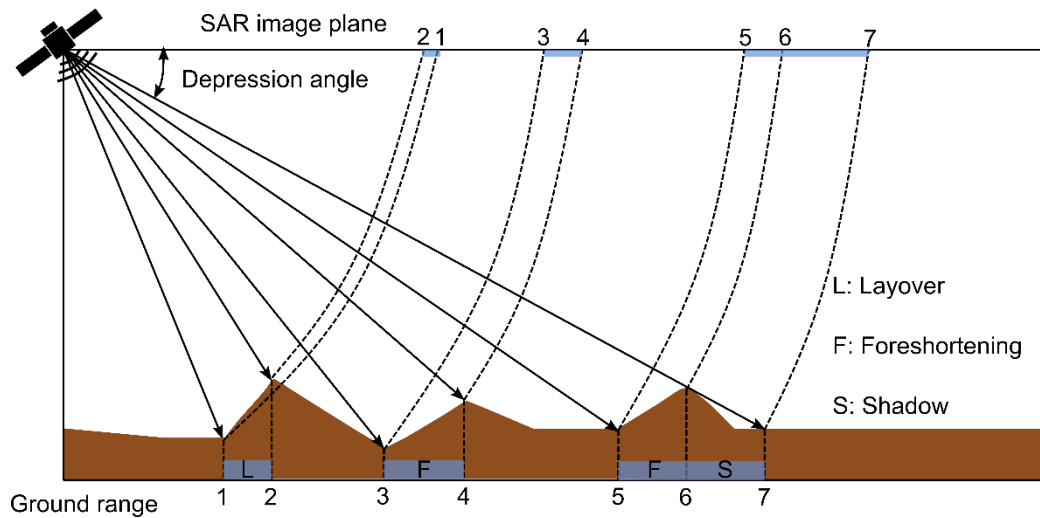


Fig. 2.2 Terrain distortions in SAR image.

## 2.3 Backscattering signal

The backscattering of incident energy from Earth's surface targets depends upon the SAR system properties such as wavelength, incidence angle, and polarization as well as the surface

## Synthetic Aperture Radar imaging system

targets' characteristics such as roughness, dielectric constant, and geometric characteristics. There are several mechanisms by which energy can be scattered back to sensors. The three most common backscattering mechanisms occurring at the land surface are *surface scattering*, *volume scattering*, and *hard target scattering*. Fig 2.3 shows these mechanisms including two kinds of surface scattering: specular reflection and diffuse surface scattering and two types of hard target scattering: double-bounce scattering and facet scattering.

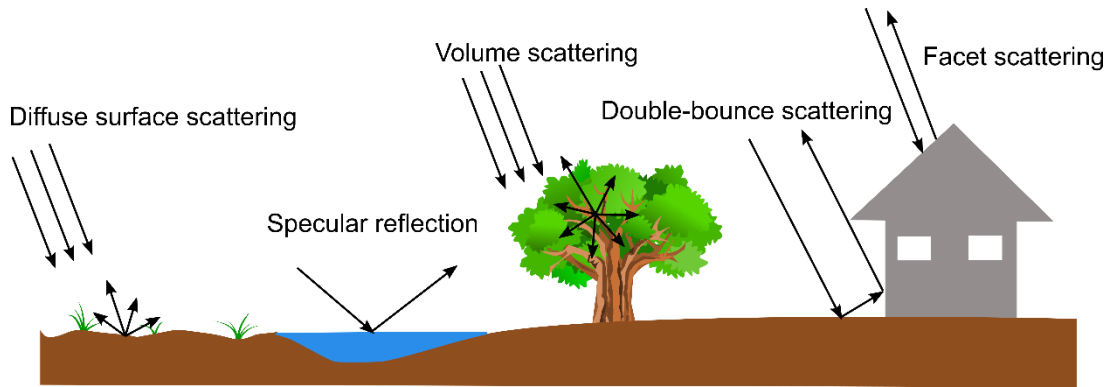


Fig. 2.3 Common scattering mechanisms of land surfaces.

### 2.3.1 Surface scattering

In surface scattering, the energy can be seen to backscatter from a well-defined interface. There are two kinds of surface scattering, specular scattering, and diffuse scattering, in which the energy scatters from a very smooth surface (aka specular) or rough surface, respectively. Whether a surface is considered smooth or rough depends on the relationship between the surface roughness, the microwave wavelength, and the incidence angle. A surface is regarded as specular if the vertical height variation of  $h$  satisfies the Rayleigh criterion:

$$h < \frac{\lambda}{8 \cos \theta} \quad (5)$$

The specular (e.g., a calm water surface) scatters the energy away from the sensor, therefore it has a lower backscattering coefficient ( $\sigma^0$ ) and appears darker in SAR images than rougher surfaces such as barren soils. The incidence angle  $\theta$  also affects  $\sigma^0$ .  $\sigma^0$  decreases with the increase of  $\theta$ , and the dependence of  $\theta$  is weaker when surface roughness increases. The

## Synthetic Aperture Radar imaging system

---

wavelength of the SAR system is long and the transmitted microwave can penetrate into the Earth's surface materials, the longer the wavelength the deeper the penetration. Therefore, the scattering can also occur from within the medium itself and the dielectric constant  $\epsilon_r$  affects the scattered energy. In nature, all media have a dielectric constant  $\epsilon_r \geq 1$ , e.g., the  $\epsilon_r$  of dry soil is about 4, and the  $\epsilon_r$  of water is about 81 (Richards, 2009). For a given surface roughness and incidence angle, the backscattering coefficient is a function of the dielectric constant. An increasing dielectric constant leads to a stronger surface scattering (Richards, 2009; Ulaby et al., 1982). All wavelengths have nearly the same sensitivity to soil moisture but longer wavelengths provide a better capability to discriminate surface roughness variations. Apart from the aforementioned factors, backscattering is also polarization dependent. For example, in the soil surface, the cross-polarized backscattering is always below the co-polarized responses, and the backscattering of VV is higher than HH:  $\sigma_{HV}^0 < \sigma_{HH}^0 < \sigma_{VV}^0$  (Paloscia, 1998). The depolarization in surface scattering depends on the surface roughness. The greatest cross-polarized response occurs for very rough and highly moist surfaces whereas smooth surfaces generate only low depolarization (Richards, 2009; Ulaby et al., 1978). The backscattering difference between VV and HH diminishes at extremely rough surfaces (Richards, 2009).

### 2.3.2 Volume scattering

Volume scattering occurs from a myriad of scattering elements with discontinuous dielectric constants that there is no identifiable single or a countable number of scatterers. The volume scattering strength is proportional to the dielectric discontinuities and the density of the inhomogeneities in the interacted medium (Ulaby et al., 1982). As discussed in the above paragraph, in surface scattering, the backscattering coefficient of the extremely rough surface has a very weak dependence on the incidence angle. The dependence in volume scattering is even weaker. If the volume consists of scatterers with uniform density, it would look much the same when seen from any angle. Thus the amount of backscattering is only weakly dependent on the incidence angle. Another reason why volume scattering is almost independent of the incidence angle is that the scattering elements in volume could be

## Synthetic Aperture Radar imaging system

---

considered small compared with the wavelength of radar microwaves so that they can be assumed to scatter almost isotropically. Compared to surface scattering, volume scattering leads to appreciable levels of depolarization because the scattering from targets leads to the rotation of the polarization vector of the incoming signal. The HV (VH) reflection in volume scattering could be comparable (but still lower) in strength to HH and VV scattering, unless the wavelengths are so long that the scattering geometries have little influence (Wang et al., 1993). HV backscattering coefficients are most sensitive to the forest biomass due to the volume scattering from the foliage layer consisting of randomly oriented leaves, twigs, and branches (Dobson et al., 1992; Le Toan et al., 1992). With the increase of the foliage layer density the multi-scattering mechanism might become stronger for the cross-polarization (Karam et al., 1992).

### 2.3.3 Hard target scattering

Hard target scattering occurs in point-like individual scatters which produce very strong radar returns such as buildings. In very high-resolution SAR data, a resolution cell can be dominated by hard targets such as a tree. Facet scattering happens when flat reflectors are oriented towards the incoming radar beam such as house roofs. A vertical surface adjacent to a horizontal plane forms a dihedral corner reflector and leads to double-bounce scattering, appearing very bright in the SAR image. The double-bounce effect is very common in urban areas between building walls and the ground (Thiele et al., 2007; Wegner et al., 2009). When the building wall is oriented aligned with the flight path of the platform, the double-bounce effect is strongest and there will be no or little cross-polarized response. However, when the orientation angle (aka aspect angle) increases, double-bounce decreases, known as the *cardinal* effect, and the probability of large cross-polarized response increases and volume scattering might become the dominant backscattering mechanism (Dong et al., 1997; Ferro et al., 2011; Xiang et al., 2016). VV and HH response is more sensitive to the orientation angle compared to HV response (Dong et al., 1997). Besides buildings, double-bounce can also arise from corner reflectors formed by ships at sea and near-vertically standing tree trunks (Richards, 2009).

### 2.3.4 Speckle effect

The *speckle* effect is the main drawback of SAR images, which is a signal-dependent granular noise, inherent of all active coherent imaging systems (Argenti et al., 2013). SAR is a coherent imaging system and the total signal backscattered from distributed targets is the coherent summation of the scattering contributions from the randomly distributed elementary scatterers within a resolution cell, resulting in variations of the resultant amplitude and phase values from pixel to pixel. The speckle effect leads to a salt-and-pepper appearance in SAR images and a higher variance of the measured information. Therefore, it may complicate image interpretation and decline the performance of automated image analysis and information extraction techniques. The speckle effect can be commonly reduced by the well-known *multi looking* processing or despeckling filters such as Sigma filter (Lee, 1983), Map filter (Lopes et al., 1990), Lee filter (Lee, 1980), Refined Lee filter (Lee, 1981), and Non-local filtering (Deledalle et al., 2015). A comprehensive review of speckle deduction can be found in (Argenti et al., 2013).

## 2.4 Interferometric coherence

A SAR system records the complex radar backscatter which includes both amplitude and phase information. With two phase observations, we can generate a digital elevation model (DEM) by the Interferometric SAR (InSAR) technique (Crosetto, 2002) and obtain the surface deformation estimates by the Differential InSAR (DInSAR) technique (Lanari et al., 2007; Massonnet and Feigl, 1998). The signal echoes of two observations cannot be completely coherent, and if the two images bear no correlation, interferometric information cannot be generated. The degree of *coherence* is a quality indicator of the interferometric phase (Rodriguez and Martin, 1992). The complex coherence  $\gamma$  between two zero-mean circular Gaussian variables  $s_1$  and  $s_2$  is defined as (Hanssen, 2002; Papoulis, 1991):

$$\gamma = \frac{E\{s_1 s_2^*\}}{\sqrt{E\{|s_1|^2\}E\{|s_2|^2\}}} \quad (6)$$

$E\{\cdot\}$  is the expectation operation. Ideally, the expectation values are obtained with ensemble

## Synthetic Aperture Radar imaging system

---

averages for every single pixel by acquiring a large number of interferograms simultaneously and under exactly the same circumstances. Unfortunately, this procedure is infeasible as every full-resolution pixel is observed only once during each SAR acquisition. In practice, the ensemble average is replaced by the spatial average that is obtained over a limited area surrounding the pixel of interest. The maximum likelihood estimator (MLE) of the coherence magnitude  $|\gamma|$  over an estimation window of  $L$  pixels is used to measure the degree of the cross-correlation between two SAR acquisitions (Hanssen, 2002; Seymour and Cumming, 1994; Touzi et al., 1999),

$$|\gamma| = \frac{\left| \sum_{l=1}^L s_1^{(l)} s_2^{*(l)} \right|}{\sqrt{\sum_{l=1}^L |s_1^{(l)}|^2 \sum_{l=1}^L |s_2^{(l)}|^2}} \quad (7)$$

which ranges between 0 (fully incoherent) and 1 (fully coherent). The coherence magnitude  $|\gamma|$  is biased toward higher values, especially between areas of differing low coherence (Monti Guarnieri and Prati, 1997; Touzi et al., 1999). For a given  $|\gamma|$  the bias is only a function of the number of independent samples  $L$ , the bias decreases with an increasing number of  $L$  (Bickel, 2014; Touzi et al., 1999).

Coherence can be expressed as the product of a number of individual decorrelation components (Moreira et al., 2013; Richards, 2009; Zebker and Villasenor, 1992):

$$\gamma = \gamma_{baseline} \gamma_{noise} \gamma_{temporal} \quad (8)$$

Baseline decorrelation  $\gamma_{baseline}$  is a function of system parameters such as the orthogonal baseline  $B_{\perp}$ , the ground range resolution  $\delta_g$ , the slant range  $R_0$ , the incidence angle  $\theta$ , and the operating wavelength  $\lambda$  (Richards, 2009; Zebker and Villasenor, 1992):

$$\gamma_{baseline} = 1 - \frac{2B_{\perp} \delta_g \cos \theta}{\lambda R_0} \quad (9)$$

Noise decorrelation  $\gamma_{noise}$  can be expressed as a function of the signal to noise ratio (SNR) (Bamler and Just, 1993; Zebker and Villasenor, 1992):

$$\gamma_{noise} = \frac{1}{1 + SNR^{-1}} \quad (10)$$

## Synthetic Aperture Radar imaging system

---

which should be close to unity for a very high receiver SNR. Temporal decorrelation  $\gamma_{temporal}$  is caused by the random motion of scatterers within a resolution cell in the period between two observations (Zebker and Villasenor, 1992):

$$\gamma_{temporal} = \exp \left\{ -\frac{1}{2} \left( \frac{4\pi}{\lambda} \right)^2 (\delta_y^2 \sin^2 \theta + \delta_z^2 \cos^2 \theta) \right\} \quad (11)$$

where  $\delta_y$  and  $\delta_z$  is horizontal change and vertical change in surface, respectively. Temporal decorrelation is our interested component when we use coherence for classification (Koskinen et al., 2001; Moeremans and Dautrebande, 1998; Weydahl, 2001a), segmentation (Abdelfattah and Nicolas, 2010; Askne et al., 1997; Dammert et al., 1999), and change detection, namely *coherent change detection* (Jung et al., 2016; Monti-Guarnieri et al., 2018; Preiss and Stacy, 2006).



### **3. Physical principles of flood mapping with SAR intensity and InSAR coherence**

#### **3.1 Flood mapping with SAR intensity**

As discussed in Section 2.3, the interaction between the SAR signal and the Earth's surface results in different backscattering mechanisms varying by landcover types. These differences give rise to a contrast between the floodwater and the dry terrain in SAR intensity images, making it possible to detect floodwater with intensity. In general, three kinds of flood conditions are considered separately according to the surrounding landcover characteristics of the inundated area: open floodwater (e.g., flooded bare soils and totally submerged short vegetation); flooded vegetation (e.g., partially submerged tall vegetation); and flooded urban areas (Fig. 3.1).

##### **- Open floodwater**

Open floodwater with calm surfaces acts as a specular related to the wavelengths of SAR systems according to the Rayleigh criterion (Badji and Dautrebande, 1997; Martinis et al., 2015; Mason et al., 2007). The radiation is reflecting away from the side-looking SAR sensors. Thus the returned signal is very weak and floodwater appears dark in the intensity image, showing a clear contrast to a brighter tone of drylands that are characterized by diffuse surface scattering. The land/water tonal contrast makes it possible to extract open floodwater based on intensity data using a variety of image processing techniques (Chini et al., 2017; Giustarini et al., 2016; Horritt, 1999; Kittler and Illingworth, 1986; Li and Lee, 1993; Martinis et al., 2009; Matgen et al., 2011; Otsu, 1979; Pulvirenti et al., 2011; Shen et al., 2019). The land/water contrast increases with the incidence angle as the scattering from a smooth surface decays more rapidly than that of a rough surface (Wdowinski et al., 2008; Weydahl, 1996). A larger incidence angle is preferable for floodwater extraction (Barber et al., 1996; Foster and Hall, 1981; Manavalan, 2018; Richards, 2009; Solbø and Solheim, 2004; Töyrä et al., 2001).

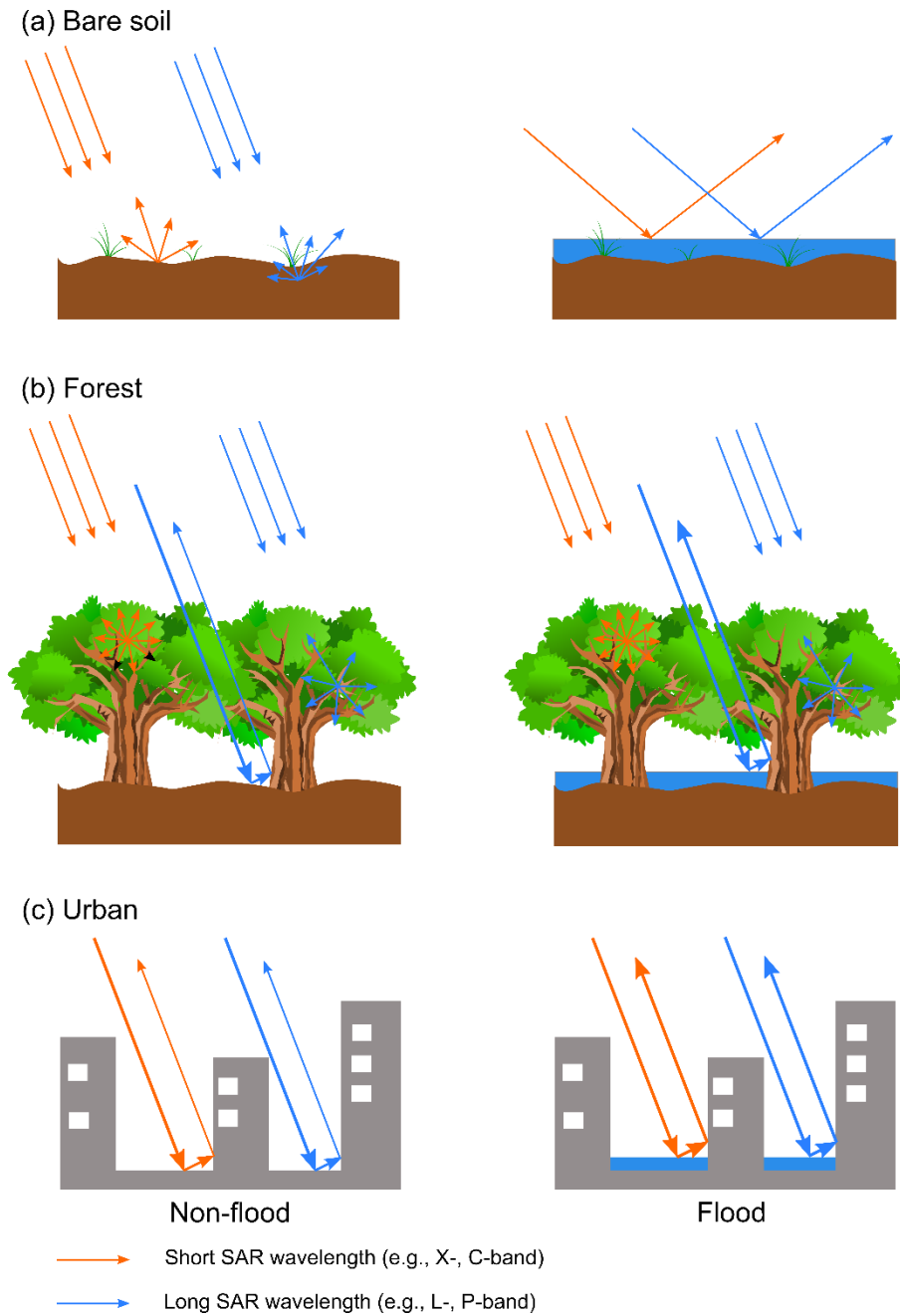


**Fig. 3.1** Schematic illustration of dominant backscattering mechanisms of short (e.g., X/C) and long (e.g., L/P) wavelength electromagnetic signals for various land cover under non-flood and flood conditions (adapted from Schumann and Moller, 2015).

However, a larger incidence angle leads to a larger shadowing. This may cause a larger overestimation of floodwater (e.g., false alarms) (Gelautz et al., 1998; Kropatsch and Strobl, 1990). The overestimation can be also attributed to some other water look-alike surfaces such as bare ground, sand surface, and asphalted areas which appear smooth surface at the scale of

## **Physical principles of flood mapping with SAR intensity and InSAR coherence**

---

the measuring wavelength. For a given scene, larger water look-alike areas would be found in longer wavelength data as more surface features might appear smooth with a longer wavelength. Change detection based on a pre- and co-flood SAR image is widely applied, on the one hand, to isolate floodwater from permanent water bodies, on the other hand, to overcome the over-detection of floodwater on water look-alike surfaces (Bazi et al., 2005; Cian et al., 2018; Giustarini et al., 2013; Martinis et al., 2018; Matgen et al., 2011; Moser and Serpico, 2006; Shen et al., 2019). However, in change detection, the non-flood reference (pre-flood) image introduces additional uncertainty and may bring a negative effect to the final result. Therefore the selection of an adequate and representative reference image is critical in change detection based flood mapping (Hostache et al., 2012).

Generally, all polarization modes can be employed for open floodwater mapping (Manjusree et al., 2012), but many studies show that HH polarization provides the best water-land discrimination due to its highest radiometric dynamics (Bourgeau-Chavez et al., 2001; Brisco et al., 2008; Henry et al., 2006; Hess et al., 1995; Manavalan, 2018; Schumann et al., 2007; Townsend and Foster, 2002). Compared to HH polarization, VV polarization is more susceptible to wind-induced small surface roughness in water bodies (Henry et al., 2006; Moser et al., 2016; Ulaby et al., 1986). VV is favored over cross-polarization VH for calm floodwater mapping (Martinis et al., 2018; Twele et al., 2016). Several studies indicate that cross-polarization HV (VH) outperforms VV polarization in the extraction of floodwater with a roughened surface (e.g., with high-speed wind) (Henry et al., 2006; Horritt et al., 2003; Schumann et al., 2007; Solbø and Solheim, 2004; Zhang et al., 2011) since VV polarization is more sensitive to surface roughness (Barber et al., 1996; Ulaby et al., 1986).

### **- Flooded vegetation**

The backscattering coefficient of flooded vegetation is a function of the vegetation properties and the SAR system parameters (Horritt et al., 2003; Lang et al., 2008). The presence of floodwater results in an enhanced double-bounce effect from the corner reflector formed by the water surface and tree trunks than that from dry conditions when the radar signal is able

## **Physical principles of flood mapping with SAR intensity and InSAR coherence**

---

to penetrate into the vegetation and reach the water surface. Thus flooded vegetation appears brighter intensity image tones than non-flooded vegetation (Henderson, 1995; Hess et al., 1990; Martinis and Rieke, 2015; Moser et al., 2016; Pulvirenti et al., 2013; Richards et al., 1987; Townsend, 2002; Wang et al., 1995). The benefit of SAR data for flooded vegetation detection relies on the sensitivity of microwave energy to the presence or absence of standing water and its ability to penetrate vegetation canopies, even during the leaf-on seasons (Hall, 1996; Kasischke et al., 1997; Lang et al., 2008; Rao et al., 1999). The attenuation of microwave is a function of a related fraction of the wavelength so that SAR systems with a longer measuring wavelength have a deeper penetration in the vegetation canopy (Hess et al., 2003; Töyrä et al., 2001; Wang, 2002). Therefore, SAR systems with a long wavelength such as L-band SAR sensors are preferred for flooded vegetation mapping (Chapman et al., 2015; Hess et al., 1995, 2003, 1990; Manavalan et al., 2017; Pope et al., 1997; Thomas et al., 2011). In general, microwaves at short wavelengths such as C- and X-bands interact mostly with the upper canopy layer and the backscattering tends to be dominated by volume and surface scattering. Thus the contrast between flooded and non-flooded vegetation is decreased. Nevertheless, some studies have shown the success of C-band data for mapping floodwater beneath some types of forest canopies (Brisco et al., 2019; Costa, 2004; Lang et al., 2008; Rao et al., 1999; Townsend, 2002; Townsend and Walsh, 1998). C-band data also has the potential to map paddy rice cultivation (Bazzi et al., 2019; Brisco, et al., 2013a; Park et al., 2018), flooded savannah (Long et al., 2014; Tsyganskaya et al., 2018a) and wetlands (Bolanos et al., 2016; Canisius et al., 2019; Grings et al., 2008; Kwoun and Lu, 2009). The successful detection of floodwater beneath forest with X-band is limited due to its weak penetration. The enhanced X-band double-bounce effect from flooded forests can only be observed at the edges where penetration of the canopy is not an issue (Henderson, 1995). It is also reported that it is possible to use X-band data to map flooded forests for sparse vegetation or during leaf-off conditions (Martinis and Rieke, 2015; Voormansik et al., 2014). Besides, X-band data has been successfully used for mapping flooded vegetation in wetlands and marshlands (Hong et al., 2010; Horritt et al., 2003; Irwin et al., 2017; Kim et al., 2011; Moser et al., 2016; Wohlfart et al., 2018).

## **Physical principles of flood mapping with SAR intensity and InSAR coherence**

---

The intensity of the double-bounce effect is also affected by the incidence angle. Many studies conclude that steeper incidence angles are preferable for the differentiation between flooded and non-flooded forests (Bourgeau-Chavez et al., 2001; Costa et al., 2002; Hess et al., 1990; Kandus et al., 2001; Lang et al., 2008; Richards et al., 1987; Töyrä et al., 2001; Wang et al., 1995). This is due to the fact that the path through the canopy layer is shorter for steeper incidence angles. Thus the canopy attenuation is smaller and the penetration depth is larger. Volume scattering increases at shallower incidence angles as SAR signals interact more with the intervening canopy layer. However, several investigations indicate that the incidence angle is insignificant for flooded vegetation detection (Imhoff et al., 1986; Ormsby et al., 1985). In a short summary, it is difficult to give a general conclusion at which incidence angle high increase of the double-bounce intensity occurs, however, extreme conditions (e.g., grazing or very steep observations) should be avoided and relatively small angles are preferred to guarantee a deeper penetration (Pierdicca et al., 2018). Lang et al. (2008) demonstrate that incidence angles of  $27.5^\circ$  and  $33.5^\circ$  can provide the best discrimination between flooded and non-flooded forests.

Polarization plays an important role in flooded vegetation mapping as well. For single-polarized data, several studies suggest that HH polarization outperforms VV polarization in flooded vegetation mapping (Bourgeau-Chavez et al., 2001; Lang and Kasischke, 2008; Townsend, 2002; Wang et al., 1995). This mainly due to the fact that the specular reflection from the horizontal surface is much higher for horizontally polarized waves compared to vertical waves, thus HH polarization is preferred for detecting the enhanced double-bounce effect occurring between the water surface and tree trunks compared to VV polarization (Pierdicca et al., 2018; Wang et al., 1995). Another reason is that HH polarization generally penetrates vegetation canopy deeper than VV polarization since most vegetation elements are predominantly vertically oriented so that VV polarized waves interact more with the canopy layer (Pierdicca et al., 2018, 2013). It is known that the co-polarized backscatter responses are more sensitive to double-bounce, whereas the cross-polarized ones are more sensitive to volume scattering (Marti-Cardona et al., 2010). Therefore, co-polarized

## **Physical principles of flood mapping with SAR intensity and InSAR coherence**

---

data is expected to be more suitable for detecting the enhanced double-bounce intensity in flooded vegetation than the cross-polarized data (Hess et al., 1990). Nevertheless, the combination of co- and cross-polarized data, for instance, HH/HV ratio (Mougin et al., 1999) or VV/VH ratio (Tsyganskaya et al., 2018a) shows promising results in flooded vegetation detection. Compared to single-polarized data which only provides backscatter values, dual- and quad-polarized data preserve the phase information, offering more comprehensive information for flooded vegetation detection with decomposition techniques. Several studies report the successful extraction of flooded vegetation by the decomposition of dual- (Betbeder et al., 2014; Moser et al., 2016; Schmitt et al., 2012) and quad-polarized data (Brisco, et al., 2013b; Morandeira et al., 2016; Plank et al., 2017; Robertson et al., 2015). A recent comprehensive review of flooded mapping with SAR data can be found in Tsyganskaya et al. (2018b).

### **- Flooded urban area**

Due to the high variability of urban landscapes, the complex combinations of natural and man-made elements, the varying building types, heights and shapes SAR backscattering in urban areas is composed of specular reflection, surface scattering, single, double and multiple bounces (Dong et al., 1997; Franceschetti et al., 2002; Schumann and Moller, 2015). Therefore, it is challenging to detect floods in urban areas with SAR data (Giacomelli et al., 1995; Oberstadler et al., 1997; Solbø and Solheim, 2004). The intensity image tone of floodwater in urban areas depends on the location of the water body and the surrounding structures. Generally speaking, floodwater in open areas such as wide roads without obscuration appears as dark tone due to specular reflection, whereas floodwater in front of buildings appears as very bright lines because of the strong double-bounce scattering occurring between the water surface and building walls. Due to the side-looking viewing geometry of SAR systems, radar shadow (AB in Fig 3.2) and layover (CD in Fig 3.2) caused by buildings make flood detection more difficult. Floodwater on a road (e.g., point F in Fig 3.2) between two buildings can only be sensed by SAR signals with a single specular reflection if the road width  $w$  holds (Mason et al., 2014, 2010; Soergel et al., 2003):

$$w > AB + CD = h_1 \tan \theta + h_2 \cot \theta \quad (12)$$

where  $\theta$  is the incidence angle,  $h_1$  and  $h_2$  are building heights. The wider the road and the higher the resolution of the SAR sensor, the greater the likelihood to detect the inundated area in built-up areas. However, shadow areas and smooth surfaces such as tarmac areas and parking lots are easily misclassified as inundated areas even if they are dry as they also appear dark in SAR images. These false alarms can be partially reduced by the introduction of an additional non-flooded reference image in some cases but cannot be totally removed (Giustarini et al., 2013; Pulvirenti et al., 2016). For the floodwater in shadowed areas that cannot be captured by SAR signals, the assimilation of the SAR-based flood maps into hydraulic models could be helpful to solve this problem (Giustarini et al., 2011; Hostache et al., 2009; Wood et al., 2016). Floodwater in layover areas (e.g., point E in Fig 3.2) could be detected by the enhanced double-bounce scattering as the increase of surface dielectric constant, in principle, results in a considerable increase of the double-bounce effect (Mason et al., 2014; Pulvirenti et al., 2016; Watanabe et al., 2010). Fig 3.3 shows how radar returns from different parts of a building and adjacent road are mapped on the slant-range SAR image due to the fact that they reach the receiver at different times. Proceeding on the SAR image from near to far range at constant azimuth, a bright stripe corresponding to the superposition of backscattering from the ground, wall, and roof (i.e., layover) is first obtained. This is followed by a (usually very) bright line return from wall-ground and ground-wall double scattering, and double scattering ray paths all have the same length (Franceschetti et al., 2002; Guida et al., 2010). Next higher-order multiple scattering (in particular, triple scattering) may occur with a gray area (it is usually negligible with respect to other contributions). Finally, there is a dark area corresponding to building shadow.

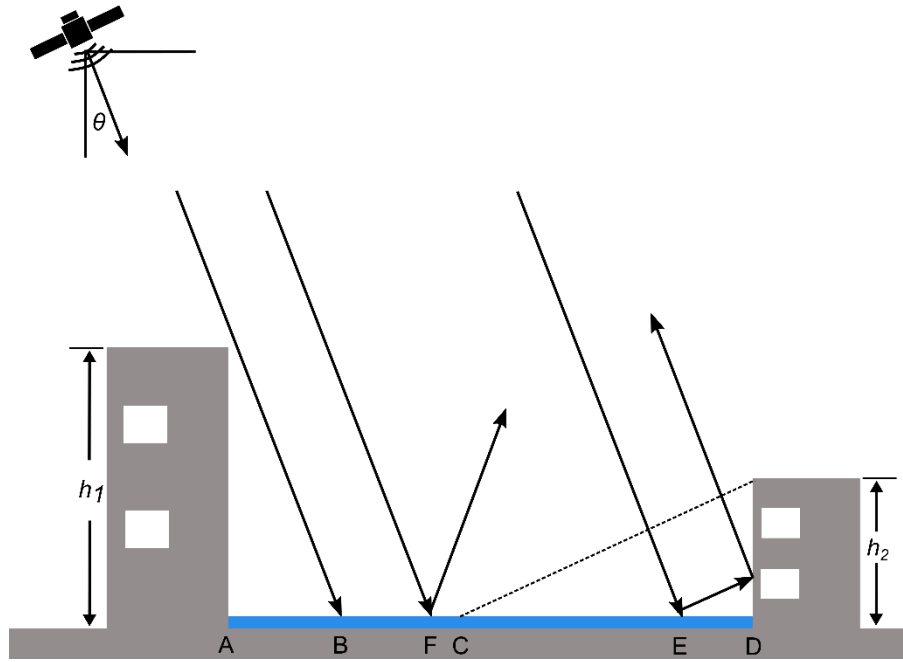


Fig. 3.2 Shadow (AB) and layover (CD) regions in a flooded road (AD) between adjacent buildings of height  $h_1$  and  $h_2$ ,  $\theta$  is the incidence angle (adapted from Mason et al., 2014).

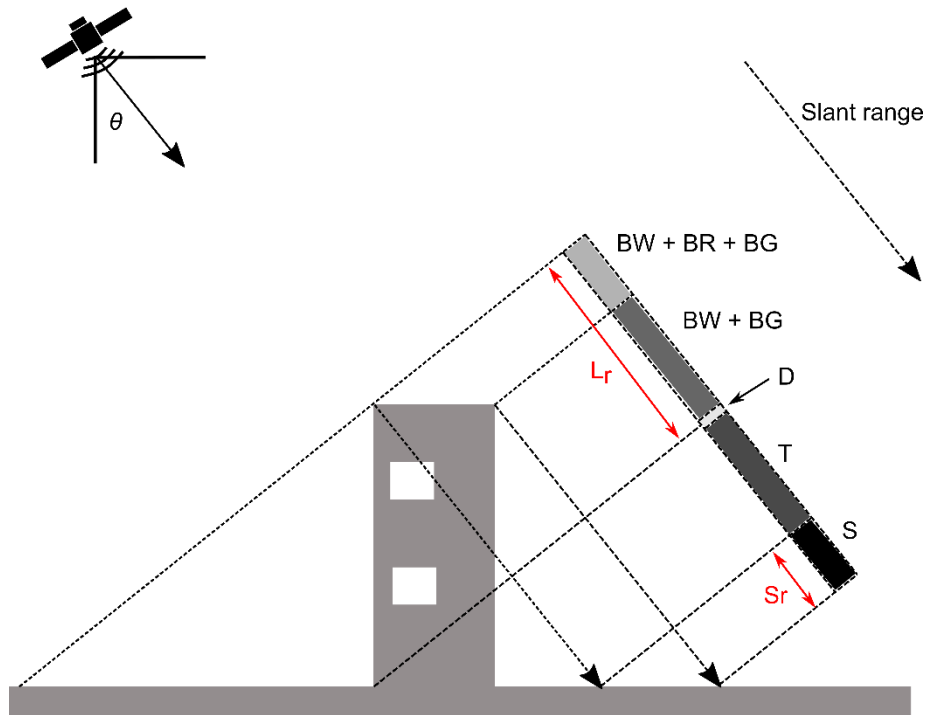
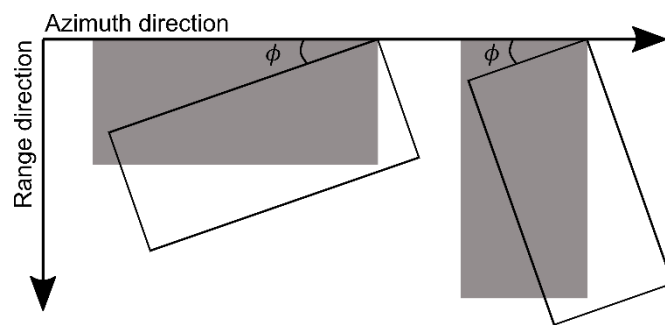


Fig. 3.3 Composition of different contributions from a building in the SAR slant range (adapted from Guida et al., 2010). BW, backscattering from wall; BR, backscattering from roof; BG, backscattering from ground; D, double-bounce scattering; T, triple scattering; S, shadow;  $L_r$ , slant range size of layover;  $S_r$ , slant range size of shadow.



## Physical principles of flood mapping with SAR intensity and InSAR coherence

In general, the double scattering from a wall-ground dihedral corner is higher in HH polarization than that in VV polarization (Hussin, 1995; Thirion-Lefevre and Guinvarc'h, 2015). Besides, HH scattering shows only a weak response to the incidence angle, while VV polarization is strongly governed by the incidence angle in the vicinity of the Brewster angle (Atwood and Thirion-Lefevre, 2018; Thirion-Lefevre and Guinvarc'h, 2015). The difference between pre- and co-flood double-bounce intensity is more remarkable in HH polarization (Watanabe et al., 2008). Even though the feasibility of flood detection in urban areas can be increased by leveraging the enhanced double-bounce scattering, the situation is more complicated in real practice due to other factors such as the orientation angle of buildings and the water level. The strong double scattering from dihedral corners in urban areas occurs when the intersection line of the building wall and road is aligned parallel to the platform flight line (e.g., the orientation angle  $\phi = 0^\circ$ ) (Fig 3.4) and will decrease dramatically with the orientation angle increasing (Dong et al., 1997; Ferro et al., 2011). According to the experiments of Pulvirenti et al. (2016), the increase of backscattering due to the presence of floodwater is in the order of 11.5 dB when  $\phi = 0^\circ$ , and reduces to  $\sim 3.5$  dB for  $\phi > 5^\circ - 10^\circ$ . Moreover, if the water level is not negligible with respect to the wall height, the wall-ground dihedral size diminishes, resulting in a reduced scattering coefficient instead of an enhancement (Iervolino et al., 2015).



**Fig. 3.4** Illustration of aspect angle  $\phi$  of a building. The buildings in gray are oriented parallel to the azimuth direction with  $\phi = 0^\circ$ , while the buildings with black lines are rotated counterclockwise by  $\phi$  with respect to the azimuth direction (adapted from Brunner et al., 2010).

### 3.2 Flood mapping with InSAR coherence

As given in Section 2.4, InSAR coherence (the  $\gamma_{temporal}$  component) characterizes the magnitude of the sample complex cross correlation between two repeat-pass SAR acquisitions, which quantifies the changes in the observed amplitude and phase of the image pixels. It can be used to detect very subtle scene changes at the sub-pixel level since the observed pixel amplitude and phase is sensitive to the relative spatial geometry of the scattering contributions within a pixel (Preiss et al., 2006). Temporal decorrelation also depends on the microwave length and polarization. According to the simulated experiments of Zebker and Villasenor (1992), complete decorrelation of L-band (24 cm) signals needs 10 cm of rms motion while at C-band (5.66 cm) only 2-3 cm rms motion is needed. Hong et al. (2010) show that  $\gamma_{HH} > \gamma_{VV} > \gamma_{VH}$  over wetlands and urban areas.

#### - Open floodwater

The usage of InSAR coherence for flood mapping is under the principle that floodwater changes the surface physical parameters of natural terrains, thus a significant temporal decorrelation is occurring and the co-event coherence (e.g., coherence produced from one image acquired before and another during the flood event) is expected to be very low in areas that have been inundated during the interval of the two InSAR acquisitions (Refice et al., 2014; Zebker and Villasenor, 1992). Several studies demonstrate that the additional interferometric coherence can improve flood mapping compared to only use intensity (Dellepiane et al., 2000; Nico et al., 2000; Selmi et al., 2014). However, many other factors such as vegetation dynamics and radar shadow effects can also result in low coherence values (Bamler and Harlt, 1998). Therefore, it is preferred to use very short temporal baseline coherence such as the COSMO-SkyMed constellation coherence (D'Addabbo et al., 2016; Refice et al., 2014), ERS1/ERS2 tandem coherence (Giordano et al., 2005) with 1-day temporal baseline or bistatic coherence such as TanDEM-X/TerraSAR-X coherence (Chaabani et al., 2018) for flood detection. In deserts with limited vegetation, coherence with a temporal baseline of 35 days can use to detect flash floods successfully as this area keeps a high coherence value in dry periods (Schepanski et al., 2012). It is worth mentioning that in

## **Physical principles of flood mapping with SAR intensity and InSAR coherence**

---

non-inundated areas, the variation of soil moisture leads to a low coherence as well (De Zan et al., 2014; Rabus et al., 2010; Scott et al., 2017; Zwieback et al., 2015).

### **- Flooded vegetation**

Coherence value in the vegetated area is usually low (even for short temporal baseline) due to the random motion of leaves caused by wind and changes in the plant growth stage, which is also affected by vegetation type and density (Hall-Atkinson and Smith, 2001; Luckman et al., 2000). In the absence of water, coherence has the potential to replace the optical normalized difference vegetation index (NDVI) to identify vegetation from bare surfaces in agricultural areas (Pulvirenti et al. 2016). Generally, water bodies decorrelate within tens of milliseconds and show no coherence in a repeat-pass InSAR pair (Bamler and Harlt, 1998). However, when standing water beneath the vegetation canopy causes a double-bounce effect involving tree trunks/stems, it becomes coherent between the two repeat-pass acquisitions (e.g., both images are acquired during the presence of water) and exhibits a high coherence value (Richards, 2009). Therefore, post-event coherence (i.e., both images are acquired after the flood event while floodwater is still existing) can be used to detect the inundated vegetation (Jung and Alsdorf, 2010; Kim et al., 2017; Mohammadimanesh et al., 2018a; Pulvirenti et al., 2016). Through the double-bounce mechanism, many studies use SAR interferometry to track water level changes in vegetated areas (Alsdorf et al., 2000, 2001; Hong et al., 2010; Jaramillo et al., 2018; Kim et al., 2009; Lu and Kwoun, 2008; Wdowinski et al., 2008). Furthermore, coherence is also widely used in wetlands classification and monitoring (Brian Brisco et al., 2017; Canisius et al., 2019; Hall-Atkinson and Smith, 2001; Kim et al., 2013; Mohammadimanesh et al., 2018b).

### **- Flooded urban area**

Man-made features are temporary stable targets, thus, coherence in urban areas is considerably high regardless of temporal baseline (Fanelli et al., 2000; Usai and Klees, 1999; Weydahl, 2001b). The highest coherence is located at the dihedral corner reflector formed from the ground and the wall of a building. Homogeneous amplitude data of building roofs

## **Physical principles of flood mapping with SAR intensity and InSAR coherence**

often have high coherence, the larger the average amplitude the better (Thiele et al., 2007). Although high coherence does not necessarily follow high amplitude which can be also found in medium even low amplitude areas, in most cases it comes from targets of strong backscatter especially when the temporal baseline is relatively large (Weydahl, 2001b). It is expected that flooded built-up areas have much lower co-event coherence than non-flooded ones since the change in surface physical properties produces decorrelation (Chini et al., 2012). Coherence is less affected by the orientation angle than intensity and can help to distinguish some flooded built-up areas which are hardly detectable by the increase of intensity (Ohki et al., 2019). However, anthropogenic activities on roads and parking lots can also lead to low coherence and, thus, result in false alarms. Investigating the difference between pre- and co-event coherence can help suppress these false alarms and isolate the temporal decorrelation caused by flooding (Chini et al., 2019; Pulvirenti et al., 2016). It is worth mentioning that coherence decorrelation in built-up areas is primarily influenced by spatial baseline, especially in short wavelengths such as X-band as spatial baseline decorrelation is proportional to the inverse of the wavelength (Zebker and Villasenor, 1992). Therefore, when using the change information between pre- and co-event coherence in flooded built-up area detection, it is necessary to take into account the spatial baseline perturbation between the two coherence pairs.

## **4. An automatic change detection approach for rapid flood mapping in Sentinel-1 SAR data**

Li, Y., Martinis, S., Plank, S., Ludwig, R., 2018. An automatic change detection approach for rapid flood mapping in Sentinel-1 SAR data. *Int. J. Appl. Earth Obs. Geoinf.* 73, 123–135.

DOI: [10.1016/j.jag.2018.05.023](https://doi.org/10.1016/j.jag.2018.05.023)

LY designed the study and conducted the image acquisition, analysis and results interpretation. PS provided validation data. LY drafted the manuscript, MS, PS, and LR contributed to the discussion and review of the manuscript.



# An automatic change detection approach for rapid flood mapping in Sentinel-1 SAR data

Yu Li<sup>a,b,\*</sup>, Sandro Martinis<sup>a</sup>, Simon Plank<sup>a</sup>, Ralf Ludwig<sup>b</sup>

<sup>a</sup> German Remote Sensing Data Center (DFD), German Aerospace Center (DLR), Oberpfaffenhofen, Münchner Straße 20, 82234 Weßling, Germany

<sup>b</sup> Department of Geography, Ludwig-Maximilians-Universität München, Luisenstraße 37, 80333 München, Germany

## ARTICLE INFO

### Keywords:

Floods  
Change detection  
Saliency detection  
Generalized Gaussian mixture model  
Fully-connected conditional random field

## ABSTRACT

In this paper, a two-step automatic change detection chain for rapid flood mapping based on Sentinel-1 Synthetic Aperture Radar (SAR) data is presented. First, a reference image is selected from a set of potential image candidates via a Jensen-Shannon (JS) divergence-based index. Second, saliency detection is applied on log-ratio data to derive the prior probabilities of changed and unchanged classes for initializing the following expectation-maximization (EM) based generalized Gaussian mixture model (GGMM). The saliency-guided GGMM is capable of capturing the primary pixel-based change information and handling highly imbalanced datasets. A fully-connected conditional random field (FCRF) model, which takes long-range pairwise potential connections into account, is integrated to remove the ambiguities of the saliency-guided GGMM and to achieve the final change map. The whole process chain is automatic with an efficient computation. The proposed approach was validated on flood events at the Evros River, Greece and the Wharfe River and Ouse River in York, United Kingdom. Kappa coefficients ( $k$ ) of 0.9238 and 0.8682 were obtained respectively. The sensitivity analysis underlines the robustness of the proposed approach for rapid flood mapping.

## 1. Introduction

Floods are one of the most frequent and destructive natural disasters on earth. Earth Observation (EO) data enable the mapping of flood extent over large areas, providing the key information to disaster management authorities timely. Contrary to optical data, which are heavily affected by the weather condition, satellite-based synthetic aperture radar (SAR) data are of special attraction in disaster monitoring because of their day/night and all-weather image collection ability.

Change detection based on multi-temporal SAR images is widely used for disaster monitoring (Bovolo and Bruzzone, 2007; Gamba et al., 2007; Martinez and Le Toan, 2007; Martinis et al., 2011) as disasters like flood events are usually marked by abrupt changes on the land surface. Compared to flood mapping with a single image (Twele et al., 2016), change detection based methods have an advantage in masking out the permanent water bodies and some water look-alike objects. At least two images from the same sensor, with the same orbit track, the same polarization, and the same coverage are required for change detection, namely the reference image (pre-event) and the target image (co-event), respectively. In the literature, the reference image is usually manually selected from images that have been acquired at the same

season as the target image in past years (Ban and Yousif, 2012) or the latest available image prior to the event (O'Grady et al., 2011), depending on the application. Within the increasing volume of SAR data, e.g. from the Sentinel-1 mission of the European Space Agency (ESA), which has a high repetition rate (6 days) based on a constellation of two satellites configuration (Sentinel-1A and Sentinel-1B), there is more choice for reference data selection from the huge archives. The selection process should be accomplished carefully, as the result of change detection is affected by the quality of the reference image (Matgen et al., 2011). To our knowledge, only a few studies addressed this issue (Hostache et al., 2012; Schaffer et al., 2015).

Unsupervised change detection is most widely used due to the lack of training samples for supervised algorithms in real applications (Fernandez-Prieto and Marconcini, 2011). In general, unsupervised change detection is based on the difference image (change indicator), for which a proper unsupervised classification algorithm is adopted. There exist several unsupervised approaches for change detection in SAR data. Commonly the ratio (Rignot and van Zyl, 1993) or log-ratio operator (Ban and Yousif, 2012; Bazi et al., 2005; Bovolo and Bruzzone, 2005) is used as change indicator due to multiple speckle noise of SAR data. Other comparison operators like similarity measures based on the local probability density function (Cui et al., 2016; Inglada and Mercier,

\* Corresponding author at: German Remote Sensing Data Center (DFD), German Aerospace Center (DLR), Oberpfaffenhofen, Münchner Straße 20, 82234 Weßling, Germany.  
E-mail address: [Yu.Li@dlr.de](mailto:Yu.Li@dlr.de) (Y. Li).

2007) have also been used in unsupervised change detection. The histogram-based thresholding (Bazi et al., 2005, 2007; Bovolo et al., 2008; Moser and Serpico, 2006) and distance-based clustering (Celik, 2009a; Giustarini et al., 2015; Li et al., 2015) are very frequently used to extract the changed information from the change indicator. However, these pixel-based methods fail to suppress speckle noise and thus lead to unsatisfactory results. As a result, several contextual based descriptors were introduced, like the mathematical morphology (Pulvirenti et al., 2011), Gabor feature representation (Li et al., 2015), and second-order texture parameters (Giustarini et al., 2015). Due to the complexity of these methods, they may not be the first choice in time-oriented cases. Region growing (Giustarini et al., 2013) is a widely used post-processing method to improve pixel-based performance. A major drawback of this method is that it heavily relies on the initial seed pixels and the predefined similarity criteria between pixels. This behavior makes it non-robust in some scenarios. If no seed pixels are detected in a region of interest, this region will be completely ignored during the region growing procedure. Alternatively, in several studies (Bruzzone and Prieto, 2000; Martinis et al., 2011; Moser et al., 2007; Moser and Serpico, 2009) the spatial-context information is extensively integrated by the Markov Random Field (MRF) model (Geman and Geman, 1984) to remove the noise and improve the change detection accuracy. Particularly, the graph-cut based inference with the high availability of tractable attracts more attention in change detection (Cao et al., 2018; Gong et al., 2014) recently. Conditional Random Field (CRF) (Lafferty et al., 2001) is another contextual based model which raises a lot of attention in the computer vision field (Shotton et al., 2006; Toyoda and Hasegawa, 2008; Verbeek and Triggs, 2007). As opposed to MRF, CRF is a discriminative framework which relaxes the assumption of the conditional independence of the observation space (Ban, 2016; He et al., 2004). Wegner et al. (2011) applied a CRF model for building detection with a combination of InSAR and optical images. Ding et al. (2014) proposed a CRF model for SAR image classification. Zhou et al. (2016) and Cao et al. (2016) applied CRF-based methods on change detection using optical satellite images. In spite of the advantages of the random field models in image classification and change detection, traditional random field models suffer the risk of removing fine structures due to their local-connected limitation (Schindler, 2012; Su et al., 2011). To overcome this drawback, Yousif and Ban (2014) introduced a nonlocal probability MRF model to enforce the global consistency in change detection with SAR data. However, the increased computational complexity makes it not suitable to deal with SAR images in applications such as rapid flood mapping over large areas. The higher-order potentials CRF (Kohli et al., 2009) and hierarchical CRF (Ladicky et al., 2009) have been proposed to incorporate the long-range connection based on segments or superpixels. The drawback of these models is that the final result relies on the accuracy of the segmentation. The reliability of the unsupervised segmentation algorithms cannot be guaranteed, especially when the image covers a very complex environment. Furthermore, the accuracy of unary potential plays a critical role for the final result during the implementation of random field models (Schindler, 2012; Vineet et al., 2012). When random field modeling is applied to unsupervised change detection, the corresponding unary potential is commonly achieved by unsupervised classification algorithms. Zhou et al. (2016) and Cao et al. (2016) initialized the CRF model in optical image change detection with fuzzy c-mean clustering. However, fuzzy c-mean clustering is sensitive to data noise and performs poorly on imbalanced data, which is not uncommon in flood extent mapping with SAR data over large areas. Bruzzone and Prieto (2000) and Yousif and Ban (2014) employed the expectation-maximization (EM) based parametric statistical model for the MRF model initialization in SAR image change detection. Within their studies, some approximate knowledge of the change information in the study area from the user is needed, which means it is not fully automatic. Although the EM-based parametric statistical model is guaranteed to converge (Bilmes, 1998), accurate prior information is required to speed up the

convergence and to improve the accuracy of parameters estimation, especially when the prior probabilities are highly imbalanced (Bazi et al., 2007; Glasbey, 1993; Naim and Gildea, 2012).

Summarizing the above, to achieve an accurate delineation of flooded area using an automatic change detection method in SAR data, the employed method should be equipped with the following features: a) be capable of selecting an adequate reference image; b) be capable of handling highly imbalanced distribution between flooded and unflooded area; c) be robust to speckle noise while preserving the detailed flooded information. The failure in any of the aforementioned perspective leads to a reduction of mapping accuracy. This paper aims at filling the gaps between these perspectives by introducing an automatic change detection processing chain for rapid flood mapping in Sentinel-1 SAR data. The proposed processing chain consists of two main steps: (1) a Jensen-Shannon (JS) divergence-based index is proposed for proper reference data selection from archive data; (2) a saliency-guided generalized Gaussian mixture model (SGGMM) is employed on the difference image based on step (1), followed by a fully-connected CRF (FCRF) model, which incorporates pairwise connections of all pixels with an efficient inference to refine the primary result. Experiments on flooding at the Ervos River, Greece, and the Wharfe and Ouse River in York, United Kingdom, prove the effectiveness and efficiency of the proposed method. In the case of change detection for flood mapping, two kinds of change could occur (i.e., the negative change caused by open water, and the positive change caused by flooded vegetation or flooded urban areas). It is also true that most cases of large-scale flooding are dominated by one type of change (Chini et al., 2017). The method proposed in this paper only deals with the negative change caused by open water in rural areas as it is the most common case in rapid flood mapping task and we leave the two-type change situations for our future work.

## 2. Method

As the reference image is crucial for change detection, the proposed method starts with the automatic reference image selection. The JS divergence-based reference image index is introduced first in this section. Subsequently, the saliency-guided generalized Gaussian model is applied, which extracts primary change information from the difference image. Finally, the fully-connected conditional random field is employed to achieve the final change detection result. The flowchart is shown in Fig. 1.

### 2.1. Reference image index

The reference image selection process consists of two steps. Firstly, some potential image candidates are collected from the Copernicus Open Access Hub, which should fulfill the following criteria: the data should be acquired from the same relative orbit and with the same polarization configuration as the flood image. Especially in regions with pronounced seasonal flooding, only images acquired in the same period of the year as the target image should be collected (Hostache et al., 2012). Secondly, the final reference image is selected from the collected images based on the reference index (describe later in this section). The optimal candidate should be acquired during a period without flood (noted as “non-flooded”) and should represent the “normal behavior” of the scene. It is worth to mention that too many collected potential candidates could

be time-consuming with the corresponding preprocessing and increase the storage burden as well, a too small volume of candidates will degrade the optimization of the final reference image. Considering the high temporal resolution (12 days for a single satellite and 6 days for the constellation of two satellites) of Sentinel-1 data and the systematic global acquisition plan of the satellite mission, it can be assumed that images acquired during the latest year prior to the flood could be a proper potential candidate set.

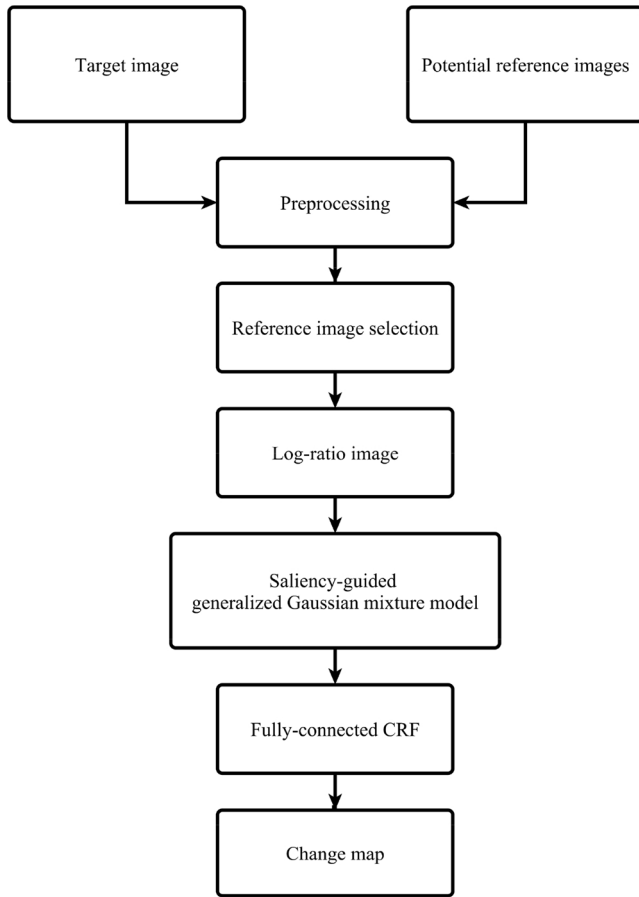


Fig. 1. Flowchart of the proposed change detection processing chain.

It is known that open flood surfaces lead to low backscattering coefficients due to the specular reflection of the SAR signal on the water surface and the high permittivity of water (Ulaby and Dobson, 1989). This leads to a distribution variation of image gray values compared to the image without flood over the same area. Therefore, it is straightforward to compare the probability density functions (pdf) between interested images. Hostache et al. (2012) compared the empirical distribution functions between flood image and reference image based on Euclidean distance, however, this feature is dominated by high values of the absolute difference between two histograms. When flooded area occupies a minor portion of the image, the tiny variation in histogram attributed to flood may not be captured when Euclidean distance is applied to histogram comparison. To overcome this shortcoming, JS divergence, the symmetric and bounded version of Kullback-Leibler (KL) divergence, is employed to evaluate the similarity of pdfs of interested images.

KL divergence (Kullback and Leibler, 1951) is one of the most widely used similarity measures for image comparison in many application fields, such as image retrieval (Choy and Tong, 2010), image quantitative evaluation (Pheng et al., 2016), change detection (Cui et al., 2016). Suppose  $p_X(x)$  and  $p_Y(x)$  are the densities of random variables  $X$  and  $Y$ , respectively, the KL divergence from  $X$  to  $Y$  is given by

$$K(X|Y) = \int \log\left(\frac{p_X(x)}{p_Y(x)}\right) p_X(x) dx \quad (1)$$

$K(X|Y)$  has a value  $\geq 0$  and it is small when two pdfs are close to each other. When KL divergence is performed on local similarity measures like in a sliding window, which is generally used in change detection, one parametric SAR image model could be used to make the KL

divergence analytically tractable with a closed-form expression (Cui et al., 2016). It is not valid to use a single statistic model for global similarity measure between two SAR images over large areas as they are heterogeneous with different land cover types. Here, the empirical distribution function is used to substitute the pdf in computing KL divergence. Due to the asymmetric property of KL divergence, the symmetric version of KL divergence, JS divergence is used in this paper, which is defined as

$$J(X|Y) = \int \left( \log\left(\frac{p_X(x)}{m(x)}\right) p_X(x) + \log\left(\frac{p_Y(x)}{m(x)}\right) p_Y(x) \right) dx \quad (2)$$

where  $m(x) = (p_X(x) + p_Y(x))/2$ . The JS divergence is symmetric and bounded; furthermore, it is numerically stable, robust to noise, and insensitive to the size of histogram bins in contrast to the KL divergence (Puzicha et al., 1997).

Considering the “non-flooded” and “normal behavior” properties of the reference image, the JS divergence-based reference index is defined as the combination of two terms:

$$Ref_{index}(i) = \sqrt{\left(\frac{1}{J(X(i)|X_{flood})}\right)^2 + J(X(i)|X_{median})^2} \quad (3)$$

where  $X(i)$  is the  $i$ th image of the collected potential candidates from the data hub,  $X_{flood}$  is the flood image, and  $X_{median}$  is the median image calculated from the median values for each pixel over the whole collected images, which represents the normal behavior of the scene to some extent. The first term  $\frac{1}{J(X(i)|X_{flood})}$  represents the “non-flooded” degree related to the flood image. The higher “non-flooded” degree of  $X(i)$  means the less similarity between the pdfs of  $X(i)$  and  $X_{flood}$ , and the smaller value of  $\frac{1}{J(X(i)|X_{flood})}$ . The second term  $J(X(i)|X_{median})$  represents the “normal” degree related to the median image. The higher “normal” degree of  $X(i)$  means the more similarity between the pdfs of  $X(i)$  and  $X_{median}$ , and the smaller value of  $J(X(i)|X_{median})$ . Each term is rescaled between 0 and 1 first. The  $Ref_{index}$  could be regarded as the Euclidean distance between these two terms. The image with the smallest value of  $Ref_{index}$  is the selected reference image.

## 2.2. Saliency-guided generalized Gaussian mixture model

The log-ratio operator between the flood image and the reference image as shown in Eq. (4) is used in this paper as Bujor et al. (2004) pointed out that the ratio operator is proper to detect sharp changes like those associated with flood areas.

$$X_{lr} = \log\left(\frac{X_{flood}}{X_{ref}}\right) \quad (4)$$

$X_{ref}$  is the reference image selected by the reference index described in Section 2.1. The log-ratio image  $X_{lr}$  is scaled to 256 possible gray-level values in the range  $[0, 255]$  for the subsequent analysis. We can take the pdf  $p(x)$  of the log-ratio image  $X_{lr}$  as a mixture of two probability density functions associated with the changed (flooded) and unchanged (non-flooded) components. The conditional density of each component is modeled by a Generalized Gaussian distribution because of its flexibility, stability, and tractability (Bazi et al., 2005, 2007). Then  $p(x)$  is given by (Bazi et al., 2007; Do and Vetterli, 2002):

$$p(x) = \sum_{i=1}^2 P_i \frac{\beta_i}{2\alpha_i \Gamma(1/\beta_i)} e^{-[|x-\mu_i|/\alpha_i]^{\beta_i}} \quad (5)$$

$$\alpha_i = \sigma_i \sqrt{\frac{\Gamma(1/\beta_i)}{\Gamma(3/\beta_i)}} \quad (6)$$

$P_i$  is the prior probability of each component,  $\mu_i$ ,  $\sigma_i$ ,  $\alpha_i$ , and  $\beta_i$  are the mean, standard deviation, scale and shape parameters of the conditional distribution of each component. The Laplacian and Gaussian



distributions are special cases of the generalized Gaussian distribution, where and  $\beta_i = 2$ , respectively. As limiting cases, for  $\beta_i \rightarrow 0$ , it becomes impulsive, for  $\beta_i \rightarrow \infty$ , it converges to a uniform distribution. The parameters  $\theta = [P_1, \mu_1, \alpha_1, \beta_1, P_2, \mu_2, \alpha_2, \beta_2]$  could be derived by the EM algorithm (Dempster et al., 1977) with an initial parameter set  $\theta^{(0)} = [P_1^{(0)}, \mu_1^{(0)}, \alpha_1^{(0)}, \beta_1^{(0)}, P_2^{(0)}, \mu_2^{(0)}, \alpha_2^{(0)}, \beta_2^{(0)}]$ . Several approaches are used to achieve the initialization, such as the widely used clustering algorithms (McLachlan and Peel, 2000; Nguyen et al., 2014), and a heuristic search algorithm like genetic algorithm (GA) (Bazi et al., 2007). However, clustering algorithms cannot get adequate initial values for the noisy and imbalanced dataset as mentioned in Section 1, and GA strongly depends on the parameters itself and the fitness function. Alternatively, a saliency detection-based initialization is applied in this paper.

The changed (flooded) area in the log-ratio image could be regarded as the salient area because it appears as a strong contrast to the unchanged (unflooded) area. Therefore, the saliency detection could be applied to the log-ratio image to extract the changed areas and thus acquiring the appropriate prior probabilities of changed and unchanged components. The context-aware saliency detection method (Goferman et al., 2012) is used in this paper for its efficiency and independence of prior knowledge of the objects. Contrary to the pixel-based statistical clustering algorithms, context-aware saliency detection measures the similarity between image patches at multiple scales, which is robust to speckle noise on the one hand and performs well on the highly imbalanced classes on the other hand. Let  $x_i$  and  $x_j$  be two vectorized patches extracted from  $X_{lr}$  centered at pixel  $i$  and  $j$ , respectively, and  $d_{value}(x_i, x_j)$  be the Euclidean distance between the values of  $x_i$  and  $x_j$ , normalized to the range  $[0, 1]$ . Let  $d_{position}(x_i, x_j)$  be the Euclidean distance between the positions of patches  $x_i$  and  $x_j$ , normalized by the larger image dimension. The dissimilarity between the pair of patches is defined as:

$$d(x_i, x_j) = \frac{d_{value}(x_i, x_j)}{1 + c \cdot d_{position}(x_i, x_j)} \quad (7)$$

where  $c$  is a constant assigned to a value of 3 in our study as used in (Goferman et al., 2012). In practice, it is sufficient to consider the  $K$  most similar patches, which also speeds up the computation. Furthermore, considering that the background area likely has similar patches at multiple scales, while the salient area has similar patches at fewer scales. It is reasonable to incorporate multiple scales. Hence, the saliency value of pixel  $i$  at scale  $r$  is given by:

$$S_i^r = \left[ 1 - \exp \left\{ -\frac{1}{K} \sum_{j=1}^K d(x_i^r, x_j^r) \right\} \right] \quad (8)$$

where  $\eta_k \in \{r, \frac{1}{2}r, \frac{1}{4}r\}$ .  $K$  is set to 64 and the patch size is set to  $7 \times 7$  with 50% overlapping in our experiments. The saliency map  $S_i^r$  at each scale is normalized to the range  $[0, 1]$  and interpolated back to the original image size. It suggests that the regions close to foci of attention should be explored significantly. The final saliency value of pixel  $i$  is defined as:

$$\hat{S}_i = \frac{1}{M} \sum_{r \in R} S_i^r (1 - d_{foci}^r(i)) \quad (9)$$

where  $M$  is the number of scales. Four scales are used in this paper:  $R = \{100\%, 80\%, 50\%, 30\%\}$ .  $d_{foci}^r(i)$  is denoted as the Euclidean positional distance between pixel  $i$  and the closest attended pixel at scale  $r$ , which is normalized to the range of  $[0, 1]$ .

After the saliency map is calculated, see Figs. 2c and 3c, a thresholding value  $t$  is applied to extract the coarse changed area. As the extracted area is too rough to map the accurate positions of changed pixels, we only use the salient area to initialize the prior probability of changed component. Pixel  $i$  is a salient pixel if  $\hat{S}_i \geq t$ , we found the value of  $t$  in the range of 0.2 to 0.5 works well in practice, and  $t$  is set to

a value of 0.2 in this paper, more detailed analysis of  $t$  is described in Section 4.2. Let  $len(\hat{S}_i \geq t)$  be the number of salient pixels extracted from  $X_{lr}$ , and  $len(X_{lr})$  be the dimension of the log-ratio image, then the initial prior probability of the changed component  $P_1^{(0)} = \frac{len(\hat{S}_i \geq t)}{len(X_{lr})}$  and the initial prior probability of the unchanged component  $P_2^{(0)} = 1 - P_1^{(0)}$ . The initial value of  $\beta_i^{(0)}$  is set to  $\frac{2}{P_1^{(0)}}$ , and  $\mu_i^{(0)}, \alpha_i^{(0)}$  could be easily calculated.

### 2.3. Fully-connected conditional random field

CRF is a popular discriminative model for modeling spatial information of images in computer vision tasks (Quattoni et al., 2007; Rabinovich et al., 2007; Torralba et al., 2004). In contrast to the traditional local-range CRF models, which consider contextual information in the neighborhood, the recently proposed fully-connected CRF (Philipp and Koltun, 2011) establishes pairwise potentials on all pair of pixels in the image, refining pixel-based classification significantly. When billions of edges need to be considered in the fully-connected CRF, traditional inference methods such as belief propagation and graph cuts become impractical in this case within a high complexity of inference (Zhang and Chen, 2012). Mean-field approximation inference is used in the fully-connected CRF (Philipp and Koltun, 2011), which enables the model to integrate long-range connection in an efficient way. Consider a random field  $Y = \{Y_1, \dots, Y_N\}$  in the domain of label set  $\mathcal{L} = \{l_1, \dots, l_L\}$  that is conditioned on a given image  $X = \{X_1, \dots, X_N\}$  of size  $N$ .  $X_j$  is the feature vector of pixel  $j$  and  $Y_j$  is the label assigned to pixel. The number of labels  $L$  is set to 2 in our change detection case. The conditional random field is characterized by a Gibbs distribution  $P(Y = y|X) = \frac{1}{Z(X)} \exp(-E(y|X))$ , where  $E(y|X)$  is the Gibbs energy for labeling  $y \in \mathcal{L}^N$  conditioned on  $X$  and  $Z(X)$  is the partition function. In the fully-connected pairwise CRF model, the corresponding Gibbs energy is defined as

$$E(y|X) = \sum_i \varphi_u(y_i) + \sum_{i < j} \varphi_p(y_i, y_j) \quad (10)$$

where the unary potential  $\varphi_u(y_i)$  is computed independently for each pixel  $i$  taking the label  $y_i$  by a classifier given image features and the global pairwise potential  $\varphi_p(y_i, y_j)$  represents the label compatibility between pixel  $y_i$  and  $y_j$ .

Usually, the unary potential is calculated from supervised classifiers, such as SVM (Ding et al., 2014) and boosted algorithms (Torralba et al., 2007). Here, the unary potential is obtained based on the pixel value of the log-ratio image  $X_{lr}$  via the unsupervised saliency guided GGMM introduced in Section 2.2:

$$\varphi_u(y_i|X) = -\log P(y_i|X_{lr_i}) \quad (11)$$

where  $X_{lr_i}$  is the value of pixel  $i$  in the log-ratio image  $X_{lr}$ . The pairwise potential is as described in (Philipp and Koltun, 2011)

$$\varphi_p(y_i, y_j) = \mu(y_i, y_j) \sum_{m=1}^K \omega^{(m)} k^{(m)}(\mathbf{f}_i, \mathbf{f}_j) \quad (12)$$

where  $k^{(m)}$  is a Gaussian kernel,  $\omega^{(m)}$  is the weight of the kernel,  $\mu$  is the label compatibility function, and  $\mathbf{f}_i, \mathbf{f}_j$  are feature vectors for pixel  $i$  and  $j$ . The Potts model,  $\mu(y_i, y_j) = [y_i \neq y_j]$  is used in this paper, and the smoothness kernel and appearance kernel are included in the pairwise potential:

$$k^{(1)}(\mathbf{f}_i, \mathbf{f}_j) = \omega^{(1)} \exp\left(-\frac{|p_i - p_j|^2}{2\theta_\gamma^2}\right) \quad (13)$$

$$k^{(2)}(\mathbf{f}_i, \mathbf{f}_j) = \omega^{(2)} \exp\left(-\frac{|p_i - p_j|^2}{2\theta_\alpha^2} - \frac{|X_{lr_i} - X_{lr_j}|^2}{2\theta_\beta^2}\right) \quad (14)$$

where  $p_i$  is the position of pixel  $i$ ,  $X_{lr_i}$  is the value of pixel  $i$  in the log-ratio image  $X_{lr}$ ,  $\theta_\alpha$  and  $\theta_\gamma$  reflect the degree of nearness between pixel  $i$

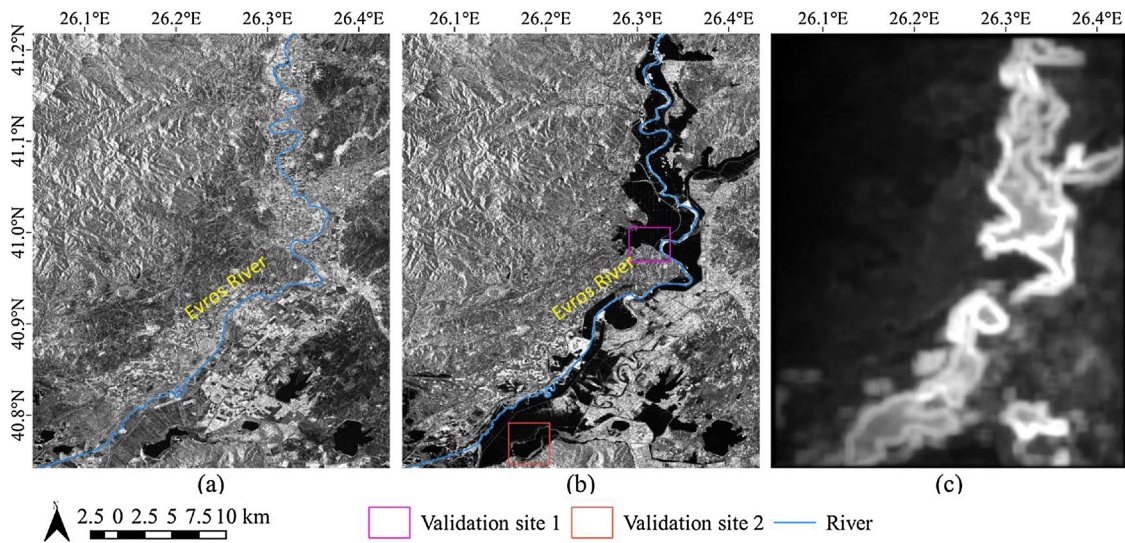


**Fig. 2.** The image pair and corresponding saliency image of the Evros River, Greece. (a) Sentinel-1 reference image acquired on 20 September 2014; (b) Sentinel-1 target image acquired on 12 March 2015; (c) saliency image based on log-ratio image between (a) and (b).

and  $j$ .  $\theta_\beta$  reflects the similarity of pixel  $i$  and  $j$ . The result is insensitive to smooth kernel parameters  $\omega^{(1)}$  and  $\theta_\gamma$ . We found  $\omega^{(1)} = 1$  and  $\theta_\gamma = 3$  work well in practice. Other kernel parameters are learned by grid search.

### 3. Experiments

#### 3.1. Study area and data set

The proposed method was tested and evaluated on Sentinel-1 C band Interferometric Wide (IW) swath mode Ground range detected (GRD) datasets over two test sites: the Evros River, Greece, and the Wharfe and Ouse River in York, UK. For each experiment, the radiometric calibration, speckle filtering, co-registration, and Range-Doppler terrain correction were performed within the open source software Sentinel Application Platform (SNAP). During the pre-processing step, the refined Lee filter with  $7 \times 7$  window size was used in all experiments.

The first dataset covers the lower portion of the Evros River, at the border between Greece and Turkey. Days of heavy rain caused a long-lasting and widespread flood during February 2015 and April 2015 in this area. The target flood image is a Sentinel-1 VV scene acquired in ascending pass direction from relative orbit 29 on 12 March 2015, shown in Fig. 2b. 26 images with the

same configuration as the target image acquired from 19 October 2014 to 25 December 2015 (see Table A1) were collected for reference image selection. The test image size is  $4342 \times 5314$  pixels. The flood event occupied  $\sim 20\%$  of the whole test image. Two subsets were selected for validation (see the rectangles in Fig. 2b) and the ground truth was generated by manual digitalization based on a pan-sharpened WorldView-2 scene acquired on 11 March 2015 with a spatial resolution of 0.5 m.

The second dataset covers the area of the cities York and Selby, which is largely rural. There are two rivers flowing through it, the Wharfe River and Ouse River. This area suffered from spatially and temporally variable flooding during December 2015 and January 2016. A Sentinel-1 VV scene acquired in descending pass direction from relative orbit 81 on 29 December 2015 was used as the target image, shown in Fig. 3b. 18 images with the same configuration as the target image acquired from 28 March 2015 to 15 February 2016 (see Table A2) were collected for reference image selection. The test image has a size of  $7210 \times 6031$  pixels with  $\sim 3\%$  covered by flooding. A subarea to the south of York town was selected for validation (see the rectangle in Fig. 3b). An optical Sentinel-2 data acquired on 29 December 2015 was used as the validation data. The flood extent from the Sentinel-2 data was derived via the modified normalized difference water index (MNDWI) (Xu, 2006).

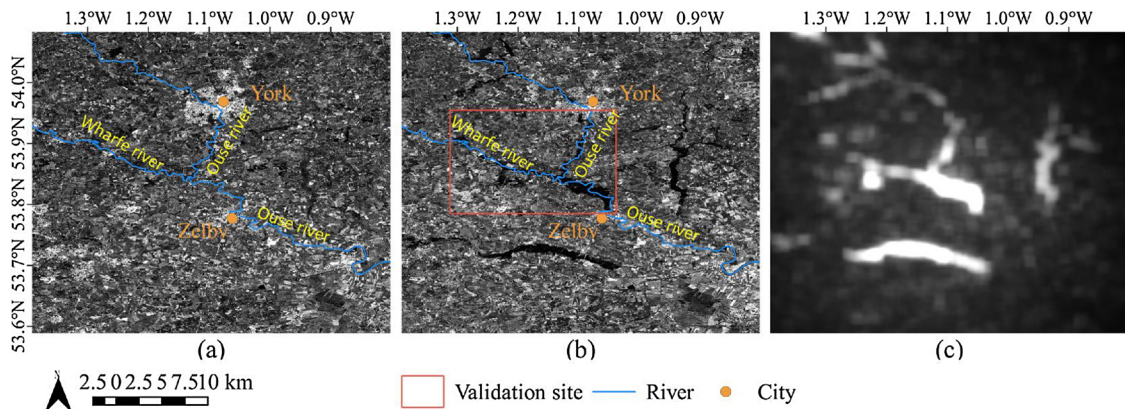


**Fig. 3.** The image pair and corresponding saliency image of York, UK. (a) Sentinel-1 reference image acquired on 12 September 2015; (b) Sentinel-1 target image acquired on 29 December 2015; (c) saliency image based on log-ratio image between (a) and (b).

### 3.2. Experimental design

The PCA-k-means (Celik, 2009b) method and MRF with the graph cut inference (Cao et al., 2018) were implemented to compare with the proposed method (SGGMM-FCRF). The window size of PCA-k-means was set to  $h = 5$ , and the weight of pairwise potential  $\beta$  in MRF was set to 0.6 by trial and error. Further,  $\omega^{(2)} = 5$ ,  $\theta_\alpha = 30$ ,  $\theta_\beta = 20$  were set in the FCRF model. The unary potential of MRF was defined by SGGMM (SGGMM-MRF). To further explore the influence of different ways of the unary estimation on labeling smooth, the unary potential estimated by fuzzy c-means (FCM) for both MRF (FCM-MRF) and FCRF (FCM-FCRF) (Cao et al., 2016) were applied for comparison as well. The PCA-k-means, FCM, and SGGMM were implemented in Python, and the MRF and FCRF were implemented using Python<sup>1</sup> and C++ . All the experiments were conducted on a laptop with 32GB RAM and Intel i7 Processor.

## 4. Results and discussion

### 4.1. Results and quantitative analysis

The results for both study areas are shown in the form of binary maps (Figs. 4–6). False alarms (FA), which denote unchanged pixels misclassified as changed pixels, missed alarms (MA), which denote changed pixels misclassified as unchanged pixels, the overall accuracy (OA), and the kappa coefficient  $k$  (Foody, 2004) were used as evaluation metric to evaluate the experiments quantitatively. Furthermore, as the changed and unchanged classes of the study cases are imbalanced, the  $F1$  score (Chinchor and Sundheim, 1993), which is the harmonic mean of precision and recall, was also used for classification evaluation. In addition, as this study focuses on rapid flood mapping, the implementation time (in seconds) were included to show the efficiency of the proposed method.

The selected reference image of the Evros River is a scene acquired on 20 September 2014 (Fig. 2a), the selection procedure takes 30 s (after pre-processing). The results of validation site 1 and site 2 are shown in Figs. 4 and 5, respectively, and the corresponding quantitative evaluations are listed in Table 1. In general, all of the methods can achieve a satisfactory result in the test sites of the Evros River. The PCA-k-means method also has the capability to remove noise as it performs on patches of an image which takes the spatial information into account. According to the results listed in Table 1, all the random field model-based methods outperform the PCA-k-

means approach in both validation sites in terms of OA,  $k$ , and  $F1$ . The proposed method (SGGMM-FCRF) achieves the best result. However, there is no significant difference to other random field model-based methods (FCM-MRF, FCM-FCRF, SGGMM-MRF). This indicates that on the one hand, both of the FCM and SGGMM algorithms can obtain appropriate unary potential estimations for random field models of this test data, on the other hand, both of the local-range MRF and long-range FCRF can successfully reduce noise and remain the changed information at the same time. The reason could be that the flood occupies a relatively large portion of the target image ( $\sim 20\%$ ), and the study area of Evros River is relatively homogeneous with widespread farmland that is less affected by the speckle noise. It enables the FCM algorithms to be sufficient to distinguish the changed area and unchanged area without a lot of noise. Both local-range MRF and long-range FCRF are capable to smooth out the noise with a little-changed information lost. One drawback of unary estimation by FCM is that a further postprocessing is needed to associate the identified clusters with changed or unchanged label (Bovolo et al., 2008). However, if we take a closer inspection of the Figs. 4 and 5, although the PCA-k-means

method can get smooth results in both validation sites, there are some changed areas undetected along the riverside of site

1 (see the rectangle in Fig. 4a), and along the lakeside of site 2 (see the rectangles in Fig. 5a), responding to the highest MA in Table 1. Similar situations are related to the results (see Figs. 4b, d, 5b, and 5d) based on MRF models (FCM-MRF and SGGMM-MRF). As only locally connected labels are compared in the MRF, this approach tends to over-smooth the classification results and removes some detailed information. In contrary, the FCRF considers the long-range relationship in both the observation and the label domain. Further, it enables to eliminate noise and preserves fine structures meanwhile (see Figs. 4c, e, 5c, and 5e).

The selected reference image for the York test site is a scene acquired on 12 September 2015 (Fig. 3a), the selection procedure takes 36 s (after pre-processing). The results of the validation site derived by the different methods are shown in Fig. 6. From Fig. 6a, we can find that the PCA-k-means method can detect the changed areas, but with a lot of noise and false detected areas. This leads to a high FA and unsatisfactory result, see the low value of  $k$  (0.3759) and  $F1$  (0.4378)

listed in Table 2. Fig. 6b and c show that the application of the FCM-MRF and FCM-FCRF is destructive as the real changed area cannot be depicted. Further, there are large areas and a lot of isolate points misclassified as changed area. This indicates that in a complex environment and highly skewed dataset ( $\sim 3\%$  changed pixels in York dataset), the FCM algorithm is unfeasible to separate the changed and unchanged pixels accurately. The unary potential estimated by FCM with high noise leads to unusable results from MRF and FCRF. Compared with the aforementioned methods, SGGMM-MRF (Fig. 6d) and SGGMM-FCRF (Fig. 6e) achieve much better results. SGGMM-FCRF performs the best with the highest value of  $k$  (0.8682) and  $F1$  (0.8769). The results of SGGMM-MRF and SGGMM-FCRF indicate that the SGGMM is insensitive and stable to highly imbalanced datasets and are thus able to estimate appropriate unary potentials for MRF and FCRF. Similar to the Evros River test site, thanks to the long-range connection of the FCRF, SGGMM-FCRF preserves the fine and thin structures of the changed area and gain a higher accurate result respect to SGGMM-MRF (see details of the rectangle in Fig. 6d and e).

The implementation times of each method on the Evros River and the York datasets are listed in Table 1 and 2, respectively. The PCA-k-means is the fastest method but performs worse than the random field model-based methods. The total computation time of the SGGMM-FCRF on the Evros River dataset (4342\*5314 pixels) is 186 s, in which the SGGMM takes 127 s and the inference of FCRF costs 59 s. Even though it is slower than the alternatives, it achieves the best performance and this time cost could be thought as efficient for real applications. The runtime of the SGGMM-FCRF on the York dataset (7210\*6031) is 249 s, where the computing time for SGGMM is 137 s and the inference time of FCRF is 112 s. It is interesting to compare the processing time of each method between these two datasets. It indicates that the disadvantage in processing time of the SGGMM-FCRF is less distinct when the image size becomes larger. For efficient computation, the longest dimension of the image is resized to 250 pixels when the saliency detection is applied. Moreover, the iterative procedure of the EM-GGMM is based on image gray level rather than based on image pixel like the FCM algorithm. Thus, the implementation time of the SGGMM is roughly independent of the image size and more efficient than the FCM on a large-size image (see Table 2). One can also find that the runtime of the SGGMM-FCRF is slightly faster than the SGGMM-MRF on the York dataset. As noted in Boykov and Kolmogorov (2004), the worst case time complexity of the graph-cut is  $O(mn^2 |C|)$ , where  $n$  is the number of variables,  $m$  is the number of edges, and  $|C|$  is the cut cost. The mean-field approximate inference algorithm for FCRF is linear in the number of variables and sublinear in the number of edges (Philipp and Koltun, 2011). Therefore, the SGGMM-FCRF method is capable of handling a high-dimensional image efficiently.

<sup>1</sup> The python wrapper for fully-connected CRFs is from <https://github.com/lucasb-eyer/pydensecrf>.



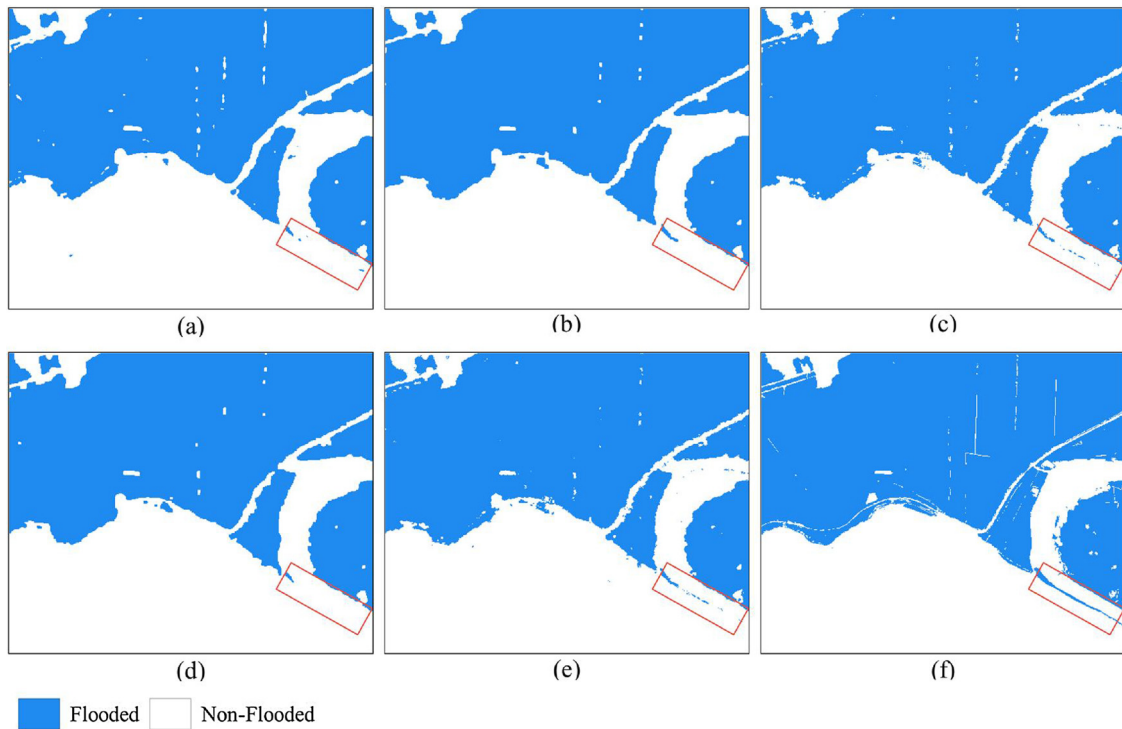


**Fig. 4.** Results of different methods on validation site1 of the Evros River dataset. (a) PCA-k-means; (b) FCM-MRF; (c) FCM-FCRF; (d) SGGMM-MRF; (e) SGGMM-FCRF; (f) flood reference mask derived from WorldView-2 data.

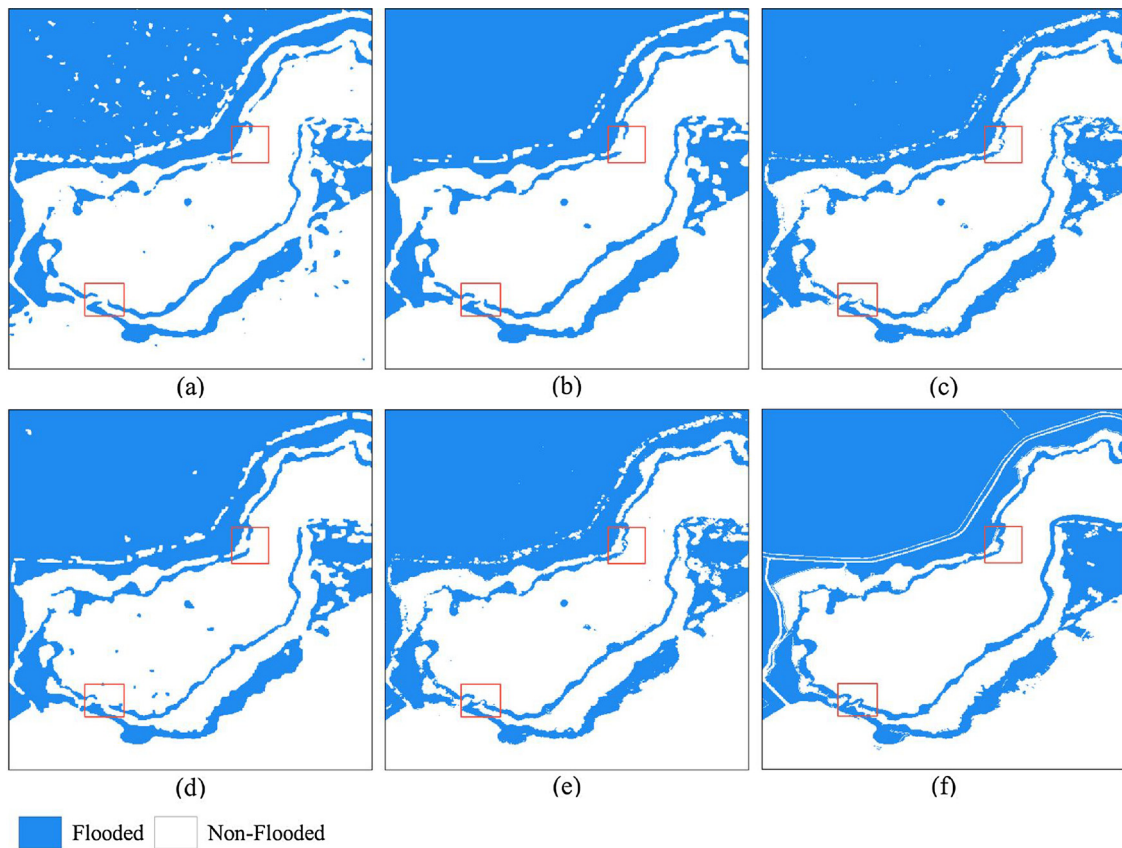


**Fig. 5.** Results of different methods on validation site 2 of the Evros River dataset. (a) PCA-k-means; (b) FCM-MRF; (c) FCM-FCRF; (d) SGGMM-MRF; (e) SGGMM-FCRF; (f) flood reference mask derived from WorldView-2 data.

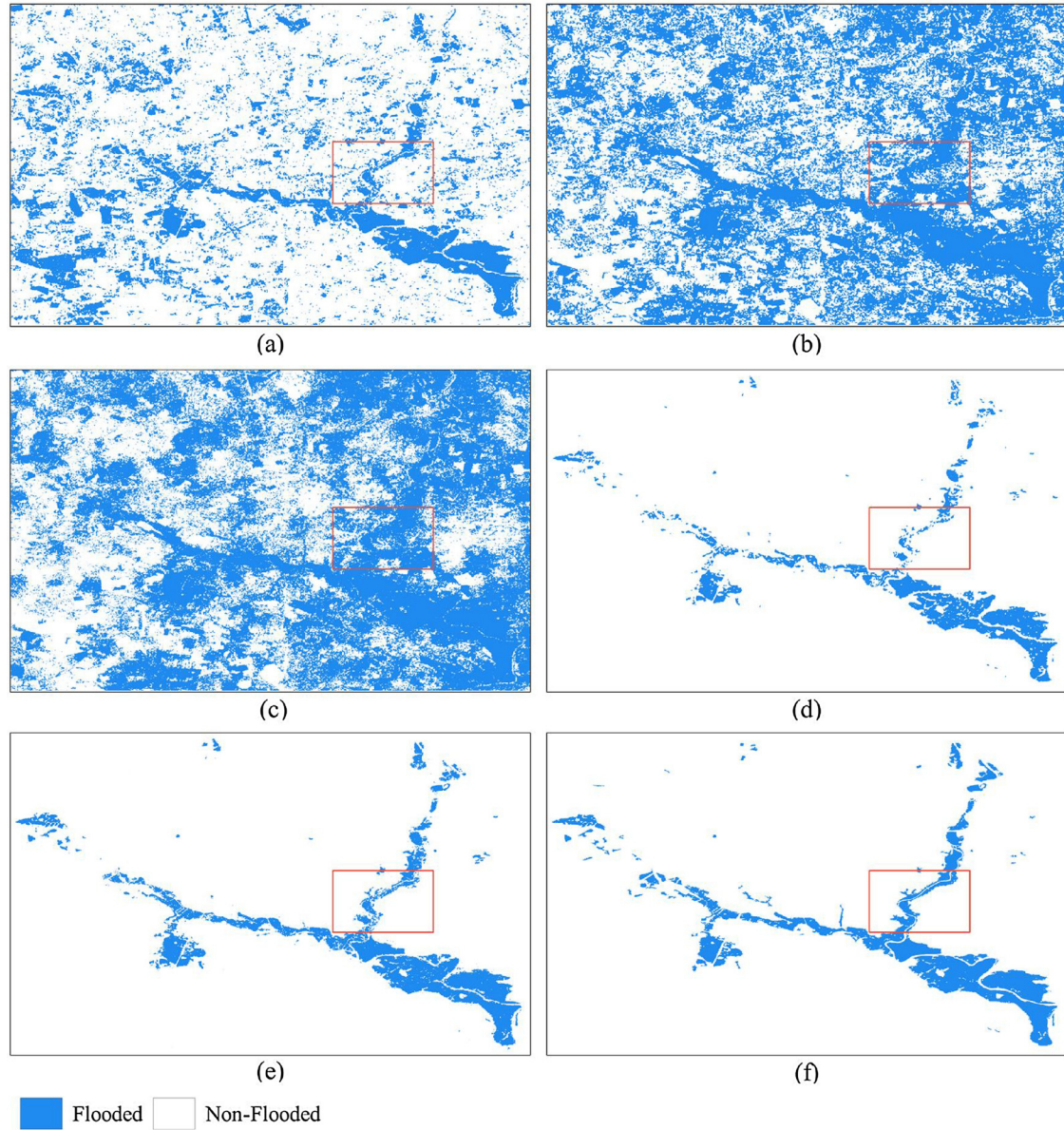


**Fig. 6.** Results of different methods on validation site of the York dataset. (a) PCA-k-means; (b) FCM-MRF; (c) FCM-FCRF; (d) SGGMM-MRF; (e) SGGMM-FCRF; (f) flood reference mask derived from Sentinel-2 data.

**Table 1**  
Quantitative comparison on validation sites of the Evros River dataset.

Method	Validation site 1 (Fig. 4)					Time (s)	Validation site 2 (Fig. 5)				
	OA (%)	FA (%)	MA (%)	k	F1		OA (%)	FA (%)	MA (%)	k	F1
PCA-k-means	96.41	0.46	3.13	0.9277	0.9670	56	93.47	1.18	5.35	0.8667	0.9235
FCM-MRF	97.09	0.70	2.21	0.9414	0.9735	166	95.22	1.62	3.16	0.9032	0.9458
FCM-FCRF	97.01	0.66	2.33	0.9397	0.9728	195	95.16	1.60	3.24	0.9019	0.9450
SGGMM-MRF	97.11	0.71	2.18	0.9417	0.9737	157	94.68	1.79	3.53	0.8921	0.9395
SGGMM-FCRF	97.17	0.77	2.06	0.9428	0.9743	186	95.30	1.83	2.87	0.9047	0.9469

#### 4.2. Parameter sensitivity analysis

The first parameter that needs to be set is the saliency detection threshold value  $t$ , which provides the prior information to the following EM-GGMM and plays an important role in the whole processing chain. Fig. 7a shows the prior probability of the changed component  $P_{changed}$  against  $t$ . If  $t = 0$ , all pixels in the image are treated as the changed

component and it is easy to remove the unchanged pixels at this stage. As shown in Fig. 7a, at the beginning stage  $P_{changed}$  decreases sharply with the increase of  $t$ . If  $t$  is close to the critical value, most of the unchanged pixels are removed and the remained parts are mainly changed pixels. Increase  $t$  value continuously will enforce the algorithm to remove more pixels as the unchanged component and this procedure becomes slow. Therefore, the critical value, which is corresponding to

**Table 2**  
Quantitative comparison on validation site of the York dataset.

Method	OA (%)	FA (%)	MA (%)	k	F1	Time (s)
PCA-k-means	84.37	14.55	0.72	0.3749	0.4378	162
FCM-MRF	53.60	46.28	0.12	0.1156	0.2203	440
FCM-FCRF	51.63	48.27	0.10	0.1073	0.2135	412
SGGMM-MRF	97.79	0.28	1.93	0.8002	0.8116	277
SGGMM-FCRF	98.38	0.74	0.88	0.8682	0.8769	249

the inflection point of the curves in Fig. 7a could be considered as a reasonable threshold value. The inflection point is around 0.2 in our experiments. From Fig. 7b (the average performance of the validation site 1 and site 2 is presented for the Evros River dataset) one can find that it does not impact the performance significantly when  $t$  is in the range of 0.2 to 0.5. It is worth noting that a (very) large value of  $t$  bears the risk of underestimating  $P_{\text{changed}}$ . This (significant) underestimation of  $P_{\text{changed}}$  leads it to be less meaningful from a statistical point of view, especially for the case that the changed area occupies a minor portion of the whole image. Thus a (very) large value of  $t$  should be avoided.

The parameter sensitivity analysis of FCRF is shown in Fig. 8. The average performances of the validation site 1 and site 2 are presented in Fig. 8a and c. As noted in Philipp and Koltun (2011), the smoothness kernel does not significantly affect the result. We kept  $\omega^{(1)} = 1$  for all the sensitivity analyses. Fig. 8a and 8b show the  $k$  statistic against parameters  $\theta_\gamma$  and  $\omega^{(2)}$  on Evros River and York datasets, respectively, from which one can find the results are insensitive to the smoothness kernel spatial parameter  $\theta_\gamma$ . The weight  $\omega^{(2)}$  of appearance kernel plays a more important role on York dataset, a too small value is undesirable. Nevertheless, it obtains acceptable results on both datasets within a certain range of these two parameters, with  $k$  above 0.92 and 0.83, respectively. In Fig. 8c and d we tested  $k$  against the different parameter combinations of  $\theta_\alpha$  and  $\theta_\beta$ , while fixing all of the other parameters. It can be seen that the  $k$  statistic changes slightly with a large range of parameter pairs. All of the parameter pairs achieved  $k$  statistic above 0.92 in Fig. 8c, most of them are located between 0.920 and 0.925. The flat shape of each individual curve and the interval between curves indicate that in the homogeneous area like the Evros River, the spatial parameter  $\theta_\alpha$  affects classification accuracy more significantly than the feature parameter  $\theta_\beta$ . On the opposite, the result of York area in Fig. 8d varies much faster with the variation of the feature parameter  $\theta_\beta$  respect to the spatial parameter  $\theta_\alpha$ . As this area consists of a lot of thin and fine structures, the result is more sensitive to  $\theta_\beta$ . When  $\theta_\beta$  exceeds a certain value (30 in this study), value  $k$  drops off steeply with increasing value of  $\theta_\beta$ . As noted in Philipp and Koltun (2011), too large values of  $\theta_\alpha$  and

$\theta_\beta$  can lead to misleading information propagation, eroding detailed information and reducing the classification accuracy. In our experiments, the results are acceptable within a certain range of parameters  $\theta_\alpha$  and  $\theta_\beta$ , with  $k$  statistic above 0.92 and 0.84 for the Evros river and the York datasets, respectively. The results compared in Fig. 6 and the sensitivity analysis in Fig. 8 show that with an appropriate unary estimation, the FCRF performs stable in a certain range of parameters when applied on unsupervised rapid flood mapping.

#### 4.3. Evaluation of reference image index

To evaluate the performance of reference index  $Ref_{\text{index}}$  in change detection for flood extent mapping, we applied SGGMM-FCRF on different log-ratio images by varying the reference images from different dates while keeping all other sets the same. The results of the Evros river (average performance of validation site 1 and 2) and York are listed in Table 3 and 4, respectively. For each study area, five reference images with different  $Ref_{\text{index}}$  values are compared in terms of FA, MA, and  $k$ . The comparison experiments for both study areas show that

the reference image with lowest  $Ref_{\text{index}}$  value obtains the best result. This indicates that the proposed index is able to select an adequate reference image for change detection based rapid flood mapping. In the study area of the Evros River, the reference images from dates of 31 October 2014, 14 October 2015, and 20 September 2015 achieve good results, with high values of  $k$  (0.8526, 0.9175, and 0.9238, respectively). In contrast, the reference images from dates of 06 December 2014 and 04 June 2015 result in low values of  $k$  (0.5077 and 0.5403, respectively). The area was partially affected by flood at these two dates, leading to an underestimation of flood extent, see the high MA (22.03% and 18.01%, respectively) in Table 3. In the study area of York, the reference images with relatively low value of  $Ref_{\text{index}}$  from 05 December 2015, 28 March 2015, and 07 August 2015 gain satisfactory results in terms of  $k$  (0.7321, 0.7338, and 0.7478, respectively), but worse than the best result (0.8682 of  $k$  statistic) achieved from the reference image with lowest  $Ref_{\text{index}}$  value at the date of 12 September 2015. The reduced accuracy of the former reference images could be attributed to the existence of areas covered by flood (05 December 2015) or water look-alike areas (28 March 2015 and 07 August 2015), leading to higher MA (2.39%, 2.46%, and 2.37%, respectively). The reference image acquired on 20 June 2015 obtains an unsatisfactory result with a low value of  $k$  (0.5783). This could be explained by the variation of intensity in the reference image (20 June 2015) and the target image (29 December 2015) caused by the different growth stage of crops in farmland. The higher intensity due to the crops in the

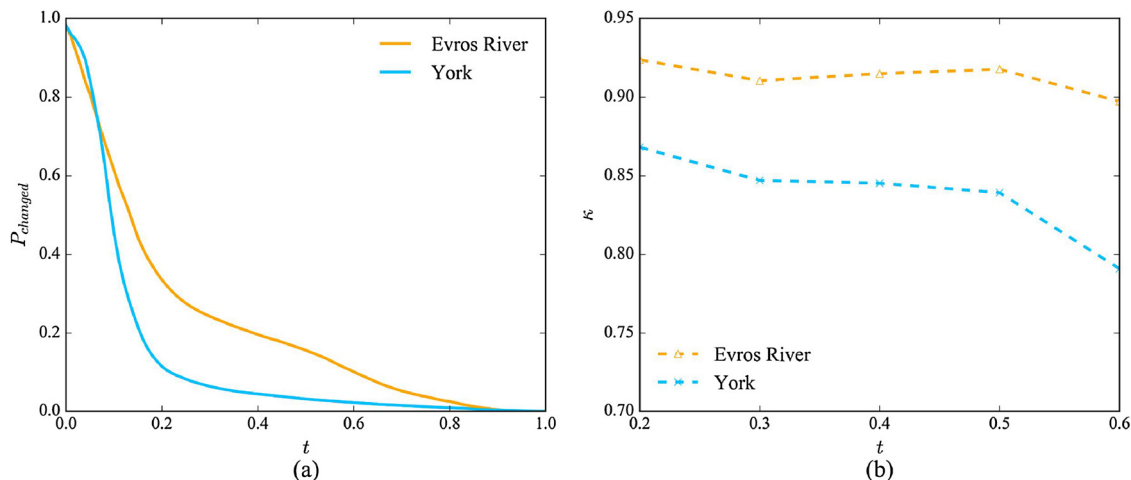


**Fig. 7.** Influence of saliency detection threshold value  $t$  on change detection using SGGMM-FCRF. (a) prior probability of changed component versus threshold value  $t$ ; (b) kappa coefficient versus threshold value  $t$ .



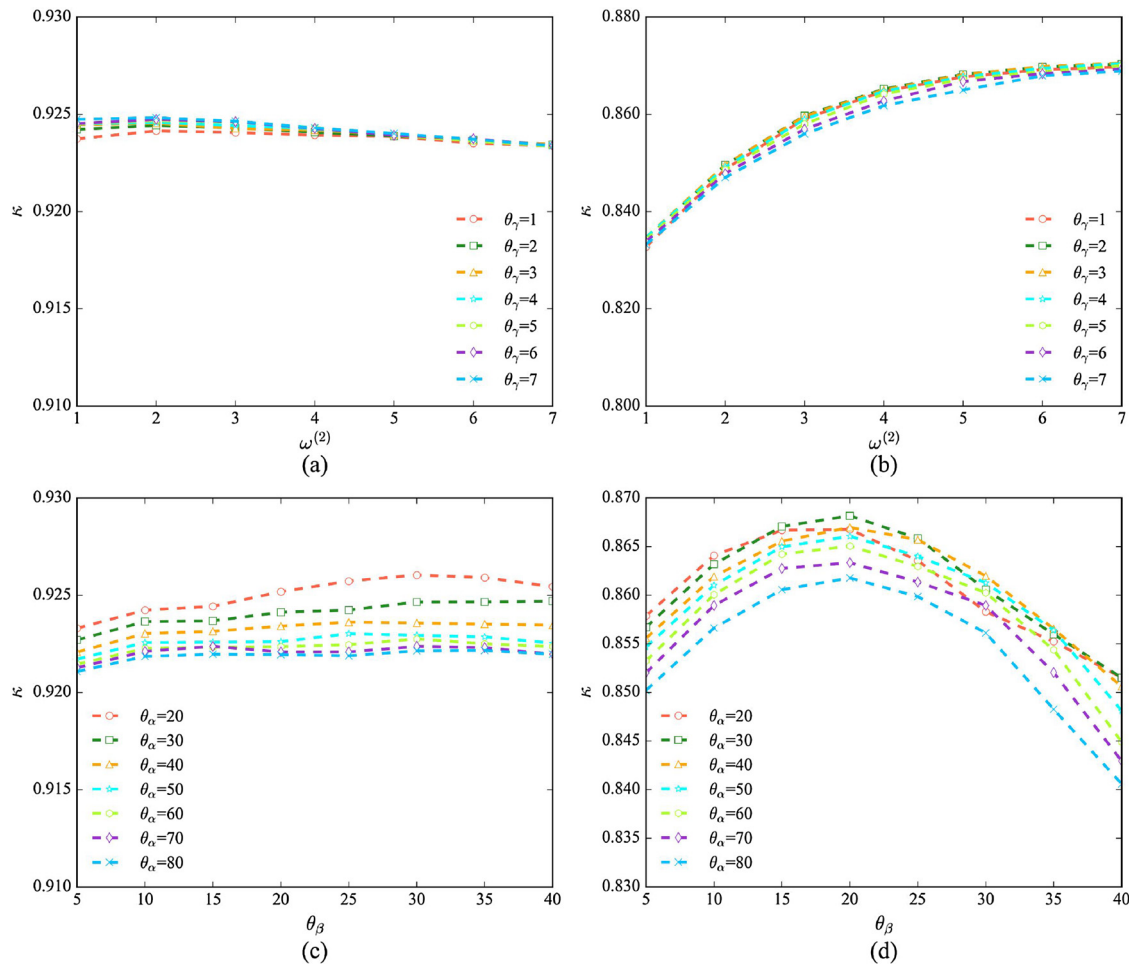


**Fig. 8.** Influence of long-range connections on change detection using SGGMM-FCRF. (a) kappa coefficient versus  $\theta_\gamma$  and  $\omega^{(2)}$  on the Evros River dataset; (b) kappa coefficient versus  $\theta_\gamma$  and  $\omega^{(2)}$  on the York dataset; (c) kappa coefficient versus  $\theta_\alpha$  and  $\theta_\beta$  on the Evros River dataset; (d) kappa coefficient versus  $\theta_\alpha$  and  $\theta_\beta$  on the York dataset.

**Table 3**

Comparison of classification results based on different reference images on the Evros River dataset.

Date	Ref <sub>index</sub>	FA (%)	MA (%)	k
31/10/2014	0.1306	1.72	5.51	0.8526
06/12/2014	0.6032	0.46	22.03	0.5077
04/06/2015	0.2996	4.95	18.01	0.5403
20/09/2015	0.0885	1.30	2.46	0.9238
14/10/2015	0.0932	1.52	2.56	0.9175

**Table 4**

Comparison of classification results based on different reference images on the York dataset.

Date	Ref <sub>index</sub>	FA (%)	MA (%)	k
28/03/2015	0.1964	0.36	2.46	0.7338
07/08/2015	0.1672	0.31	2.37	0.7478
20/06/2015	0.9534	7.31	0.45	0.5783
12/09/2015	0.0698	0.74	0.88	0.8682
05/12/2015	0.3595	0.50	2.39	0.7321

reference image than that in the target image leads to a negative change in the log-ratio image, giving rise to a high FA (7.31%).

## 5. Conclusion

In this study, an automatic change detection processing chain for rapid flood mapping in Sentinel-1 data is presented. Change detection-based algorithms play a critical role in flood monitoring using remote sensing data, while the selection of a reference image is crucial in order to get an accurate thematic map. The JS divergence-based reference image index is proposed for reference image selection, which consists of two terms. The first term evaluates the similarity of the empirical distribution functions between a reference image candidate and the target flood image, expressing the “non-flooded” degree of the image candidate. The second term measures the similarity of the empirical distribution functions between a reference image candidate and the median image of all image candidates, representing the “normal behavior” property of the image candidate. The image candidate with the lowest reference index value is supposed to be the optimal reference image. The Saliency-guided generalized Gaussian mixture model (SGGMM) is proposed to extract primary change detection information based on the log-ratio image that is generated from the reference and target image. The multi-scale context-aware saliency detection is insensitive to the speckle noise and data distribution and capable to achieve a good estimation of the prior probability of changed and

unchanged components regardless of their imbalance. Further, it provides an adequate guidance to the EM-based GGMM. The SGGMM method is efficient in computation time and flexible and robust to highly unbalanced datasets, which is the common situation for flood extent detection in remote sensing data over large areas. We further introduce the fully-connected conditional random field (FCRF) to the change detection process chain in order to smooth the result and improve the accuracy. In contrast to the traditional local-connected MRF and CRF, the FCRF considers a global view in both label and observation domains, thus enabling it to eliminate noise and to preserve detailed information at the same time. Thanks to the mean-field approximation, the inference of FCRF is efficient and makes it practical to implementation on large-size remote sensing images.

The qualitative and quantitative analysis of experiments on Sentinel-1 Ground range detected (GRD) data over the Evros River and the York area demonstrate the effectiveness and efficiency of the proposed method. Kappa coefficients ( $k$ ) of the two study areas are 0.9238 and 0.8682 respectively, with processing times ranging from 216 s (4342\*5314 pixels with 26 reference image candidates) to 285 s (7210\*6031 pixels with 18 reference image candidates) on a laptop with 32GB RAM and Intel i7 Processor, which is acceptable for rapid flood mapping application. However, the most time-consuming steps

during the whole process are reference image candidates download and pre-processing, which could cost several hours. The volume of the candidate set can be regarded as a trade-off between reference image optimization and time burden. To reduce the pre-processing time, the reference image could be selected from the data set acquired one year (e.g., one or two images for each month) before the flood event, or from the data set acquired at the same season as the flood data over several years. Due to the limited penetration capacity of C band, Sentinel-1 data with the proposed method is restricted to work in rural areas without dense vegetation. Furthermore, for more challenging tasks like flood mapping in vegetated and urban areas, additional information other than amplitude may be preferable. Future work will focus on considering interferometric coherence and polarimetric scattering to detect flooded surfaces in urban areas and to identify flooded vegetation.

## Acknowledgements

This work is supported by the Chinese Scholarship Council (CSC). The WorldView-2 imagery was kindly provided by European Space Imaging Ltd. (EUSI). The authors would like to thank the anonymous reviewers for their helpful comments and constructive suggestions.

## Appendix A

**Table A1**

Dates of collected images for reference image selection at the Evros River study area.

19/10/2014	31/10/2014	24/11/2014
06/12/2014	18/12/2014	30/12/2014
11/01/2015	04/02/2015	16/02/2015
24/03/2015	05/04/2015	17/04/2015
11/05/2015	04/06/2015	16/06/2015
28/06/2015	15/08/2015	27/08/2015
08/09/2015	20/09/2015	14/10/2015
26/10/2015	19/11/2015	01/12/2015
13/12/2015	25/12/2015	

**Table A2**

Dates of collected images for reference image selection at the York study area.

28/03/2015	21/04/2015	15/05/2015
08/06/2015	20/06/2015	14/07/2015
26/07/2015	07/08/2015	19/08/2015
31/08/2015	12/09/2015	24/09/2015
06/10/2015	18/10/2015	30/10/2015
11/11/2015	05/12/2015	15/02/2016

## References

- Ban, Y. (Ed.), 2016. Multitemporal Remote Sensing, Multitemporal Remote Sensing. Springer International Publishing. <http://dx.doi.org/10.1007/978-3-319-47037-5>.
- Ban, Y., Yousif, O.A., 2012. Multitemporal spaceborne SAR data for urban change detection in China. *IEEE J. Sel. Top. Appl. Earth Obs. Remote Sens.* 5, 1087–1094. <http://dx.doi.org/10.1109/JSTARS.2012.2201135>.
- Bazi, Y., Bruzzone, L., Melgani, F., 2005. An unsupervised approach based on the generalized Gaussian model to automatic change detection in multitemporal SAR images. *IEEE Trans. Geosci. Remote Sens.* 43, 874–887. <http://dx.doi.org/10.1109/TGRS.2004.842441>.
- Bazi, Y., Bruzzone, L., Melgani, F., 2007. Image thresholding based on the EM algorithm and the generalized Gaussian distribution. *Pattern Recognit.* 40, 619–634. <http://dx.doi.org/10.1016/J.PATCOG.2006.05.006>.
- Bilmes, J.A., 1998. A Gentle Tutorial of the EM Algorithm and its Application to Parameter Estimation for Gaussian Mixture and Hidden Markov Models.
- Bovolo, F., Bruzzone, L., 2005. A detail-preserving scale-driven approach to change detection in multitemporal SAR images. *IEEE Trans. Geosci. Remote Sens.* 43, 2963–2972. <http://dx.doi.org/10.1109/TGRS.2005.857987>.
- Bovolo, F., Bruzzone, L., 2007. A split-based approach to unsupervised change detection in large-size multitemporal images: application to tsunami-damage assessment. *IEEE Trans. Geosci. Remote Sens.* 45, 1658–1670. <http://dx.doi.org/10.1109/TGRS.2007.895835>.
- Bovolo, F., Bruzzone, L., Marconcini, M., 2008. A novel approach to unsupervised change detection based on a semisupervised SVM and a similarity measure. *IEEE Trans. Geosci. Remote Sens.* 46, 2070–2082. <http://dx.doi.org/10.1109/TGRS.2008.916643>.
- Boykov, Y., Kolmogorov, V., 2004. An experimental comparison of min-cut/max-flow algorithms for energy minimization in vision. *IEEE Trans. Pattern Anal. Mach. Intell.* 26, 1124–1137. <http://dx.doi.org/10.1109/TPAMI.2004.60>.
- Bruzzone, L., Prieto, D.F., 2000. Automatic analysis of the difference image for unsupervised change detection. *IEEE Trans. Geosci. Remote Sens.* 38, 1171–1182. <http://dx.doi.org/10.1109/36.843009>.
- Bujor, F., Troune, E., Valet, L., Nicolas, J.-M., Rudant, J.-P., 2004. Application of log-cumulants to the detection of spatiotemporal discontinuities in multitemporal SAR



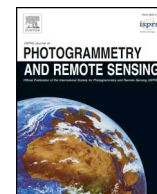
- images. *IEEE Trans. Geosci. Remote Sens.* 42, 2073–2084. <http://dx.doi.org/10.1109/TGRS.2004.835304>.
- Cao, G., Zhou, L., Li, Y., 2016. A new change-detection method in high-resolution remote sensing images based on a conditional random field model. *Int. J. Remote Sens.* 37, 1173–1189. <http://dx.doi.org/10.1080/01431161.2016.1148284>.
- Cao, W., Twele, A., Plank, S., Martinis, S., 2018. A three-class change detection methodology for SAR-data based on hypothesis testing and Markov Random field modelling. *Int. J. Remote Sens.* 39, 488–504. <http://dx.doi.org/10.1080/01431161.2017.1384590>.
- Celik, T., 2009a. Multiscale change detection in multitemporal satellite images. *IEEE Geosci. Remote Sens. Lett.* 6, 820–824. <http://dx.doi.org/10.1109/LGRS.2009.2026188>.
- Celik, T., 2009b. Unsupervised change detection in satellite images using principal component analysis and k-means clustering. *IEEE Geosci. Remote Sens. Lett.* 6, 772–776. <http://dx.doi.org/10.1109/LGRS.2009.2025059>.
- Chinchor, N., Sundheim, B., 1993. MUC-5 evaluation metrics, Morristown, NJ, USA. Proceedings of the 5th Conference on Message Understanding - MUC5'93. Association for Computational Linguistics 69. <http://dx.doi.org/10.3115/1072017.1072026>.
- Chini, M., Hostache, R., Giustarini, L., Matgen, P., 2017. A hierarchical split-based approach for parametric thresholding of SAR images: flood inundation as a test case. *IEEE Trans. Geosci. Remote Sens.* 55, 6975–6988. <http://dx.doi.org/10.1109/TGRS.2017.2737664>.
- Choy, S.K., Tong, C.S., 2010. Statistical wavelet subband characterization based on generalized gamma density and its application in texture retrieval. *IEEE Trans. Image Process.* 19, 281–289. <http://dx.doi.org/10.1109/TIP.2009.2033400>.
- Cui, S., Schwarz, G., Datcu, M., 2016. A benchmark evaluation of similarity measures for multitemporal SAR image change detection. *IEEE J. Sel. Top. Appl. Earth Obs. Remote Sens.* 9, 1101–1118. <http://dx.doi.org/10.1109/JSTARS.2015.2486038>.
- Dempster, A.P., Laird, N.M., Rubin, D.B., 1977. Maximum likelihood from incomplete data via the EM algorithm. *J. R. Stat. Soc. Ser. B* 39, 1–38.
- Ding, Y., Li, Y., Yu, W., 2014. SAR image classification based on CRFs with integration of local label context and pairwise label compatibility. *IEEE J. Sel. Top. Appl. Earth Obs. Remote Sens.* 7, 300–306. <http://dx.doi.org/10.1109/JSTARS.2013.2262038>.
- Do, M.N., Vetterli, M., 2002. Wavelet-based texture retrieval using generalized Gaussian density and Kullback-Leibler distance. *IEEE Trans. Image Process.* 11, 146–158. <http://dx.doi.org/10.1109/83.982822>.
- Fernandez-Prieto, D., Marconcini, M., 2011. A novel partially supervised approach to targeted change detection. *IEEE Trans. Geosci. Remote Sens.* 49, 5016–5038. <http://dx.doi.org/10.1109/TGRS.2011.2154336>.
- Footy, G.M., 2004. Thematic map comparison. *Photogramm. Eng. Remote Sens.* 70, 627–633. <http://dx.doi.org/10.14358/PERS.70.5.627>.
- Gamba, P., Dell'Acqua, F., Trianni, G., 2007. Rapid damage detection in the bam area using multitemporal SAR and exploiting ancillary data. *IEEE Trans. Geosci. Remote Sens.* 45, 1582–1589. <http://dx.doi.org/10.1109/TGRS.2006.885392>.
- Geman, S., Geman, D., 1984. Stochastic relaxation, Gibbs distributions, and the bayesian restoration of images. *IEEE Trans. Pattern Anal. Mach. Intell.* PAMI-6 721–741. <http://dx.doi.org/10.1109/TPAMI.1984.4767596>.
- Giustarini, L., Hostache, R., Matgen, P., Schumann, G.J., Bates, P.D., Mason, D.C., 2013. A change detection approach to flood mapping in urban areas using TerraSAR-X. *IEEE Trans. Geosci. Remote Sens.* 51, 2417–2430. <http://dx.doi.org/10.1109/TGRS.2012.2210901>.
- Giustarini, L., Vernieuwe, H., Verwaeren, J., Chini, M., Hostache, R., Matgen, P., Verhoest, N.E.C., De Baets, B., 2015. Accounting for image uncertainty in SAR-based flood mapping. *Int. J. Appl. Earth Obs. Geoinf.* 34, 70–77. <http://dx.doi.org/10.1016/J.JAG.2014.06.017>.
- Glasbey, C.A., 1993. An analysis of histogram-based thresholding algorithms. *CVGIP Graph. Model. Image Process.* 55, 532–537. <http://dx.doi.org/10.1006/cgip.1993.1040>.
- Goferman, S., Zelnik-Manor, L., Tal, A., 2012. Context-aware saliency detection. *IEEE Trans. Pattern Anal. Mach. Intell.* 34, 1915–1926. <http://dx.doi.org/10.1109/TPAMI.2011.272>.
- Gong, M., Li, Y., Jiao, L., Jia, M., Su, L., 2014. SAR change detection based on intensity and texture changes. *ISPRS J. Photogramm. Remote Sens.* 93, 123–135. <http://dx.doi.org/10.1016/J.ISPRSJPRS.2014.04.010>.
- He, X., Zemel, R.S., Carreira Perpinan, M.A., 2004. Multiscale conditional random fields for image labeling. *CVPR 2004. IEEE. Proceedings of Computer Vision and Pattern Recognition*, 2004 695–702. <http://dx.doi.org/10.1109/CVPR.2004.1315232>.
- Hostache, R., Matgen, P., Wagner, W., 2012. Change detection approaches for flood extent mapping: how to select the most adequate reference image from online archives? *Int. J. Appl. Earth Obs. Geoinf.* 19, 205–213. <http://dx.doi.org/10.1016/J.JAG.2012.05.003>.
- Inglada, J., Mercier, G., 2007. A New statistical similarity measure for change detection in multitemporal SAR images and its extension to multiscale change analysis. *IEEE Trans. Geosci. Remote Sens.* 45, 1432–1445. <http://dx.doi.org/10.1109/TGRS.2007.893568>.
- Kohli, P., Ladický, L., Torr, P.H.S., 2009. Robust Higher order potentials for enforcing label consistency. *Int. J. Comput. Vis.* 82, 302–324. <http://dx.doi.org/10.1007/s11263-008-0202-0>.
- Kullback, S., Leibler, R.A., 1951. On information and sufficiency. *Ann. Math. Stat.* 22, 79–86. <http://dx.doi.org/10.1214/aoms/117729694>.
- Ladický, L., Ubor, Russell, C., Kohli, P., Torr, P.H.S., 2009. Associative hierarchical CRFs for object class image segmentation. *International Conference on Computer Vision*. pp. 739–746.
- Lafferty, J., McCallum, A., Pereira, F.C.N., Pereira, F., 2001. Conditional random fields: probabilistic models for segmenting and labeling sequence data. *International Conference on Machine Learning 2001 (ICML 2001)*. pp. 282–289.
- Li, H.C., Celik, T., Longbotham, N., Emery, W.J., 2015. Gabor feature based unsupervised change detection of multitemporal SAR images based on two-level clustering. *IEEE Geosci. Remote Sens. Lett.* 12, 2458–2462. <http://dx.doi.org/10.1109/LGRS.2015.2484220>.
- Martinez, J.M., Le Toan, T., 2007. Mapping of flood dynamics and spatial distribution of vegetation in the Amazon floodplain using multitemporal SAR data. *Remote Sens. Environ.* 108, 209–223. <http://dx.doi.org/10.1016/J.RSE.2006.11.012>.
- Martinis, S., Twele, A., Voigt, S., 2011. Unsupervised extraction of flood-induced backscatter changes in SAR data using Markov Image Modeling on irregular graphs. *IEEE Trans. Geosci. Remote Sens.* 49, 251–263. <http://dx.doi.org/10.1109/TGRS.2010.2052816>.
- Matgen, P., Hostache, R., Schumann, G., Pfister, L., Hoffmann, L., Savenije, H.H.G., 2011. Towards an automated SAR-based flood monitoring system: lessons learned from two case studies. *Phys. Chem. Earth Parts A/B/C* 36, 241–252. <http://dx.doi.org/10.1016/J.PCE.2010.12.009>.
- McLachlan, G.J., Peel, D., 2000. *Finite Mixture Models*. Wiley, New York.
- Moser, G., Serpico, S.B., 2006. Generalized minimum-error thresholding for unsupervised change detection from SAR amplitude imagery. *IEEE Trans. Geosci. Remote Sens.* 44, 2972–2982. <http://dx.doi.org/10.1109/TGRS.2006.876288>.
- Moser, G., Serpico, S.B., 2009. Unsupervised change detection from multichannel SAR data by Markovian data fusion. *IEEE Trans. Geosci. Remote Sens.* 47, 2114–2128. <http://dx.doi.org/10.1109/TGRS.2009.2012407>.
- Moser, G., Serpico, S., Vernazza, G., 2007. Unsupervised change detection from multichannel SAR images. *IEEE Geosci. Remote Sens. Lett.* 4, 278–282. <http://dx.doi.org/10.1109/LGRS.2007.890549>.
- Naim, I., Gildea, D., 2012. Convergence of the EM algorithm for Gaussian mixtures with unbalanced mixing coefficients. *Proceedings of the 29th International Conference on Machine Learning (ICML 2012)*. pp. 1655–1662.
- Nguyen, T.M., Jonathan Wu, Q.M., Zhang, H., 2014. Bounded generalized Gaussian mixture model. *Pattern Recognit.* 47, 3132–3142. <http://dx.doi.org/10.1016/J.PATCOG.2014.03.030>.
- O'Grady, D., Leblanc, M., Gillieson, D., 2011. Use of ENVISAT ASAR global monitoring Mode to complement optical data in the mapping of rapid broad-scale flooding in Pakistan. *Hydrol. Earth Syst. Sci.* 15, 3475–3494. <http://dx.doi.org/10.5194/hess-15-3475-2011>.
- Pheng, H.S., Shamsuddin, S.M., Leng, W.Y., Alwee, R., 2016. Kullback Leibler divergence for image quantitative evaluation. *AIP Conference Proceedings* 20003. <http://dx.doi.org/10.1063/1.4954516>. AIP Publishing LLC.
- Philipp, Koltun, V., 2011. Efficient inference in fully connected CRFs with Gaussian edge potentials. *Advances in Neural Information Processing Systems* 24 (NIPS 2011). pp. 109–117.
- Pulvirenti, L., Chini, M., Pierdicca, N., Guerriero, L., Ferrazzoli, P., 2011. Flood monitoring using multi-temporal COSMO-SkyMed data: image segmentation and signature interpretation. *Remote Sens. Environ.* 115, 990–1002. <http://dx.doi.org/10.1016/J.RSE.2010.12.002>.
- Puzicha, J., Hofmann, T., Buhmann, J.M., 1997. Non-parametric similarity measures for unsupervised texture segmentation and image retrieval. *IEEE Comput. Soc. Proceedings of IEEE Computer Society Conference on Computer Vision and Pattern Recognition* 267–272. <http://dx.doi.org/10.1109/CVPR.1997.609331>.
- Quattoni, A., Wang, S., Morency, L.-P., Collins, M., Darrell, T., 2007. Hidden conditional random fields. *IEEE Trans. Pattern Anal. Mach. Intell.* 29, 1848–1852. <http://dx.doi.org/10.1109/TPAMI.2007.1124>.
- Rabinovich, A., Vedaldi, A., Galleguillos, C., Wiewiora, E., Belongie, S., 2007. Objects in context. *IEEE. 2007 IEEE 11th International Conference on Computer Vision* 1–8. <http://dx.doi.org/10.1109/ICCV.2007.4408986>.
- Rignot, E.J.M., van Zyl, J.J., 1993. Change detection techniques for ERS-1 SAR data. *IEEE Trans. Geosci. Remote Sens.* 31, 896–906. <http://dx.doi.org/10.1109/36.239913>.
- Schindler, K., 2012. An overview and comparison of smooth labeling methods for land-cover classification. *IEEE Trans. Geosci. Remote Sens.* 50, 4534–4545. <http://dx.doi.org/10.1109/TGRS.2012.2192741>.
- Schlaffer, S., Matgen, P., Hollaus, M., Wagner, W., 2015. Flood detection from multitemporal SAR data using harmonic analysis and change detection. *Int. J. Appl. Earth Obs. Geoinf.* 38, 15–24. <http://dx.doi.org/10.1016/J.JAG.2014.12.001>.
- Shotton, J., Winn, J., Rother, C., Criminisi, A., 2006. TextonBoost: joint appearance, shape and context modeling for multi-class object recognition and segmentation. *IN ECCV*. pp. 1–15.
- Su, X., He, C., Feng, Q., Deng, X., Sun, H., 2011. A supervised classification method based on conditional random fields with multiscale region connection calculus model for SAR image. *IEEE Geosci. Remote Sens. Lett.* 8, 497–501. <http://dx.doi.org/10.1109/LGRS.2010.2089427>.
- Torrallba, A., Torrallba, A., Murphy, K.P., Freeman, W.T., 2004. Contextual models for object detection using boosted random fields. *Advances in Neural Information Processing Systems* 17 (NIPS 2004).
- Torrallba, A., Murphy, K.P., Freeman, W.T., 2007. Sharing visual features for multiclass and multiview object detection. *IEEE Trans. Pattern Anal. Mach. Intell.* 29, 854–869. <http://dx.doi.org/10.1109/TPAMI.2007.1055>.
- Toyoda, T., Hasegawa, O., 2008. Random Field model for integration of local information and global information. *IEEE Trans. Pattern Anal. Mach. Intell.* 30, 1483–1489. <http://dx.doi.org/10.1109/TPAMI.2008.105>.
- Twele, A., Cao, W., Plank, S., Martinis, S., 2016. Sentinel-1-based flood mapping: a fully automated processing chain. *Int. J. Remote Sens.* 37, 2990–3004. <http://dx.doi.org/10.1080/01431161.2016.1192304>.
- Ulabay, F.T., Dobson, M.C., 1989. *Handbook of Radar Scattering Statistics for Terrain*. Artech House, MA, USA.
- Verbeek, J., Triggs, W., 2007. Scene segmentation with CRFs learned from partially

- labeled images. NIPS 2007 - Advances in Neural Information Processing Systems. pp. 1553–1560 MIT Press.
- Vineet, V., Warrell, J., Sturges, P., Torr, P.H.S., 2012. Improved initialisation and Gaussian mixture pairwise terms for dense random fields with mean-field inference. *Proceedings British Machine Vision Conference*. pp. 1–11.
- Wegner, J.D., Hansch, R., Thiele, A., Soergel, U., 2011. Building detection from one orthophoto and high-resolution InSAR data using conditional random fields. *IEEE J. Sel. Top. Appl. Earth Obs. Remote Sens.* 4, 83–91. <http://dx.doi.org/10.1109/JSTARS.2010.2053521>.
- Xu, H., 2006. Modification of normalised difference water index (NDWI) to enhance open water features in remotely sensed imagery. *Int. J. Remote Sens.* 27, 3025–3033. <http://dx.doi.org/10.1080/01431160600589179>.
- Yousif, O., Ban, Y., 2014. Improving SAR-based urban change detection by combining MAP-MRF classifier and nonlocal means similarity weights. *IEEE J. Sel. Top. Appl. Earth Obs. Remote Sens.* 7, 4288–4300. <http://dx.doi.org/10.1109/JSTARS.2014.2347171>.
- Zhang, Y., Chen, T., 2012. Efficient inference for fully-connected CRFs with stationarity. *IEEE. 2012 IEEE Conference on Computer Vision and Pattern Recognition* 582–589. <http://dx.doi.org/10.1109/CVPR.2012.6247724>.
- Zhou, L., Cao, G., Li, Y., Shang, Y., 2016. Change detection based on conditional random field with region connection constraints in high-resolution remote sensing images. *IEEE J. Sel. Top. Appl. Earth Obs. Remote Sens.* 9, 3478–3488. <http://dx.doi.org/10.1109/JSTARS.2016.2514610>.

## **5. Urban flood mapping with an active self-learning convolutional neural network based on TerraSAR-X intensity and interferometric coherence**

Li, Y.; Martinis, S.; Wieland, M., 2019. Urban flood mapping with an active self-learning convolutional neural network based on TerraSAR-X intensity and interferometric coherence. *ISPRS J. Photogramm. Remote Sens.* 152, 178–191. DOI: [10.1016/j.isprsjprs.2019.04.014](https://doi.org/10.1016/j.isprsjprs.2019.04.014)

LY designed the study, developed the method and conducted the experiments. MS conceptualized the study and acquired the TerraSAR-X data. WM contributed to method development. LY drafted the manuscript, MS and WM contributed to the discussion and review of the manuscript.



# Urban flood mapping with an active self-learning convolutional neural network based on TerraSAR-X intensity and interferometric coherence

Yu Li\*, Sandro Martinis, Marc Wieland

German Remote Sensing Data Center (DFD), German Aerospace Center (DLR), Oberpfaffenhofen, Münchner Straße 20, 82234 Weßling, Germany

## ARTICLE INFO

### Keywords:

Urban flooding  
Multi-temporal SAR  
Interferometric coherence  
Active learning  
Self-learning  
Convolution neural network

## ABSTRACT

Synthetic Aperture Radar (SAR) remote sensing has been widely used for flood mapping and monitoring. Nevertheless, flood detection in urban areas still proves to be particularly challenging by using SAR. In this paper, we assess the roles of SAR intensity and interferometric coherence in urban flood detection using multi-temporal TerraSAR-X data. We further introduce an active self-learning convolution neural network (A-SL CNN) framework to alleviate the effect of a limited annotated training dataset. The proposed framework selects informative unlabeled samples based on a temporal-ensembling CNN model. These samples are subsequently pseudo-labeled by a multi-scale spatial filter. Consistency regularization is introduced to penalize incorrect labels caused by pseudo-labeling. We show results for a case study that is centered on flooded areas in Houston, USA, during hurricane Harvey in August 2017. Our experiments show that multi-temporal intensity (pre- and co-event) plays the most important role in urban flood detection. Adding multi-temporal coherence can increase the reliability of the inundation map considerably. Meanwhile, encouraging results are achieved by the proposed A-SL CNN framework: the  $\kappa$  statistic is improved from 0.614 to 0.686 in comparison to its supervised counterpart.

## 1. Introduction

Remote sensing systems have been widely recognized as suitable resources to provide cost- and time-efficient situational awareness over large areas in case of natural disasters (Bello and Aina, 2014; Benz et al., 2004; Tralli et al., 2005). Synthetic Aperture Radar (SAR) imagery is most commonly used for flood mapping due to its day-night and all-weather imaging capability. Especially SAR systems with long wavelengths (e.g., L and P band) can penetrate the canopy and provide information about the inundation state beneath vegetation. The detection capability of optical remote sensing systems in this situation is restricted. Unlike optical data, which detect geochemical properties of the earth surface, SAR data characterize geophysical features such as surface roughness and permittivity. These geophysical responses and the side-looking viewing geometry of the SAR system lead to different backscatter mechanisms in various land cover types, which potentially allows categorizing different flood situations (e.g., flooded open areas, flooded urban areas, and flooded vegetation). In the past two decades, a growing number of SAR satellite constellations in orbit assure increasingly short revisit periods of 6 days (e.g. Sentinel-1) or less (e.g. COSMO SkyMed) and higher spatial resolutions of 3 m or better (e.g. TerraSAR-X, RADARSAT-2, and ALOS-2).

Several studies (Martinis et al., 2011; Pulvirenti et al., 2011; Rimba

and Miura, 2017; Tanguy et al., 2017; Twele et al., 2016) have demonstrated successful flood mapping applications based on the aforementioned systems. Most of the literature on SAR-based flood mapping, however, focused on inundated rural areas and left urban areas largely unexplored. Considering their vulnerability to flooding (e.g., due to low slopes and a high percentage of impervious surfaces) and the increased risk of loss of human lives and damage to economic infrastructures, it is crucial to dedicate more research efforts to SAR-based urban flood mapping. The scarcity of existing studies in that direction might lie in the complex backscatter mechanisms in urban environments (see Section 2 for details), which make it difficult to incorporate knowledge about backscatter phenology into generic analysis algorithms. Among previous studies in urban areas, Mason et al. (2010, 2012) proposed a near-real-time algorithm for urban flood detection with TerraSAR-X data. They employed a SAR simulator in conjunction with high-resolution LiDAR data to mask shadow and layover regions in order to suppress false alarms. Mason et al. (2014) successfully detected flood in layover regions based on the double-bounce effect involving ground and vertical walls. A change detection approach with bi-temporal TerraSAR-X data was applied by Giustarini et al. (2013) for flood detection in urban areas in order to reduce false alarms generated by shadows and other water look-alike surfaces. More recently, Tanguy et al. (2017) used very high-resolution SAR imagery combined with

\* Corresponding author.

<https://doi.org/10.1016/j.isprsjprs.2019.04.014>

Received 18 December 2018; Received in revised form 18 April 2019; Accepted 22 April 2019

0924-2716/ © 2019 International Society for Photogrammetry and Remote Sensing, Inc. (ISPRS). Published by Elsevier B.V. All rights reserved.

hydraulic data (flood return period) to yield flood delineation in urban areas. Apart from SAR intensity ( $\sigma^0$ ), which was employed in the aforementioned studies, SAR interferometric coherence ( $\gamma$ ) has demonstrated its potential in urban flood mapping (Chini et al., 2012; Pulvirenti et al., 2016). Understanding the roles of different SAR information (e.g., uni-temporal or multi-temporal data, intensity and/or coherence) in urban flood mapping both theoretically and experimentally is important for practical applications. While the aforementioned studies consider parts of this issue, a quantitative and systematic investigation of the influence of different SAR information on the mapping of flooded urban areas is yet missing in the literature to the best of our knowledge.

From a methodological perspective, both unsupervised methods like histogram thresholding (Chini et al., 2019, 2017; Twele et al., 2016), fuzzy c-means clustering (Li et al., 2015), fuzzy decision (Amitrano et al., 2018), active contour modeling (Tong et al., 2018), saliency detection (Y. Li et al., 2018) and supervised classifiers such as support vector machines (SVM) (Insom et al., 2015) and artificial neural networks (Skakun, 2010) were employed for flood extent mapping. Recently, deep convolutional neural networks (CNNs) have shown promising results in remote sensing applications (Ball et al., 2017; Zhu et al., 2017), such as land cover and land use classification (Kussul et al., 2017; Maggiori et al., 2017; Zhang et al., 2019) and object detection (Cheng et al., 2016; Deng et al., 2018; Kellenberger et al., 2018), as well as earthquake (Vettrivel et al., 2018) and tsunami (Bai et al., 2018) damage detection. Unlike traditional machine learning models, CNNs are trained in an end-to-end manner, which not only trains a classifier but also extracts tailored features for the specific task at hand. Although deep CNN models have been reported as being superior to conventional models, the scarcity of training samples could degrade their performance. Augmentation methods and their advanced variants (e.g., sample synthesis through generative adversarial networks) might be the most popular technologies to artificially increase the number of training samples in limited training sample scenarios. Transfer learning (Pan and Yang, 2010) is also one of the widely used methods to alleviate the problem of insufficient training samples. Several studies have successfully applied transfer learning in optical remote sensing (Huang et al., 2018; Jean et al., 2016; Marmanis et al., 2016). However, the publicly available pre-trained models are based on natural images and might not be applicable to SAR data. Semi-supervised learning (SSL), which jointly leverages both labeled and unlabeled data, provides another powerful framework to improve classifiers when training samples are limited. SVM-based SSL is the most widely used paradigm in remote sensing (Bruzzone et al., 2006; Camps-Valls et al., 2007; Muñoz-mari et al., 2010). Recently, SSL under the deep CNN framework has achieved huge success in computer vision (Laine and Aila, 2017; Rasmus et al., 2015; Salimans et al., 2016; Tarvainen and Valpola, 2017), and has attracted considerable attention in remote sensing (He et al., 2017; Zhan et al., 2018; Zhu et al., 2018). Most of the state-of-the-art SSL methods introduce regularization to make the decision boundary lie in low density regions under the smoothness assumption. These methods usually require a large number of unlabeled samples to capture the underlying distribution or manifold structure of the dataset. It is available to get a large bulk of freely charged mid-resolution SAR (e.g., Sentinel-1) and optical data (e.g., Sentinel-2 and Landsat), and CNNs are capable of dealing with millions of data, however, the computational bottleneck in the training phase may impede the operational adoption of CNN-based SSL methods in large-scale applications. A computationally more efficient alternative could be the integration of the activate learning concept and self-learning, which has demonstrated to achieve promising results in remote sensing classification on the basis of SVM (Dópido et al., 2013; Persello and Bruzzone, 2014) and conditional random fields (F. Li et al., 2018), and is intuitively transferable to the deep CNN framework.

Based on the aforementioned literature research the objectives of this study are to:

- (1) Systematically assess the roles of different SAR information in urban flood mapping based on a supervised deep CNN model. In particular, we consider the following scenarios: I. uni-temporal co-event interferometric coherence; II. uni-temporal co-event intensity; III. multi-temporal interferometric coherence (e.g., post- and co-event pair); IV. multi-temporal intensity (e.g., pre- and co-event); V. the combination of multi-temporal intensity and coherence. An end-to-end training deep CNN model is employed in this investigation, thus the bias introduced by the hand-crafted features is avoided and the roles of raw information are compared in an intuitive and fair manner.
- (2) Introduce a novel semi-supervised deep neural network framework to yield improved performance compared to its supervised counterpart. More specifically, a temporal-ensembling active self-learning deep convolutional neural network (A-SL CNN) framework is proposed, which integrates active learning and self-learning at the conceptual level. The proposed framework has the following advantages: arbitrary CNN architectures can be applied in this framework; model committees can be obtained by training only one model; no additional human annotation is needed, which renders the iteration process a machine-machine instead of a machine-human interaction.

Our experiments focus on flooded areas in Houston, USA, during hurricane Harvey in August 2017, for which multi-temporal TerraSAR-X and respective optical reference data were acquired. The remainder of this paper is structured as follows. Section 2 introduces the characteristics of SAR intensity and coherence in urban flood mapping and describes the proposed A-SL CNN framework. Section 3 introduces the study area, datasets, and the experimental setup. Section 4 provides results and discussions. Finally, Section 5 draws the conclusion of this paper.

## 2. Method

### 2.1. Intensity and coherence in urban areas

The SAR backscatter in urban areas is composed of specular reflection, surface backscatter, as well as single, double, and triple bounces. Specular reflection occurs mostly from roads that are oriented along the line of sight of the SAR sensor, parking lots, and airports; whereas surface backscatter could happen for grasslands and bare soils. Single bounce scattering usually originates from sloping flat tile roofs, which are hardly detectable if interaction effects occur between adjacent buildings and trees (Thiele et al., 2007). A dihedral corner reflector formed from the wall-ground and a trihedral corner reflector formed from the wall-wall-ground structure causes double bounce and triple bounce, respectively. However, triple bounce structures are not as common as double bounce structures in urban areas, and the backscattering from triple bounce structures is much weaker than that from double bounce structures (Dong et al., 1997). Moreover, scattering from other elements like window frames and steel structures makes backscatter in urban areas more complex. Due to the side-looking viewing geometry, built-up structures cause shadowing and layover, which are affected by the incident angle. A larger incident angle results in a smaller layover area and larger shadow area, and vice versa. The double bounce backscattering is almost invariant to the variation of the incident angle (Thiele et al., 2007), but could be impacted by the orientation of buildings (Dong et al., 1997; Ferro et al., 2011): the strength of the double bounce effect decreases with the increase of the orientation (aspect) angle  $\phi$  (i.e., the angle between the orientation of the wall and the azimuth direction).

Due to the aforementioned backscattering mechanisms, flooded urban areas can have different appearances in SAR intensity images. Generally speaking, floodwater in urban areas appears in either a darker or a brighter image tone depending on the difference in



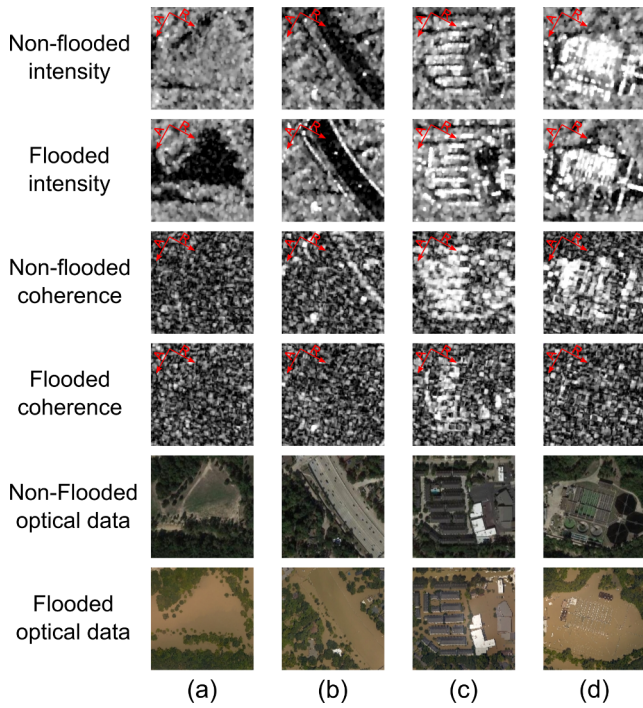


**Fig. 1.** Variation of intensity and coherence for different surface cover types under non-flooded and flooded conditions in TerraSAR-X data, and the associated optical reference data. Non-flooded optical data is from Google Earth and flooded optical data is from National Oceanic and Atmospheric Administration (NOAA). (a) Grassland: surface backscatter changes to specular reflection in case of flooding; the coherence is low under both flooded and non-flooded conditions; (b) Roads: specular backscatter occurs under both conditions; the coherence is low under both flooded and non-flooded conditions; (c) Buildings with low level floodwater: the double bounce effect is enhanced and the coherence decreases in case of flooding; (d) Buildings with high level floodwater: the intensity remains the same or decreases and the coherence decreases in case of flooding.

backscattered energy between flooded and non-flooded surfaces. Open areas covered by flood (without wind) cause specular reflection, which could result in a darker appearance with a lower  $\sigma^0$ . For instance, the surface backscatter changes to specular reflection if grassland and bare soils were submerged by floodwater. This results in a noticeable decrease of  $\sigma^0$  (see Fig. 1a). However, this phenomenon does not hold for specular reflection structures such as roads, parking lots, and airports as they are very smooth in both flooded and non-flooded cases. Thus the variation of surface roughness caused by floodwater might be negligible (see Fig. 1b). Meanwhile, although the increase of ground dielectric constant leads to a larger  $\sigma^0$ , the detection of this change is hampered as the backscattered energy is predominantly directed in the specular direction. Conversely, floodwater standing in built-up areas is generally represented by a brighter line structure because of the double bounce effect (see Fig. 1c). In cases when buildings are surrounded by smooth asphalt roads, the enhancement of reflectivity is mainly attributed to the increase of the dielectric constant as the change of surface roughness is negligible. Nevertheless, an increase of the double bounce effect is affected by  $\phi$  as mentioned above. The maximum increase is achieved when  $\phi = 0^\circ$ , but is reduced at larger angles. According to simulation experiments by Pulvirenti et al. (2016), the increase of  $\sigma^0$  drops from 11.5 dB to  $\sim 3.5$  dB when  $\phi$  increases from  $0^\circ$  to greater than  $5-10^\circ$ . Additionally, the water level relative to the height of the wall is another considerable factor. An imperceptible attenuation of the wall-ground dihedral factor induced by floodwater could lead to a decrease of  $\sigma^0$  (Iervolino et al., 2015) (see Fig. 1d). Overall, considering all of the foregoing aspects, mapping flood extent in complex urban areas based only on SAR intensity is a challenging task.

Interferometric coherence, which indicates the correlation of two complex (amplitude and phase) observations, provides additional information for urban flood mapping since an urban settlement can generally be considered a stable target characterized by high coherence. Interferometric coherence is estimated in a sliding window as

$$\gamma = \frac{|E(s_1 s_2^*)|}{\sqrt{E(s_1 s_1^*) E(s_2 s_2^*)}} \quad (1)$$

where  $E(\cdot)$  and  $*$  indicate expectation and complex conjugation operations,  $s_1$  and  $s_2$  are two complex SAR acquisitions. The window size for Eq. (1) determines the performance of the coherence estimator. Large windows reduce spatial resolution, and the inclusion of other structures like vegetation may lead to a decrease in the coherence of built-up areas (Amitrano et al., 2016). On the contrary, smaller windows allow higher spatial estimation accuracy but could suffer from a higher estimation bias (Touzi et al., 1999). Nonetheless, the estimation bias is smaller at high correlation values and a window size of  $5 \times 5$  was found to be a good compromise for urban areas (Schneider et al., 2006). Several factors contribute to the coherence decorrelation, such as receiver noise, temporal decorrelation, spatial baseline ( $B_p$ ) and volume decorrelation (Moreira et al., 2013). Urban settlements typically exhibit high coherence regardless of the temporal baseline ( $B_t$ ), whereas  $B_p$  impacts the coherence value dominantly. The influence of  $B_p$  is especially prominent for X-band as the  $B_p$  decorrelation is proportional to the inverse of the wavelength (Pulvirenti et al., 2016; Zebker et al., 1992). The highest coherence exists at dihedral corner locations (Thiele et al., 2007), where roads and parking lots in principle have low coherence as a result of anthropogenic activities (see Fig. 1b). Standing floodwater causes changes in the spatial distribution of scatterers within a resolution cell, resulting in a drop-off in the co-event pair coherence (i.e., the interferometric coherence produced from one image acquired before and another during the flood) compared to the pre-event pair coherence (i.e., the interferometric coherence produced from two images both acquired before the flood), since the pre-event image pair was not available in this study, the post-event pair (i.e., the interferometric coherence produced from two images both acquired after the flood where no floodwater exists anymore) was used instead (see Fig. 1c and d). The variation of coherence makes the flooded built-up areas distinguishable from the non-flooded ones.

## 2.2. Temporal-ensembling active self-learning deep CNN

The proposed framework aims to leverage both labeled and unlabeled samples by integrating active learning and self-learning at the conceptual level under the temporal-ensembling deep CNN model. It works in an iterative fashion based on two steps: (1) (re)training the temporal-ensembling deep CNN; (2) updating informatively unlabeled samples within pseudo-labels to the training dataset. Firstly, a deep CNN model, which we term as a student model, is trained with the initially labeled training samples. At the same time a teacher model is achieved by ensembling the parameters of the student model over training steps. In this manner, two models (or even more) are gained with the effort of training only one model. Secondly, the informative unlabeled samples are queried by disagreements between student and teacher models from both the same view and multi-view of data in the candidate pool. Under the assumption that spatially adjacent samples belong to the same class, the selected samples are filtered and self-labeled by a multi-scale spatial constraint. In addition, consistency regularization is introduced to penalize errors in the pseudo-labels.

### 2.2.1. Temporal ensembling

The structure of the temporal-ensembling model consists of two deep CNN models that share an arbitrary architecture, namely the student model and the teacher model, as shown in Fig. 2. During the training phase, the weights of the teacher model ( $\theta'$ ) are updated by

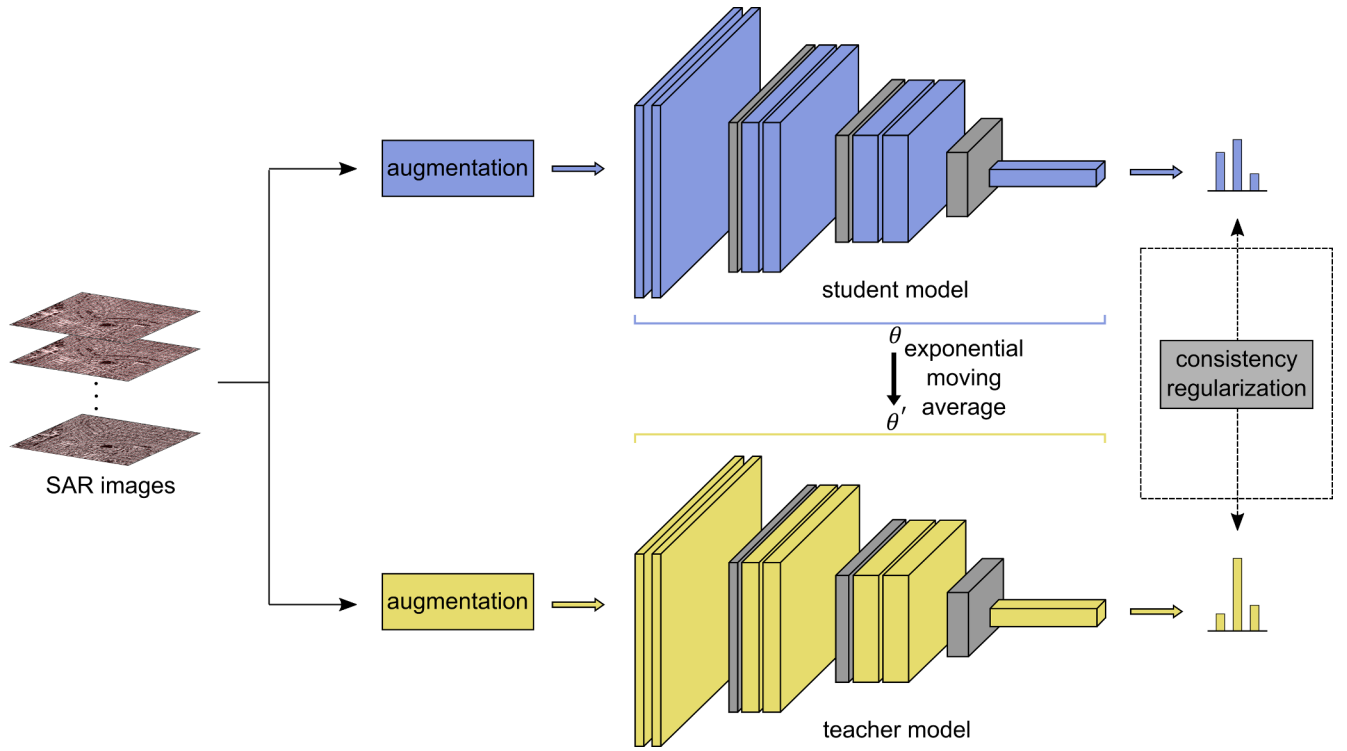


Fig. 2. Structure of the temporal-ensembling CNN model.

ensembling the student model weights ( $\theta$ ) with an exponential moving average (Tarvainen and Valpola, 2017):

$$\theta'_t = \alpha\theta'_{t-1} + (1 - \alpha)\theta_t \quad (2)$$

where  $\alpha$  is a smoothing coefficient hyperparameter, and  $\theta'_t$  defines model weights at training step  $t$ . This means that the weights for each sample are formed by an ensemble of the model's current version and its earlier versions that evaluated the same sample. Averaging model weights temporally tends to produce a more accurate model compared to using the final weights directly, and may further lead to better test accuracy (Polyak and Juditsky, 1992). Using weights instead of predictions in the temporal ensembling has the benefit that information can be aggregated after every training step rather than after every epoch, which significantly speeds up the training process. Moreover, since gradients are propagated only through the student model, and  $\theta'$  is treated as a constant regarding the optimization, two different models could be achieved with the effort of training one model.

#### 2.2.2. Active self-learning

The overall A-SL framework is shown in Fig. 3. Let  $D_l = \{\mathbf{x}_i, y_i\}_{i=1}^l$  denote a training dataset of labeled samples, with  $\mathbf{x}_i \in \mathcal{X}$  and  $y_i = \{1, \dots, K\}$ .  $\mathcal{X}$  is the  $d$ -dimensional input space  $\in \mathbb{R}^d$  and  $K$  is the class number.  $D_u = \{\mathbf{x}_i\}_{i=l+1}^{l+u} \in \mathcal{X}$  denotes the unlabeled sample set. At the first step, the temporal-ensembling model is trained by the initially labeled training samples  $D_l$ , where each training sample is stochastically augmented (see Section 3.3 for further details on augmentation) before being fed into the model (Fig. 2). Subsequently, the unlabeled sample set  $D_u$  is predicted by both trained student and teacher models, and the informative samples are selected by an uncertainty criterion according to the disagreement between the student and teacher models. In contrast to traditional active learning, the supervisor (e.g., human experts) interaction in the proposed framework is omitted during the training sample update step. The selected informative samples are filtered and pseudo-labeled by a multi-scale spatial constraint and updated to the training dataset. To account for errors in the pseudo-labels of newly updated training samples, consistency regularization is

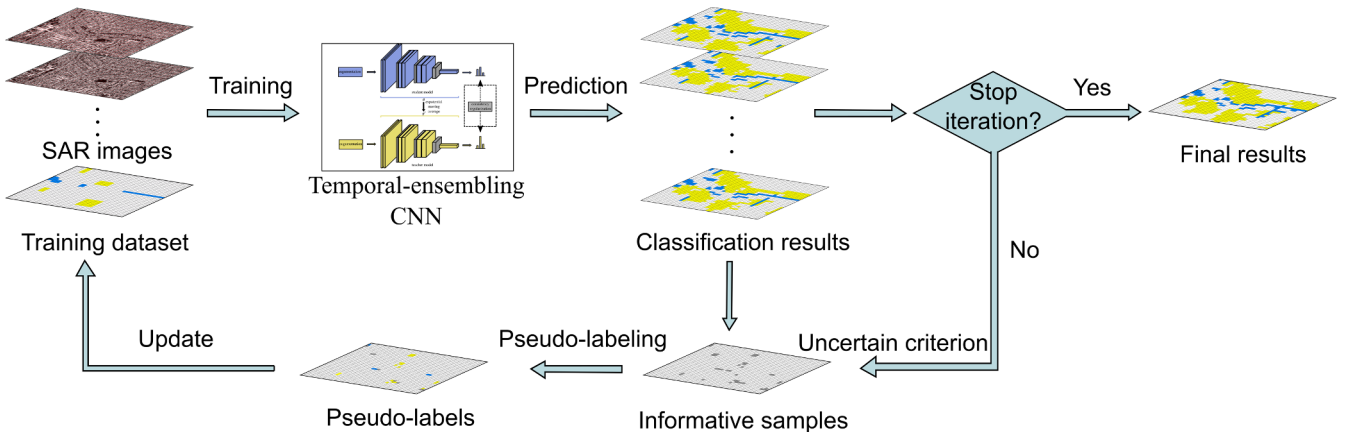


Fig. 3. Active self-learning framework.

adopted when the model is retrained with the updated training dataset. This process is iterated until a stopping criterion is met, for example, until a certain number of filtered unlabeled samples is obtained. The aforementioned uncertainty criterion, multi-scale spatial constraint, and consistency regularization are described in detail as follows:

- (1) Disagreement uncertainty: For the unlabeled sample set  $D_u$ , the informative samples are selected based on the disagreement between the student and teacher models for input data both with and without augmentation:

$$(G_w \neq G'_w) \cup (G_{wo} \neq G'_{wo}) \quad (3)$$

where  $G_w/G_{wo}$  and  $G'_w/G'_{wo}$  are predicted results of an arbitrary unlabeled sample with/without augmentation given by the current student and teacher models, respectively. All samples queried by Eq. (3) are retained and filtered by a multi-scale spatial constraint. This is unlike query approaches surveyed in Tuia et al. (2011), which aim to collect a fixed number of samples (e.g., the batch-mode) (Demir et al., 2011) according to a ranked uncertainty score. In this study, we chose to keep as many as informative samples at this step, because the deep CNN training phase is usually time-consuming and fewer iteration steps are preferable. The training sample update is processed in a self-labeling manner without extra human annotation effort (as described below).

- (2) Multi-scale spatial constraint: Following Tobler's law of spatial autocorrelation (Tobler, 1970) it is reasonable to assume that spatially adjacent samples are more likely to share the same class than distant samples. Therefore, any uncertain sample (as identified by Eq. (3)) is assigned to label  $l_{n\_max}$  that occurs most frequently in a given neighborhood window centered on the uncertain sample, provided that the following constraint is fulfilled:

$$N_{l_{n\_max}}/N > h \quad (4)$$

where  $N_{l_{n\_max}}$  is the number of samples with label  $l_{n\_max}$ ,  $N$  is the number of samples in the window, and  $h$  is the homogeneity threshold set by the user. Taking into account the variation of homogeneity where uncertain samples are located, a multi-scale window size is adopted. Four scales are set in this study:  $[9 \times 9, 7 \times 7, 5 \times 5, 3 \times 3]$ . The filtering process is implemented from a larger scale to a smaller scale. For example, as shown in Fig. 4, Eq. (4) is not met at the scale of  $9 \times 9$  when  $h = 0.7$  is set, but it is fulfilled at the scale of  $7 \times 7$ . The pseudo-labeling is performed at this scale and the label of 1 is assigned to the uncertain sample. If it was not fulfilled at the smallest scale (e.g.,  $3 \times 3$ ), the uncertain sample is ignored and no label is assigned. Since the pseudo-labeling depends upon the label of neighbor samples, only samples with reliable labels should be considered. The  $N_{l_{n\_max}}$  in Eq. (4) is calculated for neighbor samples that satisfy:

$$(G_{wo} = G'_{wo}) \cap (p'_{wo\_b}/p'_{wo\_a} < \tau) \quad (5)$$

where  $p'_{wo\_a}$  and  $p'_{wo\_b}$  are the largest and second largest score of different labels of an arbitrary unlabeled sample given by the

current teacher model, and  $\tau$  is a threshold indicating the distinguishability between two potential labels.

- (3) Consistency regularization: Since automatic pseudo-labeling in (2) could bring label noise to the updated training samples, consistency regularization (Laine and Aila, 2017; Tarvainen and Valpola, 2017) is introduced to mitigate the associated adverse effect. Consistency regularization is defined as the distance  $D(\theta, \theta')$  between the softmax outputs of the student and teacher models with given input  $\mathbf{x}$ , as displayed in the dashed box in Fig. 2. In practice, Kullback-Leibler divergence and mean squared error could be used to measure the distance. We chose the mean squared error here:

$$D(\theta, \theta') = \mathbb{E}_{\mathbf{x}, r', r} [\|p(\mathbf{x}, \theta', r') - p(\mathbf{x}, \theta, r)\|^2] \quad (6)$$

where  $r'$  and  $r$  are different stochastic augmentations introduced to the teacher model and the student model, respectively. Therefore, the final loss function of the temporal-ensembling model described in Section 2.2.1 is given by:

$$l(\theta) + \beta D(\theta, \theta') \quad (7)$$

where  $l(\theta)$  is the cross-entropy term and  $\beta$  is the weight of consistency regularization. It is worth to mention that the consistency regularization is not activated during the initial training step, in other words,  $\beta = 0$  is set when the model is trained with initially labeled training samples.

### 3. Dataset and experiments

#### 3.1. Study area and dataset

The study area is located in Houston, Texas, which was affected by flooding related to heavy rainfalls accompanying hurricane Harvey in August 2017. It is a representation of a typical urban landscape that is mainly occupied by dense residential houses/apartments and some commercial and industrial districts with schools, storages, stadiums, parks, and parking lots. In this study, four TerraSAR-X HH-polarized Stripmap datasets were acquired: one pre-flood image (August 10, 2017), one co-flood image (September 01, 2017) and two post-flood images (October 26, November 17 and 28, 2017). The detailed characteristics of TerraSAR-X data and baselines of interferometric pairs are summarized in Table 1 and 2, respectively. All experimental results were assessed based on very high-resolution ( $\sim 35$  cm) optical data acquired on August 30 and 31, 2017 using an airborne Trimble Digital Sensor System (DSS) provided by the NOAA Remote Sensing Division (NOAA, 2017).

#### 3.2. Data preprocessing and preparation

The raw TerraSAR-X data were calibrated and transformed to the backscattering coefficient (in dB). A Lee sigma filter with a size of  $5 \times 5$  pixels was applied to each image to reduce speckle noise. Interferometric coherence was estimated by a moving window of  $5 \times 5$  pixels. All intensity and coherence data were co-registered and geo-coded to WGS1984 UTM Zone 15 N with a pixel spacing of 1.25 m and a size of  $4800 \times 6400$  pixels. The preprocessed images were split into non-overlapping patches with a size of  $32 \times 32$  pixels. Patch-wise classifications were implemented in our experiments under consideration of three classes: flooded open areas (FO) (image patches filled with floodwater but no buildings), flooded built-up areas (FB) (image patches containing both floodwater and buildings), and non-flooded areas (NF) (rest of image patches). Since floodwater beneath dense trees/forests is visible neither in the TerraSAR-X nor in the optical data, this situation could not be considered in this study. A total number of 30,000 image patches were obtained, with 1130 patches belonging to class FO, 2500 to class FB, and 26,370 to class NF.

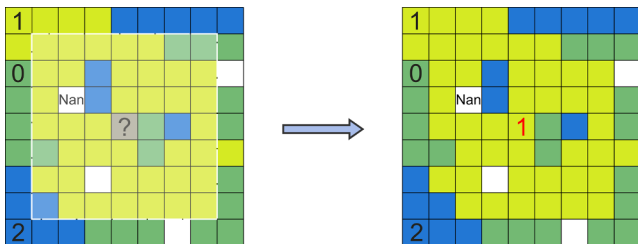


Fig. 4. Pseudo-labeling example. Nan means the prediction of this sample is not fulfilled in Eq. (5) and no label is assigned.



**Table 1**

Characteristics of available TerraSAR-X images in this study (flooded acquisition is marked in blue color).

Acquisition date (yyyy/mm/dd)	Polarization	Incidence angle (°)	Resolution (m) (range × azimuth)	Orbit
2017/08/10	HH	31	1.2 × 3.3	Descending
2017/09/01	HH	31	1.2 × 3.3	Descending
2017/10/26	HH	31	1.2 × 3.3	Descending
2017/11/17	HH	31	1.2 × 3.3	Descending

**Table 2**Interferometric pairs obtained from available images ( $B_t$ : temporal baseline;  $B_p$ : spatial baseline).

Interferometric Pair	$B_t$ (days)	$B_p$ (m)
2017/08/10 - 2017/09/01	22	196
2017/09/01 - 2017/10/26	55	266
2017/10/26 - 2017/11/17	22	33

the training phase: random crop with a size of  $32 \times 32$  pixels, and random horizontal and vertical flips. In the test phase, each image patch was center-cropped to  $32 \times 32$  pixels and no other augmentation was used. Since the flooded areas occupied a small portion of the whole image and the number of non-flooded samples was highly over-represented, we limited the number of non-flooded samples and balanced the dataset for this experiment, obtaining 1100 randomly chosen samples per class. Among these samples, 1600 samples (400 samples

**Table 3**

Overview of the different tested scenarios in this study.

Scenarios	Description	Number of channels
Scenario I	Co-event coherence (2017/08/10–2017/09/01)	1
Scenario II	Co-event intensity (2017/09/01)	1
Scenario III	Co-event coherence (2017/08/10–2017/09/01) + Post-event coherence (2017/10/26–2017/11/17)	2
Scenario IV	Co-event intensity (2017/09/01) + Pre-event intensity (2017/08/10)	2
Scenario V	Co-event coherence (2017/08/10–2017/09/01) + Post-event coherence (2017/10/26–2017/11/17) + Co-event intensity (2017/09/01) + Pre-event intensity (2017/08/10)	4

### 3.3. Flood detection with different SAR information

In this experiment, five scenarios with different SAR information combinations were investigated for flood detection (see Table 3). We used a 13-layer CNN model (see Table 4) architecture as it achieves state-of-the-art results for semi-supervised learning on benchmark datasets (Laine and Aila, 2017; Tarvainen and Valpola, 2017), and its lightweight parameters make it favorable for training from scratch. Different images were stacked together when multi-channel data were employed, and the pixel values of each channel were normalized to [0, 1] before the subsequent processing. Image patches with a size of  $36 \times 36$  pixels were extracted by striding with a step of 32 pixels. To reduce overfitting the following types of augmentation were implemented in

per class) were used for training, 300 samples (100 samples per class) were used for validation and 1800 samples (600 samples per class) were used for testing. We further compared scenarios with a varying number of training samples. In all scenarios, overall accuracy (OA),  $\kappa$  statistic, precision, recall, and F1 score were reported by averaging ten independent Monte Carlo runs. We trained CNN models in all cases with a batch size of 32 and used Adam Optimizer (Kingma and Ba, 2015) with initial learning rate  $1e^{-4}$ , momentum parameters  $\beta_1 = 0.9$ ,  $\beta_2 = 0.999$ , and weight decay with coefficient  $2e^{-4}$ . All models were trained for 400 epochs, delaying the learning rate with cosine annealing (Loshchilov and Hutter, 2017) (without restart). Instead of using early stopping we saved model weights every 20 epochs and then chose the best model for testing. All models were implemented in PyTorch<sup>1</sup>.

### 3.4. Classification with temporal-ensembling active self-learning CNN

According to the results of the experiments in Section 3.3 (described in Section 4.1), only Scenario V was considered in this section. We used the same CNN architecture and training parameters as in Section 3.3, but only five independent Monte Carlo runs were conducted in every experiment to limit the time consumption. Results were reported on the whole image of the study area. Hyperparameter  $\alpha$  in the temporal-ensembling model was set to 0.999, the weight of consistency regularization was set to  $\beta = 10$ , and thresholds  $h = 0.6$  and  $\tau = 0.1$  were set to investigate the effectiveness of the proposed framework. In order to mitigate the accumulation of label errors during the iteration process, the tightest constraint (e.g.,  $h = 0.9$  and  $\tau = 0.1$ ) was set after the second iteration. To further investigate the influence of thresholds on the multi-scale spatial constraint, we implemented comparison experiments by varying the value of  $h$  (e.g., from 0.5 to 0.9). The values of  $h$  and  $\tau$  control the trade-off between the number and accuracy of newly updated training samples together. We kept  $\tau = 0.1$  when the most

**Table 4**

CNN architecture used in this study.

Layer	Description
input	$32 \times 32 \times n^*$
conv1a	$3 \times 3$ , 96 lReLU ( $\alpha = 0.1$ ), pad = 'same'
conv1b	$3 \times 3$ , 96 lReLU ( $\alpha = 0.1$ ), pad = 'same'
conv 1c	$3 \times 3$ , 96 lReLU ( $\alpha = 0.1$ ), pad = 'same'
pool1	$2 \times 2$ Maxpool, stride 2
drop1	Dropout, $p = 0.3$
conv2a	$3 \times 3$ , 192 lReLU ( $\alpha = 0.1$ ), pad = 'same'
conv2b	$3 \times 3$ , 192 lReLU ( $\alpha = 0.1$ ), pad = 'same'
conv2c	$3 \times 3$ , 192 lReLU ( $\alpha = 0.1$ ), pad = 'same'
pool2	$2 \times 2$ Maxpool, stride 2
drop2	Dropout, $p = 0.3$
conv3a	$3 \times 3$ , 192 lReLU ( $\alpha = 0.1$ ), pad = 'valid'
conv3b	$1 \times 1$ , 192 lReLU ( $\alpha = 0.1$ )
conv3b	$1 \times 1$ , 192 lReLU ( $\alpha = 0.1$ )
pool3	Global average pool, $6 \times 6 \rightarrow 1 \times 1$
dense	Fully connected $192 \rightarrow 3$
output	Softmax

$n^*$  is the channel number of the input image

<sup>1</sup> <http://pytorch.org/>.

**Table 5**  
Classification results of the test dataset in different scenarios.

Scenarios	Classes	Precision	Recall	F1	OA (%)	$\kappa$
Scenario I	FO	$0.514 \pm 0.016$	$0.956 \pm 0.010$	$0.667 \pm 0.011$	$56.87 \pm 1.45$	$0.353 \pm 0.022$
	FB	$0.618 \pm 0.025$	$0.229 \pm 0.050$	$0.330 \pm 0.053$		
Scenario II	FO	$0.827 \pm 0.017$	$0.839 \pm 0.033$	$0.833 \pm 0.011$	$69.30 \pm 0.60$	$0.540 \pm 0.010$
	FB	$0.752 \pm 0.023$	$0.582 \pm 0.063$	$0.654 \pm 0.031$		
Scenario III	FO	$0.589 \pm 0.017$	$0.935 \pm 0.012$	$0.723 \pm 0.009$	$66.37 \pm 0.89$	$0.496 \pm 0.013$
	FB	$0.732 \pm 0.021$	$0.518 \pm 0.029$	$0.607 \pm 0.016$		
Scenario IV	FO	$0.902 \pm 0.018$	$0.861 \pm 0.028$	$0.881 \pm 0.007$	$80.85 \pm 0.93$	$0.713 \pm 0.014$
	FB	$0.897 \pm 0.021$	$0.693 \pm 0.052$	$0.781 \pm 0.026$		
Scenario V	FO	$0.918 \pm 0.016$	$0.923 \pm 0.017$	$0.921 \pm 0.003$	$86.91 \pm 0.45$	$0.804 \pm 0.007$
	FB	$0.890 \pm 0.015$	$0.822 \pm 0.017$	$0.854 \pm 0.007$		

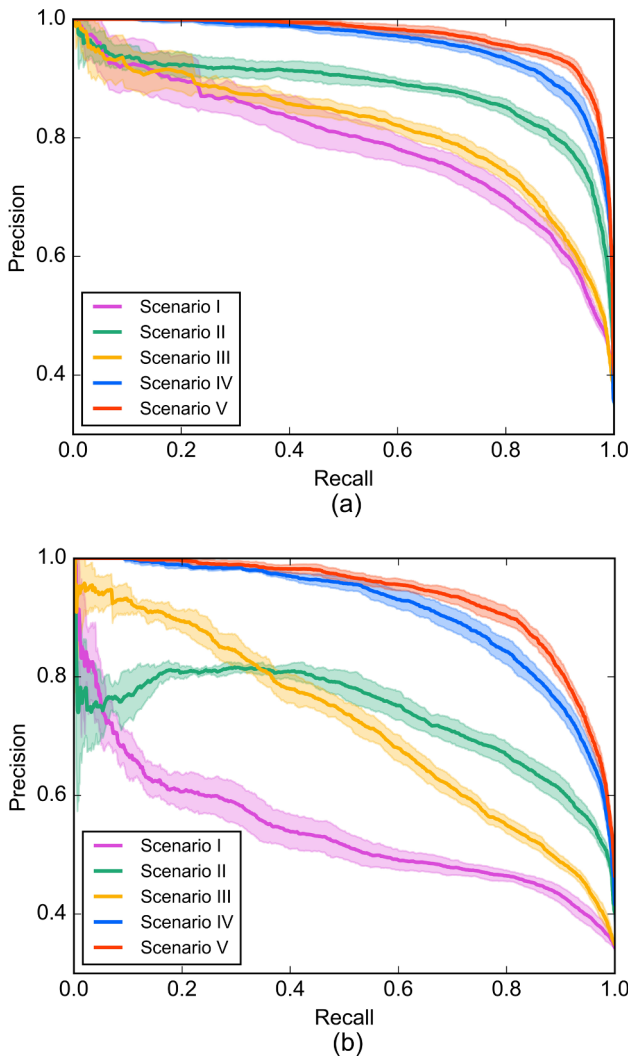


**Fig. 5.** Precision-recall curves of the test dataset in different scenarios. (a) precision-recall curves of flooded open areas; (b) precision-recall curves of flooded built-up areas.

distinguishable and reliable predicted labels could be achieved. Further, an ablation study was conducted to explore the effect of consistency regularization. The iteration process of all experiments terminated until the number of newly updated training samples was less than 50. All experiments terminated in 3 iterations and we found that the results improved significantly after only one iteration. Since the number of samples was highly skewed to NF, and a large intra-class diversity was associated within this class, the updated training samples tended to

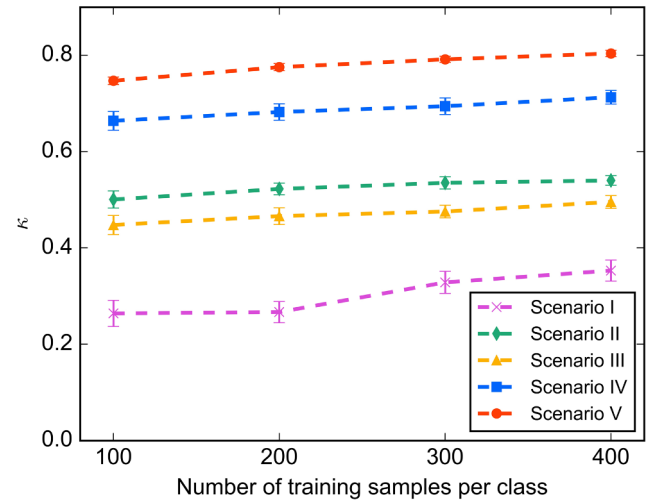


**Fig. 6.**  $\kappa$  statistic of the test dataset in different scenarios with a different number of training dataset.

be biased towards NF. Several strategies could be adopted to balance the training dataset. For instance, oversampling the under-presented class has been shown to perform well in some classification tasks with deep neural networks (Buda et al., 2018), however, it was not applicable in our case as oversampling results in the accumulation of incorrect labels. Inversely, downsampling the over-represented class failed to learn the variability of the NF class. Alternatively, as was done in Kellenberger et al. (2018), we set class weights according to the inverse of the occurrence frequency of each class in the training dataset.

## 4. Results and discussion

### 4.1. Accuracy of flood detection in different scenarios

Classification results of the test dataset in different scenarios with 400 training samples per class are listed in Table 5, and the associated precision-recall curves are shown in Fig. 5. It indicates that the multi-temporal intensity (Scenario IV) is the most important information for mapping both flooded open areas and flooded built-up areas. With additional multi-temporal coherence (Scenario V), the OA and  $\kappa$  statistic increase from 80.85% to 86.91% and from 0.713 to 0.804, respectively. Particularly, the added multi-temporal coherence has more influence in FB than in FO, with improvements of 7% (e.g., from 0.781 to 0.854) and 4% (e.g., from 0.881 to 0.921) in terms of F1 score, respectively. The worst result is found by using only co-event coherence (Scenario I). The accuracy is improved when post-event coherence is added (Scenario III) but is slightly outperformed by using only co-event intensity (Scenario II). Overall, unsatisfactory results are obtained from



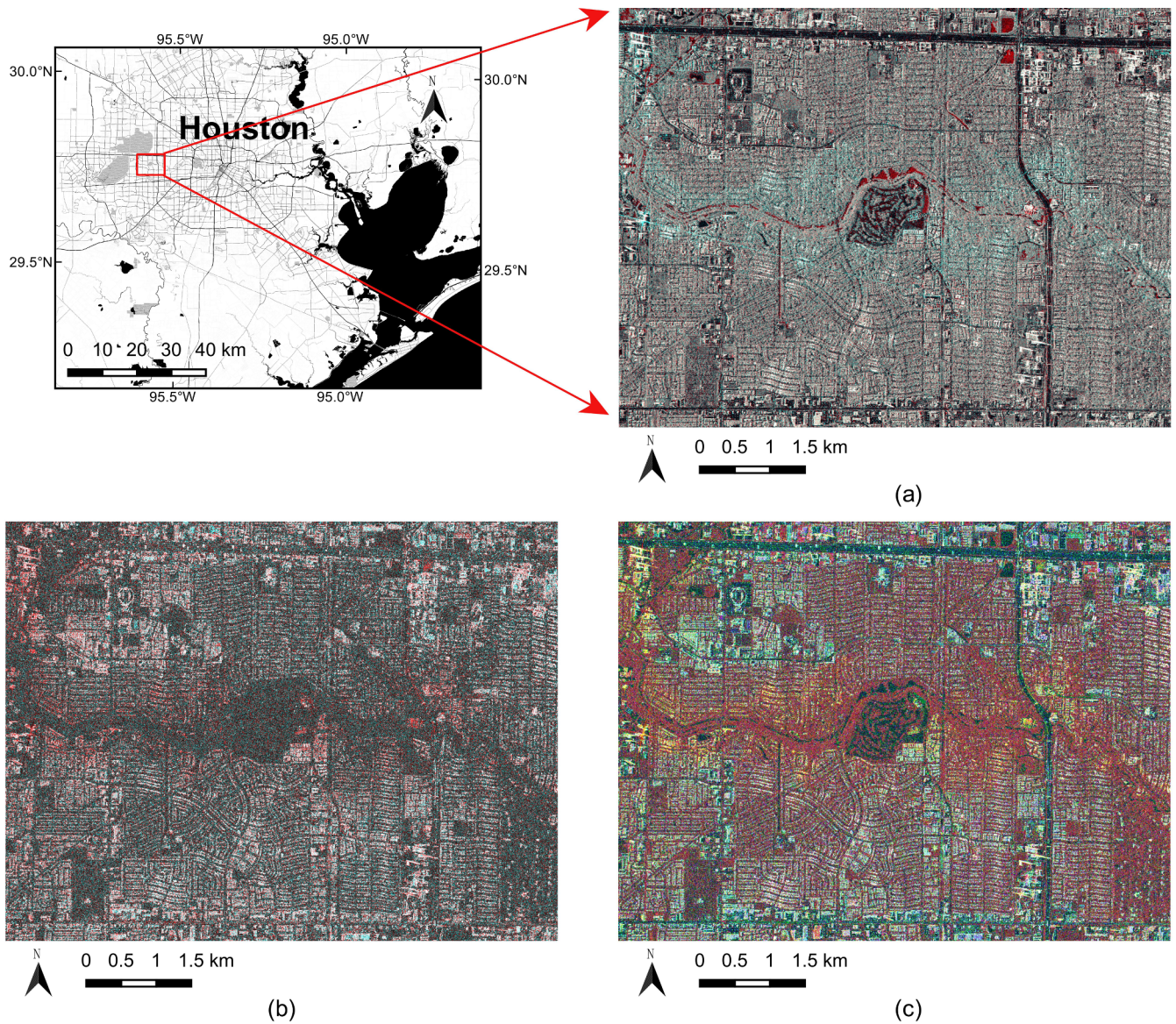


**Fig. 7.** RGB color composites of the study area in Houston. (a)  $R = \sigma^0$  of August 10, 2017,  $G = B = \sigma^0$  of September 01, 2017; (b)  $R = \gamma$  of October 26–November 17, 2017,  $G = B = \gamma$  of August 10–September 01, 2017; (c)  $R = \sigma^0$  of September 01, 2017,  $G = \gamma$  of October 26–November 17, 2017,  $B = \gamma$  of August 10–September 01, 2017. (For interpretation of the references to colour in this figure legend, the reader is referred to the web version of this article.)

Scenario I, II and III. Fig. 6 shows the performances of different scenarios in terms of the  $\kappa$  statistic by varying the number of training samples. Scenario V outperforms other scenarios even with less training samples, meaning that the FO, FB, and NF classes are less overlapping and more distinguishable in the space of the combination of multi-temporal intensity and coherence.

The synoptic view of multi-temporal SAR data in the form of RGB combinations are known to be helpful in the interpretation of land cover and surface dynamics (Amitrano et al., 2015; Liu et al., 2001). In previous studies, the combinations of multi-temporal intensity images and coherence images have been employed in the qualitative interpretation of flood monitoring (Chini et al., 2012; Dellepiane and Angiati, 2012; Pulvirenti et al., 2016; Refice et al., 2014). In this study, we adopt different RGB combinations to facilitate the understanding of the theoretical analysis described in Section 2.1. Fig. 7a shows the color composite given by R: the August 10, 2017 intensity (pre-event), G and B: the September 01, 2017 intensity (co-event). The reddish color indicates a lower intensity for co-event than for pre-event, which could be attributed to the presence of floodwater in the co-event data on

September 01, 2017. The white color indicates the presence of buildings with high intensity caused by the double bounce effect. The black color delineates roads (including roads covered by floodwater) and permanent water bodies that show specular reflection. The cyan areas demonstrate an increase of intensity in the co-event image, which could be explained by the enhancement of the double bounce effect caused by standing floodwater around buildings and between sparse trees. However, white color surrounded by cyan color may suggest that some possibly flooded buildings are not detectable by the difference in multi-temporal intensity images. Fig. 7b shows the color composite given by R: the October 26–November 17, 2017 coherence (post-event), G and B: the August 10–September 01, 2017 coherence (co-event). The dark tone in this figure spots low coherence areas in both acquisition dates, e.g., vegetated areas and areas with intensive anthropogenic activity like parking lots and roads. White reveals stable coherent targets like buildings, whereas the reddish color indicates the decorrelation of coherence over buildings caused by standing floodwater. It can be seen that the reddish color is widely spread in Fig. 7b, which can be attributed to a shorter baseline  $B_p$  (with larger coherence) of the post-



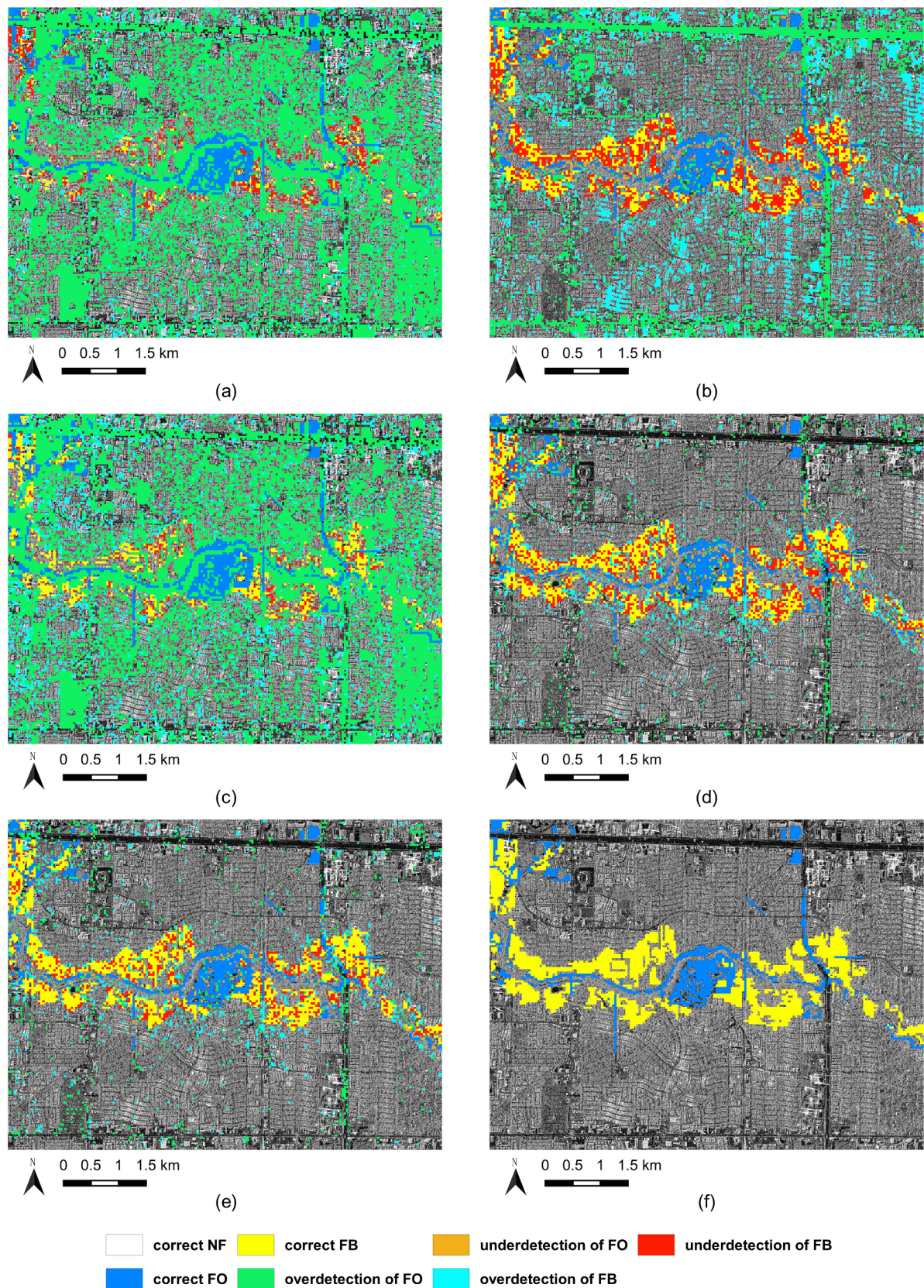


**Fig. 8.** Classification results of different scenarios in the study area of Houston. (a) Scenario I; (b) Scenario II; (c) Scenario III; (d) Scenario IV; (e) Scenario V; (f) flood reference mask derived on the basis of the optical data provided by NOAA.



**Table 6**  
Classification results of the supervised CNN and A-SL CNN in the study area of Houston.

Methods	Classes	Precision	Recall	F1	OA (%)	$\kappa$
supervised CNN	FO	$0.506 \pm 0.053$	$0.842 \pm 0.043$	$0.630 \pm 0.032$	$90.39 \pm 0.32$	$0.614 \pm 0.010$
	FB	$0.642 \pm 0.042$	$0.698 \pm 0.037$	$0.656 \pm 0.013$		
A-SL CNN	FO	$0.684 \pm 0.035$	$0.824 \pm 0.027$	$0.746 \pm 0.011$	$92.82 \pm 0.10$	$0.686 \pm 0.004$
	FB	$0.680 \pm 0.024$	$0.716 \pm 0.033$	$0.696 \pm 0.009$		

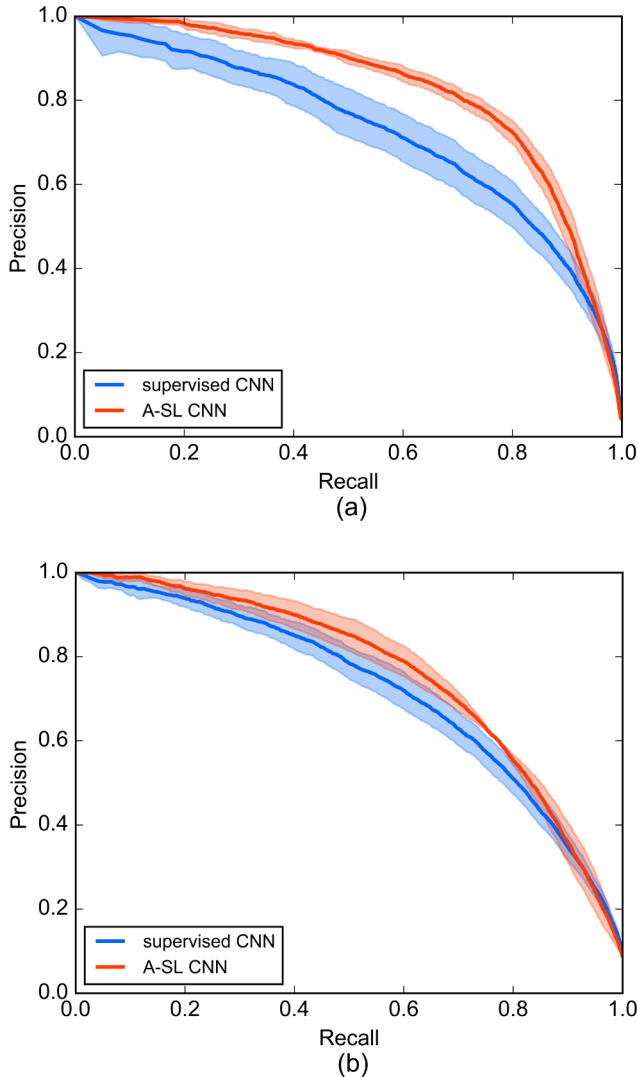


**Fig. 9.** Precision-recall curves of the supervised CNN and A-SL CNN in the study area of Houston with 200 initial training samples per class under Scenario V. (a) precision-recall curves of flooded open areas; (b) precision-recall curves of flooded built-up areas.

event pair (33 m) than that of the co-event pair (196 m). As mentioned in Section 2.1, the coherence of built-up areas is predominantly influenced by  $B_p$ , and the perturbation of  $B_p$  could impede the detection of truly flooded built-up areas by comparing the difference between pre-event and co-event coherences. Fig. 7c shows the RGB combination of intensity and coherence: the red, green, and blue channels are assigned to September 01, 2017 intensity, October 26 - November 17, 2017 coherence, and August 10 - September 01, 2017 coherence, respectively. In this RGB combination flooded built-up areas appear in yellowish color (e.g., high co-event intensity, high post-event coherence, and low co-event coherence) and are visually clearly discernible. The white and cyan colors represent unflooded buildings, and the black

color indicates possibly flooded open areas. The line structures with the mixed greenish and blueish colors are roads, as they have a very low intensity and the coherence decorrelation is mainly caused by irregular traffic activities. Vegetation with medium intensity and low coherence is represented in reddish color, which indicates that this RGB combination could play a similar role as the normalized difference vegetation index in optical data.

Finally, we also display the inference results for the five scenarios in Fig. 8. Visually, Scenario IV and V outperform the others significantly, whereas Scenario V achieves the best result. This is consistent with the results reported in Table 5. At close inspection, it can be seen that most of the FO are successfully detected by co-event coherence (Fig. 8a) at the cost of a very large overestimation, which results in a very high recall but very low precision. Overestimated areas can largely be associated with vegetation and roads since they show similar response as flooded open areas (e.g., very low coherence). Only a small portion of FB is correctly detected, with both large over- and underestimation, which means that co-event coherence is insufficient to distinguish between flooded and unflooded built-up areas. With the application of multi-temporal coherence (e.g., co- and post-event), a smaller underestimation of FB can be observed in Fig. 8c in comparison with that in Fig. 8a. Nonetheless, a large overestimation is still present in this scenario. This could be induced by the variation in multi-temporal coherence due to the perturbation of  $B_p$  as discussed above. Concerning the FO class, no significant visual difference between Fig. 8a and c can be observed, as there is no notable difference in coherence between open areas with and without floodwater. In Fig. 8b, where only co-event intensity is used, a smaller overestimation of FO can be found than in Fig. 8a and c. The overestimation of FO is mainly associated with main roads, due to the fact that both FO and roads are specular reflectors. A large portion of FB is miss detected, and the overestimation of FB could be caused by buildings and sparse trees that have double bounce structures. Similar to co-event coherence and multi-temporal coherence, co-event intensity alone is not sufficient to detect FO or FB correctly. In Scenario IV (Fig. 8d) FO and FB are largely classified correctly. Some flooded roads could also be detected, but the false alarm rate of flooded roads is not negligible. By adding multi-temporal coherence to multi-temporal intensity, more FB could be detected as shown in Fig. 8e, with only a subtle visible difference in FO existing between Fig. 8d and e.

#### 4.2. Classification results of the supervised and active self-learning CNN

Table 6 reports the results on the whole image of the study area of the supervised CNN and the proposed A-SL CNN with 200 training samples per class under Scenario V. An overall improvement of 7% (from 0.614 to 0.686) in terms of the  $\kappa$  statistic is achieved by the A-SL CNN. To be more detailed, improved precision for FO (from 0.506 to 0.684) is obtained at the cost of a slight decrease in recall (from 0.842 to 0.824), while both precision and recall for FB increase. As a result, notable increases of F1 score can be found for both FO (e.g., from 0.630 to 0.746) and FB (e.g., from 0.656 to 0.696), which is also visible in the precision-recall curves (Fig. 9). From the classification results displayed in Fig. 10 it can be seen that false alarms are reduced by the A-SL CNN compared to the results of the supervised CNN. Due to the over-representation of the NF background in the study area and a large

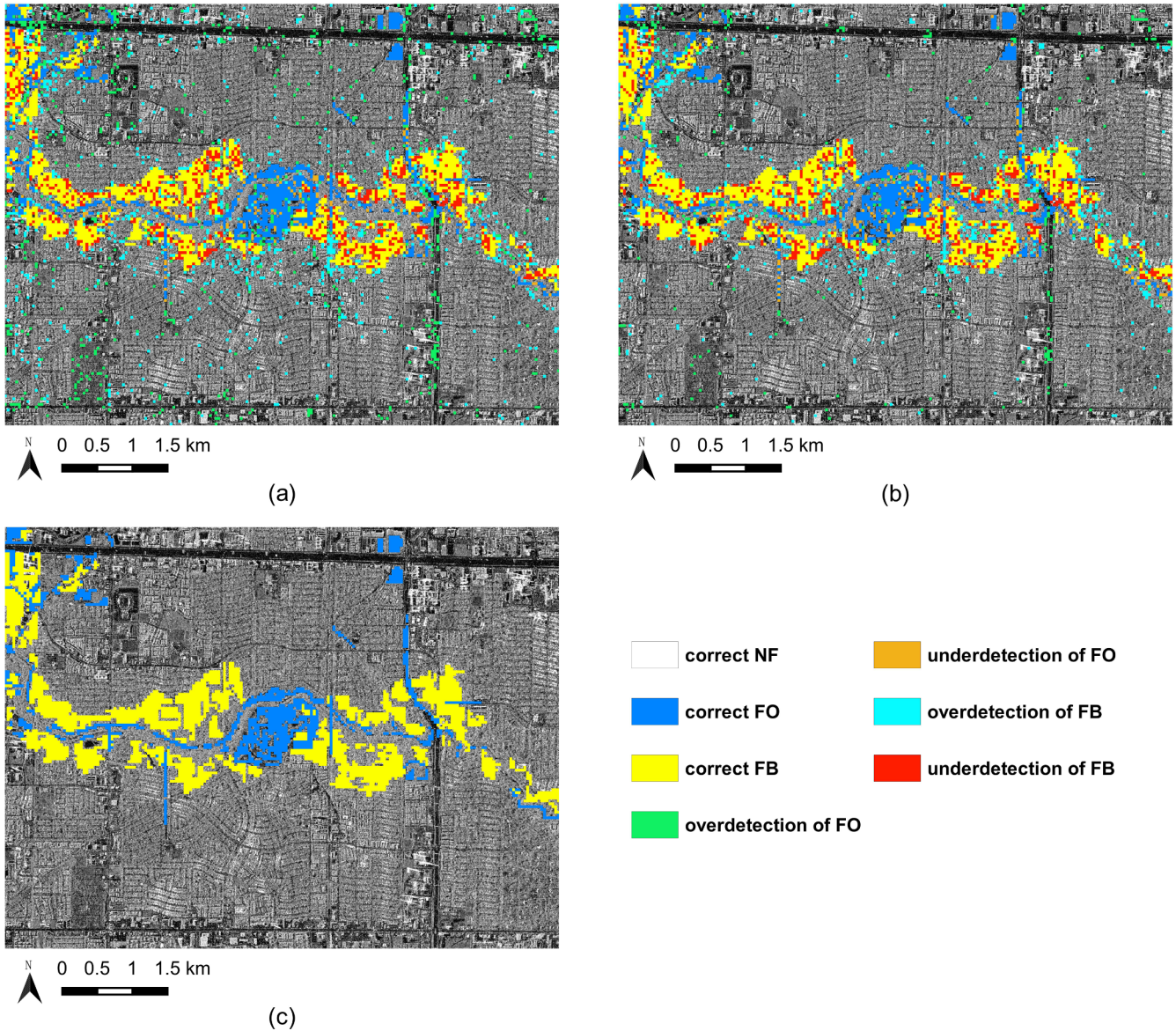


**Fig. 10.** Classification results in the study area of Houston with 200 initial training samples per class under Scenario V. (a) supervised CNN; (b) A-SL CNN; (c) flood reference mask derived on the basis of the optical data provided by NOAA.

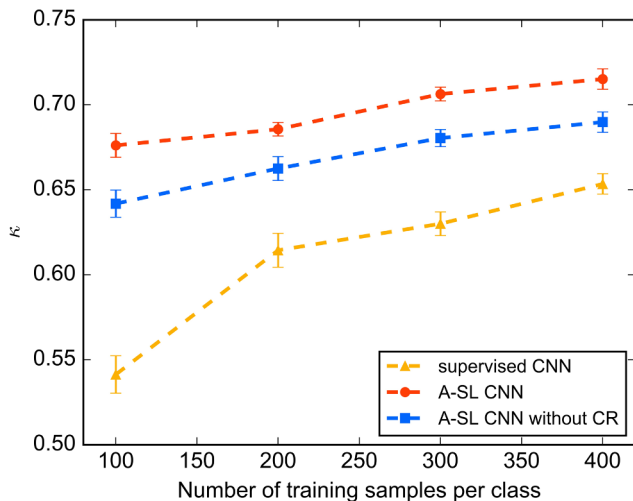


**Fig. 11.** Classification results against  $\kappa$  statistic of different models with a different number of training samples per class. CR: consistency regularization.

diversity in the image space, a large number of NF samples are updated to the training dataset in the process of active self-learning. Therefore, it enables the model to learn the variability of the NF background in a more thorough manner, reducing false alarms and increasing precisions in both FO and FB. Furthermore, the insufficiently updated training samples of FO and FB bring a modest influence on recalls of FO and FB. Overall, it is noteworthy that the proposed A-SL CNN model produces a more reliable inundation map than the supervised counterpart without extra human effort. In general, the misclassified FO are mainly found in areas like roads and parking lots. Floodwater in the street between adjoining buildings could be located in layover or shadow areas, depending on the relationships between the width of streets, the height of buildings and the incident angle (Mason et al., 2010, 2014). In principle, floodwater in layover areas could be detected by the variation in double bounce effect and coherence, whereas in shadow areas this could be hardly detected. Therefore, floodwater detection in very narrow streets, especially, between high buildings is rather challenging. FB could not be detected if floodwater stands between closely adjoining buildings or buildings that are surrounded by heavy vegetations. Moreover, floodwater presence between sparse trees might be falsely



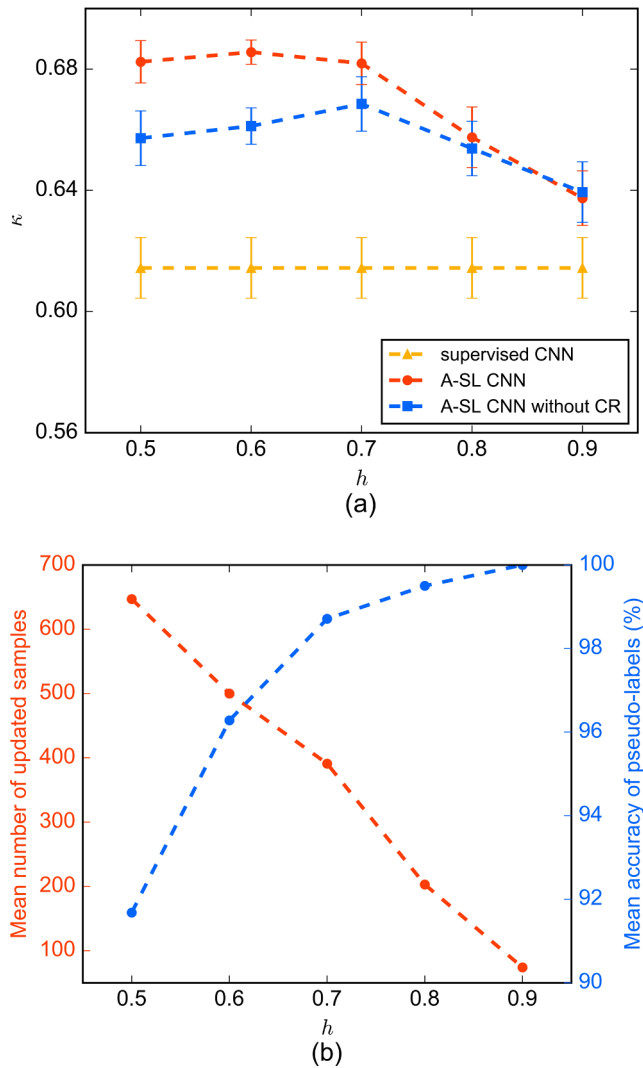


**Fig. 12.** Classification results by varying values of  $h$  with 200 initial training samples per class. (a) classification results against  $\kappa$  statistic of different models; (b) the average number of updated samples and the associated average accuracy of pseudo-labels in active self-learning. CR: consistency.

classified as FB.

Furthermore, to explore the effect of consistency regularization, Fig. 11 shows the  $\kappa$  statistic of supervised CNN, A-SL CNN with and without consistency regularization by varying the number of training samples per class. It indicates that A-SL CNN without consistency regularization realizes remarkable improvements than the supervised counterpart, although some noisy labels are brought in the newly updated training samples. The label noise is not more than 5% with  $\geq 500$  updated training samples in every case. As noted in Rolnick et al. (2017), both the number of training samples and the CNN architecture influence the label noise tolerance: a larger number of training samples and deeper layers in the CNN architecture generally tend to be more robust to label noise. It turns out that the benefits from the updated training samples overcome the adverse effects of label noise to the model in our experiments. Besides, a further improvement could be gained when consistency regularization is added to the model (e.g., with a difference of around 4% in  $\kappa$  statistic when 200 initial training samples per class are used). Consistency regularization smooths the mapping function and decision boundaries, hence provides resistance to wrong labels. It merges the inputs into coherent clusters, while the correct labels in each class bond the clusters to the right output vectors via the cross-entropy term (Laine and Aila, 2017).

The sensitivity analysis of the homogeneity threshold  $h$  is shown in Fig. 12. The value of  $h$  controls the trade-off between the number of updated training samples and the accuracy of the associated pseudo-labels. Larger  $h$  results in fewer updated samples with higher label accuracy, and vice versa (see Fig. 12b). It illustrates that  $h = 0.7$  gets the best trade-off between the number of updated samples and the pseudo-label accuracy without consistency regularization. According to the experiments of Rolnick et al. (2017), a sufficiently large training set makes CNN accommodate a wide range of noise levels. In our experiments, it can be found that the network can benefit from more data despite being accompanied by larger label errors, with the results from  $h = 0.5, 0.6$  and  $0.7$  outperforming the results from  $h = 0.8$  and  $0.9$ . Even though the newly updated training samples are free from label errors when the strongest constraint is assigned (e.g.,  $h = 0.9$ ), the improvement that the highly restricted number of informative samples makes to the initially trained model is limited.

In addition, the employment of consistency regularization makes the model more tolerant to label noise and boosts the performance. The difference in  $\kappa$  statistic between the models with and without consistency regularization diminishes with the decrease of label errors. Medium values of  $h$  (e.g.,  $h = 0.5, 0.6$ , and  $0.7$ ) might be preferable than large values (e.g.,  $h = 0.8$  and  $0.9$ ) as consistency regularization amplifies the benefits from a larger dataset to the model. With 30,000 image patches in total, the dataset used in this paper is not very large, but when the proposed framework is implemented on a very large dataset (e.g., millions of data) and different values of  $h$  are used, the difference in the number of updated informative samples and the pseudo-label accuracy could be enlarged. In this context, also the increasing time consumption of model retraining on a very large data volume should be considered when determining the final value of  $h$ . This is particularly relevant in time-critical applications such as emergency response.

## 5. Conclusion

In this paper, we investigated the roles of SAR intensity and interferometric coherence in urban flood detection based on a deep convolution neural network (CNN). We compared the results from the usage of uni-temporal co-event interferometric coherence, uni-temporal co-event intensity, multi-temporal interferometric coherence (e.g., post- and co-event pair), multi-temporal intensity (e.g., pre- and co-event), and the combination of multi-temporal intensity and coherence. In a case study of urban flooding in Houston during hurricane Harvey in August 2017 based on TerraSAR-X data, we demonstrated that multi-temporal intensity plays the most important role in urban flood mapping and enables to delineate the accurate distribution pattern of the flooded areas. Additionally, adding multi-temporal coherence to multi-temporal intensity enables a considerable increase in classification accuracy. The synergistic use of multi-temporal intensity and coherence makes flooded and unflooded areas more distinguishable from each other. Thus, it enables to achieve better results than other scenarios even with less training samples.

Furthermore, to mitigate the effect of limited training samples, an active self-learning temporal-ensembling convolution neural network (A-SL CNN) framework was proposed. It combines active learning and self-learning at the conceptual level. Specifically, informative samples are queried based on the disagreement between a student and a teacher CNN model. These samples are subsequently filtered and pseudo-labeled by a multi-scale spatial constraint without extra labeling effort from human experts. Additional consistency regularization between the student model and the teacher model makes the framework more tolerant to errors in the pseudo-labels. Our experiments have illustrated encouraging results: an overall 7% improvement in terms of  $\kappa$  statistic (e.g., from 0.614 to 0.686) is achieved by the proposed A-SL framework in comparison to its supervised counterpart. Although in this study we focused on urban flood detection with SAR data, the proposed

framework is generic and could be applied to other classification applications with different types of remote sensing data. Accordingly, future work will focus on utilizing time series and polarimetry information and on adapting the framework to other sensors. In particular, the Sentinel-1 mission, due to its high temporal resolution (revisit time of 6 days for the constellation of Sentinel-1A and Sentinel-1B) and systematic observation scenario shows large potentials to provide rapid response to floods over large urban areas globally.

## Acknowledgements

This work is funded by the China Scholarship Council (CSC). The authors would like to thank National Oceanic and Atmospheric Administration (NOAA) for releasing the DSS high-resolution optical imagery. TerraSAR-X data were kindly provided by DLR. The authors would also like to thank anonymous reviewers for their constructive comments and suggestions, which greatly helped to improve the manuscript.

## References

- Amitrano, D., Belfiore, V., Cecinati, F., Di Martino, G., Iodice, A., Mathieu, P., Medagli, S., Poreh, D., Riccio, D., Ruello, G., 2016. Urban areas enhancement in multitemporal SAR RGB images using adaptive coherence window and texture information. *IEEE J. Sel. Top. Appl. Earth Obs. Remote Sens.* 9, 3740–3752.
- Amitrano, D., Di Martino, G., Iodice, A., Riccio, D., Ruello, G., 2018. Unsupervised rapid flood mapping using sentinel-1 GRD SAR images. *IEEE Trans. Geosci. Remote Sens.* 56, 3290–3299. <https://doi.org/10.1109/TGRS.2018.2797536>.
- Amitrano, D., Di Martino, G., Iodice, A., Riccio, D., Ruello, G., 2015. A new framework for SAR multitemporal data RGB representation: rationale and products. *IEEE Trans. Geosci. Remote Sens.* 51, 117–133.
- Bai, Y., Gao, C., Singh, S., Koch, M., Adriano, B., Mas, E., Koshimura, S., 2018. A framework of rapid regional tsunami damage recognition from post-event TerraSAR-X imagery using deep neural networks. *IEEE Geosci. Remote Sens. Lett.* 15, 43–47. <https://doi.org/10.1109/LGRS.2017.2772349>.
- Ball, J.E., Anderson, D.T., Chan, C.S., 2017. Comprehensive survey of deep learning in remote sensing: theories, tools, and challenges for the community. *J. Appl. Remote Sens.* 11, 042609. <https://doi.org/10.1117/1.JRS.11.042609>.
- Bello, O.M., Aina, Y.A., 2014. Satellite remote sensing as a tool in disaster management and sustainable development: towards a synergistic approach. *Procedia - Soc. Behav. Sci.* 120, 365–373. <https://doi.org/10.1016/j.sbspro.2014.02.114>.
- Benz, U.C., Hofmann, P., Willhauck, G., Lingenfelder, I., Heynen, M., 2004. Multi-resolution, object-oriented fuzzy analysis of remote sensing data for GIS-ready information. *ISPRS J. Photogramm. Remote Sens.* 58, 239–258. <https://doi.org/10.1016/j.isprsjprs.2003.10.002>.
- Bruzzzone, L., Chi, M., Marconcini, M., 2006. A novel transductive SVM for semisupervised classification of remote-sensing images. *IEEE Trans. Geosci. Remote Sens.* 44, 3363–3373. <https://doi.org/10.1109/TGRS.2006.877950>.
- Buda, M., Maki, A., Mazurowski, M.A., 2018. A systematic study of the class imbalance problem in convolutional neural networks. *Neural Networks* 106, 249–259.
- Camps-Valls, G., Marsheva, T.B., Zhou, D., 2007. Semi-supervised graph-based hyperspectral image classification. *IEEE Trans. Geosci. Remote Sens.* 45, 3044–3054.
- Cheng, G., Zhou, P., Han, J., 2016. Learning rotation-invariant convolutional neural networks for object detection in VHR optical remote sensing images. *IEEE Trans. Geosci. Remote Sens.* 54, 7405–7415. <https://doi.org/10.1109/TGRS.2016.2601622>.
- Chini, M., Hostache, R., Giustarini, L., Matgen, P., 2017. A hierarchical split-based approach for parametric thresholding of SAR images: flood inundation as a test case. *IEEE Trans. Geosci. Remote Sens.* 55, 6975–6988. <https://doi.org/10.1109/TGRS.2017.2737664>.
- Chini, M., Pelich, R., Pulvirenti, L., Pierdicca, N., Hostache, R., Matgen, P., 2019. Sentinel-1 InSAR coherence to detect floodwater in urban areas: houston and hurricane harvey as a test case. *Remote Sens.* 11, 107. <https://doi.org/10.3390/rs11020107>.
- Chini, M., Pulvirenti, L., Pierdicca, N., 2012. Analysis and interpretation of the COSMO-SkyMed observations of the 2011 Japan tsunami. *IEEE Geosci. Remote Sens. Lett.* 9, 467–471. <https://doi.org/10.1109/LGRS.2011.2182495>.
- Dellepiane, S.G., Angiati, E., 2012. A new method for cross-normalization and multi-temporal visualization of SAR images for the detection of flooded areas. *IEEE Trans. Geosci. Remote Sens.* 50, 2765–2779.
- Demir, B., Persello, C., Bruzzzone, L., 2011. Batch-mode active-learning methods for the interactive classification of remote sensing images. *IEEE Trans. Geosci. Remote Sens.* 49, 1014–1031.
- Deng, Z., Sun, H., Zhou, S., Zhao, J., Lei, L., Zou, H., 2018. Multi-scale object detection in remote sensing imagery with convolutional neural networks. *ISPRS J. Photogramm. Remote Sens.* 145, 3–22. <https://doi.org/10.1016/j.isprsjprs.2018.04.003>.
- Dong, Y., Forster, B., Ticehurst, C., 1997. Radar backscatter analysis for urban environments. *Int. J. Remote Sens.* 18, 1351–1364. <https://doi.org/10.1080/014311697218467>.
- Dópido, I., Li, J., Marpu, P.R., Plaza, A., Dias, J.M.B., Benediktsson, J.A., 2013. Semisupervised self-learning for hyperspectral image classification. *IEEE Trans. Geosci. Remote Sens.* 51, 4032–4044.
- Ferro, A., Brunner, D., Bruzzzone, L., Lemoine, G., 2011. On the relationship between double bounce and the orientation of buildings in VHR SAR images. *IEEE Geosci. Remote Sens. Lett.* 8, 612–616. <https://doi.org/10.1109/LGRS.2010.2097580>.
- Giustarini, L., Hostache, R., Matgen, P., Schumann, G.J., Bates, P.D., Mason, D.C., 2013. A change detection approach to flood mapping in urban areas using TerraSAR-X. *IEEE Trans. Geosci. Remote Sens.* 51, 2417–2430. <https://doi.org/10.1109/TGRS.2012.2210901>.
- He, Z., Liu, H., Wang, Y., Hu, J., 2017. Generative adversarial networks-based semi-supervised learning for hyperspectral image classification. *Remote Sens.* 9. <https://doi.org/10.3390/rs9101042>.
- Huang, B., Zhao, B., Song, Y., 2018. Urban land-use mapping using a deep convolutional neural network with high spatial resolution multispectral remote sensing imagery. *Remote Sens. Environ.* 214, 73–86. <https://doi.org/10.1016/j.rse.2018.04.050>.
- Iervolino, P., Guida, R., Iodice, A., Riccio, D., 2015. Flooding water depth estimation with high-resolution SAR. *IEEE Trans. Geosci. Remote Sens.* 53, 2295–2307. <https://doi.org/10.1109/TGRS.2014.2358501>.
- Insom, P., Cao, C., Boonsrimuang, P., Liu, D., Saokarn, A., Yomwan, P., Xu, Y., 2015. A support vector machine-based particle filter method for improved flooding classification. *IEEE Geosci. Remote Sens. Lett.* 12, 1943–1947. <https://doi.org/10.1109/LGRS.2015.2439575>.
- Jean, N., Burke, M., Xie, M., Davis, W.M., Lobell, D.B., Ermon, S., 2016. Combining satellite imagery and machine learning to predict poverty. *Science* (80) 353, 790–794.
- Kellenberger, B., Marcos, D., Tuia, D., 2018. Detecting mammals in UAV images: best practices to address a substantially imbalanced dataset with deep learning. *Remote Sens. Environ.* 216, 139–153. <https://doi.org/10.1016/j.rse.2018.06.028>.
- Kingma, D.P., Ba, J.L., 2015. Adam: A method for stochastic optimization. In: *International Conference on Learning Representations*.
- Kussul, N., Lavreniuk, M., Skakun, S., Shelestov, A., 2017. Deep learning classification of land cover and crop types using remote sensing data. *IEEE Geosci. Remote Sens. Lett.* 14, 778–782.
- Laine, S., Aila, T., 2017. Temporal Ensembling for Semi-Supervised Learning. In: *International Conference on Learning Representations*. <https://doi.org/10.1111/j.1439-0531.2008.01139.x>.
- Li, F., Clausi, D.A., Xu, L., Wong, A., 2018. ST-IRGS: A region-based self-training algorithm applied to hyperspectral image classification and segmentation. *IEEE Trans. Geosci. Remote Sens.* 56, 3–16.
- Li, H.C., Celik, T., Longbotham, N., Emery, W.J., 2015. Gabor feature based unsupervised change detection of multitemporal SAR images based on two-level clustering. *IEEE Geosci. Remote Sens. Lett.* 12, 2458–2462. <https://doi.org/10.1109/LGRS.2015.2484220>.
- Li, Y., Martinis, S., Plank, S., Ludwig, R., 2018. An automatic change detection approach for rapid flood mapping in Sentinel-1 SAR data. *Int. J. Appl. Earth Obs. Geoinf.* 73, 123–135. <https://doi.org/10.1016/j.jag.2018.05.023>.
- Liu, J.G., Black, A., Lee, H., Hanaizumi, H., Moore, J.M., 2001. Land surface change detection in a desert area in Algeria using multi-temporal ERS SAR coherence images. *Int. J. Remote Sens.* 22, 2463–2477.
- Loshchilov, I., Hutter, F., 2017. SGDR: Stochastic gradient descent with warm restarts. *International Conference on Learning Representations*.
- Maggiore, E., Tarabalka, Y., Charpiat, G., Alliez, P., 2017. Convolutional neural networks for large-scale remote-sensing image classification. *IEEE Trans. Geosci. Remote Sens.* 55, 645–657. <https://doi.org/10.1109/TGRS.2016.2612821>.
- Marmanis, D., Datcu, M., Esch, T., Stilla, U., 2016. Deep learning earth observation classification using imagenet pretrained networks. *IEEE Geosci. Remote Sens. Lett.* 13, 105–109. <https://doi.org/10.1109/LGRS.2015.2499239>.
- Martinis, S., Twele, A., Voigt, S., 2011. Unsupervised extraction of flood-induced backscatter changes in SAR data using markov image modeling on irregular graphs. *IEEE Trans. Geosci. Remote Sens.* 49, 251–263. <https://doi.org/10.1109/TGRS.2010.2052816>.
- Mason, D.C., Davenport, I.J., Neal, J.C., Schumann, G.J.-P., Bates, P.D., 2012. Near real-time flood detection in urban and rural areas using high-resolution synthetic aperture radar images. *IEEE Trans. Geosci. Remote Sens.* 50, 3041–3052.
- Mason, D.C., Giustarini, L., Garcia-Pintado, J., Cloke, H.L., 2014. Detection of flooded urban areas in high resolution Synthetic Aperture Radar images using double scattering. *Int. J. Appl. Earth Obs. Geoinf.* 28, 150–159. <https://doi.org/10.1016/j.jag.2013.12.002>.
- Mason, D.C., Speck, R., Devereux, B., Schumann, G.J.-P., Neal, J.C., Bates, P.D., 2010. Flood detection in urban areas using TerraSAR-X. *IEEE Trans. Geosci. Remote Sens.* 48, 882–894. <https://doi.org/10.1109/tgrs.2009.2029236>.
- Moreira, A., Prats-Iraola, P., Younis, M., Papathinassiou, K., 2013. A tutorial on synthetic aperture radar. *IEEE Geosci. Remote Sens. Mag.* 32.
- Muñoz-marí, J., Bovolo, F., Gómez-chova, L., Bruzzzone, L., Camps-valls, G., 2010. Semisupervised one-class support vector machines. *IEEE Trans. Geosci. Remote Sens.* 48, 3188–3197.
- NOAA, 2017. Hurricane harvey: emergency response imagery of the surrounding regions. < <https://storms.ngs.noaa.gov/storms/harvey/index.html#7/28.400/-96.690> > .
- Pan, S.J., Yang, Q., 2010. A survey on transfer learning. *IEEE Trans. Knowl. Data Eng.* 22, 1345–1359.
- Persello, C., Bruzzzone, L., 2014. Active and semisupervised learning for the classification of remote sensing images. *IEEE Trans. Geosci. Remote Sens.* 52, 6937–6956.
- Polyak, B.T., Juditsky, A.B., 1992. Acceleration of stochastic approximation by averaging. *SIAM J. Control Optim.* 30, 838–855. <https://doi.org/10.1137/0330046>.
- Pulvirenti, L., Chini, M., Pierdicca, N., Boni, G., 2016. Use of SAR data for detecting floodwater in urban and agricultural areas: the role of the interferometric coherence. *IEEE Trans. Geosci. Remote Sens.* 54, 1532–1544. <https://doi.org/10.1109/TGRS.2016.2612821>.



- 2015.2482001.
- Pulvirenti, L., Chini, M., Pierdicca, N., Guerriero, L., Ferrazzoli, P., 2011. Flood monitoring using multi-temporal COSMO-SkyMed data: Image segmentation and signature interpretation. *Remote Sens. Environ.* 115, 990–1002. <https://doi.org/10.1016/J.RSE.2010.12.002>.
- Rasmus, A., Valpola, H., Honkala, M., Berglund, M., Raiko, T., 2015. Semi-supervised learning with ladder networks. In: *Proceedings of the Advances in Neural Information Processing Systems*. pp. 3532–3540.
- Refice, A., Capolongo, D., Pasquariello, G., Addabbo, A.D., Bovenga, F., Nutricato, R., Lovergine, F.P., Pietranera, L., 2014. SAR and InSAR for flood monitoring: examples with COSMO-SkyMed data. *IEEE J. Sel. Top. Appl. Earth Obs. Remote Sens.* 7, 2711–2722.
- Rimba, A.B., Miura, F., 2017. Evaluating the extraction approaches of flood extended area by using ALOS-2/PALSAR-2 images as a rapid response to flood disaster. *J. Geosci. Environ. Prot.* 05, 40–61. <https://doi.org/10.4236/gep.2017.51003>.
- Rolnick, D., Veit, A., Belongie, S., Shavit, N., 2017. Deep Learning is Robust to Massive Label Noise. *arXiv Prepr.*
- Salimans, T., Goodfellow, I., Zaremba, W., Cheung, V., Radford, A., Chen, X., 2016. Improved Techniques for Training GANs. In: *Proceedings of the Advances in Neural Information Processing Systems*. pp. 2226–2234.
- Schneider, R.Z., Papathanassiou, K.P., Hajnsek, I., Moreira, A., 2006. Polarimetric and interferometric characterization of coherent scatterers in urban areas. *IEEE Trans. Geosci. Remote Sens.* 44, 971–984. <https://doi.org/10.1109/TGRS.2005.860950>.
- Skakun, S., 2010. A neural network approach to flood mapping using satellite imagery. *Comput. Informatics* 29, 1013–1024.
- Tanguy, M., Chokmani, K., Bernier, M., Poulin, J., Raymond, S., 2017. River flood mapping in urban areas combining Radarsat-2 data and flood return period data. *Remote Sens. Environ.* 198, 442–459. <https://doi.org/10.1016/j.rse.2017.06.042>.
- Tarvainen, A., Valpola, H., 2017. Mean teachers are better role models: weight-averaged consistency targets improve semi-supervised deep learning results. *Proc. Adv. Neural Inf. Process. Syst.* 1195–1204.
- Thiele, A., Cadario, E., Karsten, S., Thönnessen, U., Soergel, U., 2007. Building recognition from multi-aspect high-resolution InSAR data in urban areas. *IEEE Trans. Geosci. Remote Sens.* 45, 11.
- Tobler, W.R., 1970. A computer movie simulating urban growth in the detroit region. *Econ. Geogr.* 46, 234–240. <https://doi.org/10.2307/143141>.
- Tong, X., Luo, X., Liu, S., Xie, H., Chao, W., Liu, S., Liu, S., Makhinova, A.N., Makhinova, A.F., Jiang, Y., 2018. An approach for flood monitoring by the combined use of Landsat 8 optical imagery and COSMO-SkyMed radar imagery. *ISPRS J. Photogramm. Remote Sens.* 136, 144–153. <https://doi.org/10.1016/j.isprsjprs.2017.11.006>.
- Touzi, R., Lopes, A., Bruniquel, J., Vachon, P.W., 1999. Coherence estimation for SAR imagery. *IEEE Trans. Geosci. Remote Sens.* 37, 135–149.
- Tralli, D.M., Blom, R.G., Zlotnicki, V., Donnellan, A., Evans, D.L., 2005. Satellite remote sensing of earthquake, volcano, flood, landslide and coastal inundation hazards. *ISPRS J. Photogramm. Remote Sens.* 59, 185–198. <https://doi.org/10.1016/j.isprsjprs.2005.02.002>.
- Tuia, D., Volpi, M., Copa, L., Kanevski, M., Muñoz-Marí, J., 2011. A Survey of active learning algorithms for supervised remote sensing image classification. *IEEE J. Sel. Top. Signal Process.* 5, 606–617. <https://doi.org/10.1109/JSTSP.2011.2139193>.
- Twele, A., Cao, W., Plank, S., Martinis, S., 2016. Sentinel-1-based flood mapping: a fully automated processing chain. *Int. J. Remote Sens.* 37, 2990–3004. <https://doi.org/10.1080/01431161.2016.1192304>.
- Vetrivel, A., Gerke, M., Kerle, N., Nex, F., Vosselman, G., 2018. Disaster damage detection through synergistic use of deep learning and 3D point cloud features derived from very high resolution oblique aerial images, and multiple-kernel-learning. *ISPRS J. Photogramm. Remote Sens.* 140, 45–59. <https://doi.org/10.1016/j.isprsjprs.2017.03.001>.
- Zebker, H.A., Member, S., Villasenor, J., 1992. Decorrelation in interferometric radar echoes. *IEEE Trans. Geosci. Remote Sens.* 30, 950–959.
- Zhan, Y., Hu, D., Wang, Y., Yu, X., 2018. Semisupervised hyperspectral image classification based on generative adversarial networks. *IEEE Geosci. Remote Sens. Lett.* 15, 212–216.
- Zhang, C., Sargent, I., Pan, X., Li, H., Gardiner, A., Hare, J., Atkinson, P.M., 2019. Joint Deep Learning for land cover and land use classification. *Remote Sens. Environ.* 221, 173–187. <https://doi.org/10.1016/j.rse.2018.11.014>.
- Zhu, L., Chen, Y., Ghamisi, P., 2018. Generative adversarial networks for hyperspectral image classification. *IEEE Trans. Geosci. Remote Sens.* 56, 5046–5063.
- Zhu, X.X., Tuia, D., Mou, L., Xia, G.-S., Zhang, L., Xu, F., Fraundorfer, F., 2017. Deep learning in remote sensing: a review. *IEEE Geosci. Remote Sens. Mag.* 5, 8–36. <https://doi.org/10.1109/MGRS.2017.2762307>.

## **6. Urban flood mapping using SAR intensity and interferometric coherence via Bayesian network fusion**

Li, Y.; Martinis, S.; Wieland, M.; Schlaffer, S.; Natsuaki, R., 2019. Urban Flood Mapping Using SAR Intensity and Interferometric Coherence via Bayesian Network Fusion. *Remote Sens.* 11, 2231. DOI: [10.3390/rs11192231](https://doi.org/10.3390/rs11192231)

LY designed and conducted the experiments. MS conceptualized the study and acquired the ALOS-2/PALSAR-2 data. WM contributed to method discussion and review. SS and NR contributed to results interpretation. LY drafted the manuscript, all co-authors contributed to the discussion and review of the manuscript.

Article

# Urban Flood Mapping Using SAR Intensity and Interferometric Coherence via Bayesian Network Fusion

Yu Li <sup>1,2,\*</sup>, Sandro Martinis <sup>1</sup>, Marc Wieland <sup>1</sup> , Stefan Schlaffer <sup>1</sup> and Ryo Natsuaki <sup>3,4</sup> 

<sup>1</sup> German Remote Sensing Data Center (DFD), German Aerospace Center (DLR), Oberpfaffenhofen, Münchener Straße 20, 82234 Weßling, Germany; sandro.martinis@dlr.de (S.M.); marc.wieland@dlr.de (M.W.); stefan.schlaffer@dlr.de (S.S.)

<sup>2</sup> Department of Geography, Ludwig-Maximilians-Universität München, Luisenstraße 37, 80333 München, Germany

<sup>3</sup> Microwaves and Radar Institute, German Aerospace Center (DLR), Oberpfaffenhofen, Münchener Straße 20, 82234 Weßling, Germany; natsuaki@ee.t.u-tokyo.ac.jp

<sup>4</sup> Department of Electrical Engineering and Information Systems, School of Engineering, The University of Tokyo, 7-3-1 Hongo, Bunkyo-ku, Tokyo 113-8656, Japan

\* Correspondence: yu.li@dlr.de; Tel.: +49-8153281445

Received: 27 August 2019; Accepted: 23 September 2019; Published: 25 September 2019



**Abstract:** Synthetic Aperture Radar (SAR) observations are widely used in emergency response for flood mapping and monitoring. However, the current operational services are mainly focused on flood in rural areas and flooded urban areas are less considered. In practice, urban flood mapping is challenging due to the complicated backscattering mechanisms in urban environments and in addition to SAR intensity other information is required. This paper introduces an unsupervised method for flood detection in urban areas by synergistically using SAR intensity and interferometric coherence under the Bayesian network fusion framework. It leverages multi-temporal intensity and coherence conjunctively to extract flood information of varying flooded landscapes. The proposed method is tested on the Houston (US) 2017 flood event with Sentinel-1 data and Joso (Japan) 2015 flood event with ALOS-2/PALSAR-2 data. The flood maps produced by the fusion of intensity and coherence and intensity alone are validated by comparison against high-resolution aerial photographs. The results show an overall accuracy of 94.5% (93.7%) and a kappa coefficient of 0.68 (0.60) for the Houston case, and an overall accuracy of 89.6% (86.0%) and a kappa coefficient of 0.72 (0.61) for the Joso case with the fusion of intensity and coherence (only intensity). The experiments demonstrate that coherence provides valuable information in addition to intensity in urban flood mapping and the proposed method could be a useful tool for urban flood mapping tasks.

**Keywords:** urban flood mapping; synthetic aperture radar (SAR); InSAR coherence; Bayesian network

## 1. Introduction

Flooding is a widespread and dramatic natural disaster that affects lives, infrastructures, economics and local ecosystems in the world. It is reported that flood events were the main cause of internal displacement in 2008 to 2015 [1,2], and global economic losses due to floods in economically strong and populated areas are projected to reach US \$597 billion in 2016–2035 [3]. Remote sensing data can offer a synoptic view over large areas systematically and provides useful information about the extent and dynamics of floods. Several international initiatives such as the International Charter “Space and Major Disasters” and the European Copernicus Emergency Management Service – Mapping have leveraged Earth Observation (EO) data to provide products and services for crisis

response in the context of disaster management. Synthetic aperture radar (SAR) sensors are the most widely used EO sources in flood mapping due to their all-weather and day-night imaging capability. Nowadays, the growing number of Synthetic Aperture Radar (SAR) satellite missions in orbits such as the Constellation of small Satellites for Mediterranean basin Observation (COSMO-SkyMed) [4], TerraSAR-X [5], Sentinel-1 [6], RADARSAT-2 [7], and the Phased-Array L-band SAR-2 (PALSAR-2) aboard the Advanced Land Observation Satellite-2 (ALOS-2) [8] have shortened the revisit periods (e.g., 6 days with the Sentinel-1A/B constellation, and 1 day with the full COSMO-SkyMed constellation) and facilitated rapid flood mapping within the context of emergency response.

SAR-based flood mapping in rural areas (e.g., bare soils and sparse vegetation) has been extensively studied and explored [3–13]. The specular reflection occurring on smooth water surfaces results in a dark tone in SAR data, which makes floodwater distinguishable from dry land surfaces. Both uni- [10,14,15] and multi-temporal [9,12,16–19] SAR data have been employed in flood mapping based on either supervised [14,19] methods with available training data or unsupervised [9,10,12,15–18] methods without any training data. Urban areas with low slopes and a high percentage of impervious surfaces are vulnerable to flooding and the increased risk of loss of human lives and damage to economic infrastructures makes urban flood mapping greatly valuable in terms of disaster risk reduction. However, flood detection in urban areas is challenging to SAR due to the complex backscatter mechanisms associated with varying building types and heights, vegetation areas, and different road topologies [20]. Several studies [21–25] have led to noteworthy progress in the understanding of SAR backscatter characteristics in the urban environment and further made considerable advances in flood mapping in urban areas. Nevertheless, it is not easy to incorporate knowledge about backscatter phenology into generic analysis algorithms and specific algorithms are required.

A couple of studies have demonstrated the success of high-resolution SAR data in urban flood mapping. Mason et al. [26,27] proposed a near real-time approach for urban flood detection based on high-resolution TerraSAR-X image of the Tewkesbury (England) flood in the summer of 2007. They used a SAR simulator in conjunction with a very high-resolution LiDAR digital surface model (DSM) to account for misclassification due to layover and shadow. Automatic change detection based on bi-temporal TerraSAR-X data on the same flood event was suggested by Giustarini et al. [28] to suppress false alarms caused by shadow and water look-alike surfaces. Mason et al. [29] adopted the GO-GO scattering model to detect floodwater in layover areas via double-bounce scattering. More recently, Tanguy et al. [30] applied high-resolution RADARSAT-2 data combined with hydraulic data (flood return period) for flood detection in urban areas based on case studies of the 2011 Richelieu River flood (Canada) and achieved promising results. Nonetheless, the aforementioned studies only leveraged SAR intensity ( $\sigma^0$ ) that provides limited information for flood mapping in urban environments for the following reasons. In principle, floodwater in front of buildings can be detected by the strengthened double-bounce effect in SAR intensity data. However, the increase of double-bounce effect is affected by the aspect angle  $\phi$  (i.e., the angle between the orientation of the wall and the SAR azimuth direction). According to the simulation experiments by Pulvirenti et al. [31], the increase of intensity drops from 11.5 dB to ~3.5 dB when  $\phi$  increases from  $0^\circ$  to greater than  $5\text{--}10^\circ$ . Furthermore, the floodwater level is another factor which needs to be considered when detecting flooding via the double-bounce effect. The enhancement of this effect diminishes when the floodwater is on a high-level relative to the height of the surrounding buildings [32]. Several studies have shown that SAR interferometric coherence ( $\gamma$ ) is valuable information for urban flood mapping and can reduce the abovementioned drawbacks [31,33]. An urban settlement can generally be considered as a stable target with high coherence, and the coherence decorrelation is roughly irrelative to the temporal baseline ( $B_t$ ) (time interval between two SAR acquisitions) while dominantly impacted by the spatial baseline ( $B_p$ ) (spatial separation between repeat satellite orbits) [31,34]. Standing floodwater between buildings causes changes in the spatial distribution of scatterers within a resolution cell, resulting in a drop-off in the co-event pair coherence (i.e., the interferometric coherence produced from one image acquired before and another during the flood) compared to pre-event pair coherence (i.e., the interferometric

coherence produced from two images both acquired before the flood). More details of SAR intensity and coherence response of floodwater over different land types in the urban environment can be found in Li et al. [35]. Chini et al. [33] interpreted intensity and coherence characteristics of the Sendai (Japan) flood related to the tsunami of 2011 with high-resolution COSMO-SkyMed data and found a lower coherence of flooded urban areas than non-flooded ones. Also, with high-resolution COSMO-SkyMed data, in Pulvirenti et al. [31], coherence was used complementary to intensity and substantially reduced missed alarms in flooded urban areas of the 2014 Secchia River flood (Italy). Li et al. [35] employed multi-temporal high-resolution TerraSAR-X intensity and coherence for urban flood detection of the 2017 Houston flood (US) accompanying Hurricane Harvey with an active self-learning Convolutional Neural Network (CNN) model, and suggested that both multi-temporal intensity and coherence are required to produce an accurate inundation map in urban areas. This work presented an active self-learning framework that improves classification results with limited training samples. However, the requirement of training samples limits its application in scenarios that no training samples are available. More recently, Chini et al. [36] first applied mid-resolution Sentinel-1 intensity and coherence for urban flood detection for a case study of the 2017 Houston flood. In that study, the authors first extracted built-up areas with co- and cross-polarized (VV and VH) intensity time series and filtered false alarms with time series VV coherence. Subsequently, an adaptive thresholding-based change detection [16] was adopted to map flooded bare soils and flooded built-up areas with VV intensity and coherence, respectively. However, as noted by the authors, the influence of vegetation can lead to a decrease in coherence of built-up areas. This may result in an under-estimation of the flood extent in vegetated built-up areas. Intensity can complement coherence, in this case, to reduce under-estimation as flooded vegetation causes strong double-bounce scattering as well. Therefore, in practical urban flood mapping, the integrated information of intensity decrease, intensity increase, and coherence drop-off is required to account for different flood conditions in urban environments.

In this paper, we introduce a method for flood detection in urban (and suburban) environments with synergistic use of SAR intensity and coherence based on Bayesian network fusion. It leverages SAR intensity and coherence time series to map non-obstructed-flood (e.g., flooded bare soils and short vegetation); obstructed-flooded non-coherent areas (e.g., flooded vegetation and vegetated built-up areas); and obstructed-flooded coherent areas (e.g., flooded predominantly built-up areas). The method is flexible with respect to the time spans of data sequences (at least one pre- and co-event intensity pair, and one pre- and co-event coherence pair are needed). As mentioned above, the growing number of SAR missions in orbit that offer a consistent observation scenario with short revisit times increases the chance of both observing a flood event and, at the same time, having a suitable pre-event scene acquired by the same sensor. This makes the method favorable for operational emergency responses. Bayesian networks are statistically well-founded methods with highly flexible structures for explicitly displaying relationships among different variables, combining expert knowledge and data, and characterizing uncertainties [37–39]. Bayesian networks have been widely used in risk analysis and management [40], uncertainty quantification [37], and classification with the incorporation of multi-source remote sensing data [41,42]. D’Addabbo et al. [43,44] employed a Bayesian network for flood detection in rural areas combining SAR intensity, coherence, and ancillary data. In their study, they made use of coherence information with a very short temporal baseline (e.g., 1 day) to complement intensity for more robust inundation extent mapping in rural areas. However, their approach is difficult to transfer to more general cases with longer temporal baselines (e.g., 6 days with Sentinel-1A and Sentinel-1B constellation, and can be even longer for sensors such as TerraSAR-X and ALOS-2/PALSAR-2) as temporal decorrelation between subsequent acquisitions may outweigh the effect of coherence decrease due to flooding. For the scenario of flood mapping in an urban area, which comprises a variety of landscapes such as bare soil, vegetated areas, and man-made structures, it is essential to distinguish the variation in coherence from unstable scatterers and the changes caused by a flood event. Furthermore, in the work of D’Addabbo et al. [43,44] user-designed thresholding values are required, which are sensor and scene dependent.

The stability of scatterers in urban areas is considered in the fusion of intensity and coherence in this paper, and the thresholding values are learned from the data, thus making the method automatic so that it is independent of sensors and study areas. To preserve the probability information of Bayesian network outputs and incorporate the global contexture information, considering the pairwise relationships on all pairs of pixels in the image, we adopted a fully-connected Conditional Random Field (CRF) [45] which has seen demonstrated success in flood mapping in our previous study [18]. The method is unsupervised and further provides a supplement to the current Sentinel-1 Flood Service [15] of the German Aerospace Center (DLR) to account for flood in urban areas. We show the effectiveness of the approach on the 2017 Houston flood (US) event with Sentinel-1 time series and the 2015 Joso flood (Japan) event with ALOS-2/PALSAR-2 time series. The remainder of this paper is structured as follows: Section 2 describes the details of methods. Details of the dataset and experiment setup are introduced in Section 3. Section 4 gives the results and discussions. Finally, Section 5 concludes this paper with some remarks.

## 2. Methods

A Bayesian network is a probabilistic graphical model for compactly specifying joint probability distribution over a fixed set of random variables. It is a directed acyclic graph (DAG), where nodes represent variables and links between nodes represent dependencies between them [46]. The DAG specifies conditional independence statements of variables on their ancestors—namely which ancestors are direct “causes” for the variable [47]. Assuming  $x_1, \dots, x_N$  are the random variables, the joint distribution under a Bayesian network is given by

$$p(x_1, \dots, x_N) = \prod_{i=1}^N p(x_i | \text{pa}(x_i)), \quad (1)$$

where  $\text{pa}(x_i)$  represent the parental variables of variable  $x_i$ , with an arrow pointing from a parent variable to child variable in the DAG. The Bayesian network thus provides information about the underlying process and any conditional distribution(s) can be expressed via inference.

The structure of the Bayesian network for flood mapping based on the fusion of intensity and coherence is visualized in Figure 1a. It combines information from both the backscatter intensity and interferometric coherence time series. The shaded nodes in Figure 1 indicate observed variables whereas open nodes mask unknown variables. In detail, the random variable  $F$  indicates the flood state (e.g.,  $F = 1$  for flood state and  $F = 0$  for non-flood state, respectively) of each pixel; this is our target variable for which we want to infer its posterior probability conditioned on all the other variables. The variable  $D$  corresponds to the combination of intensity and coherence time series: stacked imagery of multitemporal intensity and coherence.  $C$  is a hidden variable, which links the influence of variable  $F$  on the observed image series  $D$ . It is difficult to find a simple causality between flood state and the observed SAR signatures, especially in urban areas associated with the complex backscattering mechanisms due to varying land covers. Therefore, it is necessary to introduce an intermediate variable  $C$  with  $K$  possible states that represent different temporal behaviors of the area of interest (AOI), corresponding to different land covers from a SAR (e.g., intensity and coherence) point of view [43,48]. Intensity and coherence characterize different physical properties of a scene: intensity provides information about surface roughness and permittivity, whereas coherence measures the random variation of individual scatterers between two SAR acquisitions, indicating temporal similarity within a cell. Therefore, intensity and coherence could be sensitive to and provide useful information on different flooded land covers. For instance, intensity is sensitive to flooded bare soils and flooded vegetation, both intensity and coherence are sensitive to flooded built-up areas, and coherence is also sensitive to some flooded built-up areas that are insensitive for intensity (as described in the Introduction section). Considering this phenomenon, the hidden variable  $C$  is decoupled to two variables of  $C_i$  and  $C_\gamma$  corresponding to the intensity and coherence temporal signature,



respectively (Figure 1b), as the flood state of a given class  $C = k, k = 1, \dots, K$ , should be evaluated from the perspective of intensity (e.g.,  $p(F|C_i = k)$ ) and coherence (e.g.,  $p(F|C_\gamma = k)$ ). The variable  $D$  is partitioned to intensity (e.g., variable  $D_i$ ) and coherence series (e.g., variable  $D_\gamma$ ) accordingly. The land cover segmentation (e.g., variable  $C$ ) is implemented under the conjunction of intensity and coherence time series (e.g., variable  $D$ ) to retain the internal dependencies between these two data sources and preserve compact clusters of the AOI. Another reason is that the conditional probabilities of  $p(F|C_i)$  and  $p(F|C_\gamma)$  are evaluated interactively (described in detail later in this section). Therefore, consistent clusters of intensity and coherence are required.

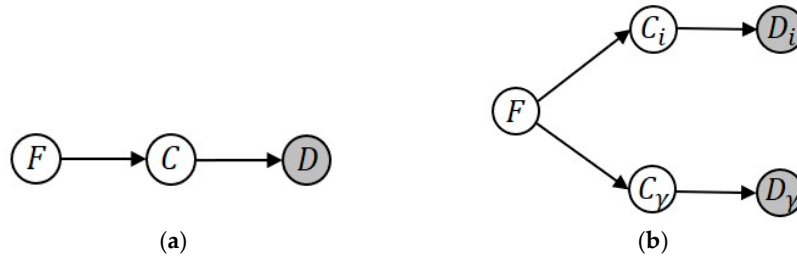


**Figure 1.** The Bayesian network structure for flood mapping. The variable  $F$  indicates flood states,  $C$  is a hidden variable, and  $D$  is a variable of observed Synthetic Aperture Radar (SAR) data. The subscript  $i$  and  $\gamma$  indicate intensity and coherence, respectively: (a) The original Bayesian network; (b) Bayesian network with decoupled variables  $C$  and  $D$ .

The joint probability of  $p(D_i, D_\gamma, F)$  in Figure 1b is given by:

$$p(D_i, D_\gamma, F) = \sum_{C_i} p(D_i|C_i)p(C_i|F) \sum_{C_\gamma} p(D_\gamma|C_\gamma)p(C_\gamma|F)p(F), \quad (2)$$

and the posterior probability of  $F = 1$  can be expressed as:

$$p(F = 1|D_i, D_\gamma) = \frac{\sum_{C_i} p(D_i|C_i)p(C_i|F = 1) \sum_{C_\gamma} p(D_\gamma|C_\gamma)p(C_\gamma|F = 1)p(F = 1)}{\sum_F \sum_{C_i} p(D_i|C_i)p(C_i|F) \sum_{C_\gamma} p(D_\gamma|C_\gamma)p(C_\gamma|F)p(F)}, \quad (3)$$

where  $p(C_i|F)$  and  $p(C_\gamma|F)$  can be calculated via the Bayes rule:

$$p(C_j|F) = \frac{p(F|C_j)p(C_j)}{\sum_{C_j} p(F|C_j)p(C_j)}, \quad (4)$$

with  $j \in \{i, \gamma\}$ .

Each term in Equation (3) can be calculated analytically. The distribution of  $D = \begin{pmatrix} D_i \\ D_\gamma \end{pmatrix}$  is estimated by a finite Gaussian Mixture Model (GMM) involving the hidden variable  $C$ . Each assignment of  $C$  is a Gaussian component, thus  $p(D|C = k) = \mathcal{N}(D|\mu_k, \Sigma_k)$ ,  $k = 1, \dots, K$ , and the parameters of each Gaussian component,  $(\mu_k, \Sigma_k)$ ,  $\mu_k = \begin{pmatrix} \mu_{ik} \\ \mu_{\gamma k} \end{pmatrix}$ ,  $\Sigma_k = \begin{pmatrix} \Sigma_{iik} & \Sigma_{i\gamma k} \\ \Sigma_{\gamma ik} & \Sigma_{\gamma\gamma k} \end{pmatrix}$ , are estimated by the expectation-maximization (EM) algorithm [49]. Therefore,  $p(D_i|C_i = k)$  and  $p(D_\gamma|C_\gamma = k)$  are also Gaussian densities and can be calculated by  $p(D_i|C_i = k) = \mathcal{N}(D_i|\mu_{ik}, \Sigma_{iik})$  and  $p(D_\gamma|C_\gamma = k) = \mathcal{N}(D_\gamma|\mu_{\gamma k}, \Sigma_{\gamma\gamma k})$ , respectively [46]. The number of Gaussian mixtures,  $K$ , depends on the homogeneity of the AOI. A smaller value of  $K$  is needed for a more homogeneous area. In practice, a relatively large  $K$  is preferable as under-clustering results in mixed clusters with variable spectral signatures and causes a compromised result, whereas over-clustering does not impact the final result [43]. We select  $K$  via the Bayesian information criterion (BIC). The flood prior probability  $p(F = 1)$  can be approximated

by auxiliary data [43]. However, auxiliary data are not always available in emergency response and a SAR data self-consistent approach is more preferable. Therefore, the non-informative prior probability is used in this paper,  $p(F = 1) = p(F = 0) = 0.5$ .

The term  $p(C_j)$  in Equation (4) is a vector of weights of  $K$  Gaussian components.  $p(F|C_j)$  is a conditional probability table (CPT) that contains the flood probability of each component. It is the core part of the whole process and determines the final result. The CPT can be assigned manually by an expert or be learned from the data. The latter strategy is adopted in this paper to make the whole chain automatic. Under the assumption that the existence of floodwater may cause an abrupt change in either intensity or coherence, the CPT is estimated based on the variation between the average of pre-event series and the co-event acquisition for each component centroid (e.g.,  $\mu_{jk}$ ,  $j \in \{i, \gamma\}$ , and  $k = 1, \dots, K$ ). Intensity could decrease or increase due to the specular reflection or double-bounce, whereas coherence drops because of decorrelation caused by floodwater. Let  $\Delta_j$ ,  $j \in \{i, \gamma\}$  be the variation vector that we are concerned; we intend to extract the change information related to flooding at this step:

$$\Delta_i = \max(\text{mean}(\mu_i^{\text{pre}}), \mu_i^{\text{co}}) - \min(\text{mean}(\mu_i^{\text{pre}}), \mu_i^{\text{co}}), \quad \Delta_\gamma = \text{mean}(\mu_\gamma^{\text{pre}}) - \mu_\gamma^{\text{co}}, \quad (5)$$

where  $\max(\cdot, \cdot)$  and  $\min(\cdot, \cdot)$  extract the element-wise maximum and minimum values of two vectors, respectively,  $\text{mean}(\cdot)$  is the average operator along the time axis,  $\mu_j^{\text{pre}}$  and  $\mu_j^{\text{co}}$  represent component centroids of the pre-event series and the co-event acquisition, respectively. The CPT  $p(F|C_j)$  is given by the sigmoid function of  $\Delta_j$ :

$$p(F|C_j) = \frac{1}{1 + e^{-\beta_j(\Delta_j - \alpha_j)}}, \quad (6)$$

where  $\beta_j$  is the steepness of the curve, and  $\alpha_j$  is the  $\Delta_j$  value corresponding to  $p(F|C_j) = 0.5$ . With relatively steep curves, the final result is not sensitive to the value of  $\beta_j$  and  $\beta_j = 1$  is set as the default value.  $\alpha_j$  is the most important parameter and an optimal value should be assigned. After  $\Delta_j$  is computed through Equation (5), its values are sorted in descending order.  $\Delta_{jl}$  ( $l = 1, \dots, K - 1$ ) is the potential value of  $\alpha_j$  and it separates the components to a flood-related changed set  $\Phi_{jC}$  ( $\Delta_{jk} \in \Phi_{jC}$ ,  $k \leq l$ ) and an unchanged set  $\Phi_{jU}$  ( $\Delta_{jk} \in \Phi_{jU}$ ,  $k > l$ ). A cost function is defined to find the optimal index of  $l^*$  by measuring intraclass compactness and interclass separability of the two sets [50,51]:

$$L_l = \frac{\sum_{V=\{C,U\}} \sum_{\Delta_{jk} \in \Phi_{jV}} (\Delta_{jk} - m_{jV})^2}{\sum_{V=\{C,U\}} \frac{N_{\Phi_{jV}}}{K} (m_{jV} - m_j)^2}, \quad (7)$$

where  $m_{jV}$  is the mean value of set  $\Phi_{jV}$ ,  $N_{\Phi_{jV}}$  is the component number of set  $\Phi_{jV}$ , and  $m_j$  is the mean value of the whole  $\Delta_j$ . A smaller value of  $L_l$  achieves higher intraclass compactness and interclass separability, thus  $l^*$  is determined via the minima of Equation (7):

$$l^* = \underset{l}{\operatorname{argmin}}\{L_l\}, \quad l = 1, \dots, K - 1 \quad (8)$$

The CPT  $p(F|C_j)$  needs to be further refined after being calculated via Equations (5)–(8), since we should take into account the flood uncertainty in terms of intensity and coherence depends on the land cover types. Generally speaking, the change information from intensity is reliable for flood detection in non-built-up areas and partially reliable for built-up areas. Missed alarms that happen in some particular built-up areas (see the Introduction section) need the complement of coherence information. The change information from coherence is reliable for coherent targets (e.g., built-up areas) and not reliable for non-coherent areas such as vegetated areas - especially when data with large temporal baseline (e.g., from days up to months) are used. Moreover, the different temporal baselines between the pre-event acquisitions and the co-event acquisition can also cause either false alarms or missed alarms in non-coherent areas. Therefore, we first classify the AOI to coherent (built-up) and



non-coherent (non-built-up) areas through the relationship between  $mean(\mu_{\gamma}^{pre})$  and a threshold  $t$ , and subsequently refine  $p(F|C_i)$  and  $p(F|C_{\gamma})$  as:

$$\begin{aligned} p(F|C_{ik} \in \left\{ \left[ mean(\mu_{\gamma k}^{pre}) > t \right] \& [(\Delta_{ik} < \alpha_i) \& (\Delta_{\gamma k} > \alpha_{\gamma})] \right\}) &= 0.5, \\ p(F|C_{\gamma k} \in \left\{ \left[ mean(\mu_{\gamma k}^{pre}) \leq t \right] \& [(\Delta_{ik} > \alpha_i) \& (\Delta_{\gamma k} < \alpha_{\gamma})] \right\} \parallel [(\Delta_{\gamma k} > \alpha_{\gamma}) \& (\Delta_{ik} < \alpha_i)] \right\}) &= 0.5, \end{aligned} \quad (9)$$

where  $\&$  denotes the logical AND, and  $\parallel$  denotes the logical OR, respectively. Equation (9) refines the flood evidence in terms of intensity and coherence according to the category of each component. For a given component  $k$  which belongs to the coherent (built-up) areas, when the flood evidence is favored by coherence (e.g.,  $\Delta_{\gamma k} > \alpha_{\gamma}$ ) whereas not by intensity (e.g.,  $\Delta_{ik} < \alpha_i$ ), intensity may fail to capture the flood information. Therefore,  $p(F|C_{ik}) = 0.5$  is assigned to this component to account for the uncertainty of intensity. For components that belong to non-coherent (non-built-up) areas, on the one hand, the non-flooded one can be misclassified as a flooded component by coherence due to the large temporal variation of the land cover and the (possible) difference of temporal baseline in the dataset. On the other hand, when pre-event coherence of a flooded component is already low (e.g., vegetated areas), neglectable variation can be observed between pre- and co-event coherence, thus it is difficult to detect floodwater by coherence. Therefore,  $p(F|C_{\gamma k}) = 0.5$  is assigned to the non-coherent components which show inconsistent flood evidence from intensity and coherence.

After the final  $p(F|C_j)$  is determined, the flood posterior probability of each pixel can be evaluated through Equations (3) and (4). The fully-connected CRF is adopted to refine the flood probability by integrating the long-range spatial information and the final binary flood extent is obtained via the maximum a posteriori (MAP) operation. In this process, the flood posterior probability of each pixel estimated via the Bayesian network is the unary potential term of the fully-connected CRF, and the difference images calculated by Equation (5) are the feature vectors of the appearance kernel [18]. Finally, the binary flood extent can be further classified to the following flood categories: non-obstructed-flood that is characterized by a decreased  $\sigma^{\circ}$  in co-event acquisition; obstructed-flooded non-coherent areas (e.g., flooded vegetation and vegetated built-up areas) that show an increased  $\sigma^{\circ}$  in the co-event acquisition and low pre-event  $\gamma$ ; obstructed-flooded coherent areas (e.g., flooded predominantly built-up areas) that present an increased/unchanged  $\sigma^{\circ}$  in co-event acquisition and high pre-event  $\gamma$ .

### 3. Data and Experiments

Two case studies were conducted with different SAR sensors to test our method. The first case is the Houston (US) flood accompanying Hurricane Harvey which took landfall on 25 August 2017 on Texas. Harvey moved on to Houston on August 26 and remained there for four days. The local National Weather Service office in Houston observed daily rainfall accumulations of 370 mm and 408 mm on August 26 and 27, respectively [36]. Multiple flash flood emergency alerts were issued in the Houston area by the night of August 26. The study area is located at the western part of Houston city with an extension of ca. 590 km<sup>2</sup>, which is mainly occupied by residential houses/apartments, commercial and industrial districts, parks, and reservoirs. Eleven Sentinel-1 (C band, 20 m resolution, five Sentinel-1A and six Sentinel-1B) VV polarized Interferometric Wide Swath (IW) mode Single Look Complex (SLC) data acquired between 1 July 2017 and 30 August 2017 (with 6 days repetition rate) were used. Intensity and coherence data details are shown in Tables 1 and 2, respectively, with the flood acquisition marked in blue color. Intensity images were preprocessed by radiometric calibration, speckle reduction with the Refined Lee speckle filter (window size of 7 × 7 pixels), and converted from linear to dB. Coherence images were obtained by sequential image pairs with a 28 × 7 (Range × Azimuth) window. Multi-looking with a 4 × 1 window was performed to all images to get a square pixel. All intensity and coherence images were stacked and geocoded with the 30 m Shuttle Radar Topography Mission (SRTM) digital elevation model (DEM) to WGS1984 UTM Zone 15 N with a square pixel size of 15 m. Each image was scaled to the range (0,255) before the subsequent processing.

The coherent (built-up) area filter was set as  $t = 0.5$  ( $0.5 * 255$  for the scaled coherence images) suggested by Watanabe et al. [52] and Lu et al. [53]. The number of Gaussian components in this case study was  $k = 100$ . The validation dataset was virtually digitized based on aerial photographs with a spatial resolution of 35 cm acquired on 30–31 August 2017 by the National Oceanic and Atmospheric Administration (NOAA) Remote Sensing Division [54].

**Table 1.** Sentinel-1 intensity data used for the Houston case study (flood acquisition is marked in blue color).

Acquisition Time	Polarization	Incidence Angle (°)	Resolution (m)	Orbit
01/07/17	VV	36.7	20	Descending
07/07/17	VV	36.7	20	Descending
13/07/17	VV	36.7	20	Descending
19/07/17	VV	36.7	20	Descending
25/07/17	VV	36.7	20	Descending
31/07/17	VV	36.7	20	Descending
06/08/17	VV	36.7	20	Descending
12/08/17	VV	36.7	20	Descending
18/08/17	VV	36.7	20	Descending
24/08/17	VV	36.7	20	Descending
30/08/17	VV	36.7	20	Descending

**Table 2.** Sentinel-1 coherence data used for the Houston case study (flood acquisition is marked in blue color).

Acquisition Time	$B_t$ (days)	$B_p$ (m)	Window Size (Range $\times$ Azimuth)
01/07 – 07/07	6	47	$28 \times 7$
07/07 – 13/07	6	31	$28 \times 7$
13/07 – 19/07	6	79	$28 \times 7$
19/07 – 25/07	6	45	$28 \times 7$
25/07 – 31/07	6	38	$28 \times 7$
31/07 – 06/08	6	38	$28 \times 7$
06/08 – 12/08	6	52	$28 \times 7$
12/08 – 18/08	6	58	$28 \times 7$
18/08 – 24/08	6	82	$28 \times 7$
24/08 – 30/08	6	55	$28 \times 7$

The second case study is the Joso (Japan) flood caused by the Kanto-Tohoku heavy rainfall on 9–11 September 2015 and the collapsed bank of Kinugawa River. The maximum rainfall accumulations exceeded 600 mm in the Kanto region and 500 mm in the Tohoku region, respectively. The water volume of the Kinugawa River increased rapidly in the city of Joso in the early morning of 10 September, and the floodwater quickly covered almost the entire area between Kinugawa River and Kokai River (Figure 5) at 12:50 pm local time [55]. The inundation area decreased from ca. 31 km<sup>2</sup> on 11 September to ca. 2 km<sup>2</sup> on 16 September [56]. The study area consists of the Joso city area and a wide rice paddy field located to the north of Joso city with an extension of ca. 114 km<sup>2</sup>. Seven ALOS-2/PALSAR-2 (L band, 3 m resolution) HH polarized Stripmap mode (SM1) SLC data were obtained for this study case. Intensity and coherence data details are shown in Tables 3 and 4, respectively, with the flood acquisition marked in blue color. The same preprocessing procedures as in the above case were performed concerning intensity and coherence except that the multi-looking step was omitted and coherence images were obtained with a  $7 \times 7$  (Range  $\times$  Azimuth) window. All images were geocoded with the 30 m SRTM DEM to WGS1984 UTM Zone 54N with a square pixel size of 2.5 m. The same experimental configuration of the Houston case was set: each data was scaled to the range (0,255) and  $t = 0.5$  was assigned. The number of Gaussian components in this case study was  $k = 40$ . It is worth noting that the acquired data span across several seasons. To mitigate the impacts from the phenological variation of rice paddy, the intensity mean values of the pre-event acquisitions were

only calculated by the acquisitions that dated in the same season of the co-event data. Therefore, only intensity data acquired on 29 August 2014 and 31 July 2015 were used for the average operation. Both 31 July 2015–11 September 2015 and 11 September 2015–23 October 2015 coherence pairs were co-event acquisitions and only the former was used. Besides, to mitigate the perturbation of  $B_p$ , coherence of 2 January 2015–13 February 2015 was not used in the experiment. The validation dataset was virtually digitized on the basis of aerial photographs with a spatial resolution of 20 cm acquired on 11 September 2015 by the Geospatial Information Authority of Japan (GSI) [57].

**Table 3.** ALOS-2/PALSAR-2 intensity data used for the Joso case study (flood acquisition is marked in blue color).

Acquisition Time	Polarization	Incidence Angle (°)	Resolution (m)	Orbit
29/08/14	HH	35.4	3	Ascending
02/01/15	HH	35.4	3	Ascending
13/02/15	HH	35.4	3	Ascending
31/07/15	HH	35.4	3	Ascending
11/09/15	HH	35.4	3	Ascending
23/10/15	HH	35.4	3	Ascending
29/01/16	HH	35.4	3	Ascending

**Table 4.** ALOS-2/PALSAR-2 coherence data used for the Joso case study (flood acquisition is marked in blue color).

Acquisition Time	$B_t$ (days)	$B_p$ (m)	Window Size (Range $\times$ Azimuth)
29/08 – 02/01	126	150	$7 \times 7$
02/01 – 13/02	42	47	$7 \times 7$
13/02 – 31/07	168	221	$7 \times 7$
31/07 – 11/09	42	123	$7 \times 7$
11/09 – 23/10	42	35	$7 \times 7$
23/10 – 29/01	98	205	$7 \times 7$

#### 4. Results and Discussion

The results of two case studies are both qualitatively and quantitatively analyzed. The synoptic view of multi-temporal SAR data in the form of RGB combinations is widely used in the qualitative interpretation of land cover and surface dynamics [58,59]. Different RGB combinations are adopted to give an intuition of flood extent in terms of intensity and coherence. For both cases, the results obtained from the fusion of intensity and coherence, and from intensity alone are quantitatively analyzed. The overall accuracy (OA), kappa coefficient ( $\kappa$ ), false-positive rate (FPR), precision (i.e., the correctly predicted positive patterns from the total predicted patterns in a positive class), recall (i.e., the fraction of positive patterns that are correctly classified), and F1 score (i.e., the harmonic mean between recall and precision) [60] are reported based on the flood reference derived from the aerial photographs mentioned in Section 3. In addition, the temporal variation of intensity and coherence as a result of flooding over different land cover types are also analyzed and discussed.

##### 4.1. Houston Flood Case

Figure 2a shows the intensity RGB composite (R = pre-event, G = B = co-event) of the Houston study area. The red color indicates non-obstructed-flood, such as flooded bare soils or wholly submersed short vegetations, without double-bounce occurring between the water surface and buildings/tree trunks. The cyan color depicts the flooded buildings or partially submersed vegetation where the enhanced double-bounce between the water surface and buildings/tree trunks incurs an increase in the co-event  $\sigma^\circ$ . The coherence RGB composite (R = pre-event, G = B = co-event) is shown in Figure 2b. The white color shows non-flooded built-up areas which are characterized by high  $\gamma$  in

both pre-event and co-event acquisitions. The appearance of floodwater between buildings results in a significant drop-off in co-event  $\gamma$  which are illustrated in the red color. However, the drop-off in  $\gamma$  could also be owing to random variation of vegetation (note the widely spread red color), thus the temporal non-coherent targets should be masked out when using  $\gamma$  in flood detection, as we discussed in Section 2. In Figure 2c, the RGB composite of intensity and coherence is adopted ( $R = \text{co-event } \sigma^\circ$ ,  $G = \text{pre-event } \gamma$ , and  $B = \text{co-event } \gamma$ ). The flooded built-up areas are discernible in yellow color (e.g., high co-event  $\sigma^\circ$ , high pre-event  $\gamma$ , and low co-event  $\gamma$ ). The green color could be related to flooded bare soils with sparse meadow which are characterized by low co-event  $\sigma^\circ$ , medium pre-event  $\gamma$ , and low co-event  $\gamma$ . Non-flooded built-up areas are shown in white color. Besides, the study area is quite vegetated, some small houses are encircled by trees, the mixed backscattering of the aforementioned objects could be presented in a single pixel of the medium resolution (e.g., 20 m) Sentinel-1 data, thus attenuating the double-bounce effect of buildings and reducing the values of both  $\sigma^\circ$  and  $\gamma$ . These areas can be found in brown color in Figure 2c.

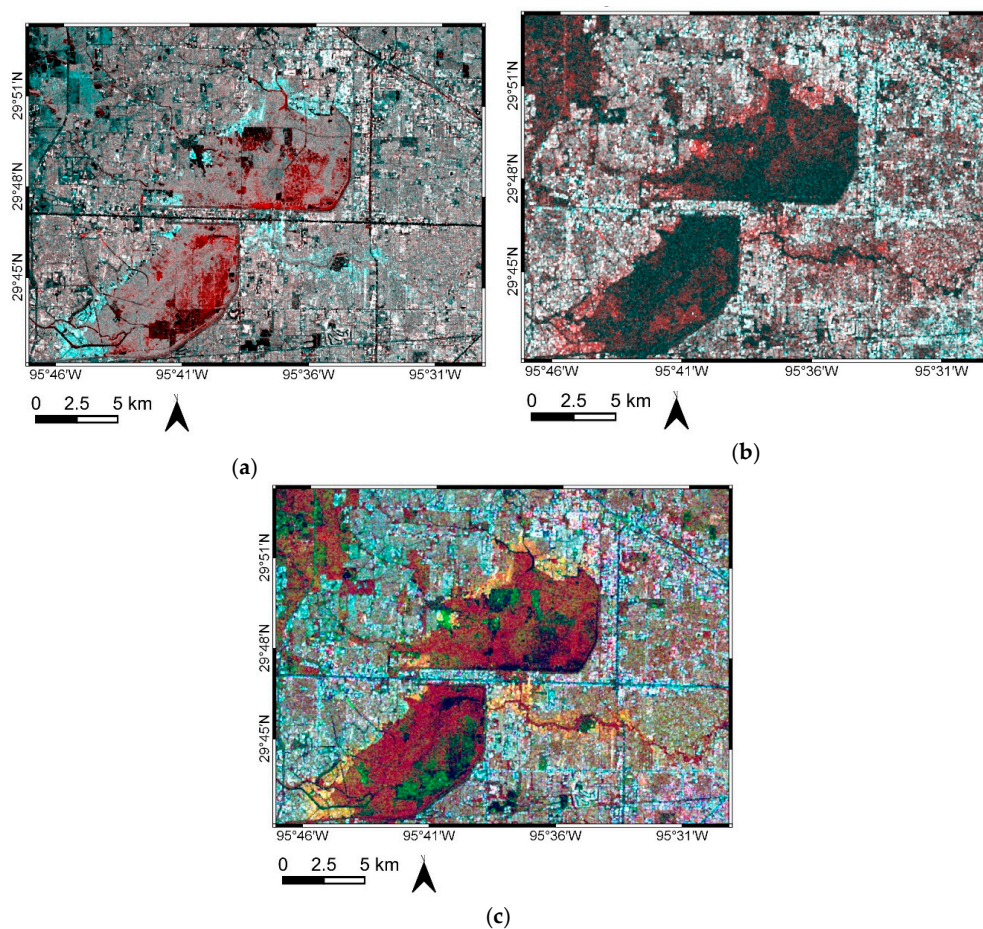


**Figure 2.** RGB color composites of the Houston case study: (a) Intensity RGB composite,  $R = \sigma^\circ$  of 24 August 2017,  $G = B = \sigma^\circ$  of 30 August 2017; (b) Coherence RGB composite,  $R = \gamma$  of 18–24 August 2017,  $G = B = \gamma$  of 24–30 August 2017; (c) Intensity and coherence RGB composite,  $R = \sigma^\circ$  of 30 August 2017,  $G = \gamma$  of 18–24 August 2017,  $B = \gamma$  of 24–30 August 2017.

The quantitative evaluations of the flood extent in the study area (Figure 2) produced by the fusion of  $\sigma^\circ$  and  $\gamma$  (Figure 3a) and  $\sigma^\circ$  alone (Figure 3c) are reported in Table 5. Although high values of OA (e.g., 94.5% vs. 93.7%) are achieved for both scenarios, OA is an inappropriate evaluation metric for this case due to the unbalanced extent of the classes (e.g., flood class occupies around 10% of the whole area). When  $\sigma^\circ$  and  $\gamma$  are synergistically used,  $\kappa$  is around 0.68 and F1 score is around 0.70. Comparing the extracted flood extent in Figure 3a with the reference flood mask in Figure 3d



it can be found that the spatial pattern of flooded areas is extracted accurately. The overestimation is very low (e.g., 0.02), however, a relatively large underestimation can be found, with 0.61 recall. The underestimated inundation areas are mainly flooded dense built-up areas with heavy vegetation. In these areas, pre-event coherence is expected to be low and the canopy attenuates the double-bounce scattering occurring between floodwater surfaces and building walls. Thus, it is difficult to detect either a significant increase in  $\sigma^\circ$  or decrease in  $\gamma$  between the pre- and co-event acquisitions. Figure 3b provides an insight of distributions of different flood categories: non-obstructed-flood; obstructed-flooded non-coherent areas such as vegetation and vegetated built-up areas; and obstructed-flooded coherent areas, predominantly built-up areas. When only  $\sigma^\circ$  data are used, lower  $\kappa$  (e.g., 0.60) and F1 score (e.g., 0.63) are achieved with slight differences in precision and FPR compared to the joint use of  $\sigma^\circ$  and  $\gamma$ . Figure 3c shows a larger underestimation especially in built-up areas compared to Figure 3a,b, corresponding to a lower recall value of 0.50. To gain an insight of the contributions from  $\sigma^\circ$  and  $\gamma$  in urban flood detection, Figure 3e,f show the flood posterior probability conditioned on  $\sigma^\circ$  and  $\gamma$ , respectively, providing a perception of distribution of the flood evidence that supported by  $\sigma^\circ$  and  $\gamma$ . It can be found that the detected non-obstructed-flood in Figure 3b is dominantly determined by  $\sigma^\circ$ . Flooded built-up areas are captured by both  $\sigma^\circ$  and  $\gamma$  but  $\gamma$  adds further comprehensive flood information.

**Table 5.** Quantitative evaluation of the Houston flood case (FPR: false-positive rate, OA: overall accuracy).

	Data	Precision	Recall	F1	FPR	OA (%)	$\kappa$
Houston city	Intensity + Coherence	0.83	0.61	0.70	0.02	94.5	0.68
	Intensity	0.85	0.50	0.63	0.01	93.7	0.60

To get a better understanding of the roles of  $\sigma^\circ$  and  $\gamma$  for flood detection in urban environments, we explore the temporal variation of spatial average values of  $\sigma^\circ$  and  $\gamma$  in 4 regions that represent different flooded land-cover types, as shown in Figure 4. R#1 is a homogenous short vegetation area that is (almost) wholly submerged in the flood event, the pre-event  $\gamma$  is low in this area (e.g., the maximum value is 0.27 and mean value is 0.18). Although the appearance of floodwater leads to a lower co-event  $\gamma$  (e.g., 0.12),  $\gamma$  is not reliable information for flood detection in this area because of the low values and large variation of the pre-event  $\gamma$ . The pre-event  $\sigma^\circ$  is around  $-8.5$  dB characterized by mixed surface and volume backscattering, however, the co-event  $\sigma^\circ$  decreases significantly to  $-13.7$  dB due to the specular reflection results from floodwater surface. Thus,  $\sigma^\circ$  provides useful information for flood detection in this area. R#2 is a predominantly built-up area. High pre-event  $\gamma$  (e.g., around 0.85) holds for this temporally stable area, the appearance of floodwater results in a significant drop-off in the co-event  $\gamma$  (e.g., 0.35). Besides, the co-event  $\sigma^\circ$  also increases substantially by the enhanced double-bounce effect, from around  $-5.5$  dB to  $-0.3$  dB. Therefore, both  $\sigma^\circ$  and  $\gamma$  are useful for flood detection in this area. R#3 consists of building blocks with trees. The pre-event  $\gamma$  of this area is around 0.36, which could be attributed to the existence of trees and anthropogenic activities in the streets around buildings. The co-event  $\gamma$  drops to 0.14, nevertheless, this drop-off is much less significant than that in R#2 and as this area is weakly coherent,  $\gamma$  is not helpful for flood detection in this area. The pre-event  $\sigma^\circ$ , however, increases from around  $-9.0$  dB to  $-4.8$  dB in co-event  $\sigma^\circ$ . The wide spaces between buildings and the relatively small  $\phi$  between building orientation and the SAR azimuth direction probably facilitate the enhancement of the double-bounce effect in the co-event acquisition. Thus,  $\sigma^\circ$  is more informative than  $\gamma$  for flood detection in this area. R#4 is an underestimated inundation area of dense buildings surrounded by trees. In this area, the pre-event  $\gamma$  drops from around 0.60 to 0.32 in the co-event  $\gamma$ , whereas the pre-event  $\sigma^\circ$  increases from around  $-7.0$  dB to  $-6.0$  dB in co-event  $\sigma^\circ$ . The variations in both  $\sigma^\circ$  and  $\gamma$  are less considerable than the successfully detected flooded built-up areas, e.g., a 0.28 drop-off of  $\gamma$  compared to a 0.5 drop-off in R#2, a 1 dB increase of  $\sigma^\circ$  compared to a 5.2 dB increase in R#2 and a 4.2 dB increase in R#3. Since the buildings, trees and streets are densely distributed,  $\gamma$  is estimated with the mixed structures especially

in medium resolution data such as Sentinel-1, thus attenuating the drop-off in the co-event  $\gamma$ . On the other hand, the double-bounce backscattering between floodwater surface and buildings could be obstructed by trees, and the floodwater could also be masked by shadow. Therefore, flood detection in this scenario is challenging especially for medium resolution data (e.g., 10 to 30 m).

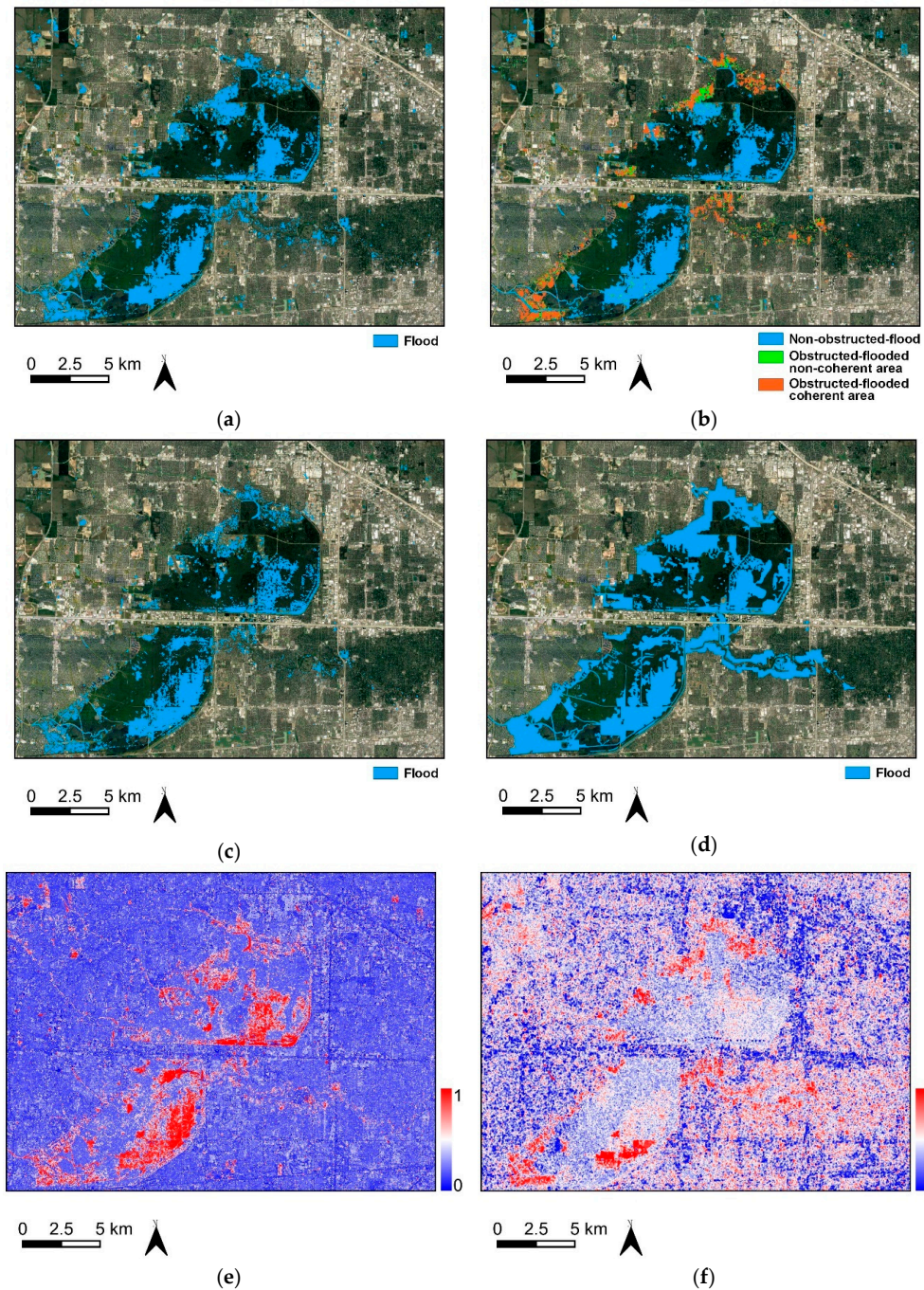


**Figure 3.** Flood extent maps of the Houston study area: (a) Binary flood extent based on the fusion of  $\sigma^0$  and  $\gamma$ ; (b) Flood category map of (a); (c) Binary flood extent based on  $\sigma^0$  alone; (d) Reference flood mask derived from high-resolution aerial photographs provided by the National Oceanic and Atmospheric Administration (NOAA); (e) Flood posterior probability conditioned on  $\sigma^0$ ; (f) Flood posterior probability conditioned on  $\gamma$ .



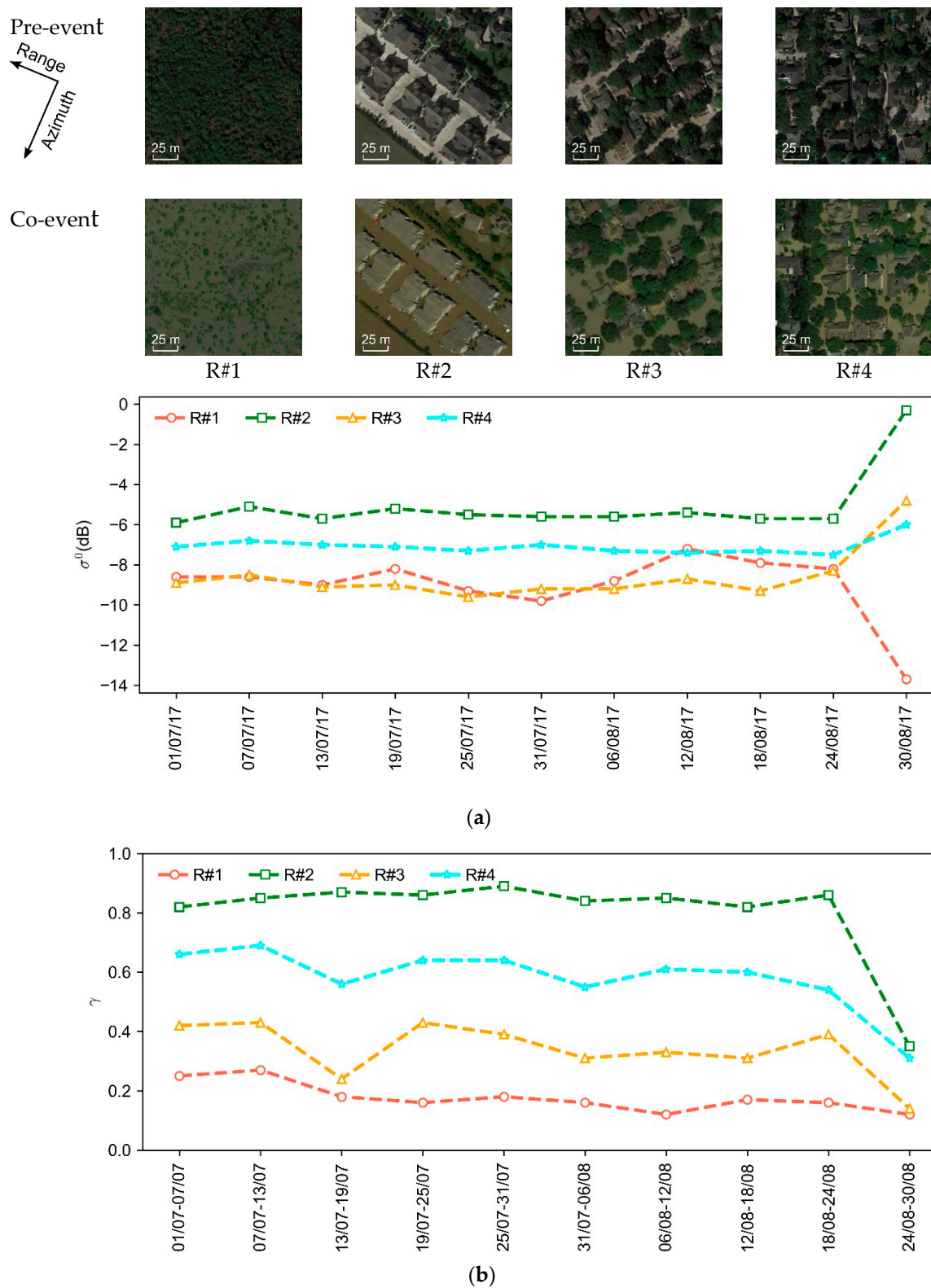


**Figure 4.** Sentinel-1  $\sigma^0$  and  $\gamma$  temporal variation for several typical landscapes within the Houston study area: (a)  $\sigma^0$  temporal trends; (b)  $\gamma$  temporal trends.

#### 4.2. Joso Flood Case

The intensity RGB composite (R = pre-event, G = B = co-event) of the Joso study area is shown in Figure 5a. The red color indicates flooded rice paddy, whereas cyan color hints potential flooded built-up

areas and partially submersed vegetation, also including broadly spread vegetation that presents higher co-event  $\sigma^\circ$  than the pre-event one probably due to potential phenological variation. The white color displays built-up areas and some paddy fields on which occur strong double-bounce effects in both acquisitions. Figure 5b visualizes the coherence RGB composite ( $R = \text{pre-event}$ ,  $G = B = \text{co-event}$ ). The red color illustrates flooded built-up areas, some rural roads, and fields which are characterized by a high value of  $\gamma$  in L band pre-event data. The colorful appearance of RGB composite of intensity and coherence ( $R = \text{co-event } \sigma^\circ$ ,  $G = \text{pre-event } \gamma$ , and  $B = \text{co-event } \gamma$ ) in Figure 5c holds a wealth of information on the flood situation in different land-cover classes. The white color shows non-flooded built-up areas whereas flooded built-up areas are shown in yellow color. The green color illustrates the flooded coherent rural roads and fields that have low co-event  $\sigma^\circ$ , high co-event  $\sigma^\circ$ , and low co-event  $\gamma$ . The black color reveals flooded rice paddy fields and permanent water such as the course of the rivers through the northern and southern part of the study area. Vegetation is depicted in red color which is largely distributed along the rivers. The purple color locates some non-flooded paddy fields that have high co-event  $\gamma$  and low pre-event  $\gamma$  probably due to the larger temporal baseline of pre-event  $\gamma$  (e.g., 168 days across seasons) compared to the co-event  $\gamma$  (e.g., 42 days in the same season).

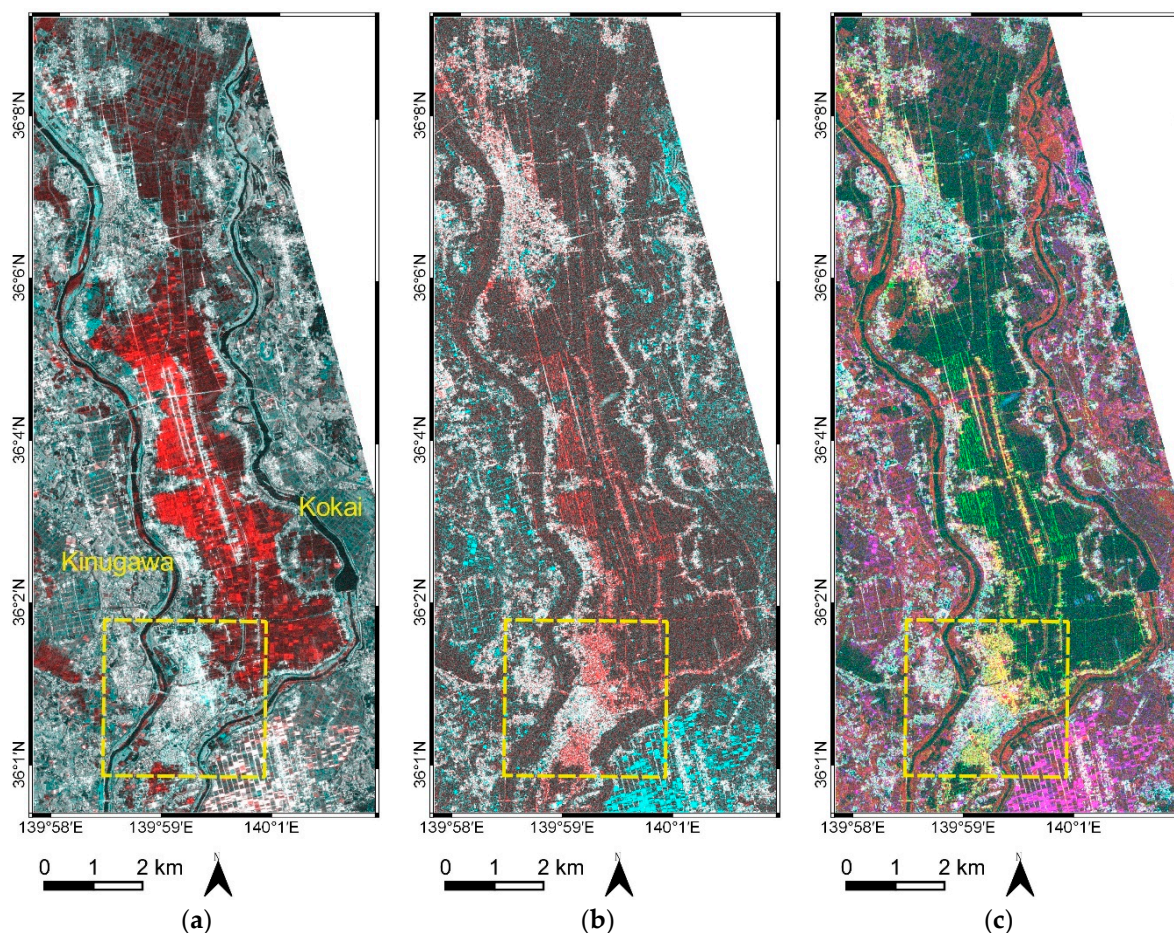


**Figure 5.** RGB color composites of the Joso case study: (a) Intensity RGB composite,  $R = \sigma^\circ$  of 31 July 2015,  $G = B = \sigma^\circ$  of 11 September 2015; (b) Coherence RGB composite,  $R = \gamma$  of 13 February–31 July 2015,  $G = B = \gamma$  of 31 July–11 September 2015; (c) Intensity and coherence RGB composite,  $R = \sigma^\circ$  of 11 September 2015,  $G = \gamma$  of 13 February–31 July 2015,  $B = \gamma$  of 31 July–11 September 2015.

As the study area contains both urban and rural areas and we intend to mainly focus on flood detection in urban areas in this paper. We report the quantitative evaluations for both the whole study area (Figure 5) and the urban area of Joso city which is located in the yellow dashed rectangle in Figure 6a. Table 6 lists the evaluations of results produced by the fusion of  $\sigma^\circ$  and  $\gamma$  (Figure 6a,g) and



$\sigma^\circ$  alone (Figure 6c,i). When combining  $\sigma^\circ$  and  $\gamma$ , the result for the urban area is slightly worse than for the whole area in terms of OA (e.g., 84.3% vs. 89.6%) and  $\kappa$  (e.g., 0.66 vs. 0.72). This degradation is mainly due to a larger underestimation in urban areas, e.g., 0.66 of recall compared to 0.70 in the whole area. This difference is enlarged when only  $\sigma^\circ$  data are used (e.g., 74.0% vs. 86.0% for OA and 0.42 vs. 0.61 for  $\kappa$ ). The occurrence of specular surfaces, such as parking lots and shadowing caused by buildings/trees, can degrade the performance in urban areas. According to the mapping result shown in Figure 6a,b, the underestimation primarily appears in parking lots, densely distributed built-up areas and bare fields that show a similar  $\sigma^\circ$  in dry and flooded situations in the rural area. A subtle overestimation is found in both validation areas (e.g., 0.03 in both areas). Figure 6b,h show the distribution of different flood categories and indicate that the obstructed-flooded non-coherent areas are largely distributed accompanying the obstructed-flooded coherent areas. This is rational as the presence of vegetation and anthropogenic activities reduce the coherence of built-up areas. The overall performance degrades when  $\sigma^\circ$  is used by itself. A large area falsely detected as flooded can be seen in Figure 6c (close to the right bottom corner of the yellow rectangle) due to the variation of  $\sigma^\circ$  in rice paddy field, and a severe underestimation can be found in the Joso city area (Figure 6i) with a low recall value of 0.45. Figure 6e,f illustrate flood posterior probability conditioned on  $\sigma^\circ$  and  $\gamma$ , respectively. It can be found that  $\sigma^\circ$  provides very strong evidence in flooded rice paddy areas but a weaker one in flooded built-up areas. However,  $\gamma$  complements the flood information of built-up areas and other coherent areas such as rural roads.

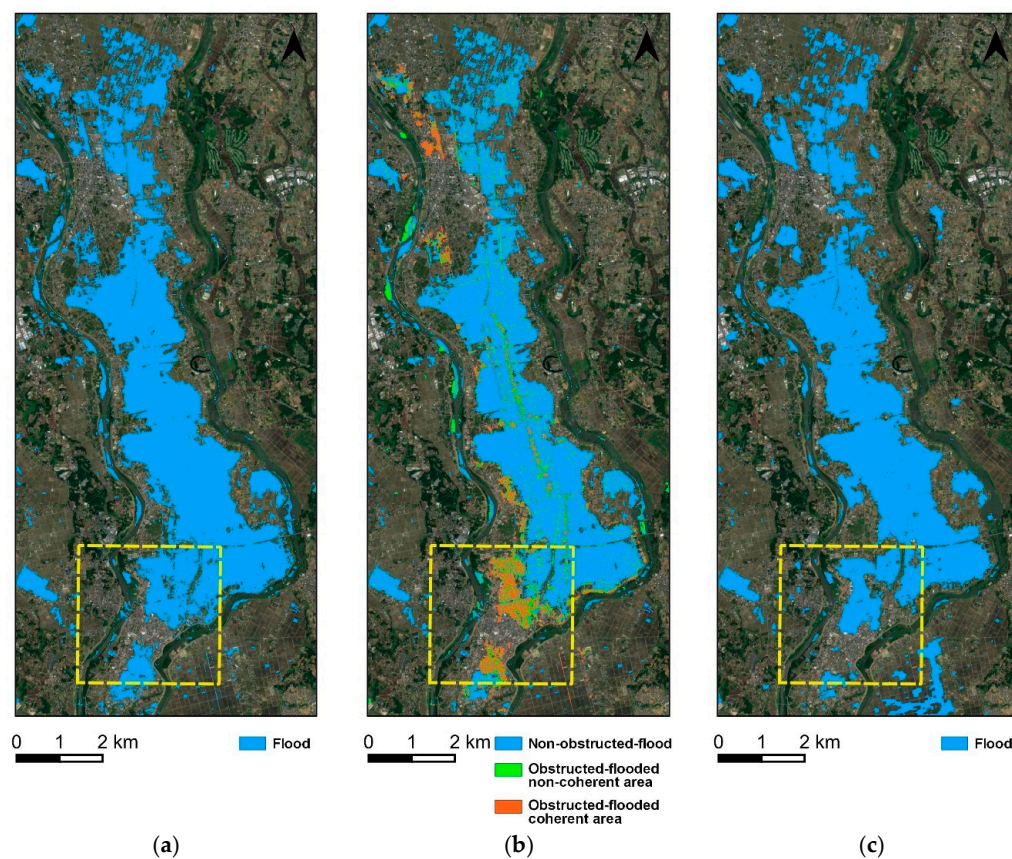
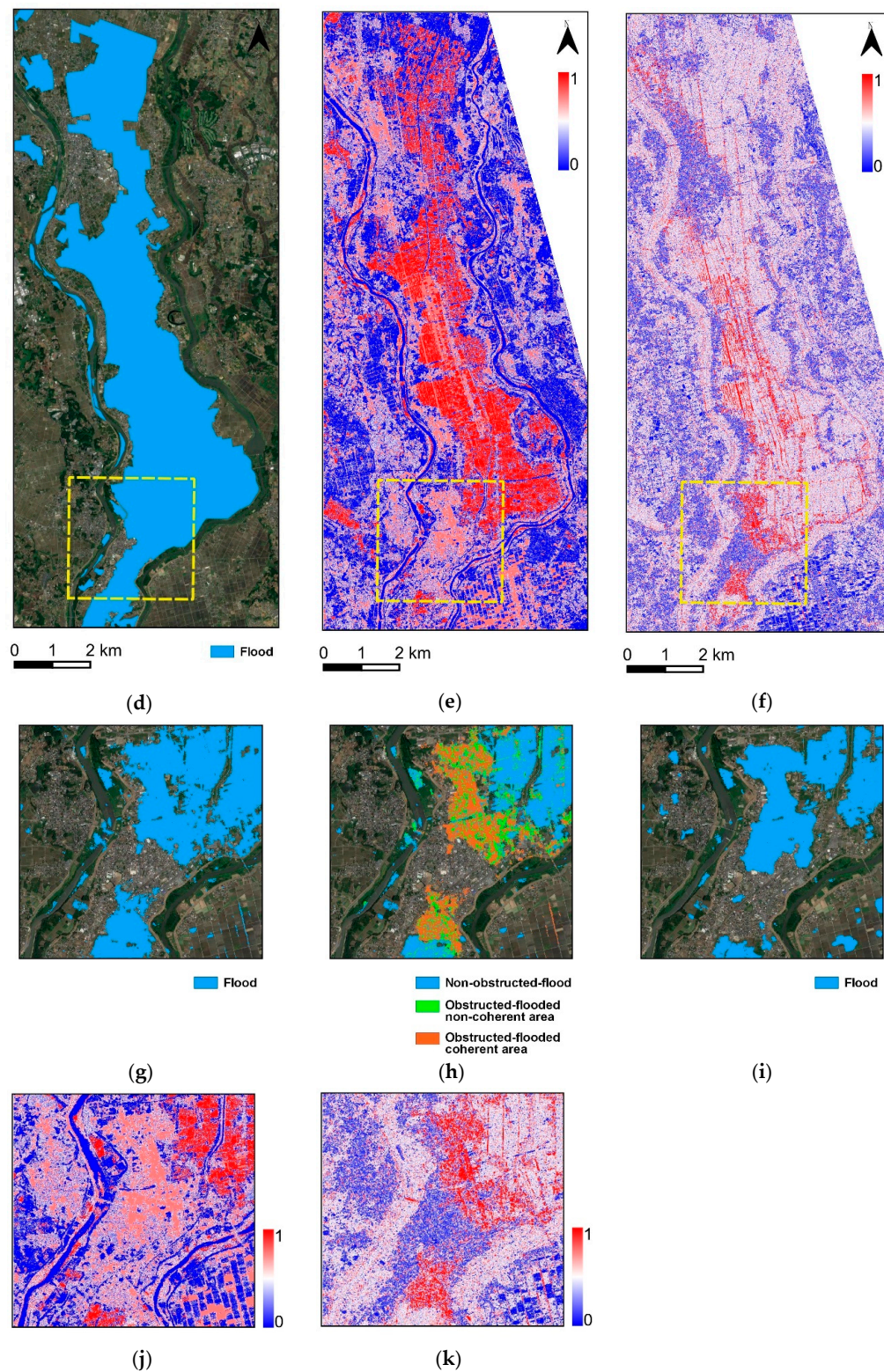


Figure 6. Cont.



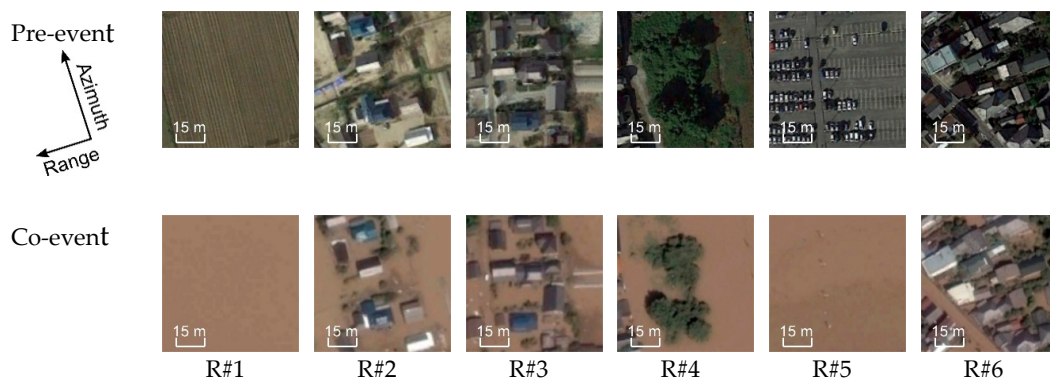
**Figure 6.** Flood extent maps of the Joso study area: (a) Binary flood extent based on the fusion of  $\sigma^\circ$  and  $\gamma$ ; (b) Flood category map of (a); (c) Binary flood extent based on  $\sigma^\circ$  alone; (d) Reference flood mask derived from high-resolution aerial photograph provided by the Geospatial Information Authority of Japan (GSI); (e) Flood posterior probability conditioned on  $\sigma^\circ$ ; (f) Flood posterior probability conditioned on  $\gamma$ ; (g) Zoom-in of the yellow box in (a); (h) Zoom-in of the yellow box in (b); (i) Zoom-in of the yellow box in (c); (j) Zoom-in of the yellow box in (e); (k) Zoom-in of the yellow box in (f).



**Table 6.** Quantitative evaluation of the Joso flood case (FPR: false-positive rate, OA: overall accuracy).

	Data	Precision	Recall	F1	FPR	OA (%)	$\kappa$
Whole study area	Intensity + Coherence	0.91	0.70	0.79	0.03	89.6	0.72
	Intensity	0.85	0.59	0.70	0.04	86.0	0.61
Joso city	Intensity + Coherence	0.94	0.66	0.78	0.03	84.3	0.66
	Intensity	0.85	0.45	0.59	0.06	74.0	0.42

Figure 7 shows the temporal variation of the spatial average values of  $\sigma^\circ$  and  $\gamma$  over 6 different regions. R#1 is a completely flooded homogeneous rice paddy field. Flooding causes a significant decrease of  $\sigma^\circ$  in this area, ranging from around  $-2.5$  dB of pre-event  $\sigma^\circ$  (only considering acquisitions on 29 August 2014 and 31 July 2015) to  $-16$  dB of co-event  $\sigma^\circ$ , whereas the change of  $\gamma$  (e.g., 0.03) between pre- and co-event data is hardly detectable. R#2 and R#3 are flooded built-up areas observed with different  $\phi$  angles. R#2 has a smaller  $\phi$  than R#3. It can be found that the increase of co-event  $\sigma^\circ$  caused by double-bounce in R#2 is larger than R#3 (e.g., around 3.6 dB against 1.6 dB). However, the drop-off in co-event  $\gamma$  has less difference between R#2 and R#3 (e.g., 0.30 against 0.31). It indicates that  $\gamma$  as a complement to  $\sigma^\circ$  can help identify floodwater in built-up areas where might fail to detect by  $\sigma^\circ$  alone. Besides, the effect of  $\phi$  can be mitigated by combing the descending and ascending acquisitions that observe the same area from different viewing angles and increase the chance of floodwater detection. R#4 consists of flooded trees. It shows a strong double-bounce effect between floodwater and tree trunks thanks to the high penetration capability of L-band. The backscattering  $\sigma^\circ$  increases from around  $-8.0$  dB to  $-5.3$  dB when inundation appears. Without surprise, the variation between pre- and co-event  $\gamma$  (e.g., 0.04) is as subtle as for R#1. The regions of R#5 and R#6 are corresponding to underestimated flooded parking lots and dense building blocks, respectively. For R#5,  $\gamma$  changes from around 0.31 in pre-event to 0.23 in co-event data. Due to busy anthropogenic activities, the low pre-event  $\gamma$  attenuates the  $\gamma$  variation caused by flooding over time and thus hampers flood detection based on  $\gamma$ . On the other hand, both pre- and co-event  $\sigma^\circ$  are very low (e.g.,  $-14.8$  dB against  $-14.6$  dB), as the backscattering from parking lots in dry conditions is also specular. Therefore, flood detection in parking lots could be challenging for both  $\sigma^\circ$  and  $\gamma$ . In the dense built-up area of R#6, radar shadows hamper flood detection in the front of buildings and the evidence of flood from  $\sigma^\circ$  is unnoticed. As the scatters are probably dominated by the roofs, the co-event  $\gamma$  is as high as the pre-event  $\gamma$  (e.g., above 0.6). Apart from the reasons of underestimation we discussed for R#5 and R#6, the underestimation in Joso city is also probably due to a floodwater recession at the time of SAR acquisition, since the inundation extent varies rapidly in time according to the inundation maps provided by GSI [56] and a large inundation area in Joso city disappeared on 12 September 2015. A large white area between the red areas in Joso city can be found in Figure 5b, which indicates that there is no significant coherence decorrelation occurring in this area.

**Figure 7.** Cont.

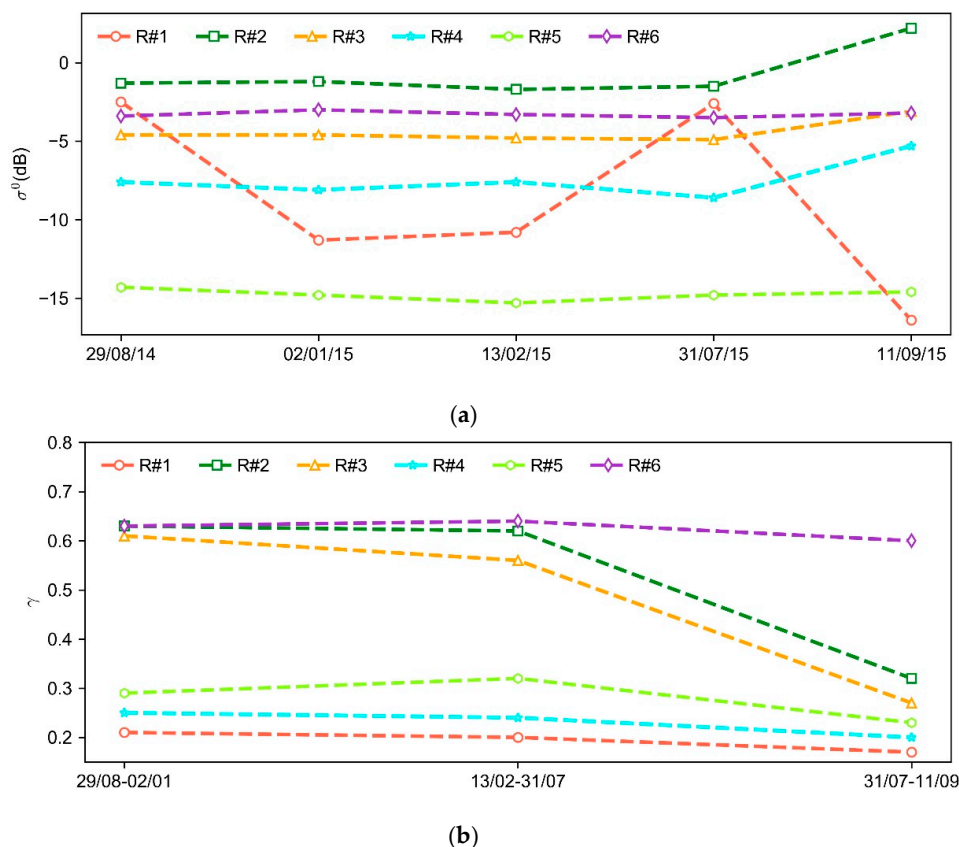


**Figure 7.** ALOS-2/PALSAR-2  $\sigma^0$  and  $\gamma$  temporal variation for several typical landscapes within the Joso study area: (a)  $\sigma^0$  temporal trends; (b)  $\gamma$  temporal trends.

#### 4.3. Limitations and Future Directions

The main limitations of the proposed method lie in data availability and scalability. Although the method is flexible to data availability that both (long) time series or bi-temporal data can be used, a longer time series produces more unbiased coherent-area estimation and subsequently achieves a better CPT. For satellite missions with irregular observation scenarios such as ALOS-2/PALSAR-2 and TerraSAR-X, it can be hard to achieve a long time series of images with consistent acquisition parameters. Nevertheless, this does not mean that the method will fail to succeed with fewer multi-temporal data, as shown in the Joso case of this study. Promising results are achieved with less than 5 coherence sequence. This could benefit from the high spatial resolution of ALOS-2/PALSAR-2 data (e.g., 3 m) so that the coherence of built-up areas can be estimated with more pure pixels thus showing low temporal variation. For data with a lower spatial resolution such as Sentinel-1 data (e.g., 20 m), a longer data sequence is preferable. Data acquisition is going to be a less crucial problem with the evolution of SAR missions. Satellite constellations such as the Sentinel-1 mission and the recently launched RADARSAT Constellation Mission (RCM) [61] with high temporal resolution can provide a long and dense observation sequence of an area of interest, and the upcoming missions such Tandem-L [62] and NASA-ISRO SAR (NISAR) [63] will increase the observation frequency of spaceborne SAR systems at the global scale. The computation bottleneck of the method is the GMM with the EM algorithm. The best-case run time for the EM algorithm is  $(KNd)$  at each iteration, where  $K$  is the cluster number,  $N$  is the data point number and  $d$  is the data dimension. Therefore, it is challenging to scale for a massive dataset with high-dimension. One possible way to deal with the scalability problem is to leverage the advanced data summarization techniques such as the coresets-based GMM [64,65], which guarantees that models fitting the  $M(M \ll N)$  coresets (weighted subsets of the original data) will also provide a good fit for the original dataset. Besides, the quality of SAR image segmentation also affects the calculation of CPT. Compared to the standard GMM used for segmentation in this paper,

the spatial constraint GMM [66] which imposes the contextual information in the mixing coefficient can achieve a better segmentation quality.

## 5. Conclusions

In this paper, we introduced a method for flood mapping in urban environments based on SAR intensity and interferometric coherence under the Bayesian network fusion framework. It integrates intensity and coherence information from a viewpoint of probability and takes into account the flood uncertainty in terms of intensity and coherence. The combination of intensity and coherence extracts flood information in varying land cover types and outputs both flood binary extent and flood category maps: including non-obstructed-flood (e.g., flooded bare soils and short vegetation); obstructed-flooded non-coherent area (e.g., flooded vegetation and vegetated built-up areas); and obstructed-flooded coherent area (e.g., flooded predominantly built-up areas). The approach is unsupervised and only based on SAR data, therefore favorable for operational emergency response with data from SAR missions with a short revisit time and systematic observation scenario such as Sentinel-1.

This method was tested on two flood events that were captured by different SAR sensors: the Houston (US) 2017 flood event with Sentinel-1 (C band, 20 m resolution) time series, and the Joso (Japan) 2015 flood event with ALOS-2/PALSAR-2 (L band, 3 m resolution) time series. The flood maps were validated by the reference flood masks derived from high-resolution aerial photographs and showed satisfying results in both case studies. The findings in the experiments demonstrate that the synergistic use of SAR intensity and coherence provides more reliable flood information in urban areas with varying landscapes than using intensity alone. Specifically, flood detection in less-coherent/non-coherent areas (e.g., bare soils, vegetation, vegetated built-up areas) relies on multi-temporal intensity, whereas multi-temporal coherence gives more comprehensive flood information in coherent areas (e.g., predominantly built-up areas). Nevertheless, some special flood situations such as flooded parking lots and flooded dense building blocks are still challenging for both intensity and coherence.

As the proposed method is sensor and scene independent, it provides opportunities for urban flood mapping at a global scale and especially in low-income countries with the highly frequent and systematic observations from SAR missions such as Sentinel-1 and the RADARSAT Constellation Mission (RCM). The upcoming missions such as Tandem-L and NISAR increase the observation frequency of spaceborne SAR systems and the possibility of flood detection in vegetated areas. Besides, the proposed method provides a supplement to the current Sentinel-1 Flood Service at the German Aerospace Center (DLR) to account for flooding in urban areas.

**Author Contributions:** Y.L. designed and performed the experiments; S.M. collected the ALOS-2/PALSAR-2 data; M.W. contributed to the critical review of the methodology; S.M., S.S., and R.N. contributed to the interpretation of the results; Y.L. wrote the original paper, S.M., M.W., S.S., and R.N. contributed to review and editing.

**Funding:** This work is funded by the China Scholarship Council (CSC). R.N. receives a grant of Overseas Research Fellowships from Japan Society for the Promotion of Science (JSPS).

**Acknowledgments:** The authors would like to thank the National Oceanic and Atmospheric Administration (NOAA) and the Geospatial Information Authority of Japan (GSI) for providing high-resolution aerial photographs. ALOS-2/PALSAR-2 data were kindly provided by the Japan Aerospace Exploration Agency (JAXA, proposal number MTH1153, PI number 3043).

**Conflicts of Interest:** The authors declare no conflict of interest.

## References

1. IDMC. *Global Report on Internal Displacement*. 2016. Available online: <http://www.internal-displacement.org/globalreport2016/pdf/2016-global-report-internal-displacement-IDMC.pdf> (accessed on 16 September 2019).
2. Willner, S.N.; Levermann, A.; Zhao, F.; Frieler, K. Adaptation required to preserve future high-end river flood risk at present levels. *Sci. Adv.* **2018**, *4*, eaao1914. [[CrossRef](#)] [[PubMed](#)]

3. Willner, S.N.; Otto, C.; Levermann, A. Global economic response to river floods. *Nat. Clim. Chang.* **2018**, *8*, 594–598.
4. Covello, F.; Battazza, F.; Coletta, A.; Lopinto, E.; Fiorentino, C.; Pietranera, L.; Valentini, G.; Zoffoli, S. COSMO-SkyMed an existing opportunity for observing the Earth. *J. Geodyn.* **2010**, *49*, 171–180.
5. Werninghaus, R.; Buckreuss, S. The TerraSAR-X Mission and System Design. *IEEE Trans. Geosci. Remote Sens.* **2009**, *48*, 606–641. [[CrossRef](#)]
6. Torres, R.; Snoeij, P.; Geudtner, D.; Bibby, D.; Davidson, M.; Attema, E.; Potin, P.; Rommen, B.Ö.; Floury, N.; Brown, M.; et al. GMES Sentinel-1 mission. *Remote Sens. Environ.* **2012**, *120*, 9–24. [[CrossRef](#)]
7. Morena, L.C.; James, K.V.; Beck, J. An introduction to the RADARSAT-2 mission. *Can. J. Remote Sens.* **2004**, *30*, 221–234. [[CrossRef](#)]
8. Kankaku, Y.; Suzuki, S.; Osawa, Y. ALOS-2 mission and development status. In Proceedings of the 2013 IEEE International Geoscience and Remote Sensing Symposium—IGARSS, Melbourne, Australia, 21–26 July 2013; pp. 2396–2399.
9. Matgen, P.; Hostache, R.; Schumann, G.; Pfister, L.; Hoffmann, L.; Savenije, H.H.G. Towards an automated SAR-based flood monitoring system: Lessons learned from two case studies. *Phys. Chem. Earth Parts A/B/C* **2011**, *36*, 241–252. [[CrossRef](#)]
10. Martinis, S.; Twele, A.; Voigt, S. Towards operational near real-time flood detection using a split-based automatic thresholding procedure on high resolution TerraSAR-X data. *Nat. Hazards Earth Syst. Sci.* **2009**, *9*, 303–314.
11. Shen, X.; Wang, D.; Mao, K.; Anagnostou, E.; Hong, Y. Inundation Extent Mapping by Synthetic Aperture Radar: A Review. *Remote Sens.* **2019**, *11*, 879. [[CrossRef](#)]
12. Pulvirenti, L.; Chini, M.; Pierdicca, N.; Guerriero, L.; Ferrazzoli, P. Flood monitoring using multi-temporal COSMO-SkyMed data: Image segmentation and signature interpretation. *Remote Sens. Environ.* **2011**, *115*, 990–1002.
13. Martinis, S.; Twele, A.; Voigt, S. Unsupervised Extraction of Flood-Induced Backscatter Changes in SAR Data Using Markov Image Modeling on Irregular Graphs. *IEEE Trans. Geosci. Remote Sens.* **2011**, *49*, 251–263. [[CrossRef](#)]
14. Insom, P.; Cao, C.; Boonsrimuang, P.; Liu, D.; Saokarn, A.; Yomwan, P.; Xu, Y. A Support Vector Machine-Based Particle Filter Method for Improved Flooding Classification. *IEEE Geosci. Remote Sens. Lett.* **2015**, *12*, 1943–1947. [[CrossRef](#)]
15. Twele, A.; Cao, W.; Plank, S.; Martinis, S. Sentinel-1-based flood mapping: A fully automated processing chain. *Int. J. Remote Sens.* **2016**, *37*, 2990–3004. [[CrossRef](#)]
16. Chini, M.; Hostache, R.; Giustarini, L.; Matgen, P. A Hierarchical Split-Based Approach for Parametric Thresholding of SAR Images: Flood Inundation as a Test Case. *IEEE Trans. Geosci. Remote Sens.* **2017**, *55*, 6975–6988.
17. Cao, W.; Twele, A.; Plank, S.; Martinis, S. A three-class change detection methodology for SAR-data based on hypothesis testing and Markov Random field modelling. *Int. J. Remote Sens.* **2018**, *39*, 488–504.
18. Li, Y.; Martinis, S.; Plank, S.; Ludwig, R. An automatic change detection approach for rapid flood mapping in Sentinel-1 SAR data. *Int. J. Appl. Earth Obs. Geoinf.* **2018**, *73*, 123–135. [[CrossRef](#)]
19. Tong, X.; Luo, X.; Liu, S.; Xie, H.; Chao, W.; Liu, S.; Liu, S.; Makhinov, A.N.; Makhinova, A.F.; Jiang, Y. An approach for flood monitoring by the combined use of Landsat 8 optical imagery and COSMO-SkyMed radar imagery. *ISPRS J. Photogramm. Remote Sens.* **2018**, *136*, 144–153.
20. Schumann, G.J.; Moller, D.K. Microwave remote sensing of flood inundation. *Phys. Chem. Earth* **2015**, *83–84*, 84–95. [[CrossRef](#)]
21. Dong, Y.; Forster, B.; Ticehurst, C. Radar backscatter analysis for urban environments. *Int. J. Remote Sens.* **1997**, *18*, 1351–1364.
22. Franceschetti, G.; Iodice, A.; Riccio, D. A canonical problem in electromagnetic backscattering from buildings. *IEEE Trans. Geosci. Remote Sens.* **2002**, *40*, 1787–1801. [[CrossRef](#)]
23. Thiele, A.; Cadario, E.; Karsten, S.; Thönnessen, U.; Soergel, U. Building Recognition From Multi-Aspect High-Resolution InSAR Data in Urban Areas. *IEEE Trans. Geosci. Remote Sens.* **2007**, *45*, 3583–3593. [[CrossRef](#)]
24. Wegner, J.D.; Hansch, R.; Thiele, A.; Soergel, U. Building Detection From One Orthophoto and High-Resolution InSAR Data Using Conditional Random Fields. *IEEE J. Sel. Top. Appl. Earth Obs. Remote Sens.* **2011**, *4*, 83–91. [[CrossRef](#)]



25. Ferro, A.; Brunner, D.; Bruzzone, L.; Lemoine, G. On the relationship between double bounce and the orientation of buildings in VHR SAR images. *IEEE Geosci. Remote Sens. Lett.* **2011**, *8*, 612–616.
26. Mason, D.C.; Speck, R.; Devereux, B.; Schumann, G.J.-P.; Neal, J.C.; Bates, P.D. Flood Detection in Urban Areas Using TerraSAR-X. *IEEE Trans. Geosci. Remote Sens.* **2010**, *48*, 882–894.
27. Mason, D.C.; Davenport, I.J.; Neal, J.C.; Schumann, G.J.-P.; Bates, P.D. Near Real-Time Flood Detection in Urban and Rural Areas Using High-Resolution Synthetic Aperture Radar Images. *IEEE Trans. Geosci. Remote Sens.* **2012**, *50*, 3041–3052. [[CrossRef](#)]
28. Giustarini, L.; Hostache, R.; Matgen, P.; Schumann, G.J.; Bates, P.D.; Mason, D.C. A Change Detection Approach to Flood Mapping in Urban Areas Using TerraSAR-X. *IEEE Trans. Geosci. Remote Sens.* **2013**, *51*, 2417–2430. [[CrossRef](#)]
29. Mason, D.C.; Giustarini, L.; Garcia-Pintado, J.; Cloke, H.L. Detection of flooded urban areas in high resolution Synthetic Aperture Radar images using double scattering. *Int. J. Appl. Earth Obs. Geoinf.* **2014**, *28*, 150–159.
30. Tanguy, M.; Chokmani, K.; Bernier, M.; Poulin, J.; Raymond, S. River flood mapping in urban areas combining Radarsat-2 data and flood return period data. *Remote Sens. Environ.* **2017**, *198*, 442–459. [[CrossRef](#)]
31. Pulvirenti, L.; Chini, M.; Pierdicca, N.; Boni, G. Use of SAR data for detecting floodwater in urban and agricultural areas: The role of the interferometric coherence. *IEEE Trans. Geosci. Remote Sens.* **2016**, *54*, 1532–1544.
32. Iervolino, P.; Guida, R.; Iodice, A.; Riccio, D. Flooding water depth estimation with high-resolution SAR. *IEEE Trans. Geosci. Remote Sens.* **2015**, *53*, 2295–2307.
33. Chini, M.; Pulvirenti, L.; Pierdicca, N. Analysis and interpretation of the COSMO-SkyMed observations of the 2011 Japan tsunami. *IEEE Geosci. Remote Sens. Lett.* **2012**, *9*, 467–471. [[CrossRef](#)]
34. Zebker, H.A.; Member, S.; Villasenor, J. Decorrelation in Interferometric Radar Echoes. *IEEE Trans. Geosci. Remote Sens.* **1992**, *30*, 950–959. [[CrossRef](#)]
35. Li, Y.; Martinis, S.; Wieland, M. Urban flood mapping with an active self-learning convolutional neural network based on TerraSAR-X intensity and interferometric coherence. *ISPRS J. Photogramm. Remote Sens.* **2019**, *152*, 178–191. [[CrossRef](#)]
36. Chini, M.; Pelich, R.; Pulvirenti, L.; Pierdicca, N.; Hostache, R.; Matgen, P. Sentinel-1 InSAR Coherence to Detect Floodwater in Urban Areas: Houston and Hurricane Harvey as A Test Case. *Remote Sens.* **2019**, *11*, 107. [[CrossRef](#)]
37. Marcot, B.G.; Penman, T.D. Advances in Bayesian network modelling: Integration of modelling technologies. *Environ. Model. Softw.* **2019**, *111*, 386–393.
38. Cheon, S.P.; Kim, S.; Lee, S.Y.; Lee, C.B. Bayesian networks based rare event prediction with sensor data. *Knowl. Based Syst.* **2009**, *22*, 336–343.
39. Landuyt, D.; Broekx, S.; D’hondt, R.; Engelen, G.; Aertsens, J.; Goethals, P.L.M. A review of Bayesian belief networks in ecosystem service modelling. *Environ. Model. Softw.* **2013**, *46*, 1–11. [[CrossRef](#)]
40. Chen, J.; Ping-An, Z.; An, R.; Zhu, F.; Xu, B. Risk analysis for real-time flood control operation of a multi-reservoir system using a dynamic Bayesian network. *Environ. Model. Softw.* **2019**, *111*, 409–420. [[CrossRef](#)]
41. Li, M.; Stein, A.; Bijker, W.; Zhan, Q. Urban land use extraction from Very High Resolution remote sensing imagery using a Bayesian network. *ISPRS J. Photogramm. Remote Sens.* **2016**, *122*, 192–205. [[CrossRef](#)]
42. Tao, J.; Wu, W.; Xu, M. Using the Bayesian Network to Map Large-Scale Cropping Intensity by Fusing Multi-Source Data. *Remote Sens.* **2019**, *11*, 168.
43. D’Addabbo, A.; Refice, A.; Pasquariello, G.; Lovergine, F.P.; Capolongo, D.; Manfreda, S. A Bayesian Network for Flood Detection Combining SAR Imagery and Ancillary Data. *IEEE Trans. Geosci. Remote Sens.* **2016**, *54*, 3612–3625.
44. D’Addabbo, A.; Refice, A.; Lovergine, F.P.; Pasquariello, G. DAFNE: A Matlab toolbox for Bayesian multi-source remote sensing and ancillary data fusion, with application to flood mapping. *Comput. Geosci.* **2018**, *112*, 64–75.
45. Krähenbühl, P.; Koltun, V. Efficient Inference in Fully Connected CRFs with Gaussian Edge Potentials. In Proceedings of the Advances in Neural Information Processing Systems 24 (NIPS 2011), Granada, Spain, 12–14 December 2011; pp. 109–117.
46. Bishop, C.M. *Pattern Recognition and Machine Learning*; Springer: New York, NY, USA, 2006.
47. Barber, D. *Bayesian Reasoning and Machine Learning*; Cambridge University Press: Cambridge, UK, 2012.

48. Frey, D.; Butenuth, M.; Straub, D. Probabilistic Graphical Models for Flood State Detection of Roads Combining Imagery and DEM. *IEEE Trans. Geosci. Remote Sens.* **2012**, *9*, 1051–1055.
49. Dempster, A.P.; Laird, N.M.; Rubin, D.B. Maximum Likelihood from Incomplete Data via the EM Algorithm. *J. R. Stat. Soc. Ser. B* **1977**, *39*, 1–38.
50. Celik, T. Image change detection using Gaussian mixture model and genetic algorithm. *J. Vis. Commun. Image Represent.* **2010**, *21*, 965–974.
51. Yang, G.; Li, H.C.; Yang, W.; Fu, K.; Celik, T.; Emery, W.J. Variational Bayesian Change Detection of Remote Sensing Images Based on Spatially Variant Gaussian Mixture Model and Separability Criterion. *IEEE J. Sel. Top. Appl. Earth Obs. Remote Sens.* **2019**, *12*, 849–861. [[CrossRef](#)]
52. Watanabe, M.; Thapa, R.B.; Ohsumi, T.; Fujiwara, H.; Yonezawa, C.; Tomii, N.; Suzuki, S. Detection of damaged urban areas using interferometric SAR coherence change with PALSAR-2. *Earth Planets Space* **2016**, *68*, 131. [[CrossRef](#)]
53. Lu, C.-H.; Ni, C.-F.; Chang, C.-P.; Yen, J.-Y.; Chuang, R. Coherence Difference Analysis of Sentinel-1 SAR Interferogram to Identify Earthquake-Induced Disasters in Urban Areas. *Remote Sens.* **2018**, *10*, 1318.
54. NOAA Hurricane Harvey: Emergency Response Imagery of the Surrounding Regions. Available online: <https://storms.ngs.noaa.gov/storms/harvey/index.html#7/28.400/-96.690> (accessed on 15 August 2019).
55. Liu, W.; Yamazaki, F. Review article: Detection of inundation areas due to the 2015 Kanto and Tohoku torrential rain in Japan based on multi-temporal ALOS-2 imagery. *Nat. Hazards Earth Syst. Sci.* **2018**, *18*, 1905–1918. [[CrossRef](#)]
56. GSI (Geospatial Information Authority of Japan): 2015 Kanto-Tohoku Heavy Rainfall. Available online: <https://www.gsi.go.jp/BOUSAI/H27.taihuu18gou.html> (accessed on 15 August 2019).
57. GSI (Geospatial Information Authority of Japan): 2015 Kanto-Tohoku Heavy Rain Joso Area Regular Radiation Image. Available online: <http://maps.gsi.go.jp/development/ichiran.html#t20150929dol> (accessed on 15 August 2019).
58. Amitrano, D.; Di Martino, G.; Iodice, A.; Riccio, D.; Ruella, G. A New Framework for SAR Multitemporal Data RGB Representation: Rationale and Products. *IEEE Trans. Geosci. Remote Sens.* **2015**, *51*, 117–133.
59. Liu, J.G.; Black, A.; Lee, H.; Hanaizumi, H.; Moore, J.M. Land surface change detection in a desert area in Algeria using multi-temporal ERS SAR coherence images. *Int. J. Remote Sens.* **2001**, *22*, 2463–2477.
60. Hossin, M.; Sulaiman, N. A Review on Evaluation Metrics For Data Classification Evaluations. *Int. J. Data Min. Knowl. Manag. Process* **2015**, *5*, 1–11.
61. Dabboor, M.; Iris, S.; Singhroy, V. The RADARSAT Constellation Mission in Support of Environmental Applications. *Proceedings* **2018**, *2*, 323. [[CrossRef](#)]
62. Moreira, A.; Krieger, G.; Hajnsek, I.; Papathanassiou, K.; Younis, M.; Lopez-Dekker, P.; Huber, S.; Villano, M.; Pardini, M. Tandem-L: A Highly Innovative Bistatic SAR Mission for Global Observation of Dynamic Processes on the Earth's Surface. *IEEE Geosci. Remote Sens. Mag.* **2015**, *3*, 8–23. [[CrossRef](#)]
63. Kumar, R.; Rosen, P.; Misra, T. NASA-ISRO synthetic aperture radar: Science and applications. In Proceedings of the Earth Observing Missions and Sensors: Development, Implementation, and Characterization IV, New Delhi, India, 4–7 April 2016; Volume 9881, p. 988103.
64. Feldman, D.; Faulkner, M.; Krause, A. Scalable Training of Mixture Models via Coresets. In Proceedings of the Advances in Neural Information Processing Systems 24 (NIPS 2011), Granada, Spain, 12–14 December 2011; pp. 2142–2150.
65. Lucic, M.; Faulkner, M.; Krause, A.; Feldman, D. Training Gaussian Mixture Models at Scale via Coresets. *J. Mach. Learn. Res.* **2018**, *18*, 5885–5909.
66. Xiong, T.; Zhang, L.; Yi, Z. Double Gaussian mixture model for image segmentation with spatial relationships. *J. Vis. Commun. Image Represent.* **2016**, *34*, 135–145.





# 7. Conclusion and Outlook

## 7.1 Conclusion

This thesis aims at developing methods for flood mapping in rural and urban areas based on multi-temporal SAR intensity and InSAR coherence. Regarding the paradigm of methodology, both unsupervised and supervised methods were investigated and employed for scientific and operational purposes. Several SAR sensors in orbit including X-band TerraSAR-X, C-band Sentinel-1A/1B, and L-band ALOS-2/PALSAR-2 were employed in this thesis. Multi-temporal TerraSAR-X and ALOS-2/PALSAR-2 datasets were explored for urban flood mapping due to their high spatial resolution. Multi-temporal mid-resolution Sentinel-1A/1B datasets were explored for both rural and urban flood mapping due to the high temporal resolution and systematic observation scenario, which are favorable for operational flood mapping purposes.

Multi-temporal change detection is widely used in flood mapping since it can reduce the overestimation caused by radar shadow effects and water look-alike surfaces, and isolate the floodwater from permanent water bodies. Research object (1) mentioned in Chapter 1 is related to change detection for rapid flood mapping in rural areas, and Chapter 4 gives solutions to these questions.

An adequate non-flood reference image is critical in change detection, an unrepresentative reference image may lead to either overestimation or underestimation. The first question is how to choose an optimal reference image. In Chapter 4, a Jensen-Shannon (JS) divergence-based index is first introduced to select a representative reference image from the archive. Data imbalance is very common in flood mapping (e.g., the flooded area only covers a small fraction of the scene), especially in a large coverage. The second question of research object (1) is how to deal with the (highly) unbalanced dataset. To cope with this issue, a saliency-guided generalized Gaussian mixture model (SGGMM) is proposed, which is

## Conclusion and Outlook

---

tolerant to the speckle effect and robust to an imbalanced dataset. Contextual information is usually integrated to refine and smooth the pixel-based result, and how to integrate appropriate contextual information effectively and efficiently is the third question of research object (1). Random field models such as Markov random field (MRF) and Conditional random field (CRF) are widely applied to the integration of contextual information. However, the traditional local-connected random field models suffer from over-smooth, the fully-connected conditional random field (FCRF) is employed instead. It takes account of pairwise connections of all pixels in the image with an efficient mean-field inference algorithm. This long-range connection overcomes the drawback of over-smooth in local-connected random field models, smoothing out false alarms and preserving the fine flooded structures simultaneously. In summary, a multi-step automatic change detection approach is proposed in Chapter 4 to address the questions in research object (1). The approach is evaluated on flood events at Evros River (Greece) (image size of 4342\*5314 pixels with 26 reference image candidates) and York (England) (image size of 7210\*6031 pixels with 18 reference image candidates) based on Sentinel-1 GRD data. Kappa coefficients of 0.924 and 0.868 are achieved with the processing time of 216s and 285s, respectively. The experiments demonstrate the effectiveness, efficiency, and robustness of the proposed method. The presented work in this chapter only deals with flood mapping in rural areas with SAR intensity, the more challenging problems in urban environments are addressed in Chapters 5 and 6.

The complicated backscattering mechanisms in urban areas due to the high variability of landscapes, the varying building types, heights, and shapes make it challenging to map urban floods. Generally, floodwater in open areas such as wide roads and bare soils is detected by specular reflection, whereas floodwater located in the ground adjacent to a building can be detected by double-bounce scattering. However, the double-bounce scattering reduces when there is a large orientation angle or the water level is high with respect to the building height. In principle, InSAR coherence can complement intensity to address these problems.

## Conclusion and Outlook

---

To find the answer to research objective (2a), Chapters 5 and 6 investigate the benefit of fusion multitemporal SAR intensity and InSAR coherence in urban flood mapping from different perspectives. In Chapter 5, multi-temporal intensity and coherence are fused at the image level with a Convolutional Neural Network (CNN), whereas in Chapter 6 these two information sources are combined at the decision level via a Bayesian Network. Experiments on Houston (US) flood event with TerraSAR-X and Sentinel-1 data as well as Joso (Japan) flood event with ALOS-2/PALSAR-2 show that the results from the fusion of intensity and coherence are superior to that from intensity only, indicating that coherence can profitably complement intensity for urban flood mapping.

For the limited training data problem in research objective (2b), Chapter 5 presents a novel active self-learning (A-SL) temporal-ensembling CNN framework to mitigate the effect of limited training samples. It consists of a student and a teacher model that shared the same CNN architecture but have different model weights, informative samples are first queried from unlabeled data and subsequently filtered and pseudo-labeled. This procedure is iterated several times until a stop criterion is met. Experiments on Houston (US) flood event with TerraSAR-X illustrate that the proposed framework outperforms its pure supervised counterpart significantly without any extra human efforts: the kappa coefficient is improved from 0.614 to 0.686.

Although the proposed framework in Chapter 5 can improve the results in the scenario of limited training data, its application might be limited to cases that at least some training datasets are accessible. Chapter 6 accomplishes research objective (3) by introducing a Bayesian Network based unsupervised method which is more favorable to operational purposes. Due to the fact that in complicated environments such as urban areas it is difficult to find causality between a flood event and the observed SAR observations at each pixel, the method brings a latent variable to bridge this gap. The method starts with image segmentation based on time series intensity and coherence using the finite Gaussian mixture model (GMM). The flooded evidence for each Gaussian component was first evaluated based on the changes

## Conclusion and Outlook

---

between pre- and co-event intensity and coherence, respectively. The uncertainties in terms of intensity and coherence are also considered according to the coherent properties of the components, corresponding to different land cover types such as bare soils, vegetated areas, and built-up areas. The flood posterior probability of each pixel is then calculated through the Bayes rule. Furthermore, the contributions of intensity and coherence in flood mapping at each pixel can be visualized through the posterior probability based on each information. Experiments on Houston (US) flood event with Sentinel-1 data and Joso (Japan) flood event with ALOS-2/PALSAR-2 data show satisfactory mapping results with the proposed method, kappa coefficients of 0.680 and 0.720 are achieved, respectively. However, some special flood situations such as flooded parking lots and very dense building blocks are still hard to detect.

## 7.2 Outlook

The methods presented in this thesis were only applied and tested at the local basin level. It is interesting for both remote sensing and disaster management communities to adjust and upscale these methods to large-scale applications. On the one hand, a powerful graphics processing unit (GPU) can accelerate the image processing, on the other hand, some advanced inference algorithms can speed up the inference procedure of probability models.

In the context of near real-time mapping, it is important to acquire the data shortly after the occurrence of a flood event. The temporal fusion of SAR and optical data can shorten the time interval between flood occurring and data acquisition. Moreover, the spatial fusion of SAR and optical data can help detect inundated areas in steep slope terrains where are hard to detect by SAR data because of radar shadowing and foreshortening.

Although the work of this thesis boosts urban flood mapping with SAR and InSAR data, it is still a challenging problem and further work is required. It is recommended to explore polarimetric SAR data as it provides more comprehensive information than single polarized data. It is also interesting to integrate social media data such as tweets (Huang et al., 2018;

## **Conclusion and Outlook**

---

Lorini et al., 2019) and Volunteered Geographic Information (VGI) (Barz et al., 2019; Feng and Sester, 2018) to improve flood mapping in urban areas.

## References

- Abdelfattah, R., Nicolas, J., 2010. Mixture model for the segmentation of the InSAR coherence map. *Int. J. Appl. Earth Obs. Geoinf.* 12, 138–144. <https://doi.org/10.1016/j.jag.2009.10.001>
- Alfieri, L., Cohen, S., Galantowicz, J., Schumann, G.J.P., Trigg, M.A., Zsoter, E., Prudhomme, C., Kruczkiewicz, A., Coughlan de Perez, E., Flamig, Z., Rudari, R., Wu, H., Adler, R.F., Brakenridge, R.G., Kettner, A., Weerts, A., Matgen, P., Islam, S.A.K.M., de Groeve, T., Salamon, P., 2018. A global network for operational flood risk reduction. *Environ. Sci. Policy* 84, 149–158. <https://doi.org/10.1016/j.envsci.2018.03.014>
- Alsdorf, D.E., Melack, J.M., Dunne, T., Mertes, L.A.K., Hess, L.L., Smith, L.C., 2000. Interferometric radar measurements of water level changes on the Amazon flood plain. *Nature* 404, 174–177. <https://doi.org/10.1038/35004560>
- Alsdorf, D.E., Smith, L.C., Melack, J.M., 2001. Amazon floodplain water level changes measured with interferometric SIR-C radar. *IEEE Trans. Geosci. Remote Sens.* 39, 423–431. <https://doi.org/10.1109/36.905250>
- Amini, J., 2010. A method for generating floodplain maps using ikonos images and dems. *Int. J. Remote Sens.* 31, 2441–2456. <https://doi.org/10.1080/01431160902929230>
- Argenti, F., Lapini, A., Alparone, L., Bianchi, T., 2013. A tutorial on speckle reduction in synthetic aperture radar images. *IEEE Geosci. Remote Sens. Mag.* 1, 6–35.
- Askne, J.I.H., Dammert, P.B.G., Ulander, L.M.H., Smith, G., 1997. C-band repeat-pass interferometric SAR observations of the forest. *IEEE Trans. Geosci. Remote Sens.* 35, 25–35. <https://doi.org/10.1109/36.551931>
- Atwood, D.K., Thirion-Lefevre, L., 2018. Polarimetric Phase and Implications for Urban Classification. *IEEE Trans. Geosci. Remote Sens.* 56, 1278–1289. <https://doi.org/10.1109/TGRS.2017.2750211>
- Badji, M., Dautrebande, S., 1997. Characterization of flood inundated areas and delineation of poor drainage soil using ERS-1 SAR imagery. *Hydrol. Process.* 11, 1441–1450. [https://doi.org/10.1002/\(SICI\)1099-1085\(199708\)11:10<1441::AID-HYP527>3.0.CO;2-Y](https://doi.org/10.1002/(SICI)1099-1085(199708)11:10<1441::AID-HYP527>3.0.CO;2-Y)
- Bamler, R., Harlt, P., 1998. Synthetic aperture radar interferometry. *Inverse Probl.* 14, R1–R54. <https://doi.org/10.1088/0266-5611/14/4/001>
- Bamler, R., Just, D., 1993. Phase statistics and decorrelation in, in: *International Geoscience and Remote Sensing Symposium (IGARSS)*. <https://doi.org/10.1109/IGARSS.1993.322637>
- Barber, D.C., Hochheim, K.P., Dixon, R., Moss crop, D.R., Mc mullan, M.T., 1996. The Role of Earth Observation Technologies in Flood Mapping: A Manitoba Case Study. *Can. J. Remote Sens.* 22, 137–143. <https://doi.org/10.1080/07038992.1996.10874644>
- Barz, B., Schröter, K., Münch, M., Yang, B., Unger, A., Dransch, D., Denzler, J., 2019. Enhancing Flood Impact Analysis using Interactive Retrieval of Social Media Images. *arXiv:1908.03361*.
- Bates, B.C., Kundzewicz, Z.W., Wu, S., Palutikof, J.P., 2008. *Climate Change and Water*. Technical Paper of the Intergovernmental Panel on Climate Change, Geneva: IPCC



## References

---

- Secretariat. <https://doi.org/10.1016/j.jmb.2010.08.039>
- Bazi, Y., Bruzzone, L., Melgani, F., 2005. An unsupervised approach based on the generalized Gaussian model to automatic change detection in multitemporal SAR images. *IEEE Trans. Geosci. Remote Sens.* 43, 874–887. <https://doi.org/10.1109/TGRS.2004.842441>
- Bazzi, H., Baghdadi, N., El Hajj, M., Zribi, M., Minh, D.H.T., Ndikumana, E., Courault, D., Belhouichette, H., 2019. Mapping Paddy Rice Using Sentinel-1 SAR Time Series in Camargue, France. *Remote Sens.* 11, 887. <https://doi.org/10.3390/rs11070887>
- Betbeder, J., Pottier, E., Corgne, S., 2014. Multitemporal classification of TerraSAR-X data for wetland vegetation mapping Samuel Corgne Laurence Hubert-Moy. <https://doi.org/10.1117/1.JRS.8.083648>
- Bickel, D.L., 2014. SAR Image Effects on Coherence and Coherence Estimation. New Mexico and California.
- Bolanos, S., Stiff, D., Brisco, B., Pietroniro, A., 2016. Operational surface water detection and monitoring using Radarsat 2. *Remote Sens.* 8. <https://doi.org/10.3390/rs8040285>
- Bourgeau-Chavez, L.L., Kasischke, E.S., Brunzell, S.M., Mudd, J.P., Smith, K.B., Frick, A.L., 2001. Analysis of space-borne SAR data for wetland mapping in Virginia riparian ecosystems. *Int. J. Remote Sens.* 22, 3665–3687. <https://doi.org/10.1080/01431160010029174>
- Brisco, B., Ahern, F., Murnaghan, K., White, L., Canisus, F., Lancaster, P., 2017. Seasonal change in wetland coherence as an aid to wetland monitoring. *Remote Sens.* 9, 1–19. <https://doi.org/10.3390/rs9020158>
- Brisco, B., Li, K., Tedford, B., Charbonneau, F., Yun, S., Murnaghan, K., 2013a. Compact polarimetry assessment for rice and wetland mapping. *Int. J. Remote Sens.* 34, 1949–1964. <https://doi.org/10.1080/01431161.2012.730156>
- Brisco, B., Schmitt, A., Murnaghan, K., Kaya, S., Roth, A., 2013b. SAR polarimetric change detection for flooded vegetation. *Int. J. Digit. Earth* 6, 103–114. <https://doi.org/10.1080/17538947.2011.608813>
- Brisco, B., Shelat, Y., Murnaghan, K., Montgomery, J., Fuss, C., Olthof, I., Hopkinson, C., Deschamps, A., Poncos, V., 2019. Evaluation of C-Band SAR for Identification of Flooded Vegetation in Emergency Response Products. *Can. J. Remote Sens.* 45, 73–87. <https://doi.org/10.1080/07038992.2019.1612236>
- Brisco, B., Touzi, R., van der Sanden, J.J., Charbonneau, F., Pultz, T.J., D'Iorio, M., 2008. Water resource applications with radarsat-2—a preview. *Int. J. Digit. Earth* 1, 130–147. <https://doi.org/10.1080/17538940701782577>
- Brunner, D., Lemoine, G., Bruzzone, L., Greidanus, H., 2010. Building height retrieval from airborne VHR SAR imagery based on an iterative simulation and matching procedure. *IEEE Trans. Geosci. Remote Sens.* 48, 1487–1504. <https://doi.org/10.1117/12.800736>
- Canisius, F., Brisco, B., Murnaghan, K., Van Der Kooij, M., Keizer, E., 2019. SAR Backscatter and InSAR Coherence for Monitoring Wetland Extent, Flood Pulse and Vegetation: A Study of the Amazon Lowland. *Remote Sens.* 11. <https://doi.org/10.3390/rs11060720>
- CEOS (Committee on Earth Observation Satellites), 2015. Satellite Earth Observations in support of disaster risk reduction, Special 2015 WCDRR Edition, ESA. ed.

## References

---

- Chaabani, C., Chini, M., Abdelfattah, R., Hostache, R., Chokmani, K., 2018. Flood mapping in a complex environment using bistatic TanDEM-X/TerraSAR-X InSAR coherence. *Remote Sens.* 10, 1–20. <https://doi.org/10.3390/rs10121873>
- Chapman, B., McDonald, K., Shimada, M., Rosenqvist, A., Schroeder, R., Hess, L., 2015. Mapping regional inundation with spaceborne L-Band SAR. *Remote Sens.* 7, 5440–5470. <https://doi.org/10.3390/rs70505440>
- Chen, Y., Zhou, H., Zhang, H., Du, G., Zhou, J., 2015. Urban flood risk warning under rapid urbanization. *Environ. Res.* 139, 3–10. <https://doi.org/10.1016/j.envres.2015.02.028>
- Chini, M., Hostache, R., Giustarini, L., Matgen, P., 2017. A Hierarchical Split-Based Approach for Parametric Thresholding of SAR Images: Flood Inundation as a Test Case. *IEEE Trans. Geosci. Remote Sens.* 55, 6975–6988. <https://doi.org/10.1109/TGRS.2017.2737664>
- Chini, M., Pelich, R., Pulvirenti, L., Pierdicca, N., Hostache, R., Matgen, P., 2019. Sentinel-1 InSAR Coherence to Detect Floodwater in Urban Areas: Houston and Hurricane Harvey as A Test Case. *Remote Sens.* 11, 107. <https://doi.org/10.3390/rs11020107>
- Chini, M., Pulvirenti, L., Pierdicca, N., 2012. Analysis and interpretation of the COSMO-SkyMed observations of the 2011 Japan tsunami. *IEEE Geosci. Remote Sens. Lett.* 9, 467–471. <https://doi.org/10.1109/LGRS.2011.2182495>
- Christopherson, J.B., Chandra, S.N.R., Quanbeck, J.Q., 2019. 2019 Joint Agency Commercial Imagery Evaluation—Land remote sensing satellite compendium, U.S. Geolo. ed. U.S. Geological Survey Circular. <https://doi.org/10.3133/cir1455>
- Cian, F., Marconcini, M., Ceccato, P., 2018. Normalized Difference Flood Index for rapid flood mapping: Taking advantage of EO big data. *Remote Sens. Environ.* 209, 712–730. <https://doi.org/10.1016/j.rse.2018.03.006>
- Costa, M.P.F., 2004. Use of SAR satellites for mapping zonation of vegetation communities in the Amazon floodplain. *Int. J. Remote Sens.* 25, 1817–1835. <https://doi.org/10.1080/0143116031000116985>
- Costa, M.P.F., Niemann, O., Novo, E., Ahern, F., 2002. Biophysical properties and mapping of aquatic vegetation during the hydrological cycle of the Amazon floodplain using JERS-1 and Radarsat. *Int. J. Remote Sens.* 23, 1401–1426. <https://doi.org/10.1080/01431160110092957>
- CRED (Centre for Research on the Epidemiology of Disasters), 2018. Natural disasters. Brussels.
- Crosetto, M., 2002. Calibration and validation of SAR interferometry. *ISPRS J. Photogramm. Remote Sens.* 57, 213–227.
- D’Addabbo, A., Refice, A., Pasquariello, G., Lovergine, F.P., Capolongo, D., Manfreda, S., 2016. A Bayesian Network for Flood Detection Combining SAR Imagery and Ancillary Data. *IEEE Trans. Geosci. Remote Sens.* 54, 3612–3625.
- Dammert, P.B.G., Askne, J.I.H., Kuhlmann, S., 1999. Unsupervised segmentation of multitemporal interferometric SAR images. *Doktorsavhandlingar vid Chalmers Tek. Högsk.* 37, 2259–2271. <https://doi.org/10.1109/36.789622>
- Danklmayer, A., Doring, B.R.J., Schwerdt, M., Chandra, M., 2009. Assessment of atmospheric propagation effects in SAR images. *IEEE Trans. Geosci. Remote Sens.* 47, 3507–3518. <https://doi.org/10.1109/TGRS.2009.2022271>

## References

---

- De Groeve, T., Thielen-Del Pozo, J., Brakenridgde, R., Adler, R., Alfieri, L., Kull, D., Lindsay, F., Imperiali, O., Pappenberg, F., Rudari, R., Salamon, P., Villars, N., Wyjad, K., 2015. Joining forces in a global flood partnership. *Bull. Am. Meteorol. Soc.* 96, ES97–ES100. <https://doi.org/10.1175/BAMS-D-14-00147.1>
- De Zan, F., Parizzi, A., Prats-Iraola, P., López-Dekker, P., 2014. A SAR interferometric model for soil moisture. *IEEE Trans. Geosci. Remote Sens.* 52, 418–425. <https://doi.org/10.1109/TGRS.2013.2241069>
- Deledalle, C.A., Denis, L., Tupin, F., Reigber, A., Jager, M., 2015. NL-SAR: A unified nonlocal framework for resolution-preserving (Pol)(In)SAR denoising. *IEEE Trans. Geosci. Remote Sens.* 53, 2021–2038. <https://doi.org/10.1109/TGRS.2014.2352555>
- Dellepiane, S., Bo, G., Monni, S., Buck, C., 2000. Improvements in flood monitoring by means of interferometric coherence, in: *SAR Image Analysis, Modeling, and Techniques III*. pp. 219–229. <https://doi.org/10.1117/12.410662>
- Dobson, M.C., Ulaby, F.T., LeToan, T., Beaudoin, A., Kasischke, E.S., Christensen, N., 1992. Dependence of Radar Backscatter on Coniferous Forest Biomass. *IEEE Trans. Geosci. Remote Sens.* 30, 412–415. <https://doi.org/10.1109/36.134090>
- Dong, Y., Forster, B., Ticehurst, C., 1997. Radar backscatter analysis for urban environments. *Int. J. Remote Sens.* 18, 1351–1364. <https://doi.org/10.1080/014311697218467>
- Drusch, M., Del Bello, U., Carlier, S., Colin, O., Fernandez, V., Gascon, F., Hoersch, B., Isola, C., Laberinti, P., Martimort, P., Meygret, A., Spoto, F., Sy, O., Marchese, F., Bargellini, P., 2012. Sentinel-2: ESA’s Optical High-Resolution Mission for GMES Operational Services. *Remote Sens. Environ.* 120, 25–36. <https://doi.org/10.1016/j.rse.2011.11.026>
- EM-DAT, 2019. The OFDA/CRED International Disaster Database [WWW Document]. Univ. Cathol. Louvain, Brussels, Belgium. URL [https://www.emdat.be/emdat\\_db/](https://www.emdat.be/emdat_db/) (accessed 8.20.19).
- Fanelli, A., Santoro, M., Vitale, A., Murino, P., Askne, J., 2000. Understanding ERS Coherence over Urban Areas, in: *Proceedings of ERS-Envisat Symposium: Looking Down to Earth in the New Millennium*. Gothenburg, Sweden.
- Feng, Y., Sester, M., 2018. Extraction of pluvial flood relevant volunteered geographic information (VGI) by deep learning from user generated texts and photos. *ISPRS Int. J. Geo-Information* 7. <https://doi.org/10.3390/ijgi7020039>
- Ferro, A., Brunner, D., Bruzzone, L., Lemoine, G., 2011. On the relationship between double bounce and the orientation of buildings in VHR SAR images. *IEEE Geosci. Remote Sens. Lett.* 8, 612–616. <https://doi.org/10.1109/LGRS.2010.2097580>
- Foster, J.L., Hall, D.K., 1981. Multisensor Analysis of Hydrologic Features With Emphasis on the Seasat Sar. *Photogramm. Eng. Remote Sensing* 47, 655–664.
- Franceschetti, G., Iodice, A., Riccio, D., 2002. A canonical problem in electromagnetic backscattering from buildings. *IEEE Trans. Geosci. Remote Sens.* 40, 1787–1801. <https://doi.org/10.1109/TGRS.2002.802459>
- Gelautz, M., Frick, H., Raggam, J., Burgstaller, J., Leberl, F., 1998. SAR image simulation and analysis of alpine terrain. *ISPRS J. Photogramm. Remote Sens.* 53, 17–38. [https://doi.org/10.1016/S0924-2716\(97\)00028-2](https://doi.org/10.1016/S0924-2716(97)00028-2)
- Giacomelli, A., Mancini, M., Rosso, R., 1995. Assessment of flooded areas from ERS-1 PRI

## References

- data: An application to the 1994 flood in Northern Italy. *Phys. Chem. Earth* 20, 469–474. [https://doi.org/10.1016/S0079-1946\(96\)00008-0](https://doi.org/10.1016/S0079-1946(96)00008-0)
- Giordano, F., Goccia, M., Dellepiane, S., 2005. Segmentation of coherence maps for flood damage assessment, in: *IEEE International Conference on Image Processing 2005*. <https://doi.org/10.1109/ICIP.2005.1530034>
- Giustarini, L., Hostache, R., Kavetski, D., Chini, M., Corato, G., Schlaffer, S., Matgen, P., 2016. Probabilistic Flood Mapping Using Synthetic Aperture Radar Data. *IEEE Trans. Geosci. Remote Sens.* 54, 6958–6969. <https://doi.org/10.1109/TGRS.2016.2592951>
- Giustarini, L., Hostache, R., Matgen, P., Schumann, G.J., Bates, P.D., Mason, D.C., 2013. A Change Detection Approach to Flood Mapping in Urban Areas Using TerraSAR-X. *IEEE Trans. Geosci. Remote Sens.* 51, 2417–2430. <https://doi.org/10.1109/TGRS.2012.2210901>
- Giustarini, L., Matgen, P., Hostache, R., Montanari, M., Plaza, D., Pauwels, V.R.N., De Lannoy, G.J.M., De Keyser, R., Pfister, L., Hoffmann, L., Savenije, H.H.G., 2011. Assimilating SAR-derived water level data into a hydraulic model: A case study. *Hydrol. Earth Syst. Sci.* 15, 2349–2365. <https://doi.org/10.5194/hess-15-2349-2011>
- Grings, F.M., Ferrazzoli, P., Karszenbaum, H., Salvia, M., Kandus, P., Jacobo-Berlles, J.C., Perna, P., 2008. Model investigation about the potential of C band SAR in herbaceous wetlands flood monitoring. *Int. J. Remote Sens.* 29, 5361–5372. <https://doi.org/10.1080/01431160802036409>
- Grove, M., Harbor, J., Engel, B., Muthukrishnan, S., 2001. Impacts of urbanization on surface hydrology, little eagle creek, Indiana, and analysis of Lthia model sensitivity to data resolution. *Phys. Geogr.* 22, 135–153. <https://doi.org/10.1080/02723646.2001.10642734>
- Guida, R., Iodice, A., Riccio, D., 2010. Height retrieval of isolated buildings from single high-resolution SAR images. *IEEE Trans. Geosci. Remote Sens.* 48, 2967–2979. <https://doi.org/10.1109/TGRS.2010.2041460>
- Hall-Atkinson, C., Smith, L.C., 2001. Delineation of delta ecozones using interferometric SAR phase coherence Mackenzie River Delta, N.W.T., Canada. *Remote Sens. Environ.* 78, 229–238. [https://doi.org/10.1016/S0034-4257\(01\)00221-8](https://doi.org/10.1016/S0034-4257(01)00221-8)
- Hall, D.K., 1996. Remote sensing applications to hydrology; imaging radar. *Hydrol. Sci. J.* 41, 609–624. <https://doi.org/10.1080/02626669609491528>
- Hall, J., Arheimer, B., Borga, M., Brázdil, R., Claps, P., Kiss, A., Kjeldsen, T.R., Kriaučiūnienė, J., Kundzewicz, Z.W., Lang, M., Llasat, M.C., Macdonald, N., McIntyre, N., Mediero, L., Merz, B., Merz, R., Molnar, P., Montanari, A., Neuhold, C., Parajka, J., Perdigão, R.A.P., Plavcová, L., Rogger, M., Salinas, J.L., Sauquet, E., Schär, C., Szolgay, J., Viglione, A., Blöschl, G., 2014. Understanding flood regime changes in Europe: A state-of-the-art assessment. *Hydrol. Earth Syst. Sci.* 18, 2735–2772. <https://doi.org/10.5194/hess-18-2735-2014>
- Hallegatte, S., Green, C., Nicholls, R.J., Corfee-morlot, J., 2013. Future flood losses in major coastal cities. *Nat. Clim. Chang.* 3, 802–806. <https://doi.org/10.1038/nclimate1979>
- Hanssen, R.F., 2002. *Radar Interferometry, Data Interpretation and Error Analysis*. Kluwer Academic Publishers, NEW YORK, BOSTON, DORDRECHT, LONDON, MOSCOW.
- Henderson, F.M., 1995. Environmental factors and the detection of open surface water areas

## References

---

- with X-band radar imagery. *Int. J. Remote Sens.* 16, 2423–2437.  
<https://doi.org/10.1080/01431169508954567>
- Henry, J.B., Chastanet, P., Fellah, K., Desnos, Y.L., 2006. Envisat multi-polarized ASAR data for flood mapping. *Int. J. Remote Sens.* 27, 1921–1929.  
<https://doi.org/10.1080/01431160500486724>
- Hess, L.L., Melack, J.M., Melack, J.M., Filoso, S., Wang, Y., Wang, Y., 1995. Delineation of Inundated Area and Vegetation Along the Amazon Floodplain with the SIR-C Synthetic Aperture Radar. *IEEE Trans. Geosci. Remote Sens.* 33, 896–904.  
<https://doi.org/10.1109/36.406675>
- Hess, L.L., Melack, J.M., Novo, E.M.L.M., Barbosa, C.C.F., Gastil, M., 2003. Dual-season mapping of wetland inundation and vegetation for the central Amazon basin. *Remote Sens. Environ.* 87, 404–428. <https://doi.org/10.1016/j.rse.2003.04.001>
- Hess, L.L., Melack, J.M., Simonett, D.S., 1990. Radar detection of flooding beneath the forest canopy: A review. *Int. J. Remote Sens.* 11, 1313–1325.  
<https://doi.org/10.1080/01431169008955095>
- Hong, S.-H., Wdowinski, S., Kim, S.-W., 2010. Evaluation of TerraSAR-X observations for wetland InSAR application. *IEEE Trans. Geosci. Remote Sens.* 48, 864–873.  
<https://doi.org/10.1109/TGRS.2009.2026895>
- Horritt, M.S., 1999. A statistical active contour model for SAR image segmentation. *Image Vis. Comput.* 17, 213–224. [https://doi.org/10.1016/s0262-8856\(98\)00101-2](https://doi.org/10.1016/s0262-8856(98)00101-2)
- Horritt, M.S., Mason, D.C., Cobby, D.M., Davenport, I.J., Bates, P.D., 2003. Waterline mapping in flooded vegetation from airborne SAR imagery. *Remote Sens. Environ.* 85, 271–281. [https://doi.org/10.1016/S0034-4257\(03\)00006-3](https://doi.org/10.1016/S0034-4257(03)00006-3)
- Hossain, F., Jeyachandran, I., Pielke Sr., R., 2009. Have large dams altered extreme precipitation patterns? *Eos Trans. Am. Geophys. Union* 90, 453–454.  
<https://doi.org/10.1029/2009EO480001>
- Hostache, R., Matgen, P., Schumann, G., Puech, C., Hoffmann, L., Pfister, L., 2009. Water level estimation and reduction of hydraulic model calibration uncertainties using satellite SAR images of floods. *IEEE Trans. Geosci. Remote Sens.* 47, 431–441.  
<https://doi.org/10.1109/TGRS.2008.2008718>
- Hostache, R., Matgen, P., Wagner, W., 2012. Change detection approaches for flood extent mapping: How to select the most adequate reference image from online archives? *Int. J. Appl. Earth Obs. Geoinf.* 19, 205–213. <https://doi.org/10.1016/j.jag.2012.05.003>
- Huang, X., Wang, C., Li, Z., 2018. Reconstructing flood inundation probability by enhancing near real-time imagery with real-time gauges and tweets. *IEEE Trans. Geosci. Remote Sens.* 56, 4691–4701. <https://doi.org/10.1109/TGRS.2018.2835306>
- Hussin, Y.A., 1995. Effect of polarization and incidence angle on radar return from urban features using L-band aircraft radar data. *Int. Geosci. Remote Sens. Symp.* 178–180.  
<https://doi.org/10.1109/igarss.1995.519683>
- IDMC (Internal Displacement Monitoring Centre), 2019. GRID 2019: Global Report on Internal Displacement. Geneva, Switzerland.
- Iervolino, P., Guida, R., Iodice, A., Riccio, D., 2015. Flooding water depth estimation with high-resolution SAR. *IEEE Trans. Geosci. Remote Sens.* 53, 2295–2307.  
<https://doi.org/10.1109/TGRS.2014.2358501>

## References

---

- Imhoff, M., Vermillion, C., Story, M., Khan, F., Polcyn, F., 1986. Forest Canopy Characterization and Vegetation Penetration Assessment with Space-Borne Radar. *IEEE Trans. Geosci. Remote Sens.* GE-24, 535–542.  
<https://doi.org/10.1109/TGRS.1986.289668>
- IPCC (Intergovernmental Panel on Climate Change), 2012. Managing the Risks of Extreme Events and Disasters to Advance Climate Change Adaptation. Cambridge University Press, Cambridge, UK, and New York, NY, USA.
- Irwin, K., Beaulne, D., Braun, A., Fotopoulos, G., 2017. Fusion of SAR, optical imagery and airborne LiDAR for surface water detection. *Remote Sens.* 9, 1–18.  
<https://doi.org/10.3390/rs9090890>
- Jaramillo, F., Brown, I., Castellazzi, P., Espinosa, L., Guittard, A., Hong, S.H., Rivera-Monroy, V.H., Wdowinski, S., 2018. Assessment of hydrologic connectivity in an ungauged wetland with InSAR observations. *Environ. Res. Lett.* 13.  
<https://doi.org/10.1088/1748-9326/aa9d23>
- Jiang, Y., Zevenbergen, C., Ma, Y., 2018. Urban pluvial flooding and stormwater management: A contemporary review of China's challenges and "sponge cities" strategy. *Environ. Sci. Policy* 80, 132–143. <https://doi.org/10.1016/j.envsci.2017.11.016>
- Joyce, K.E., Belliss, S.E., Samsonov, S. V., McNeill, S.J., Glassey, P.J., 2009. A review of the status of satellite remote sensing and image processing techniques for mapping natural hazards and disasters. *Prog. Phys. Geogr.* 33, 183–207.  
<https://doi.org/10.1177/0309133309339563>
- Jung, H.C., Alsdorf, D., 2010. Repeat-pass multi-temporal interferometric SAR coherence variations with Amazon floodplain and lake habitats. *Int. J. Remote Sens.* 31, 881–901.  
<https://doi.org/10.1080/01431160902902609>
- Jung, J., Kim, D.-J., Laval, M., Yun, S.-H., 2016. Coherent change detection using temporal decorrelation model for volcanic ash detection. *IEEE Trans. Geosci. Remote Sens.* 54, 3394–3397. <https://doi.org/10.1109/IGARSS.2016.7729877>
- Kandus, P., Pulz, T., Parmuchi, G., Bava, I., 2001. Influence of flood conditions and vegetation status on the radar backscatter of wetland ecosystems. *Can. J. Remote Sens.* 27, 663–668. <https://doi.org/10.1080/07038992.2001.10854907>
- Karam, M.A., Fung, A.K., Lang, R.H., Chauhan, N.S., 1992. Microwave Scattering Model for Layered Vegetation. *IEEE Trans. Geosci. Remote Sens.* 30, 767–784.  
<https://doi.org/10.1109/36.158872>
- Kasischke, E.S., Melack, J.M., Dobson, M.C., 1997. The use of imaging radars for ecological applications - A review. *Remote Sens. Environ.* 59, 141–156.  
[https://doi.org/10.1016/S0034-4257\(96\)00148-4](https://doi.org/10.1016/S0034-4257(96)00148-4)
- Kim, D. jin, Moon, W.M., Kim, G., Park, S.E., Lee, H., 2011. Submarine groundwater discharge in tidal flats revealed by space-borne synthetic aperture radar. *Remote Sens. Environ.* 115, 793–800. <https://doi.org/10.1016/j.rse.2010.11.009>
- Kim, J.-W., Lu, Z., Gutenberg, L., Zhu, Z., 2017. Characterizing hydrologic changes of the Great Dismal Swamp using SAR/InSAR. *Remote Sens. Environ.* 198, 187–202.  
<https://doi.org/10.1016/j.rse.2017.06.009>
- Kim, J.W., Lu, Z., Lee, H., Shum, C.K., Swarzenski, C.M., Doyle, T.W., Baek, S.H., 2009. Integrated analysis of PALSAR/Radarsat-1 InSAR and ENVISAT altimeter data for



## References

---

- mapping of absolute water level changes in Louisiana wetlands. *Remote Sens. Environ.* 113, 2356–2365. <https://doi.org/10.1016/j.rse.2009.06.014>
- Kim, S.W., Wdowinski, S., Amelung, F., Dixon, T.H., Won, J.S., 2013. Interferometric coherence analysis of the everglades Wetlands, South Florida. *IEEE Trans. Geosci. Remote Sens.* 51, 5210–5224. <https://doi.org/10.1109/TGRS.2012.2231418>
- Kittler, J., Illingworth, J., 1986. Minimum error thresholding. *Pattern Recognit.* 19, 41–47. [https://doi.org/10.1016/0031-3203\(86\)90030-0](https://doi.org/10.1016/0031-3203(86)90030-0)
- Klemas, V., 2015. Remote Sensing of Floods and Flood-Prone Areas: An Overview. *J. Coast. Res.* 31, 1005–1013. <https://doi.org/10.2112/jcoastres-d-14-00160.1>
- Koskinen, J.T., Pulliainen, J.T., Hyypä, J.M., Engdahl, M.E., Hallikainen, M.T., 2001. The seasonal behavior of interferometric coherence in Boreal forest. *IEEE Trans. Geosci. Remote Sens.* 39, 820–829. <https://doi.org/10.1109/36.917903>
- Kropatsch, W.G., Strobl, D., 1990. The Generation of SAR Layover and Shadow Maps From Digital Elevation Models. *IEEE Trans. Geosci. Remote Sens.* 28, 98–107. <https://doi.org/10.1109/36.45752>
- Kundzewicz, Z.W., Kanae, S., Seneviratne, S.I., Handmer, J., Nicholls, N., Peduzzi, P., Mechler, R., Bouwer, L.M., Arnell, N., Mach, K., Muir-Wood, R., Brakenridge, G.R., Kron, W., Benito, G., Honda, Y., Takahashi, K., Sherstyukov, B., 2014. Flood risk and climate change: global and regional perspectives. *Hydrol. Sci. J.* 59, 1–28. <https://doi.org/10.1080/02626667.2013.857411>
- Kwoun, O.I., Lu, Z., 2009. Multi-temporal RADARSAT-1 and ERS backscattering signatures of coastal wetlands in southeastern louisiana. *Photogramm. Eng. Remote Sensing* 75, 607–617. <https://doi.org/10.14358/PERS.75.5.607>
- Lanari, R., Casu, F., Manzo, M., Zeni, G., Berardino, P., Manunta, M., Pepe, A., 2007. An overview of the Small BAseline Subset algorithm: A DInSAR technique for surface deformation analysis. *Pure Appl. Geophys.* 164, 637–661. <https://doi.org/10.1007/s00024-007-0192-9>
- Lang, M.W., Kasischke, E.S., 2008. Using C-band synthetic aperture radar data to monitor forested wetland hydrology in Maryland’s coastal plain, USA. *IEEE Trans. Geosci. Remote Sens.* 46, 535–546. <https://doi.org/10.1109/TGRS.2007.909950>
- Lang, M.W., Townsend, P.A., Kasischke, E.S., 2008. Influence of incidence angle on detecting flooded forests using C-HH synthetic aperture radar data. *Remote Sens. Environ.* 112, 3898–3907. <https://doi.org/10.1016/j.rse.2008.06.013>
- Le Toan, T., Beaudoin, A., Riou, J., Guyon, D., 1992. Relating Forest Biomass to SAR Data. *IEEE Trans. Geosci. Remote Sens.* 30, 403–411. <https://doi.org/10.1109/36.134089>
- Lee, J.-S., 1983. Digital image smoothing and the sigma filter. *Comput. Vision, Graph. Image Process.* 24, 255–269. [https://doi.org/10.1016/0734-189X\(83\)90047-6](https://doi.org/10.1016/0734-189X(83)90047-6)
- Lee, J.-S., 1981. Speckle analysis and smoothing of synthetic aperture radar images. *Comput. Graph. Image Process.* 17, 24–32. [https://doi.org/10.1016/S0146-664X\(81\)80005-6](https://doi.org/10.1016/S0146-664X(81)80005-6)
- Lee, J.-S., 1980. Digital Image Enhancement and Noise Filtering.pdf 1978–1981.
- Li, C.H., Lee, C.K., 1993. Minimum cross entropy thresholding. *Pattern Recognit.* 26, 617–625. [https://doi.org/10.1016/0031-3203\(93\)90115-d](https://doi.org/10.1016/0031-3203(93)90115-d)
- Ligtvoet, W., Bouwman, A., Knoop, J., de Bruin, S., Nabielek, K., Huitzing, H., Janse, J., van Minnen, J., Gernaat, D., van Puijenbroek, P., de Ruiter, J., Visser, H., 2018. The

## References

---

- Geography of Future Water Challenges, PBL Nether. ed. PBL Netherlands Environmental Assessment Agency. <https://doi.org/10.2466/pr0.1980.47.3.699>
- Long, S., Fatoyinbo, T.E., Policelli, F., 2014. Flood extent mapping for Namibia using change detection and thresholding with SAR. *Environ. Res. Lett.* 9. <https://doi.org/10.1088/1748-9326/9/3/035002>
- Lopes, A., Nezry, E., Touzi, R., Laur, H., 1990. Maximum a posteriori speckle filtering and first order texture models in SAR images, in: *International Geoscience and Remote Sensing Symposium (IGARSS)*. pp. 2409–2412. <https://doi.org/10.1109/igarss.1990.689026>
- Lorini, V., Castillo, C., Dottori, F., Kalas, M., Nappo, D., Salamon, P., 2019. Integrating Social Media into a Pan-European Flood Awareness System: A Multilingual Approach, in: *16th ISCRAM Conference*. València, Spain May 2019.
- Lu, Z., Kwoun, O.I., 2008. Radarsat-1 and ERS InSAR analysis over southeastern coastal Louisiana: Implications for mapping water-level changes beneath swamp forests. *IEEE Trans. Geosci. Remote Sens.* 46, 2167–2184. <https://doi.org/10.1109/TGRS.2008.917271>
- Luckman, A., Baker, J., Wegmüller, U., 2000. Repeat-pass interferometric coherence measurements of disturbed tropical forest from JERS and ERS satellites. *Remote Sens. Environ.* 73, 350–360. [https://doi.org/10.1016/S0034-4257\(00\)00110-3](https://doi.org/10.1016/S0034-4257(00)00110-3)
- Lusch, D.P., 1999. *Introduction to Microwave Remote Sensing*. Center For Remote Sensing and Geographic Information Science, Michigan State University.
- Malinowski, R., Groom, G., Schwanghart, W., Heckrath, G., 2015. Detection and delineation of localized flooding from WorldView-2 multispectral data. *Remote Sens.* 7, 14853–14875. <https://doi.org/10.3390/rs71114853>
- Manavalan, R., 2018. Review of synthetic aperture radar frequency, polarization, and incidence angle data for mapping the inundated regions. *J. Appl. Remote Sens.* 12. <https://doi.org/10.1117/1.jrs.12.021501>
- Manavalan, R., Rao, Y.S., Mohan, B.K., 2017. Comparative flood area analysis of C-band VH, VV, and L-band HH polarizations SAR data. *Int. J. Remote Sens.* 38, 4645–4654. <https://doi.org/10.1080/01431161.2017.1325534>
- Manjusree, P., Prasanna Kumar, L., Bhatt, C.M., Rao, G.S., Bhanumurthy, V., 2012. Optimization of threshold ranges for rapid flood inundation mapping by evaluating backscatter profiles of high incidence angle SAR images. *Int. J. Disaster Risk Sci.* 3, 113–122. <https://doi.org/10.1007/s13753-012-0011-5>
- Marti-Cardona, B., Lopez-Martinez, C., Dolz-Ripolles, J., Bladè-Castellet, E., 2010. ASAR polarimetric, multi-incidence angle and multitemporal characterization of Doñana wetlands for flood extent monitoring. *Remote Sens. Environ.* <https://doi.org/10.1016/j.rse.2010.06.015>
- Martinez, J.M., Le Toan, T., 2007. Mapping of flood dynamics and spatial distribution of vegetation in the Amazon floodplain using multitemporal SAR data. *Remote Sens. Environ.* 108, 209–223. <https://doi.org/10.1016/J.RSE.2006.11.012>
- Martinis, S., Kersten, J., Twele, A., 2015. A fully automated TerraSAR-X based flood service. *ISPRS J. Photogramm. Remote Sens.* 104, 203–212. <https://doi.org/10.1016/j.isprsjprs.2014.07.014>

## References

---

- Martinis, S., Plank, S., Ćwik, K., 2018. The use of Sentinel-1 time-series data to improve flood monitoring in arid areas. *Remote Sens.* 10. <https://doi.org/10.3390/rs10040583>
- Martinis, S., Rieke, C., 2015. Backscatter analysis using multi-temporal and multi-frequency SAR data in the context of flood mapping at River Saale, Germany. *Remote Sens.* 7, 7732–7752. <https://doi.org/10.3390/rs70607732>
- Martinis, S., Twele, A., Voigt, S., 2011. Unsupervised Extraction of Flood-Induced Backscatter Changes in SAR Data Using Markov Image Modeling on Irregular Graphs. *IEEE Trans. Geosci. Remote Sens.* 49, 251–263. <https://doi.org/10.1109/TGRS.2010.2052816>
- Martinis, S., Twele, A., Voigt, S., 2009. Towards operational near real-time flood detection using a split-based automatic thresholding procedure on high resolution TerraSAR-X data. *Nat. Hazards Earth Syst. Sci.* 9, 303–314. <https://doi.org/10.5194/nhess-9-303-2009>
- Mason, D.C., Davenport, I.J., Neal, J.C., Schumann, G.J.-P., Bates, P.D., 2012. Near Real-Time Flood Detection in Urban and Rural Areas Using High-Resolution Synthetic Aperture Radar Images. *IEEE Trans. Geosci. Remote Sens.* 50, 3041–3052.
- Mason, D.C., Giustarini, L., Garcia-Pintado, J., Cloke, H.L., 2014. Detection of flooded urban areas in high resolution Synthetic Aperture Radar images using double scattering. *Int. J. Appl. Earth Obs. Geoinf.* 28, 150–159. <https://doi.org/10.1016/j.jag.2013.12.002>
- Mason, D.C., Horritt, M.S., Amico, J.T.D., Scott, T.R., Bates, P.D., 2007. Improving River Flood Extent Delineation From Synthetic Aperture Radar Using Airborne Laser Altimetry. *IEEE Trans. Geosci. Remote Sens.* 45, 3932–3943. <https://doi.org/10.1109/TGRS.2007.901032>
- Mason, D.C., Speck, R., Devereux, B., Schumann, G.J.-P., Neal, J.C., Bates, P.D., 2010. Flood Detection in Urban Areas Using TerraSAR-X. *IEEE Trans. Geosci. Remote Sens.* 48, 882–894. <https://doi.org/10.1109/tgrs.2009.2029236>
- Massonnet, D., Feigl, K.L., 1998. Radar interferometry and its application to changes in the Earth's surface. *Rev. Geophys.* 36, 441–500. <https://doi.org/https://doi.org/10.1029/97RG03139>
- Matgen, P., Hostache, R., Schumann, G., Pfister, L., Hoffmann, L., Savenije, H.H.G., 2011. Towards an automated SAR-based flood monitoring system: Lessons learned from two case studies. *Phys. Chem. Earth, Parts A/B/C* 36, 241–252. <https://doi.org/10.1016/J.PCE.2010.12.009>
- Merz, B., Aerts, J., Arnbjerg-Nielsen, K., Baldi, M., Becker, A., Bichet, A., Blöschl, G., Bouwer, L.M., Brauer, A., Cioffi, F., Delgado, J.M., Gocht, M., Guzzetti, F., Harrigan, S., Hirschboeck, K., Kilsby, C., Kron, W., Kwon, H.H., Lall, U., Merz, R., Nissen, K., Salvatti, P., Swierczynski, T., Ulbrich, U., Viglione, A., Ward, P.J., Weiler, M., Wilhelm, B., Nied, M., 2014. Floods and climate: Emerging perspectives for flood risk assessment and management. *Nat. Hazards Earth Syst. Sci.* 14, 1921–1942. <https://doi.org/10.5194/nhess-14-1921-2014>
- Moeremans, B., Dautrebande, S., 1998. Use of ERS SAR interferometric coherence and FRI images to evaluate crop height and soil moisture and to identify crops, in: *Remote Sensing for Agriculture, Ecosystems, and Hydrology*. pp. 9–19.
- Mohammadimanesh, F., Salehi, B., Mahdianpari, M., Brisco, B., Motagh, M., 2018a.

## References

---

- Multi-temporal, multi-frequency, and multi-polarization coherence and SAR backscatter analysis of wetlands. *ISPRS J. Photogramm. Remote Sens.* 142, 78–93.  
<https://doi.org/10.1016/j.isprsjprs.2018.05.009>
- Mohammadimanesh, F., Salehi, B., Mahdianpari, M., Motagh, M., Brisco, B., 2018b. An Efficient Feature Optimization for Wetland Mapping by Synergistic Use of SAR Intensity, Interferometry, and Polarimetry Data. *Int. J. Appl. Earth Obs. Geoinf.* 73, 450–462. <https://doi.org/10.1016/j.jag.2018.06.005>
- Monti-Guarnieri, A.V., Brovelli, M.A., Manzoni, M., Mariotti D'Alessandro, M., Molinari, M.E., Oxoli, D., 2018. Coherent change detection for multipass SAR. *IEEE Trans. Geosci. Remote Sens.* 56, 6811–6822. <https://doi.org/10.1109/TGRS.2018.2843560>
- Monti Guarnieri, A., Prati, C., 1997. Sar interferometry: a “quick and dirty” coherence estimator for data browsing. *IEEE Trans. Geosci. Remote Sens.* 35, 660–669.  
<https://doi.org/10.1109/36.581984>
- Morandeira, N.S., Grings, F., Facchinetti, C., Kandus, P., 2016. Mapping plant functional types in floodplain wetlands: An analysis of C-band polarimetric SAR data from RADARSAT-2. *Remote Sens.* 8, 1–17. <https://doi.org/10.3390/rs8030174>
- Moreira, A., Prats-Iraola, P., Younis, M., Papathinassiou, K., 2013. A Tutorial on Synthetic Aperture Radar. *IEEE Geosci. Remote Sens. Mag.* 32.
- Moser, G., Serpico, S.B., 2009. Unsupervised Change Detection From Multichannel SAR Data by Markovian Data Fusion. *IEEE Trans. Geosci. Remote Sens.* 47, 2114–2128.  
<https://doi.org/10.1109/TGRS.2009.2012407>
- Moser, G., Serpico, S.B., 2006. Generalized minimum-error thresholding for unsupervised change detection from SAR amplitude imagery. *IEEE Trans. Geosci. Remote Sens.* 44, 2972–2982. <https://doi.org/10.1109/TGRS.2006.876288>
- Moser, L., Schmitt, A., Wendleder, A., Roth, A., 2016. Monitoring of the Lac Bam wetland extent using dual-polarized X-band SAR data, *Remote Sensing*.  
<https://doi.org/10.3390/rs8040302>
- Mougin, E., Proisy, C., Marty, G., Fromard, F., Puig, H., Betoulle, J.L., Rudant, J.P., 1999. Multifrequency and Multipolarization Radar Backscattering from Mangrove Forests 37, 94–102.
- Nico, G., Pappalepore, M., Pasquariello, G., Refice, A., Samarelli, S., 2000. Comparison of SAR amplitude vs. coherence flood detection methods - a GIS application. *Int. J. Remote Sens.* 21, 1619–1631. <https://doi.org/10.1080/014311600209931>
- Nigro, J., Slayback, D., Policelli, F., Brakenridge, G.R., 2014. NASA/DFO MODIS Near Real-Time (NRT) Global Flood Mapping Product Evaluation of Flood and Permanent Water Detection.
- Oberstadler, R., Hönsch, H., Huth, D., 1997. Assessment of the mapping capabilities of ERS-1 SAR data for flood mapping: A case study in Germany. *Hydrol. Process.* 11, 1415–1425.
- Ogashawara, I., Curtarelli, M.P., Ferreira, C.M., 2013. The Use of Optical Remote Sensing For Mapping Flooded Areas. *J. Eng. Res. Appl.* 3, 1956–1960.
- Ohki, M., Tadono, T., Itoh, T., Ishii, K., Yamanokuchi, T., Watanabe, M., Shimada, M., 2019. Flood Area Detection Using PALSAR-2 Amplitude and Coherence Data: The Case of the 2015 Heavy Rainfall in Japan. *IEEE J. Sel. Top. Appl. Earth Obs. Remote Sens.* 12,

## References

---

- 2288–2298. <https://doi.org/10.1109/JSTARS.2019.2911596>
- Ormsby, J.P., Blanchard, B.J., Blanchard, A.J., 1985. Detection of Lowland Flooding Using Active Microwave Systems. *Photogramm. Eng. Remote Sensing* 51, 317–328.
- Otsu, N., 1979. A Threshold Selection Method from Gray-Level Histograms. *IEEE Trans. Syst. Man, and Cybern.* 9, 62–66. <https://doi.org/10.1109/TSMC.1979.4310076>
- Paloscia, S., 1998. An empirical approach to estimating leaf area index from multifrequency SAR data. *Int. J. Remote Sens.* 19, 359–364. <https://doi.org/10.1080/014311698216323>
- Papoulis, A., 1991. Probability, random variables, and stochastic processes, McGraw-Hill series in electrical engineering. Communications and signal processing. McGraw-Hill, New York.
- Park, Seonyoung, Im, J., Park, Seohui, Yoo, C., Han, H., Rhee, J., 2018. Classification and mapping of paddy rice by combining Landsat and SAR time series data. *Remote Sens.* 10, 1–22. <https://doi.org/10.3390/rs10030447>
- Pauleit, S., Duhme, F., 2000. Assessing the environmental performance of land cover types for urban planning. *Landsc. Urban Plan.* 52, 1–20. [https://doi.org/10.1016/S0169-2046\(00\)00109-2](https://doi.org/10.1016/S0169-2046(00)00109-2)
- Pierdicca, N., Pulvirenti, L., Chini, M., 2018. Flood Mapping in Vegetated and Urban Areas and Other Challenges: Models and Methods, in: Refice, A., D’Addabbo, A., Capolongo, D. (Eds.), *Flood Monitoring through Remote Sensing*. Springer International Publishing, Cham, Switzerland.
- Pierdicca, N., Pulvirenti, L., Chini, M., Guerriero, L., Candela, L., 2013. Observing floods from space: Experience gained from COSMO-SkyMed observations. *Acta Astronaut.* 84, 122–133. <https://doi.org/10.1016/j.actaastro.2012.10.034>
- Plank, S., Jüssi, M., Martinis, S., Twele, A., 2017. Mapping of flooded vegetation by means of polarimetric sentinel-1 and ALOS-2/PALSAR-2 imagery. *Int. J. Remote Sens.* 38, 3831–3850. <https://doi.org/10.1080/01431161.2017.1306143>
- Pope, K.O., Rejmankova, E., Paris, J.F., Woodruff, R., 1997. Detecting Seasonal Cycle of the Yucatan Peninsula with SIR-C Polarimetric Radar Imagery. *Remote Sens. Environ.* 59, 157–166.
- Preiss, M., Gray, D.A., Stacy, N.J.S., 2006. Detecting scene changes using synthetic aperture radar interferometry. *IEEE Trans. Geosci. Remote Sens.* 44, 2041–2054. <https://doi.org/10.1109/TGRS.2006.872910>
- Preiss, M., Stacy, N., 2006. Coherent change detection: theoretical description and experimental results. Defence Science and Technology Organisation, DSTO–TR–1851, Canberra, ACT, Australia.
- Pulvirenti, L., Chini, M., Pierdicca, N., Boni, G., 2016. Use of SAR data for detecting floodwater in urban and agricultural areas: The role of the interferometric coherence. *IEEE Trans. Geosci. Remote Sens.* 54, 1532–1544. <https://doi.org/10.1109/TGRS.2015.2482001>
- Pulvirenti, L., Pierdicca, N., Chini, M., Guerriero, L., 2013. Monitoring flood evolution in vegetated areas using cosmo-skymed data: The tuscan 2009 case study. *IEEE J. Sel. Top. Appl. Earth Obs. Remote Sens.* 6, 1807–1816. <https://doi.org/10.1109/JSTARS.2012.2219509>
- Pulvirenti, L., Pierdicca, N., Chini, M., Guerriero, L., 2011. An algorithm for operational

## References

---

- flood mapping from Synthetic Aperture Radar (SAR) data using fuzzy logic. *Nat. Hazards Earth Syst. Sci.* 11, 529–540. <https://doi.org/10.5194/nhess-11-529-2011>
- Rabus, B., Wehn, H., Nolan, M., 2010. The importance of soil moisture and soil structure for InSAR phase and backscatter, as determined by FDTD modeling. *IEEE Trans. Geosci. Remote Sens.* 48, 2421–2429. <https://doi.org/10.1109/TGRS.2009.2039353>
- Rao, B.R.M., Dwivedi, R.S., Kushwaha, S.P.S., Bhattacharya, S.N., Anand, J.B., Dasgupta, S., 1999. Monitoring the spatial extent of coastal wetlands using ERS-1 SAR data. *Int. J. Remote Sens.* 20, 2509–2517. <https://doi.org/10.1080/014311699211903>
- Refice, A., Capolongo, D., Pasquariello, G., Addabbo, A.D., Bovenga, F., Nutricato, R., Lovergine, F.P., Pietranera, L., 2014. SAR and InSAR for Flood Monitoring : Examples With COSMO-SkyMed Data. *IEEE J. Sel. Top. Appl. Earth Obs. Remote Sens.* 7, 2711–2722.
- Richards, J.A., 2009. *Remote Sensing with Imaging Radar*. Springer-Verlag, Berlin, Germany.
- Richards, J.A., Woodgate, P.W., Skidmore, A.K., 1987. An explanation of enhanced radar backscattering from flooded forests. *Int. J. Remote Sens.* 8, 1093–1100. <https://doi.org/10.1080/01431168708954756>
- Robertson, L.D., King, D.J., Davies, C., 2015. Object-based image analysis of optical and radar variables for wetland evaluation. *Int. J. Remote Sens.* 36, 5811–5841. <https://doi.org/10.1080/01431161.2015.1109727>
- Rodriguez, E., Martin, J.M., 1992. Theory and design of interferometric synthetic aperture radars. *IEE Proceedings, Part F Radar Signal Process.* 139, 147–159. <https://doi.org/10.1049/ip-f-2.1992.0018>
- Rogger, M., Agnoletti, M., Alaoui, A., Bathurst, J.C., Bodner, G., Borga, M., Chaplot, V., Gallart, F., Glatzel, G., Hall, J., Holden, J., Holko, L., Horn, R., Kiss, A., Kohnova, S., Leitinger, G., Lennartz, B., Parajka, J., Perdigao, R., Peth, S., Plavcova, L., Quinton, J.N., Robinson, M., Salinas, J.L., Santoro, A., Szolgay, J., Tron, S., van den Akker, J.J.H., Viglione, A., Blöschl, G., 2017. Land use change impacts on floods at the catchment scale: Challenges and opportunities for future research. *Water Resour. Res.* 53, 5209–5219. <https://doi.org/10.1002/2017WR020723>. Received
- Sadek, M., Li, X., 2019. Low-Cost Solution for Assessment of Urban Flash Flood Impacts Using Sentinel-2 Satellite Images and Fuzzy Analytic Hierarchy Process: A Case Study of Ras Ghareb City, Egypt. *Adv. Civ. Eng.* <https://doi.org/10.1155/2019/2561215>
- Schepanski, K., Wright, T.J., Knippertz, P., 2012. Evidence for flash floods over deserts from loss of coherence in InSAR imagery. *J. Geophys. Res. Atmos.* 117, 1–10. <https://doi.org/10.1029/2012JD017580>
- Schlaffer, S., Matgen, P., Hollaus, M., Wagner, W., 2015. Flood detection from multi-temporal SAR data using harmonic analysis and change detection. *Int. J. Appl. Earth Obs. Geoinf.* 38, 15–24. <https://doi.org/10.1016/J.JAG.2014.12.001>
- Schmitt, A., Leichtle, T., Huber, M., Roth, A., 2012. On the Use of Dual-Co-Polarized Terrasar-X Data for Wetland Monitoring. *ISPRS - Int. Arch. Photogramm. Remote Sens. Spat. Inf. Sci.* XXXIX-B7, 341–344. <https://doi.org/10.5194/isprsarchives-xxxix-b7-341-2012>
- Schumann, G.-P., Moller, D.K., 2015. Microwave remote sensing of flood inundation. *Phys.*

## References

---

- Chem. Earth. <https://doi.org/10.1016/j.pce.2015.05.002>
- Schumann, G., Hostache, R., Puech, C., Hoffmann, L., Matgen, P., Pappenberger, F., Pfister, L., 2007. High-resolution 3-D flood information from radar imagery for flood hazard management. *IEEE Trans. Geosci. Remote Sens.* 45, 1715–1725.  
<https://doi.org/10.1109/TGRS.2006.888103>
- Scott, C.P., Lohman, R.B., Jordan, T.E., 2017. InSAR constraints on soil moisture evolution after the March 2015 extreme precipitation event in Chile. *Sci. Rep.* 7, 1–9.  
<https://doi.org/10.1038/s41598-017-05123-4>
- Selmi, S., Abdallah, W. Ben, Abdelfattah, R., 2014. Flood mapping using InSAR coherence map, in: *International Archives of the Photogrammetry, Remote Sensing and Spatial Information Sciences - ISPRS Archives*. pp. 161–164.  
<https://doi.org/10.5194/isprsarchives-XL-7-161-2014>
- Seymour, M.S., Cumming, I.G., 1994. Maximum likelihood estimation for SAR interferometry, in: *International Geoscience and Remote Sensing Symposium (IGARSS)*. pp. 2272–2274. <https://doi.org/10.1109/igarss.1994.399711>
- Shen, X., Anagnostou, E.N., Allen, G.H., Robert Brakenridge, G., Kettner, A.J., 2019. Near-real-time non-obstructed flood inundation mapping using synthetic aperture radar. *Remote Sens. Environ.* 221, 302–315. <https://doi.org/10.1016/j.rse.2018.11.008>
- Smith, L.C., 1997. Satellite remote sensing of river inundation area, stage, and discharge: a review. *Hydrol. Process.* 11, 1427–1439.  
[https://doi.org/10.1002/\(sici\)1099-1085\(199708\)11:10<1427::aid-hyp473>3.3.co;2-j](https://doi.org/10.1002/(sici)1099-1085(199708)11:10<1427::aid-hyp473>3.3.co;2-j)
- Soergel, U., Thoennessen, U., Stilla, U., 2003. Visibility analysis of man-made objects in SAR images. 2nd GRSS/ISPRS Jt. Work. Remote Sens. Data Fusion over Urban Areas, URBAN 2003 120–124. <https://doi.org/10.1109/DFUA.2003.1219970>
- Solbø, S., Solheim, I., 2004. Towards operational flood mapping with satellite SAR, in: *ENVISAT/ERS Symposium 2004*. Salzburg, Austria.
- Tanguy, M., Chokmani, K., Bernier, M., Poulin, J., Raymond, S., 2017. River flood mapping in urban areas combining Radarsat-2 data and flood return period data. *Remote Sens. Environ.* 198, 442–459. <https://doi.org/10.1016/j.rse.2017.06.042>
- Thiele, A., Cadario, E., Karsten, S., Thönnessen, U., Soergel, U., 2007. Building Recognition From Multi-Aspect High-Resolution InSAR Data in Urban Areas. *IEEE Trans. Geosci. Remote Sens.* 45, 11.
- Thirion-Lefevre, L., Guinvarc’h, R., 2015. The brewster effect on polarimetric information, in: *International Geoscience and Remote Sensing Symposium (IGARSS)*. pp. 227–230.
- Thomas, R.F., Kingsford, R.T., Lu, Y., Hunter, S.J., 2011. Landsat mapping of annual inundation (1979-2006) of the Macquarie Marshes in semi-arid Australia. *Int. J. Remote Sens.* 32, 4545–4569. <https://doi.org/10.1080/01431161.2010.489064>
- Tingsanchali, T., 2012. Urban flood disaster management. *Procedia Eng.* 32, 25–37.  
<https://doi.org/10.1016/j.proeng.2012.01.1233>
- Touzi, R., Lopes, A., Bruniquel, J., Vachon, P.W., 1999. Coherence Estimation for SAR Imagery. *IEEE Trans. Geosci. Remote Sens.* 37, 135–149.
- Townsend, P.A., 2002. Relationships between forest structure and the detection of flood inundation in forested wetlands using C-band SAR. *Int. J. Remote Sens.* 23, 443–460.  
<https://doi.org/10.1080/01431160010014738>



## References

---

- Townsend, P.A., Foster, J.R., 2002. Assessing flooding and vegetation structure in forested wetlands using radarsat SAR imagery, in: International Geoscience and Remote Sensing Symposium (IGARSS). pp. 1171–1173. <https://doi.org/10.1109/igarss.2002.1025811>
- Townsend, P.A., Walsh, S.J., 1998. Modeling floodplain inundation using an integrated GIS with radar and optical remote sensing. *Geomorphology* 21, 295–312. [https://doi.org/10.1016/s0169-555x\(97\)00069-x](https://doi.org/10.1016/s0169-555x(97)00069-x)
- Töyrä, J., Pietroniro, A., Martz, L.W., 2001. Multisensor hydrologic assessment of a freshwater wetland. *Remote Sens. Environ.* 75, 162–173. [https://doi.org/10.1016/S0034-4257\(00\)00164-4](https://doi.org/10.1016/S0034-4257(00)00164-4)
- Tralli, D.M., Blom, R.G., Zlotnicki, V., Donnellan, A., Evans, D.L., 2005. Satellite remote sensing of earthquake, volcano, flood, landslide and coastal inundation hazards. *ISPRS J. Photogramm. Remote Sens.* 59, 185–198. <https://doi.org/10.1016/j.isprsjprs.2005.02.002>
- Tsyganskaya, V., Martinis, S., Marzahn, P., Ludwig, R., 2018a. Detection of temporary flooded vegetation using Sentinel-1 time series data. *Remote Sens.* 10. <https://doi.org/10.3390/rs10081286>
- Tsyganskaya, V., Martinis, S., Marzahn, P., Ludwig, R., 2018b. SAR-based detection of flooded vegetation—a review of characteristics and approaches. *Int. J. Remote Sens.* 39, 2255–2293. <https://doi.org/10.1080/01431161.2017.1420938>
- Twele, A., Cao, W., Plank, S., Martinis, S., 2016. Sentinel-1-based flood mapping: a fully automated processing chain. *Int. J. Remote Sens.* 37, 2990–3004. <https://doi.org/10.1080/01431161.2016.1192304>
- Ulaby, F.T., Batlivala, P.P., Dobson, M.C., 1978. Microwave Backscatter Dependence on Surface Roughness, Soil Moisture, and Soil Texture: Part I—Bare Soil. *IEEE Trans. Geosci. Electron.* 16, 286–295. <https://doi.org/10.1109/TGE.1978.294586>
- Ulaby, F.T., Moore, R.K., Fung, A.K., 1986. *Microwave Remote Sensing: Active and Passive. Vol. III – From theory to applications.* Artech House, Dedham, Massachusetts, USA.
- Ulaby, F.T., Moore, R.K., Fung, A.K., 1982. *Microwave Remote Sensing: Active and passive. Vol. II – Radar remote sensing and surface scattering and emission theory.* Addison-Wesley, Reading, Massachusetts, USA.
- Usai, S., Klees, R., 1999. SAR interferometry on a very long time scale: A study of the interferometric characteristics of man-made features. *IEEE Trans. Geosci. Remote Sens.* 37, 2118–2123. <https://doi.org/10.1109/36.774730>
- Viglione, A., Merz, B., Nguyen, D., Parajka, J., Nester, T., Blöschl, G., 2016. Attribution of regional flood changes based on scaling fingerprints. *Water Resour. Res.* 52, 5322–5340. <https://doi.org/10.1002/2016WR019036>. Received
- Volpi, M., Petropoulos, G.P., Kanevski, M., 2013. Flooding extent cartography with Landsat TM imagery and regularized kernel Fisher’s discriminant analysis. *Comput. Geosci.* 57, 24–31. <https://doi.org/10.1016/j.cageo.2013.03.009>
- Voormansik, K., Praks, J., Antropov, O., Jagomagi, J., Zalite, K., 2014. Flood mapping with terraSAR-X in forested regions in estonia. *IEEE J. Sel. Top. Appl. Earth Obs. Remote Sens.* 7, 562–577. <https://doi.org/10.1109/JSTARS.2013.2283340>
- Wang, Y., 2004. Using Landsat 7 TM data acquired days after a flood event to delineate the maximum flood extent on a coastal floodplain. *Int. J. Remote Sens.* 25, 959–974.

## References

---

- <https://doi.org/10.1080/0143116031000150022>
- Wang, Y., 2002. Mapping extent of floods: What we have learned and how we can do better. *Nat. Hazards Rev.* 3, 68–73. [https://doi.org/10.1061/\(ASCE\)1527-6988\(2002\)3:2\(68\)](https://doi.org/10.1061/(ASCE)1527-6988(2002)3:2(68))
- Wang, Y., Day, J.L., Davis, F.W., Melack, J.M., 1993. Modeling L-Band Radar Backscatter of Alaskan Boreal Forest. *IEEE Trans. Geosci. Remote Sens.* 31, 1146–1154. <https://doi.org/10.1109/36.317448>
- Wang, Y., Hess, L.L., Filoso, S., Melack, J.M., 1995. Understanding the radar backscattering from flooded and nonflooded Amazonian forests: Results from canopy backscatter modeling. *Remote Sens. Environ.* 54, 324–332. [https://doi.org/10.1016/0034-4257\(95\)00140-9](https://doi.org/10.1016/0034-4257(95)00140-9)
- Watanabe, M., Matsumoto, M., Shimada, M., Asaka, T., Nishikawa, H., Sato, M., 2010. Simultaneous observation data of GB-SAR/PiSAR to detect flooding in an urban area. *EURASIP J. Adv. Signal Process.* 2010. <https://doi.org/10.1155/2010/560512>
- Watanabe, M., Matsumoto, M., Shimada, M., Sato, M., 2008. GB-SAR/PiSAR simultaneous experiment for a trial of flood area detection, in: *International Geoscience and Remote Sensing Symposium (IGARSS)*. pp. 27–30. <https://doi.org/10.1109/IGARSS.2008.4779274>
- Wdowinski, S., Kim, S.W., Amelung, F., Dixon, T.H., Miralles-Wilhelm, F., Sonenshein, R., 2008. Space-based detection of wetlands' surface water level changes from L-band SAR interferometry. *Remote Sens. Environ.* 112, 681–696. <https://doi.org/10.1016/j.rse.2007.06.008>
- Wegner, J.D., Soergel, U., Thiele, A., 2009. Building extraction in urban scenes from highresolution InSAR data and optical imagery. 2009 *Jt. Urban Remote Sens. Event*. <https://doi.org/10.1109/URS.2009.5137481>
- Weydahl, D.J., 2001a. Analysis of ERS tandem SAR coherence from glaciers, valleys, and fjord ice on Svalbard. *IEEE Trans. Geosci. Remote Sens.* 39, 2029–2039. <https://doi.org/10.1109/36.951093>
- Weydahl, D.J., 2001b. Analysis of ERS SAR coherence images acquired over Vegetated areas and Urban Features. *Int. J. Remote Sens.* 22, 2811–2830. <https://doi.org/10.1080/01431160010006412>
- Weydahl, D.J., 1996. Flood monitoring in Norway using ERS-1 SAR images, in: *International Geoscience and Remote Sensing Symposium (IGARSS)*. pp. 151–153. <https://doi.org/10.1109/igarss.1996.516274>
- Wieland, M., Martinis, S., 2019. A Modular Processing Chain for Automated Flood Monitoring from Multi-Spectral Satellite Data. *Remote Sens.* 11, 2330. <https://doi.org/10.3390/rs11192330>
- Willner, S.N., Levermann, A., Zhao, F., Frieler, K., 2018. Adaptation required to preserve future high-end river flood risk at present levels. *Sci. Adv.* 4, 1–9. <https://doi.org/10.1126/sciadv.aao1914>
- Wohlfart, C., Winkler, K., Wendleder, A., Roth, A., 2018. TerraSAR-X and wetlands: A review. *Remote Sens.* 10, 1–24. <https://doi.org/10.3390/rs10060916>
- Wood, M., Hostache, R., Neal, J., Wagener, T., Giustarini, L., Chini, M., Corato, G., Matgen, P., Bates, P., 2016. Calibration of channel depth and friction parameters in the LISFLOOD-FP hydraulic model using medium-resolution SAR data and identifiability

## References

---

- techniques. *Hydrol. Earth Syst. Sci.* 20, 4983–4997.  
<https://doi.org/10.5194/hess-20-4983-2016>
- Wright, P.A., Quegan, S., Wheadon, N.S., Hall, C.D., 2003. Faraday rotation effects on L-band spaceborne SAR data. *IEEE Trans. Geosci. Remote Sens.* 41, 2735–2744.  
<https://doi.org/10.1109/TGRS.2003.815399>
- Xiang, D., Ban, Y., Su, Y., 2016. The cross-scattering component of polarimetric SAR in urban areas and its application to model-based scattering decomposition. *Int. J. Remote Sens.* 37, 3729–3752. <https://doi.org/10.1080/01431161.2016.1201235>
- Zebker, H.A., Villasenor, J., 1992. Decorrelation in Interferometric Radar Echoes. *IEEE Trans. Geosci. Remote Sens.* 30, 950–959.
- Zhang, B., Perrie, W., He, Y., 2011. Wind speed retrieval from RADARSAT-2 quad-polarization images using a new polarization ratio model. *J. Geophys. Res. Ocean.* 116, 1–13. <https://doi.org/10.1029/2010JC006522>
- Zwieback, S., Hensley, S., Hajnsek, I., 2015. Assessment of soil moisture effects on L-band radar interferometry. *Remote Sens. Environ.* 164, 77–89.  
<https://doi.org/10.1016/j.rse.2015.04.012>

# Curriculum Vitae

### Personal Information

Name: Yu Li  
Place of Birth: Hubei, China  
Nationality: Chinese  
Email: yulicug@gmail.com

### Education

- 2017-2020: Ph.D. in Physical Geography,  
LMU Munich
- 2012-2015 Master in Mathematical Geology,  
China University of Geosciences (Wuhan)
- 2008-2012: Bachelor in Geo-information Science and Technology,  
China University of Geosciences (Wuhan)

### Professional Experience

- 2016-2019: PhD  
German Aerospace Center (DLR)  
PhD in SAR remote sensing: “Flood mapping in rural and urban areas with multi-temporal SAR intensity and InSAR coherence”, enrollment university: LMU Munich.
- 2015-2016: Research assistant  
German Research Center for Geosciences (GFZ)  
Mining waste monitoring with hyperspectral remote sensing data.

### Research Interests

My research interests mainly focus on natural disasters (e.g., flooding) mapping and monitoring with multi-temporal SAR/InSAR data. For this purpose, I largely leverage machine learning methods including both unsupervised learning such as mixture models and (semi-) supervised/active learning with deep neural networks. I am also interested in domain knowledge integration and uncertainty quantification with Bayesian modeling.

### Publications

- Li, Y.**, Martinis, S., Wieland, M., Schlaffer, S., Natsuak, R., Ludwig, R., 2019. Urban flood mapping using SAR intensity and interferometric coherence via Bayesian network fusion. *Remote Sensing*, 11, 2231.
- Li, Y.**, Martinis, S., Wieland, M., 2019. Urban flood mapping with an active self-learning convolutional neural network based on TerraSAR-X intensity and interferometric coherence. *ISPRS Journal of Photogrammetry and Remote Sensing*, 152, 178-191
- Wieland., M., **Li, Y.**, Martinis, S., 2019. Multi-sensor cloud and cloud shadow segmentation with a convolutional neural network. *Remote Sensing of Environment*, 230, 111203.
- Li, Y.**, Martinis, S., Plank, S., Ludwig, R., 2018. An automatic change detection approach for rapid flood mapping in Sentinel-1 data. *International Journal of Applied Earth Observation and Geoinformation*, 73, 123-135.
- Li, Y.**, Zuo, R., Bai, Y., Yang, M., 2014. The relationship between magnetic susceptibility and elemental variations for mineralized rocks. *Journal of Geochemical Exploration*, 146, 17-26.

### Conference abstracts

- Li, Y.**, Martinis, S., Wieland, M., 2019. A Temporal-ensembling Active Self-learning CNN Framework for Urban Flood Mapping by Means of Multi-temporal SAR Intensity and Coherence Information. Living Planet Symposium 2019, Milan, Italy.
- Wieland, M., **Li, Y.**, Martinis, S., 2019. Towards operational multi-resolution monitoring of water bodies from optical satellite images. Living Planet Symposium 2019, Milan, Italy.
- Wieland, M., Martinis, S., **Li, Y.**, 2019. Semantic Segmentation of Water Bodies in Multi-spectral Satellite Images for Situational Awareness in Emergency Response. Munich Remote Sensing Symposium (MRSS19), Munich, Germany.